Mechanics of Solids and Fracture

Ho Sung Kim

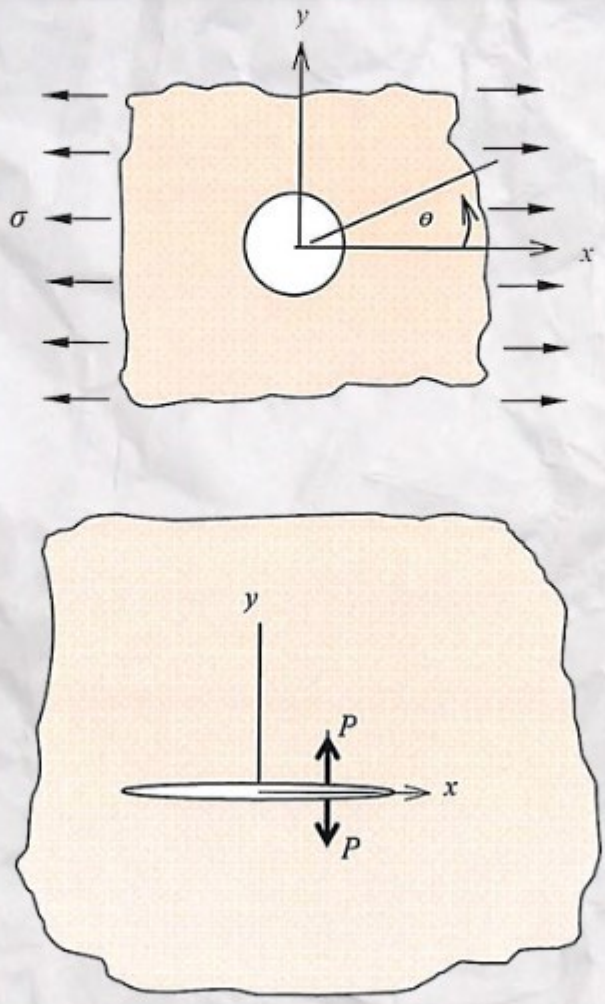

Ho Sung Kim

Mechanics of Solids and Fracture

Mechanics of Solids and Fracture
1st edition

ISBN 978-87-403-0438-1

Contents

Preface

The level of knowledge content given in this book is designed for the students who have completed elementary mechanics of solids for stresses and strains associated with various geometries including simple trusses, beams, shafts, columns, etc. At the successful completion of understanding the content provided, the students will be able to reach a stage where they can do self-directed learning at any further advanced level in the area of mechanics of solids. The emphasis is given on the fundamental concepts for students to quickly follow through for an advanced level if required in the future. Fracture mechanics is included in this book with necessary preliminary steps for those who might have had difficulties with the subject in the past.

The essence of mechanics of solids is lies in stress-strain analysis ultimately for the fail-safe design of structural components. It is important to keep in mind that such analysis would be useless without various criteria for yielding, failure, fracture, and fatigue. Materials behaviour is more complex than some students might think. Materials fail sometimes at higher or lower stress than the stress calculated. Some materials are more sensitive in failure to stress concentration than some other materials. They fail sometimes in a ductile manner and some other times in a brittle manner. The ductility of a material is not only a material property but also is affected by its geometry and loading condition. One approach would be applicable to some particular cases while the other approach is more appropriate for some other cases.

Engineering practitioners will be able to find this book useful as well for the fail-safe design, and for a way of thinking in making engineering decisions.

This book owes to the Lecture Notes developed for many years in the past. I would like to thank Ms Carol Walkins of the Univerity of Newcastle, Callaghan, for typing in earlier years. I am grateful to Mr Kam Choong Lee of PSB Academy in Singapore for the feedback on Lecture Notes before I transformed that into this textbook, and for further proofreading of the manuscript. Also, thanks go to Ms Haleh Allameh Haery of the Univerity of Newcastle, Callaghan, for assisting with some graphic material, invaluable feedback and proofreading.

Ho Sung Kim

List of Symbols

a : crack length
A : constant
B : specimen thickness, constant
C : constant, compliance
C_{ij} : compliance tensor
D : Damage
E : modulus of elasticity for axial loading (Young' modulus)
E_{fa} : fatigue modulus
F: force
G : energy release rate
H : activation energy
h_a : thickness of adhesive layer
K : stress intensity factor, bulk modulus, kinetic energy
K_t: stress concentration factor
k : constant
K_{IC} : fracture toughness for mode I
m : constant
N : number of cycles
n : constant
P : load
p : pressure
R : specific fracture energy, stress ratio in fatigue, gas constant, radius of curvature
r_p : plastic zone size
S : span
S_{ij} : stiffness tensor
T : temperature
t : time
u, v, w : components of displacement in x, y and z directions respectively
V : volume
W : width
Y : geometry factor

δ : crack tip opening displacement
δ_c : critical crack tip opening displacement
ε : strain
γ : engineering shear strain, constant

τ : shear stress
ν : poisson's ratio
σ : stress

Λ : strain energy
Λ_0 : strain energy density
Π : total potential energy

1 Stress And Strain

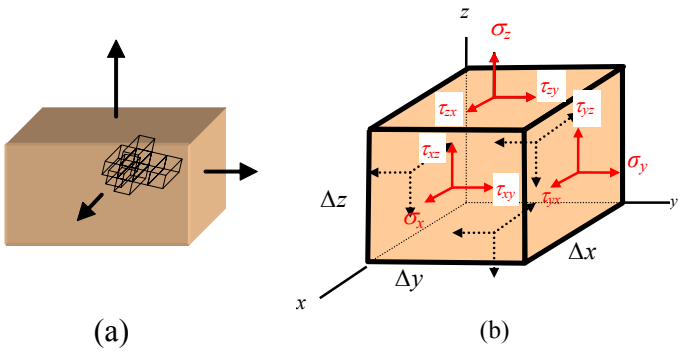

Figure 1.1 (a) A body subjected to uniform stress; and (b) one of cubes in '(a)' subjected to uniform stress distribution.

1.1 Stress at a point

The stress components on a cubical element may be useful for describing fundamental relations with reference to the coordinate system. The cubical element is one of building blocks constituting the elastic body. **Figure 1.1 (a)** shows a body subjected to normal uniform stress distribution. The body is assumed to consist of infinite number of cubical elements. **Figure 1.1 (b)** shows one of cubes, representing a point in the body, in which nine stress components are used to describe a stress state in terms of location, magnitude and direction:

$$\begin{pmatrix} \sigma_x & \tau_{xy} & \tau_{xz} \\ \tau_{yx} & \sigma_y & \tau_{yz} \\ \tau_{zx} & \tau_{zy} & \sigma_z \end{pmatrix} \text{or} \begin{pmatrix} \sigma_{xx} & \tau_{xy} & \tau_{xz} \\ \tau_{yx} & \sigma_{yy} & \tau_{yz} \\ \tau_{zx} & \tau_{zy} & \sigma_{zz} \end{pmatrix}.$$

The first subscript of each stress component indicates plane and the second direction. The nine stress components can be reduced to six components because some of stress components are equal. This can be found by taking the summation of the moments (ΣM) about z-axis, y-axis and x-axis:

$\Sigma M_z=0$ for z- axis,

$$\tau_{xy}(\Delta y\, \Delta z)\, \Delta x = \tau_{yx}\, (\Delta x \Delta z)\, \Delta y \tag{1.1}$$

and therefore $\tau_{xy} - \tau_{yx}$.

Similarly for x and y axes, $\tau_{yz} = \tau_{zy}$ and $\tau_{zx} = \tau_{xz}$. Consequently, the state of stress at a point can be now described by six components: $\sigma_x,\ \sigma_y,\ \sigma_z,\ \tau_{xy},\ \tau_{xz},\ \tau_{yz}$.

1.2 Relation of principal stress with other stress components

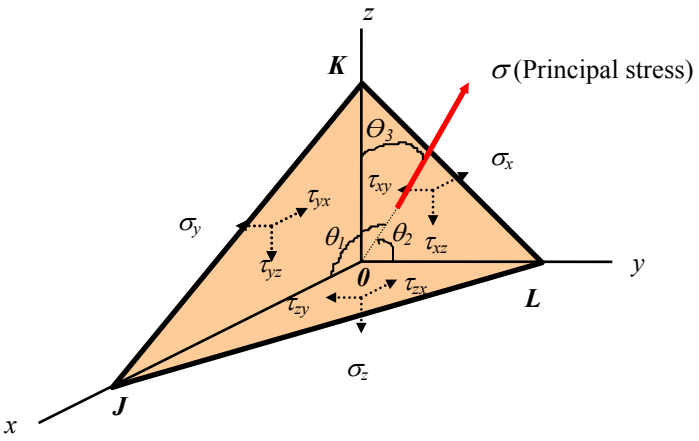

Figure 1.2 Stress components on a tetrahedron.

When a body subjected to external forces, a range of different planes may considered for stress analysis. The planes where no shearing stresses but normal stresses exist are called the *principal planes*. The normal stress on each *principal plane* is referred to as the *principal stress*. **Figure 1.2** shows the *principal stress* on area JKL as a result of choosing the coordinate system in a particular orientation and for a particular position.

Let $\cos\theta_1 = l$, $\cos\theta_2 = m$ and $\cos\theta_3 = n$. The areas on the tetrahedron are found in relation with A or area JKL:

Area K0L = Al (or = $A\cos\theta_l$)
Area K0J = Am
Area J0L = An.

The principal stress (σ) in **Figure 1.2** may be related with the stress components by taking the summation of the forces in x, y and z directions:

$\Sigma F_x=0$,

$$(\sigma - \sigma_x)Al - \tau_{yx}Am - \tau_{zx}An = 0 \tag{1.2a}$$

$\Sigma F_y=0$,

$$-\tau_{xy}Al + (\sigma - \sigma_y)Am - \tau_{zy}An = 0 \tag{1.2b}$$

$\Sigma F_z=0$,

$$-\tau_{xz}Al - \tau_{yz}Am + (\sigma - \sigma_z)An = 0 \tag{1.2c}$$

These three equations are compacted for relations between the principal stresses and other stress components:

$$\begin{Bmatrix} (\sigma-\sigma_x) & -\tau_{yx} & -\tau_{zx} \\ -\tau_{xy} & (\sigma-\sigma_y) & -\tau_{zy} \\ -\tau_{xz} & -\tau_{yz} & (\sigma-\sigma_z) \end{Bmatrix} \begin{Bmatrix} l \\ m \\ n \end{Bmatrix} = 0 \tag{1.2d}$$

The direction cosines l, m and n can be eliminated from the three equations to find an expression for σ.

$$\sigma^3 - I_1\sigma^2 + I_2\sigma - I_3 = 0 \tag{1.2e}$$

where

$$\begin{aligned} I_1 &= \sigma_x + \sigma_y + \sigma_z \\ I_2 &= \sigma_x\sigma_y + \sigma_y\sigma_z + \sigma_x\sigma_z - \tau_{xy}^2 - \tau_{xz}^2 - \tau_{yz}^2 \\ I_3 &= \sigma_x\sigma_y\sigma_z + 2\tau_{xy}\tau_{yz}\tau_{xz} - \sigma_x\tau_{yz}^2 - \sigma_y\tau_{xz}^2 - \sigma_z\tau_{xy}^2 \end{aligned} \tag{1.2f}$$

As seen in Equation (1.2e), I_1, I_2 and I_3 are not functions of direction cosines. As such, they are independent of the coordinate system location and therefore they are called the *invariants*.

1.3 Stresses on oblique plane

Any other planes than the *principal planes* may be called the *oblique planes* in which always shear stress exists when subjected to external forces [**Figure 1.3 (a)**]. The total stress (S) on the *oblique plane* can be resolved into three components (S_x, S_y, and S_z) [**Figure 1.3 (b)**] and

$$S^2 = S_x^2 + S_y^2 + S_z^2 \tag{1.3a}$$

Taking the summation of the forces in the x, y and z directions yields:

$$\begin{aligned} S_x &= \sigma_x l + \tau_{yx} m + \tau_{zx} n \\ S_y &= \tau_{xy} l + \sigma_y m + \tau_{zy} n \\ S_z &= \tau_{xz} l + \tau_{yz} m + \sigma_z n \end{aligned} \tag{1.3b}$$

The normal stress (σ_n) may be found in terms of S_x, S_y and S_z [**Figure 1.3 (c)**] by projecting the total stress components (S_x, S_y, and S_z) onto the normal stress direction:

$$\sigma_n = S_x l + S_y m + S_z n \tag{1.3c}$$

$$\text{Also, } S^2 = \sigma_n^2 + \tau^2 \tag{1.3d}$$

Therefore, the shear stress is found as a function of principle (normal) stresses (σ_1, σ_2 and σ_3):

$$\tau^2 = (\sigma_1-\sigma_2)^2 l^2 m^2 + (\sigma_1-\sigma_3)^2 l^2 n^2 + (\sigma_2-\sigma_3)^2 m^2 n^2 \tag{1.4}$$

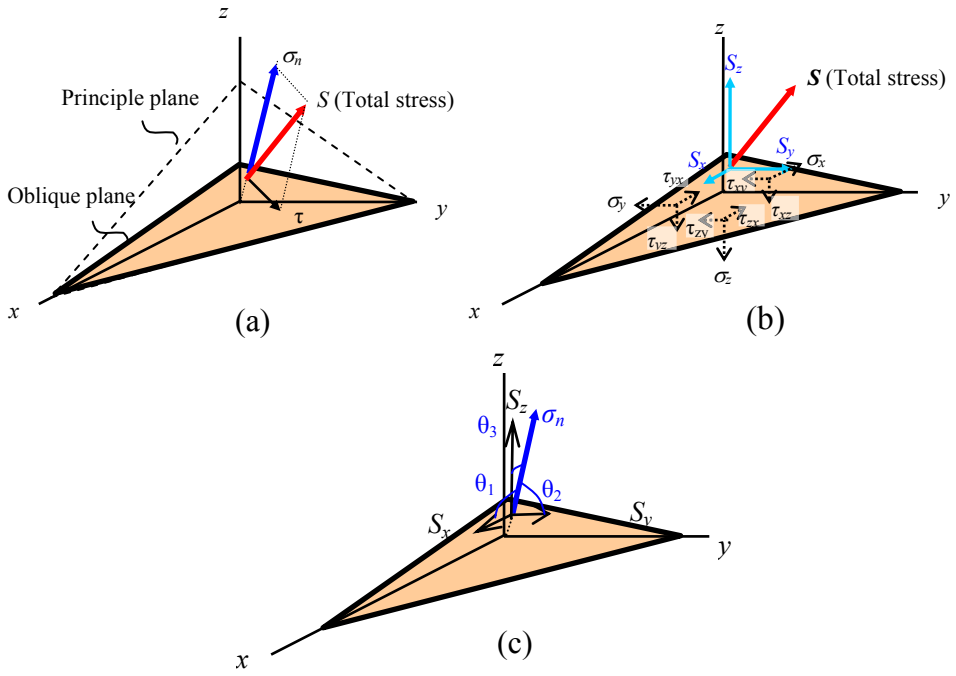

Figure 1.3 Stress components on oblique plane: (a) total stress, *S*, consisting of normal stress (σ_n) and shear stress (τ); (b) total stress components (S_x, S_y, and S_z) in *x*, *y*, and *z* directions; and (c) normal stress components of the total stress can be obtained by projecting total stress components onto the normal stress direction.

The principal (maximum) shear stresses (τ_1, τ_2, and τ_3) occur at an angle of 45° with the three principal axes as shown in **Figure 1.4** and found to be

$$\tau_1 = \frac{\sigma_2 - \sigma_3}{2}$$

$$\tau_2 = \frac{\sigma_1 - \sigma_3}{2} \tag{1.5}$$

$$\tau_3 = \frac{\sigma_1 - \sigma_2}{2}.$$

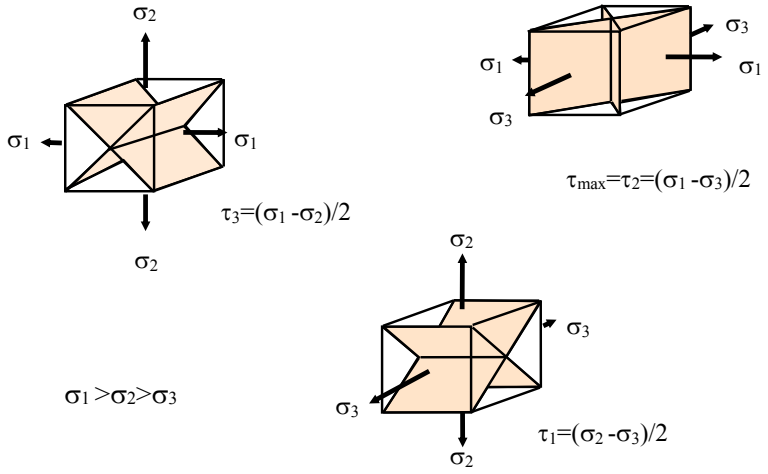

Figure 1.4 The maximum shear planes at an angle of 45° with the three principal axes.

The maximum shear stress criterion (or Tresca yield criterion) assumes that yielding occurs when the maximum shear stress ($\tau_{\max} = \frac{\sigma_1 - \sigma_3}{2}$) reaches its yielding point. In the case of uni-axial loading, the maximum principle stress (σ_1) reaches its yielding point (σ_{ys}) so that $\sigma_1 = \sigma_{ys}$, $\sigma_2 = \sigma_3 = 0$, and the maximum shear stress becomes:

$$\tau_{\max} = \frac{\sigma_1 - \sigma_3}{2} = \frac{\sigma_1 - 0}{2} = \frac{\sigma_{ys}}{2}. \tag{1.6}$$

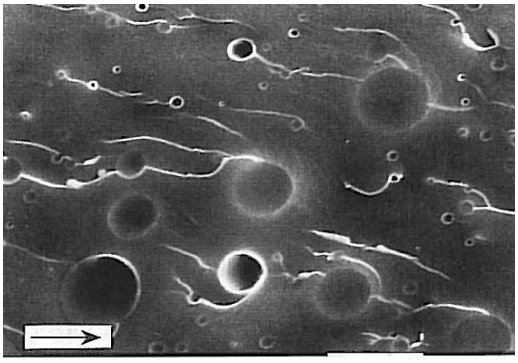

Figure 1.5 Rubber modified epoxy showing cavities on fracture surface.
The arrow indicates fracture propagation direction and the bar represents 10 μm. [After Kim and Ma, 1996] [1]

In general, the deformation of an element consists of volume and shape changes. The volume change is a result of proportional change in element edge lengths. In contrast, the shape change is a result of disproportional change in element edge lengths as well as element corner angle change. The former is associated with volumetric modulus (K) and hydrostatic stress (or mean stress) while the latter is associated with shear modulus (G) and shear stress. For example, the hydrostatic stress creates cavities during deformation as shown in **Figure 1.5** or increases the brittleness while shear stress contributes to the material flow. The total stress for deformation consists of hydrostatic stress and stress deviator i.e.

Total stress = Hydrostatic (or mean) stress (σ_m) + Stress deviator.

The *hydrostatic stress* or *mean stress* is defined as

$$\sigma_m = \frac{I_1}{3} = \frac{\sigma_x + \sigma_y + \sigma_z}{3} = \frac{\sigma_1 + \sigma_2 + \sigma_3}{3} \tag{1.7}$$

and the *stress deviator* (σ'_{ij}) can be found by subtracting the hydrostatic stress from the total stress:

$$\begin{bmatrix} \sigma_x & \tau_{xy} & \tau_{xz} \\ \tau_{yx} & \sigma_y & \tau_{yz} \\ \tau_{zx} & \tau_{zy} & \sigma_z \end{bmatrix} - \begin{bmatrix} \sigma_m & 0 & 0 \\ 0 & \sigma_m & 0 \\ 0 & 0 & \sigma_m \end{bmatrix} =$$

$$\begin{bmatrix} \frac{2\sigma_x - \sigma_y - \sigma_z}{3} & \tau_{xy} & \tau_{xz} \\ \tau_{yx} & \frac{2\sigma_y - \sigma_x - \sigma_z}{3} & \tau_{yz} \\ \tau_{zx} & \tau_{zy} & \frac{2\sigma_z - \sigma_x - \sigma_y}{3} \end{bmatrix} \tag{1.8}$$

This relation is graphically shown in **Figure 1.6**.

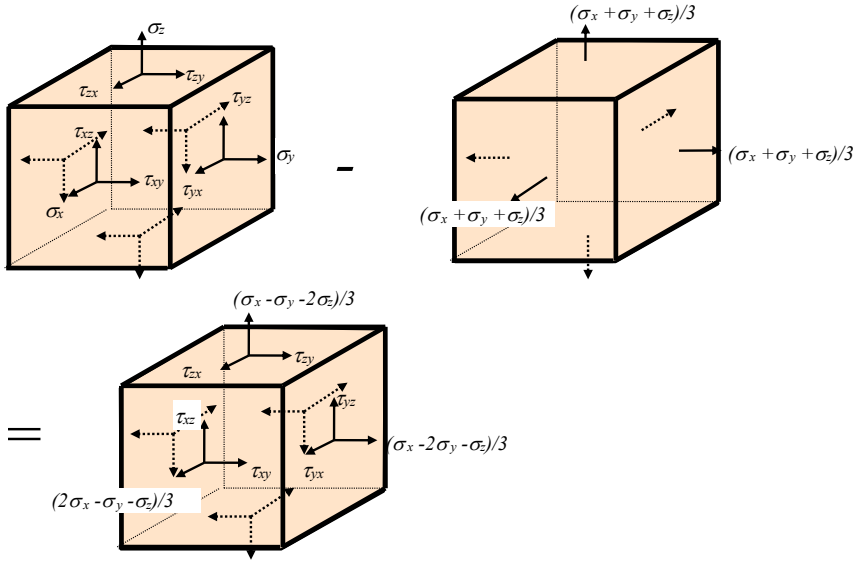

Figure 1.6 Superposition of stress components.

It can easily be shown that the *stress deviator* involves the *principal shear stresses*. For example,

$$\sigma'_x = \frac{2\sigma_x - \sigma_y - \sigma_z}{3}. \tag{1.9}$$

If we choose principal stresses in the equation, the *stress deviator* becomes a function of *principal shear stresses*,

$$\sigma'_1 = \frac{2\sigma_1 - \sigma_2 - \sigma_3}{3} = \frac{2}{3}\frac{(\sigma_1 - \sigma_2) + (\sigma_1 - \sigma_3)}{2} = \frac{2}{3}(\tau_3 + \tau_2) \tag{1.10}$$

Similarly,

$$\sigma'_2 = \frac{2\sigma_2 - \sigma_1 - \sigma_3}{3} = \frac{2}{3}\frac{(\sigma_2 - \sigma_1) + (\sigma_2 - \sigma_3)}{2} = \frac{2}{3}(-\tau_3 + \tau_1) \tag{1.11}$$

$$\sigma'_3 = \frac{2\sigma_3 - \sigma_1 - \sigma_2}{3} = \frac{2}{3}\frac{(\sigma_3 - \sigma_1) + (\sigma_3 - \sigma_2)}{2} = \frac{-2}{3}(\tau_2 + \tau_1) \tag{1.12}$$

where τ_1 τ_2 and τ_3 are the *principal shear stresses*.

1.4 3D Mohr's circle representation

The three *principal stresses* (σ_1, σ_2, σ_3) with the *maximum shear stresses* (τ_1, τ_2 and τ_3) can graphically be represented as shown in **Figure 1.7**. The radius of each circle represents the maximum (or principle) shear stress. Accordingly, Equation (1.5) can be found from the Mohr's circle. **Figure 1.7 (a)** shows a case of uni-axial

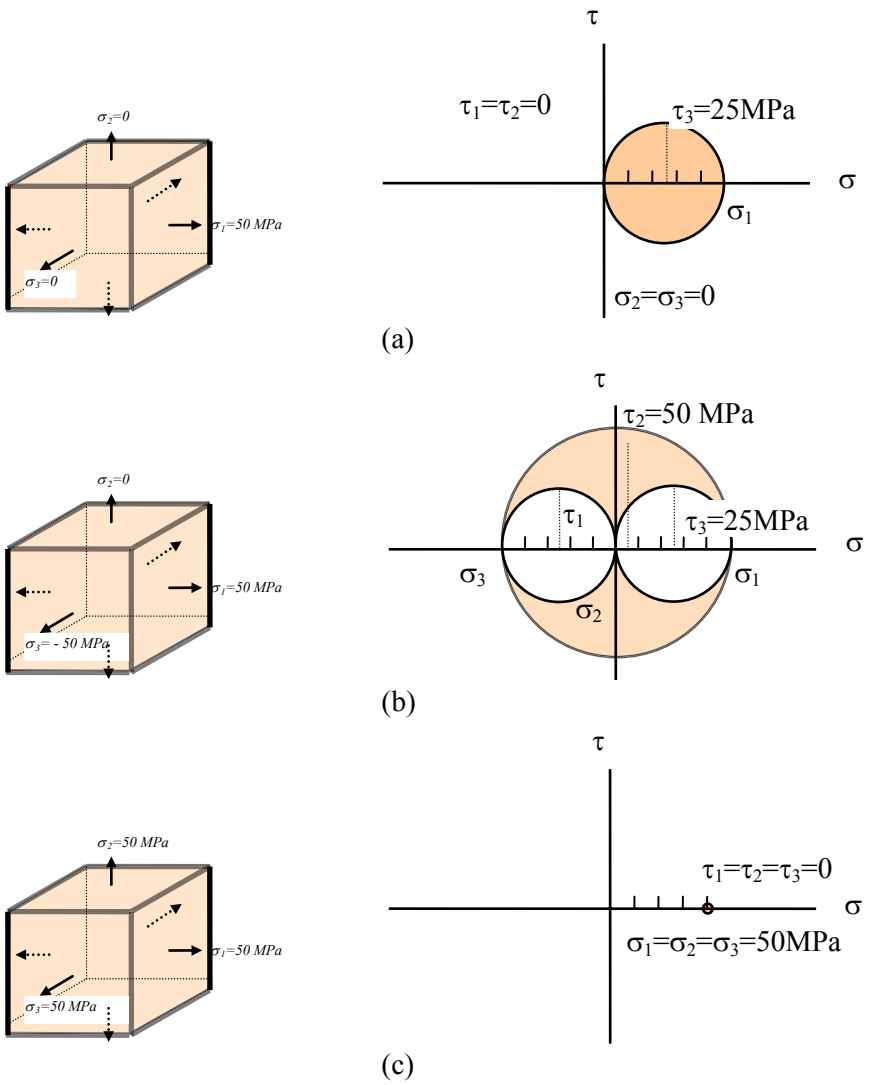

Figure 1.7 Various states of stress on elemental cube and Mohr's circles; (a) uni-axial tension; (b) tension and compression without hydrostatic stress; and (c) hydrostatic stress without shear stress.

tensile loading (σ_1) with $\sigma_2=\sigma_3=0$. If s_3 varies from zero to -50MPa (compressive stress), the principal shear stresses (τ_1 and τ_2) increase and becomes a state of stress where hydrostatic stress is zero as given in **Figure 1.7 (b)**, resulting in more chances for material flow or high ductility than that of the case in **Figure 1.7 (a)** because of the increase in shear stress. **Figure 1.7 (c)** is the limiting case where the three circles reduces to a point where $\sigma_1=\sigma_2=\sigma_3$=50MPa and the three principle shear stresses are zero. In this case, no material ductility is possible in the absence of *stress deviator.* Therefore, it is theoretically possible to have a stress state where the hydrostatic stress component exists without the stress deviator. Examples for the state of stress where relatively large *principal shear stresses* are involved are found in various processes in metal forming (e.g. wire drawing through a die) involving lateral compressive stresses and a longitudinal tensile stress. Also, some localized deformation of reinforcing particles on fracture surfaces of advanced materials is caused by such a state of stress involving large shear stresses as shown in **Figure 1.8**.

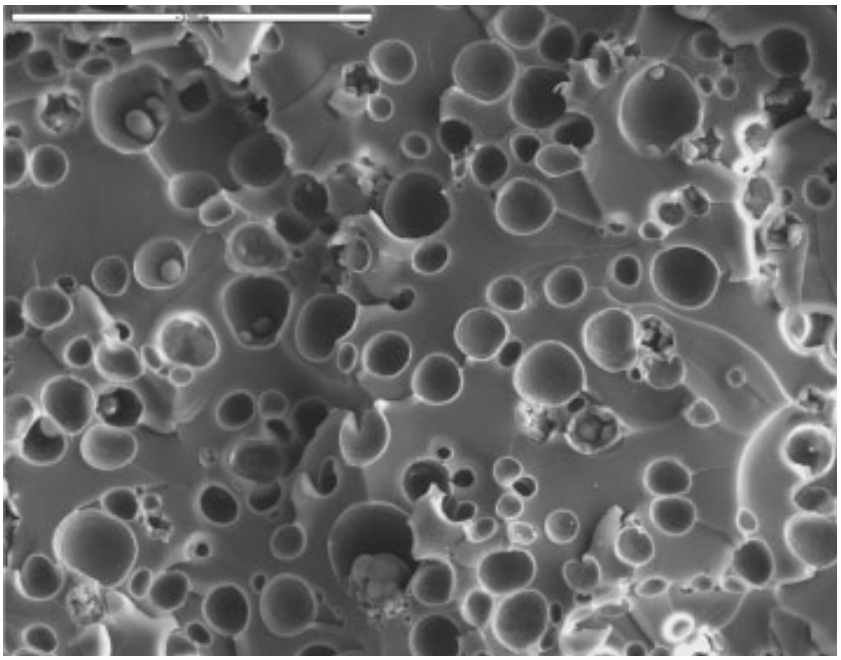

Figure 1.8 Fracture surface of hollow microsphere reinforced epoxy under plane strain in the vicinity of initial crack tip. Each hollow-microsphere experienced a tensile stress in the direction perpendicular to the fracture surface and simultaneously lateral compressive stresses. The crack propagation direction is from top to bottom. The scale bar represents 100 μm. [After Kim, 2007][2]

1.5 Strain at a point

As previously discussed, the deformation is due to the volume and shape change. We need to define the displacement components. When a point P moves to P' in coordinates x, y, z as shown in **Figure 1.9**, respective u, v and w are called displacement components. To find a general form of strain, let us consider first the length change using an element subjected to a load in the x-direction as shown in **Figure 1.10**. When the load is applied, the solid line becomes the dashed line. Accordingly, A moves to A' and B moves to B' and the x direction normal strain of the infinitesimal segment is given by

$$e_x = e_x = \frac{A'B' - AB}{AB} = \frac{dx + \frac{\partial u}{\partial x}dx - dx}{dx} = \frac{\partial u}{\partial x}. \tag{1.13a}$$

Similarly, the displacement derivatives for y and z directions can be found:

$$e_{yy} = \frac{\partial v}{\partial y},\ e_{zz} = \frac{\partial w}{\partial z}. \tag{1.13b}$$

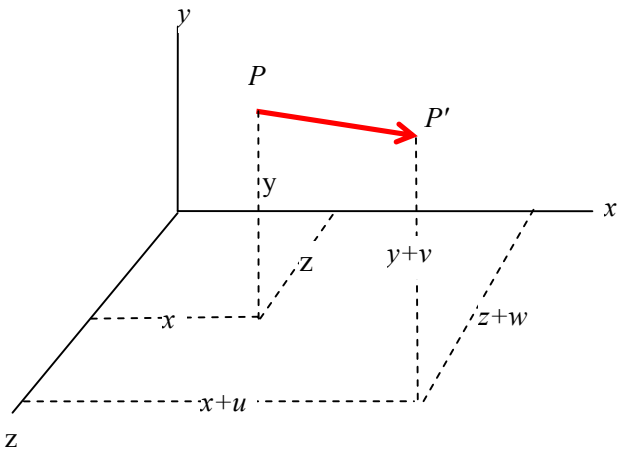

Figure 1.9 Displacement of a point P.

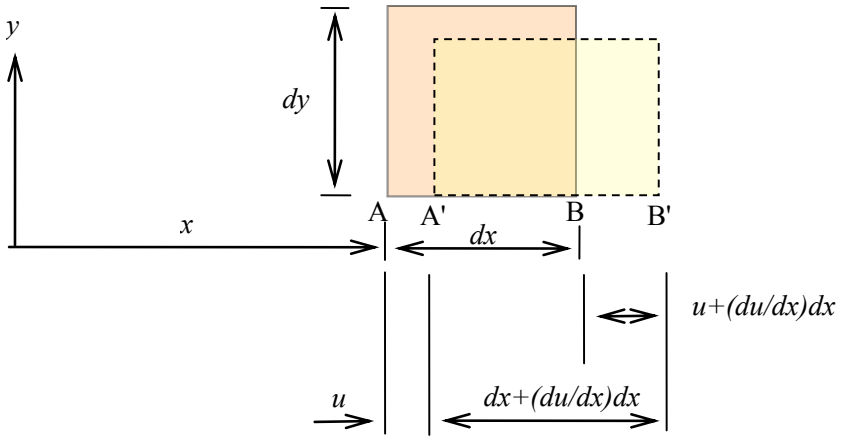

Figure 1.10 Deformation in the x-direction.

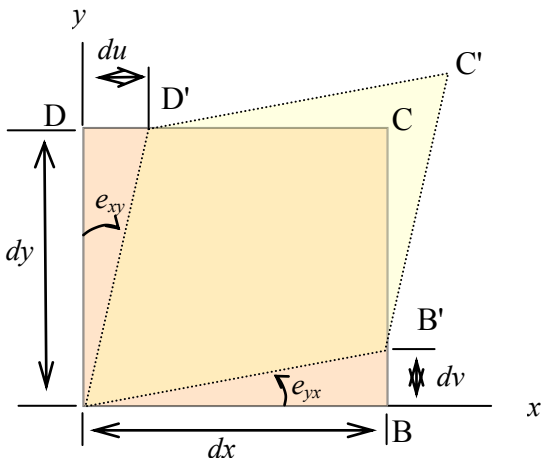

Figure 1.11 Angular distortion of an element.

For further displacement derivatives, let us consider a shape change using an element in the *xy* plane, which is subjected to shear deformation as shown in **Figure 1.11**. The element has undergone an angular distortion and thus the angular displacement derivatives along the *x* and *y* axes are given by

$$e_{yx} = \frac{BB'}{AB} = \frac{\partial v}{\partial x} \tag{1.13c}$$

and

$$e_{xy} = \frac{DD'}{DA} = \frac{\partial u}{\partial y} \tag{1.13d}$$

respectively. Similarly, the rest of components can be found:

$$e_{ij} = \begin{bmatrix} e_{xx} & e_{xy} & e_{xz} \\ e_{yx} & e_{yy} & e_{yz} \\ e_{zx} & e_{zy} & e_{zz} \end{bmatrix} = \begin{bmatrix} \frac{\partial u}{\partial x} & \frac{\partial u}{\partial y} & \frac{\partial u}{\partial z} \\ \frac{\partial v}{\partial x} & \frac{\partial v}{\partial y} & \frac{\partial v}{\partial z} \\ \frac{\partial w}{\partial x} & \frac{\partial w}{\partial y} & \frac{\partial w}{\partial z} \end{bmatrix} \tag{1.13e}$$

In general, components such as e_{xy}, e_{yx}, etc., other than those for length change produce both *shear strain and rigid-body rotation*. For example, those given in **Figure 1.12 (a)** represent a pure rotation with an average of $\frac{1}{2}\left(\frac{\partial u}{\partial y} - \frac{\partial v}{\partial x}\right)$ and **Figure 1.12 (b)** a pure rotation with an average of $\frac{1}{2}\left(\frac{\partial v}{\partial x} - \frac{\partial u}{\partial y}\right)$. Thus, the rigid body rotation components (w_{ij}) can be identified as:

$$\omega_{ij}=\begin{bmatrix}\omega_{xx} & \omega_{xy} & \omega_{xz}\\ \omega_{yx} & \omega_{yy} & \omega_{yz}\\ \omega_{zx} & \omega_{zy} & \omega_{zz}\end{bmatrix}=\begin{bmatrix}0 & \frac{1}{2}\left(\frac{\partial u}{\partial y}-\frac{\partial v}{\partial x}\right) & \frac{1}{2}\left(\frac{\partial u}{\partial z}-\frac{\partial w}{\partial x}\right)\\ \frac{1}{2}\left(\frac{\partial v}{\partial x}-\frac{\partial u}{\partial y}\right) & 0 & \frac{1}{2}\left(\frac{\partial v}{\partial z}-\frac{\partial w}{\partial y}\right)\\ \frac{1}{2}\left(\frac{\partial w}{\partial x}-\frac{\partial u}{\partial z}\right) & \frac{1}{2}\left(\frac{\partial w}{\partial y}-\frac{\partial v}{\partial z}\right) & 0\end{bmatrix}. \quad (1.14)$$

Accordingly, the strain components (w_{ij}) can be found by subtracting rigid body rotation components (ε_{ij}) from the displacement derivatives:

$$\varepsilon_{ij}=\begin{bmatrix}\varepsilon_{xx} & \varepsilon_{xy} & \varepsilon_{xz}\\ \varepsilon_{yx} & \varepsilon_{yy} & \varepsilon_{yz}\\ \varepsilon_{zx} & \varepsilon_{zy} & \varepsilon_{zz}\end{bmatrix}=\begin{bmatrix}\frac{\partial u}{\partial x} & \frac{1}{2}\left(\frac{\partial u}{\partial y}+\frac{\partial v}{\partial x}\right) & \frac{1}{2}\left(\frac{\partial u}{\partial z}+\frac{\partial w}{\partial x}\right)\\ \frac{1}{2}\left(\frac{\partial u}{\partial y}+\frac{\partial v}{\partial x}\right) & \frac{\partial v}{\partial y} & \frac{1}{2}\left(\frac{\partial v}{\partial z}+\frac{\partial w}{\partial y}\right)\\ \frac{1}{2}\left(\frac{\partial u}{\partial z}+\frac{\partial w}{\partial x}\right) & \frac{1}{2}\left(\frac{\partial v}{\partial z}+\frac{\partial w}{\partial y}\right) & \frac{\partial w}{\partial z}\end{bmatrix}. \quad (1.15)$$

For short, $\omega_{ij}=\frac{1}{2}\left(\frac{\partial u_i}{\partial x_j}-\frac{\partial u_j}{\partial x_i}\right)$, $\varepsilon_{ij}=\frac{1}{2}\left(\frac{\partial u_i}{\partial x_j}+\frac{\partial u_j}{\partial x_i}\right)$ and are called the *strain tensor* and the *rotation tensor* respectively. Also,

$$e_{ij}=\varepsilon_{ij}+\omega_{ij} \tag{1.16}$$

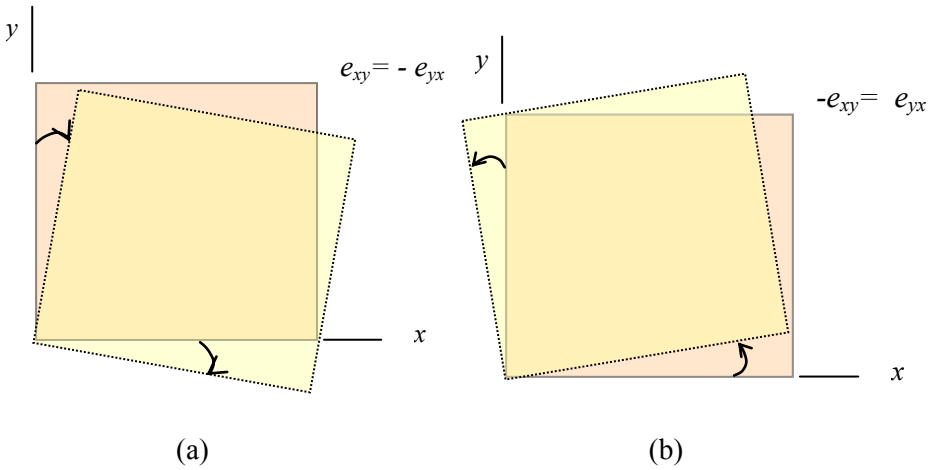

Figure 1.12 Pure rotation without shear.

Referring to **Figure 1.13,** engineering shear strain components (γ_{ij}) are defined as

$$\gamma_{xy}=e_{xy}+e_{yx}=\varepsilon_{xy}+\varepsilon_{yx}=2\varepsilon_{xy},\ \gamma_{xz}=2\varepsilon_{xz},\ \gamma_{yz}=2\varepsilon_{yz} \tag{1.17}$$

In summary, strain components are

$$\varepsilon_x=\frac{\partial u}{\partial x},\ \varepsilon_y=\frac{\partial v}{\partial y},\ \varepsilon_z=\frac{\partial w}{\partial z},$$
$$\gamma_{xy}=\frac{\partial u}{\partial y}+\frac{\partial v}{\partial x},\ \gamma_{xz}=\frac{\partial u}{\partial z}+\frac{\partial w}{\partial x},\ \gamma_{yz}=\frac{\partial v}{\partial z}+\frac{\partial w}{\partial y} \tag{1.18}$$

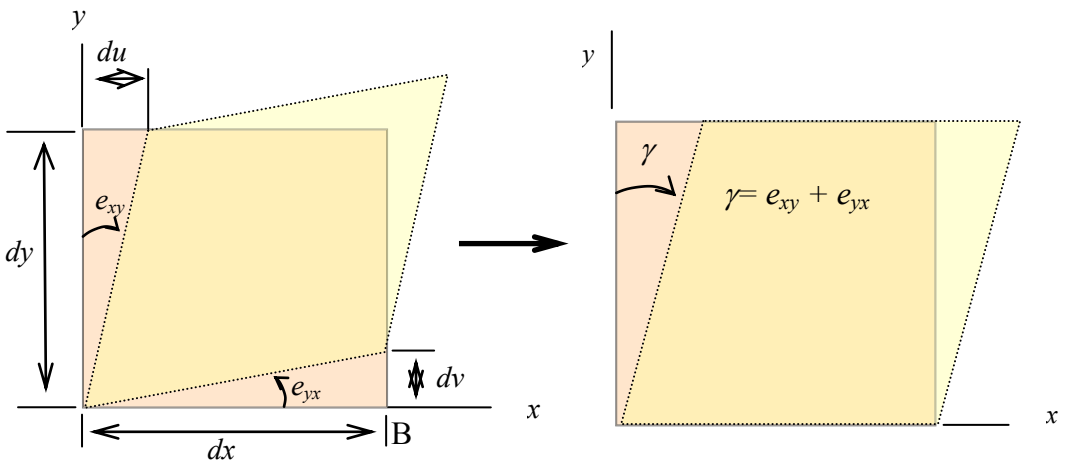

Figure 1.13 Engineering shear strain *γ*.

The volume strain (Δ) (see **Figure 1.14)** is defined as

$$\Delta = \frac{\text{Final volume - Original volume}}{\text{Original volume}}$$

or

$$\begin{aligned}\Delta &= \frac{(1+\varepsilon_x)(1+\varepsilon_y)(1+\varepsilon_z)dxdydz - dxdydz}{dxdydz} \\ &= (1+\varepsilon_x)(1+\varepsilon_y)(1+\varepsilon_z) - 1 \\ &\approx \varepsilon_x + \varepsilon_y + \varepsilon_z\end{aligned} \tag{1.19}$$

for small deformation.

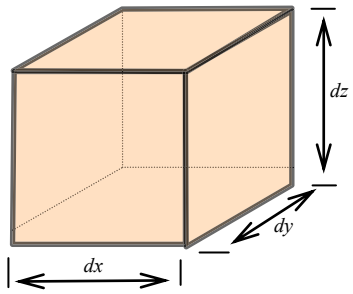

Figure 1.14 An elemental cube.

The *mean strain* or the *hydrostatic* component of strain, which contributes to volume change, is also defined as

$$\varepsilon_m = \frac{\varepsilon_x + \varepsilon_y + \varepsilon_z}{3} = \frac{\varepsilon_{kk}}{3} = \frac{\Delta}{3}. \tag{1.20}$$

Then, the *strain deviator* (ε'_{ij}) which contributes to shape change, can be obtained by subtracting from ε_m each of the normal strain components:

$$\varepsilon'_{ij}=\begin{bmatrix} \varepsilon_x-\varepsilon_m & \varepsilon_{xy} & \varepsilon_{xz} \\ \varepsilon_{yx} & \varepsilon_y-\varepsilon_m & \varepsilon_{yz} \\ \varepsilon_{zx} & \varepsilon_{zy} & \varepsilon_z-\varepsilon_m \end{bmatrix}= \begin{bmatrix} \dfrac{2\varepsilon_x-\varepsilon_y-\varepsilon_z}{3} & \varepsilon_{xy} & \varepsilon_{xz} \\ \varepsilon_{yx} & \dfrac{2\varepsilon_y-\varepsilon_z-\varepsilon_x}{3} & \varepsilon_{yz} \\ \varepsilon_{zx} & \varepsilon_{zy} & \dfrac{2\varepsilon_z-\varepsilon_x-\varepsilon_y}{3} \end{bmatrix} \tag{1.21}$$

In complete analogy between stress and strain equations, the principal strains are the roots of the cubic equation:

$$\varepsilon^3-I_1\varepsilon^2+I_2\varepsilon-I_3=0 \tag{1.22}$$

where

$$\begin{aligned} I_1&=\varepsilon_x+\varepsilon_y+\varepsilon_z \\ I_2&=\varepsilon_x\varepsilon_y+\varepsilon_y\varepsilon_z+\varepsilon_z\varepsilon_x-\frac{1}{4}(\gamma_{xy}^2+\gamma_{zx}^2+\gamma_{yz}^2) \\ I_3&=\varepsilon_x\varepsilon_y\varepsilon_z+\frac{1}{4}\gamma_{xy}\gamma_{zx}\gamma_{yz}-\frac{1}{4}(\varepsilon_x\gamma_{xy}^2+\varepsilon_y\gamma_{zx}^2+\varepsilon_z\gamma_{yz}^2). \end{aligned} \tag{1.23}$$

As already discussed for stress, I_1, I_2 and I_3 are not functions of direction cosines. As such, they are independent of the coordinate system location and therefore they are called 'invariants'.

Also, the principal (engineering) shear strains are

$$\begin{aligned} \gamma_1&=\varepsilon_2-\varepsilon_3, \\ \gamma_2&=\varepsilon_1-\varepsilon_3(=\gamma_{\max}) \\ \gamma_3&=\varepsilon_1-\varepsilon_2. \end{aligned} \tag{1.24}$$

2 Linear Elastic Stress-Strain Relations

2.1 The Hooke's law

The elastic stress (σ) is linearly related to elastic strain (ε) by means of the modulus of elasticity (E) for the isotropic materials:

$$\sigma = E\varepsilon . \tag{2.1}$$

This relation is known as the Hooke's law.

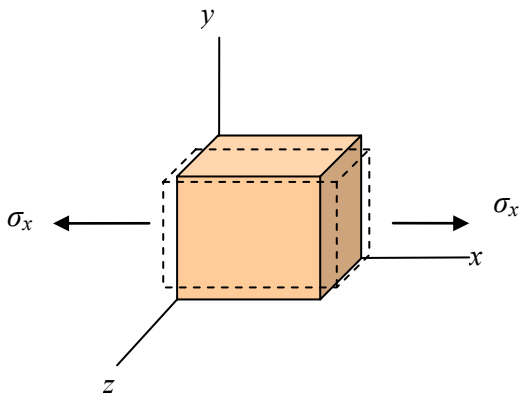

Figure 2.1 Deformation of an element subjected to a tensile force.

A tensile force in the x direction causes an extension of the element in the same direction. Simultaneously it also causes a contraction in the y and z directions (see **Figure 2.1**). The ratio of the transverse strain to the strain in the longitudinal direction is known to be constant and called the *Poisson's ratio,* denoted by the symbol ν.

$$\varepsilon_y = \varepsilon_z = -\nu\varepsilon_x = -\frac{\nu\sigma_x}{E} \tag{2.2}$$

The principle of superposition is then can be applied to determine the strain produced by more than one stress component. For example, the stress σ_x produces a normal strain ε_x and two transverse strains $\varepsilon_y = -\nu\varepsilon_x$ and $\varepsilon_z = -\nu\varepsilon_x$. Similarly, other strain components can be found as listed in **Table 2.1**.

Stress	Strain in the x direction	Strain in the y direction	Strain in the z direction
σ_x	$\varepsilon_x = \frac{\sigma_x}{E}$	$\varepsilon_y = -\frac{\nu\sigma_x}{E}$	$\varepsilon_z = -\frac{\nu\sigma_x}{E}$
σ_y	$\varepsilon_x = -\frac{\nu\sigma_y}{E}$	$\varepsilon_y = \frac{\sigma_y}{E}$	$\varepsilon_z = -\frac{\nu\sigma_y}{E}$
σ_z	$\varepsilon_x = -\frac{\nu\sigma_z}{E}$	$\varepsilon_y = -\frac{\nu\sigma_z}{E}$	$\varepsilon_z = \frac{\sigma_z}{E}$

Table 2.1 Strain components for superposition.

Accordingly, the components of strain in the *x, y,* and z directions are found:

$$\begin{aligned}
\varepsilon_x &= \frac{1}{E}\left[\sigma_x - \nu(\sigma_y + \sigma_z)\right] \\
\varepsilon_y &= \frac{1}{E}\left[\sigma_y - \nu(\sigma_z + \sigma_x)\right] \\
\varepsilon_z &= \frac{1}{E}\left[\sigma_z - \nu(\sigma_x + \sigma_y)\right]
\end{aligned} \tag{2.3}$$

The shear stresses acting on the unit cube produce shear strains independent of normal stresses:

$$\tau_{xy}=G\gamma_{xy},\ \tau_{yz}=G\gamma_{yz},\ \tau_{xz}=G\gamma_{xz} \tag{2.4}$$

The proportional constant *G* is the *modulus of elasticity in shear,* or the *modulus of rigidity.* Values of *G* are usually determined from a torsion test.

Another elastic constant is the *bulk modulus* or the *volumetric modulus of elasticity* (*K*). The bulk modulus is the ratio of the *hydrostatic stress* or the *hydrostatic pressure* to the *volume strain* that it produces

$$K=\frac{\sigma_m}{\Delta}=\frac{-p}{\Delta}=\frac{1}{\beta} \tag{2.5}$$

where *p* is the hydrostatic pressure and β is the *compressibility*. It is applicable to both fluid and solid.

Some useful relationships between the elastic constants (*E*, *G*, *v*, and *K*) may be derived. Adding up the three equations in Equation (2.3),

$$\varepsilon_x+\varepsilon_y+\varepsilon_z=\frac{1-2v}{E}\left(\sigma_x+\sigma_y+\sigma_z\right) \tag{2.6}$$

It is noted that the terms on the left of Equation (2.6) is the volume strain (Δ), and the terms $(\sigma_x+\sigma_y+\sigma_z)$ on the right is $3\sigma_m$. Accordingly,

$$\Delta=\frac{1-2v}{E}3\sigma_m \tag{2.7a}$$

or

$$K=\frac{\sigma_m}{\Delta}=\frac{E}{3(1-2v)} \tag{2.7b}$$

The following equation is often introduced in an elementary course of mechanics of solids for a relationship between *E, G,* and n:

$$G=\frac{E}{2(1+v)}. \tag{2.8}$$

Using Equations (2.7) and (2.8), other useful relationships can be found:

$$E=\frac{9K}{1+3K/G}\ , \tag{2.9a}$$

$$v=\frac{1-2G/3K}{2+2G/3K}, \tag{2.9b}$$

$$G=\frac{3(1-2v)K}{2(1+v)}, \text{ and} \tag{2.9c}$$

$$K=\frac{E}{9-3E/G}. \tag{2.9d}$$

2.2 Calculation of stresses from elastic strains

The strains are measurable while the stresses can be calculated. It may be useful to have stresses as functions of strains. From Equation (2.6),

$$\sigma_x+\sigma_y+\sigma_z=\frac{E}{1-2v}\left(\varepsilon_x+\varepsilon_y+\varepsilon_z\right). \tag{2.10}$$

We eliminate ε_y and ε_z in Equation (2.10) using Equation (2.3):

$$\varepsilon_x=\frac{1+v}{E}\sigma_x-\frac{v}{E}(\sigma_x+\sigma_y+\sigma_z). \tag{2.11}$$

Substitution of Equation (2.10) into Equation (2.11) gives:

$$\sigma_x=\frac{E}{1+v}\varepsilon_x+\frac{vE}{(1+v)(1-2v)}\left(\varepsilon_x+\varepsilon_y+\varepsilon_z\right) \tag{2.12a}$$

where

$$\frac{vE}{(1+v)(1-2v)}=\lambda \tag{2.12b}$$

and λ is known as the Lamé's constant. Further, using the volume strain $\Delta=\varepsilon_x+\varepsilon_y+\varepsilon_z$, and shear modulus ($G$):

$$\sigma_x=2G\varepsilon_x+\lambda\Delta. \tag{2.13}$$

In this way, more relations can be found for other stress components (σ_y, σ_x, and so on). It may be timely to introduce the tensorial notation to deal with a large number of equations and a specified system of components. All the stress components can now be expressed as

$$\sigma_{ij}=2G\varepsilon_{ij}+\lambda\varepsilon_{kk}\delta_{ij} \tag{2.14}$$

where i and j are free indexes, k is a dummy index, and d_{ij} is the Kronecker delta i.e.

$\delta_{ij}=1$ if $i=j$
$\delta_{ij}=0$ if $i\neq j$.

The free index assumes a specified integer that determines all dummy index values. The dummy index takes on all the values of its range. Upon expansion, Equation (2.14) gives three equations for normal stress and six equations for shear stress using indexes for a range of x, y and z. Equation (2.14) may be expanded in a matrix form:

$$\begin{bmatrix}\sigma_x\\ \sigma_y\\ \sigma_z\\ \tau_{xy}\\ \tau_{yz}\\ \tau_{zx}\end{bmatrix}=\begin{bmatrix}\lambda+2G & \lambda & \lambda & 0 & 0 & 0\\ \lambda & \lambda+2G & \lambda & 0 & 0 & 0\\ \lambda & \lambda & \lambda+2G & 0 & 0 & 0\\ 0 & 0 & 0 & G & 0 & 0\\ 0 & 0 & 0 & 0 & G & 0\\ 0 & 0 & 0 & 0 & 0 & G\end{bmatrix}\begin{bmatrix}\varepsilon_x\\ \varepsilon_y\\ \varepsilon_z\\ \gamma_{xy}\\ \gamma_{yz}\\ \gamma_{zx}\end{bmatrix} \tag{2.15}$$

or by inversion

$$\begin{bmatrix}\varepsilon_x\\ \varepsilon_y\\ \varepsilon_z\\ \gamma_{xy}\\ \gamma_{yz}\\ \gamma_{zx}\end{bmatrix}=\frac{1}{E}\begin{bmatrix}1 & -\nu & -\nu & 0 & 0 & 0\\ -\nu & 1 & -\nu & 0 & 0 & 0\\ -\nu & -\nu & 1 & 0 & 0 & 0\\ 0 & 0 & 0 & 2(1+\nu) & 0 & 0\\ 0 & 0 & 0 & 0 & 2(1+\nu) & 0\\ 0 & 0 & 0 & 0 & 0 & 2(1+\nu)\end{bmatrix}\begin{bmatrix}\sigma_x\\ \sigma_y\\ \sigma_z\\ \tau_{xy}\\ \tau_{yz}\\ \tau_{zx}\end{bmatrix} \tag{2.16}$$

As previously discussed, the stresses and the strains can be broken into deviator and hydrostatic components. The distortion is associated with the stress/strain deviator and its stress-strain relation is given by

$$\sigma_{ij}^{'}=\frac{E}{1+v}\varepsilon_{ij}^{'}=2G\varepsilon_{ij}^{'} \tag{2.17}$$

Also, the stress-strain relationship between hydrostatic stress and mean strain components in tensorial notation is given by

$$\sigma_{ii}=\frac{E}{3(1-2v)}\varepsilon_{kk}=K\varepsilon_{kk}. \tag{2.18}$$

2.3 Plane stress and plane strain

Plane stress or *plane strain* is a state of stress/strain (**Figure 2.2**). An example is given for *plane stress* in **Figure 2.2 (a)**, in which two of the faces of the cubic element are free of any stress. Another example is given for *plane strain* in **Figure 2.2 (b),** which occurs to the situations where the deformations take place within parallel planes. In practice, the *plane strain* often occurs internally within a structural component in which stress distribution is non-uniform when stress raisers such as rivet hole and notch are present whereas the *plane stress* occurs on its surfaces.

For a case of *plane stress* ($\sigma_3 = 0$ or $\sigma_z = 0$), Equation (2.3) becomes

$$\varepsilon_1=\frac{1}{E}[\sigma_1-v\sigma_2] \tag{2.19a}$$

$$\varepsilon_2=\frac{1}{E}[\sigma_2-v\sigma_1] \tag{2.19b}$$

$$\varepsilon_3=\frac{-v}{E}[\sigma_1+\sigma_2]. \tag{2.19c}$$

Then, two stress-strain relations can be obtained by solving simultaneously two of the equations:

$$\sigma_1=\frac{E}{1-v^2}(\varepsilon_1+v\varepsilon_2) \tag{2.19d}$$

$$\sigma_2=\frac{E}{1-v^2}(\varepsilon_2+v\varepsilon_1). \tag{2.19e}$$

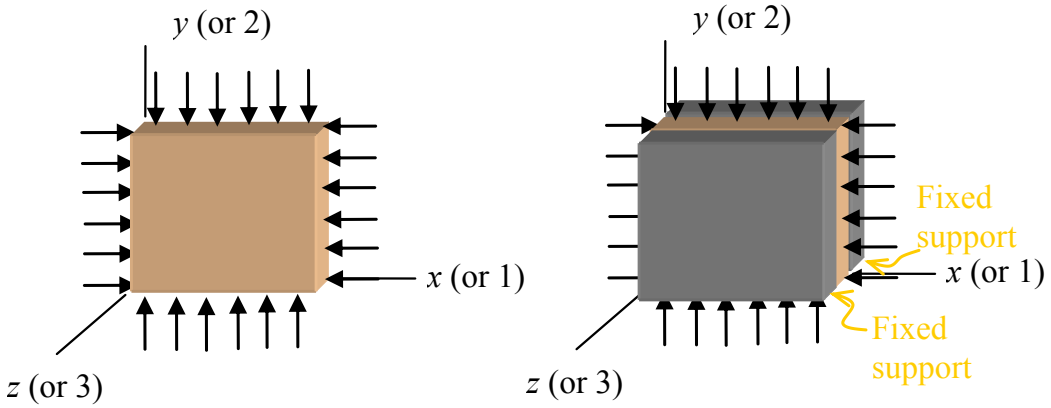

Figure 2.2 Example for: (a) plane stress; and (b) plane strain (no displacement in the z-direction).

For a case of *plane strain* ($\varepsilon_3 = 0$),

$$\varepsilon_3 = \frac{1}{E}\left[\sigma_3 - \nu(\sigma_1 + \sigma_2)\right] = 0 \tag{2.20a}$$

so that,

$$\sigma_3 = \nu(\sigma_1 + \sigma_2) \tag{2.20b}$$

Therefore, a stress exists even though the strain is zero in the z (or 1) direction. Substituting this value into Equation (2.3), we get

$$\varepsilon_1 = \frac{1-\nu^2}{E}\left(\sigma_1 - \frac{\nu}{1-\nu}\sigma_2\right) \tag{2.20c}$$

$$\varepsilon_2 = \frac{1-\nu^2}{E}\left(\sigma_2 - \frac{\nu}{1-\nu}\sigma_1\right) \tag{2.20d}$$

$$\varepsilon_3 = 0\,. \tag{2.20e}$$

Note that when $\frac{\nu}{1-\nu}$ and $\frac{1-\nu^2}{E}$ are replaced with ν and $\frac{1}{E}$ respectively plane stress equations are obtained.

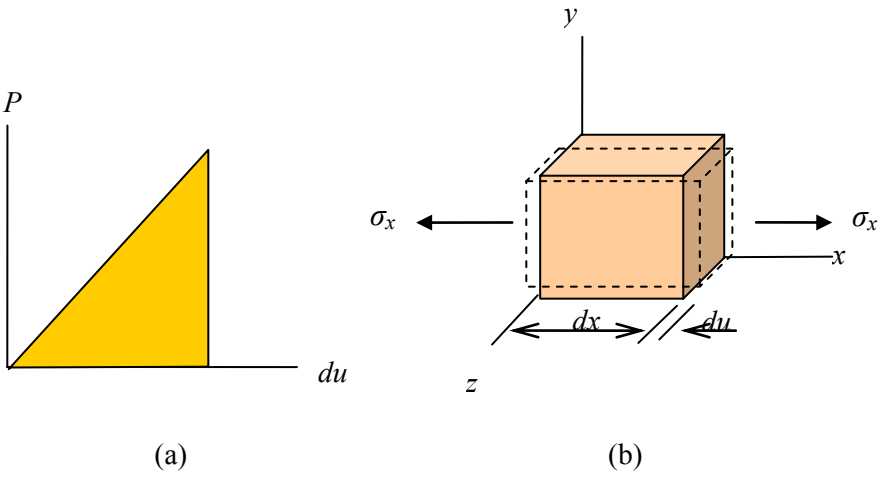

Figure 2.3 (a) An elemental cube subjected to a tensile stress. (b) Force-displacement (*P-du*) curve and strain energy.

2.4 Strain energy

In general, the strain energy is graphically an area under a force-displacement (*P*-d*u*) diagram (**Figure 2.3**). When an elemental cube is subjected to a tensile stress in the *x*-direction, its elastic strain energy (Λ) is given by

$$d\Lambda = \frac{1}{2} P du = \frac{1}{2} (\sigma_x A)(\varepsilon_x dx) = \frac{1}{2} (\sigma_x \varepsilon_x)(A dx). \tag{2.21}$$

Equation (2.21) describes the elastic energy absorbed by the element volume ($A\ dx$). If we define the *strain energy density* (Λ_0) as the *energy per unit volume*, it is given by

$$\Lambda_0 = \frac{1}{2} \sigma_x \varepsilon_x = \frac{1}{2} \frac{\sigma_x^2}{E} = \frac{1}{2} \varepsilon_x^2 E \tag{2.22}$$

Similarly, the *strain energy per unit volume* of an element subjected to pure shear (γ_{xy}) is given by

$$\Lambda_0 = \frac{1}{2} \tau_{xy} \gamma_{xy} = \frac{1}{2} \frac{\tau_{xy}^2}{G} = \frac{1}{2} \gamma_{xy}^2 G. \tag{2.23}$$

For a general three-dimensional stress distribution, it may be obtained by superimposing the six components:

$$\Lambda_0 = \frac{1}{2} \left(\sigma_x \varepsilon_x + \sigma_y \varepsilon_y + \sigma_z \varepsilon_z + \tau_{xy} \gamma_{xy} + \tau_{xz} \gamma_{xz} + \tau_{yz} \gamma_{yz} \right) \tag{2.24}$$

or in tensorial notation,

$$\Lambda_0 = \frac{1}{2} \sigma_{ij} \varepsilon_{ij}. \tag{2.25}$$

To identify volume- and shape- dependent quantitative characteristics, we first find an expression for strain energy per unit volume (Λ_0) as a function of the stress and the elastic constants. Substituting the equations of Hooke's law [Equations (2.3) and (2.4)] into Equation (2.24), we find:

$$\Lambda_0 = \frac{1}{2E} \left(\sigma_x^2 + \sigma_y^2 + \sigma_z^2 \right) - \frac{\nu}{E} \left(\sigma_x \sigma_y + \sigma_y \sigma_z + \sigma_x \sigma_z \right) + \frac{1}{2G} \left(\tau_{xy}^2 + \tau_{xz}^2 + \tau_{yz}^2 \right) \tag{2.26a}$$

where $E = \frac{9K}{1 + 3K/G}$ and $\nu = \frac{1 - 2G/3K}{2 + 2G/3K}$. The strain energy density (Λ_0) may be rewritten for separate volume and shape dependent parts:

$$\Lambda_0 = \frac{I_1^2}{18K} + \frac{1}{6G} (I_1^2 - 3I_2) \tag{2.26b}$$

where $I_1 = \sigma_1 + \sigma_2 + \sigma_3$ (first invariant) and $I_2 = \sigma_1 \sigma_2 + \sigma_2 \sigma_3 + \sigma_1 \sigma_3$ (second invariant).

The strain energy density (Λ_0) can be found for incompressible materials i.e. $K = \infty$:

$$\Lambda_0 = \frac{1}{12G}\left[(\sigma_1 - \sigma_2)^2 + (\sigma_2 - \sigma_3)^2 + (\sigma_3 - \sigma_1)^2\right]. \tag{2.27}$$

A uni-axial yield stress (σ_{ys}), can be related for the distortion energy (Λ_0) to be

$\Lambda_0 = \frac{1}{6G}\sigma_{ys}^2$ for $\sigma_1 = \sigma_{ys}$ $\sigma_2 = 0$, and $\sigma_3 = 0$ when subjected to a uni-axial loading. Accordingly Equation (2.27) becomes

$$2\sigma_{ys}^2 = (\sigma_1 - \sigma_2)^2 + (\sigma_2 - \sigma_3)^2 + (\sigma_3 - \sigma_1)^2. \tag{2.28}$$

This equation is known as the *distortion energy criterion* or *von Mises' yield criterion*.

To find stress-strain relations involving the strain energy density, the following equation is first found by substituting Equation (2.15) into Equation (2.24):

$$\Lambda_0 = \frac{1}{2}\lambda\Delta^2 + G\left(\varepsilon_x^2 + \varepsilon_y^2 + \varepsilon_z^2\right) + \frac{1}{2}G\left(\gamma_{xy}^2 + \gamma_{xz}^2 + \gamma_{yz}^2\right) \tag{2.29}$$

and then we find that the derivative of Λ_O with respect to any strain component gives the corresponding stress component and vice versa. For example,

$$\frac{\partial\Lambda_0}{\partial\varepsilon_x} = \lambda\Delta + 2G\varepsilon_x = \sigma_x \tag{2.30a}$$

$$\frac{\partial\Lambda_0}{\partial\varepsilon_y} = \lambda\Delta + 2G\varepsilon_y = \sigma_y \tag{2.30b}$$

$$\frac{\partial\Lambda_0}{\partial\varepsilon_z} = \lambda\Delta + 2G\varepsilon_z = \sigma_z \tag{2.30c}$$

or

$$\frac{\partial\Lambda_0}{\partial\sigma_x} = \varepsilon_x \tag{2.30d}$$

$$\frac{\partial\Lambda_0}{\partial\sigma_y} = \varepsilon_y \tag{2.30e}$$

$$\frac{\partial\Lambda_0}{\partial\sigma_z} = \varepsilon_z. \tag{2.30f}$$

This mathematical concept is applicable to a large structural component for force-deflection relation as described in the Castigliano's theorem.

2.5 Generalised Hooke's law

The generalized Hooke's law is not only for three-dimensional loading but also for all the possible linear elastic material properties. It may be expressed as

$$\varepsilon_{ij} = C_{ijkl}\sigma_{kl} \tag{2.31}$$

and

$$\sigma_{ij} = S_{ijkl}\varepsilon_{kl} \tag{2.32}$$

where C_{ijkl} is the compliance tensor and S_{ijkl} is the stiffness tensor (physically elastic constants). Equation (2.32) represents:

$$
\begin{aligned}
\sigma_{11} = {} & S_{1111}\varepsilon_{11} + S_{1112}\varepsilon_{12} + S_{1113}\varepsilon_{13} + S_{1121}\varepsilon_{21} + S_{1122}\varepsilon_{22} + S_{1123}\varepsilon_{23} + S_{1131}\varepsilon_{31} + \\
& S_{1132}\varepsilon_{32} + S_{1133}\varepsilon_{33} \\
\sigma_{12} = {} & S_{1211}\varepsilon_{11} + S_{1212}\varepsilon_{12} + S_{1213}\varepsilon_{13} + S_{1221}\varepsilon_{21} + S_{1222}\varepsilon_{22} + S_{1223}\varepsilon_{23} + S_{1231}\varepsilon_{31} + \\
& S_{1232}\varepsilon_{32} + S_{1233}\varepsilon_{33} \\
\sigma_{13} = {} & S_{1311}\varepsilon_{11} + S_{1312}\varepsilon_{12} + S_{1313}\varepsilon_{13} + S_{1321}\varepsilon_{21} + S_{1322}\varepsilon_{22} + S_{1323}\varepsilon_{23} + S_{1331}\varepsilon_{31} + \\
& S_{1332}\varepsilon_{32} + S_{1333}\varepsilon_{33} \\
\sigma_{21} = {} & S_{2111}\varepsilon_{11} + S_{2112}\varepsilon_{12} + S_{2113}\varepsilon_{13} + S_{2121}\varepsilon_{21} + S_{2122}\varepsilon_{22} + S_{2123}\varepsilon_{23} + S_{2131}\varepsilon_{31} + \\
& S_{2132}\varepsilon_{32} + S_{2133}\varepsilon_{33} \\
\sigma_{22} = {} & S_{2211}\varepsilon_{11} + S_{2212}\varepsilon_{12} + S_{2213}\varepsilon_{13} + S_{2221}\varepsilon_{21} + S_{2222}\varepsilon_{22} + S_{2223}\varepsilon_{23} + S_{2231}\varepsilon_{31} + \\
& S_{2232}\varepsilon_{32} + S_{2233}\varepsilon_{33} \\
\sigma_{23} = {} & S_{2311}\varepsilon_{11} + S_{2312}\varepsilon_{12} + S_{2313}\varepsilon_{13} + S_{2321}\varepsilon_{21} + S_{2322}\varepsilon_{22} + S_{2323}\varepsilon_{23} + S_{2331}\varepsilon_{31} + \\
& S_{2332}\varepsilon_{32} + S_{2333}\varepsilon_{33} \\
\sigma_{31} = {} & S_{3111}\varepsilon_{11} + S_{3112}\varepsilon_{12} + S_{3113}\varepsilon_{13} + S_{3121}\varepsilon_{21} + S_{3122}\varepsilon_{22} + S_{3123}\varepsilon_{23} + S_{3131}\varepsilon_{31} + \\
& S_{3132}\varepsilon_{32} + S_{3133}\varepsilon_{33} \\
\sigma_{32} = {} & S_{3211}\varepsilon_{11} + S_{3212}\varepsilon_{12} + S_{3213}\varepsilon_{13} + S_{3221}\varepsilon_{21} + S_{3222}\varepsilon_{22} + S_{3223}\varepsilon_{23} + S_{3231}\varepsilon_{31} + \\
& S_{3232}\varepsilon_{32} + S_{3233}\varepsilon_{33} \\
\sigma_{33} = {} & S_{3311}\varepsilon_{11} + S_{3312}\varepsilon_{12} + S_{3313}\varepsilon_{13} + S_{3321}\varepsilon_{21} + S_{3322}\varepsilon_{22} + S_{3323}\varepsilon_{23} + S_{3331}\varepsilon_{31} + \\
& S_{3332}\varepsilon_{32} + S_{3333}\varepsilon_{33}
\end{aligned}
\tag{2.33}
$$

We know that σ_{ij} and ε_{ji} are symmetric tensors ($\varepsilon_{ij} = \varepsilon_{ji}$, $C_{ijlk}\varepsilon_{ij} = C_{ijkl}\varepsilon_{ji}$, $\sigma_{ij} = \sigma_{ji}$, $\sigma_{ij} = \sigma_{ji}$). This leads to simplification of Equation (2.33):

$$
\begin{aligned}
\sigma_{11} &= S_{1111}\varepsilon_{11} + S_{1122}\varepsilon_{22} + S_{1133}\varepsilon_{33} + S_{1123}(2\varepsilon_{23}) + S_{1113}(2\varepsilon_{13}) + S_{1112}(2\varepsilon_{12}) \\
\sigma_{12} &= S_{1211}\varepsilon_{11} + S_{1222}\varepsilon_{22} + S_{1233}\varepsilon_{33} + S_{1223}(2\varepsilon_{23}) + S_{1213}(2\varepsilon_{13}) + S_{1212}(2\varepsilon_{12}) \\
\sigma_{13} &= S_{1311}\varepsilon_{11} + S_{1322}\varepsilon_{22} + S_{1333}\varepsilon_{33} + S_{1323}(2\varepsilon_{23}) + S_{1313}(2\varepsilon_{13}) + S_{1312}(2\varepsilon_{12}) \\
\sigma_{21} &= S_{2111}\varepsilon_{11} + S_{2122}\varepsilon_{22} + S_{2133}\varepsilon_{33} + S_{2123}(2\varepsilon_{23}) + S_{2113}(2\varepsilon_{13}) + S_{2112}(2\varepsilon_{12}) \\
\sigma_{22} &= S_{2211}\varepsilon_{11} + S_{2222}\varepsilon_{22} + S_{2233}\varepsilon_{33} + S_{2223}(2\varepsilon_{23}) + S_{2213}(2\varepsilon_{13}) + S_{2212}(2\varepsilon_{12}) \\
\sigma_{23} &= S_{2311}\varepsilon_{11} + S_{2322}\varepsilon_{22} + S_{2333}\varepsilon_{33} + S_{2323}(2\varepsilon_{23}) + S_{2313}(2\varepsilon_{13}) + S_{2312}(2\varepsilon_{12}) \\
\sigma_{31} &= S_{3111}\varepsilon_{11} + S_{3122}\varepsilon_{22} + S_{3133}\varepsilon_{33} + S_{3123}(2\varepsilon_{23}) + S_{3113}(2\varepsilon_{13}) + S_{3112}(2\varepsilon_{12}) \\
\sigma_{32} &= S_{3211}\varepsilon_{11} + S_{3222}\varepsilon_{22} + S_{3233}\varepsilon_{33} + S_{3223}(2\varepsilon_{23}) + S_{3213}(2\varepsilon_{13}) + S_{3212}(2\varepsilon_{12}) \\
\sigma_{33} &= S_{3311}\varepsilon_{11} + S_{3322}\varepsilon_{22} + S_{3333}\varepsilon_{33} + S_{3323}(2\varepsilon_{23}) + S_{3313}(2\varepsilon_{13}) + S_{3312}(2\varepsilon_{12})
\end{aligned}
\tag{2.34}
$$

or knowing engineering shear strain γ ($=2\varepsilon$),

$$
\begin{aligned}
&\sigma_{11} = S_{1111}\varepsilon_{11} + S_{1122}\varepsilon_{22} + S_{1133}\varepsilon_{33} + S_{1123}\gamma_{23} + S_{1113}\gamma_{13} + S_{1112}\gamma_{12} \\
&\cdots\cdots\cdots\cdots\cdots\cdots\cdots\cdots\cdots\cdots \\
&\cdots\cdots\cdots\cdots\cdots\cdots\cdots\cdots\cdots\cdots \\
&\sigma_{23} = S_{2311}\varepsilon_{11} + S_{2322}\varepsilon_{22} + S_{2333}\varepsilon_{33} + S_{2323}\gamma_{23} + S_{2313}\gamma_{13} + S_{2312}\gamma_{12} \\
&\cdots\cdots\cdots\cdots\cdots\cdots\cdots\cdots\cdots\cdots \\
&\cdots\cdots\cdots\cdots\cdots\cdots\cdots\cdots\cdots\cdots
\end{aligned}
\tag{2.35}
$$

Similarly, Equation (2.31) is expanded as:

$$\varepsilon_{11} = C_{1111}\sigma_{11} + C_{1122}\sigma_{22} + C_{1133}\sigma_{33} + 2C_{1123}\,\sigma_{23} + 2C_{1113}\,\sigma_{13} + 2C_{1112}\,\sigma_{12}$$
$$\ldots\ldots\ldots\ldots\ldots\ldots\ldots\ldots\ldots\ldots\ldots\ldots\ldots\ldots\ldots\ldots\ldots\ldots\ldots\ldots\ldots\ldots\ldots\ldots$$
$$\ldots\ldots\ldots\ldots\ldots\ldots\ldots\ldots\ldots\ldots\ldots\ldots\ldots\ldots\ldots\ldots\ldots\ldots\ldots\ldots\ldots\ldots\ldots\ldots$$
$$\gamma_{23} = 2\varepsilon_{23} = 2C_{2311}\sigma_{11} + 2C_{2322}\sigma_{22} + 2C_{2333}\sigma_{33} + 4C_{2323}\,\sigma_{23} + 4C_{2313}\,\sigma_{13} + 4C_{2312}\,\sigma_{12}$$
$$\ldots\ldots\ldots\ldots\ldots\ldots\ldots\ldots\ldots\ldots\ldots\ldots\ldots\ldots\ldots\ldots\ldots\ldots\ldots\ldots\ldots\ldots\ldots\ldots$$
$$\ldots\ldots\ldots\ldots\ldots\ldots\ldots\ldots\ldots\ldots\ldots\ldots\ldots\ldots\ldots\ldots\ldots\ldots\ldots\ldots\ldots\ldots\ldots\ldots \quad (2.36)$$

If contracted notation is used to follow the usual convention, only two subscripts instead of four for compliance and stiffness tensors are sufficient and Equations (2.35) and (2.36) are expressed as

$$\sigma_{11} = S_{11}\varepsilon_{11} + S_{12}\varepsilon_{22} + S_{13}\varepsilon_{33} + S_{14}\,\gamma_{23} + S_{15}\,\gamma_{13} + S_{16}\,\gamma_{12}$$
$$\sigma_{22} = S_{21}\varepsilon_{11} + S_{22}\varepsilon_{22} + S_{23}\varepsilon_{33} + S_{24}\,\gamma_{23} + S_{25}\,\gamma_{13} + S_{26}\,\gamma_{12}$$
$$\sigma_{33} = S_{31}\varepsilon_{11} + S_{32}\varepsilon_{22} + S_{33}\varepsilon_{33} + S_{34}\,\gamma_{23} + S_{35}\gamma_{13} + S_{36}\gamma_{12}$$
$$\sigma_{23} = S_{41}\varepsilon_{11} + S_{42}\varepsilon_{22} + S_{43}\varepsilon_{33} + S_{44}\,\gamma_{23} + S_{45}\gamma_{13} + S_{46}\gamma_{12}$$
$$\sigma_{13} = S_{51}\varepsilon_{11} + S_{52}\varepsilon_{22} + S_{53}\varepsilon_{33} + S_{54}\,\gamma_{23} + S_{55}\,\gamma_{13} + S_{56}\,\gamma_{12}$$
$$\sigma_{12} = S_{61}\varepsilon_{11} + S_{62}\varepsilon_{22} + S_{63}\varepsilon_{33} + S_{64}\,\gamma_{23} + S_{65}\,\gamma_{13} + S_{66}\,\gamma_{12}$$
$$(\sigma_{21} = S_{61}\varepsilon_{11} + S_{62}\varepsilon_{22} + S_{63}\varepsilon_{33} + S_{64}\,\gamma_{23} + S_{65}\,\gamma_{13} + S_{66}\,\gamma_{12})$$
$$(\sigma_{31} = S_{31}\varepsilon_{11} + S_{32}\varepsilon_{22} + S_{33}\varepsilon_{33} + S_{34}\,\gamma_{23} + S_{35}\,\gamma_{13} + S_{36}\,\gamma_{12})$$
$$(\sigma_{32} = S_{31}\varepsilon_{11} + S_{32}\varepsilon_{22} + S_{33}\varepsilon_{33} + S_{34}\,\gamma_{23} + S_{35}\,\gamma_{13} + S_{36}\,\gamma_{12}) \quad (2.37)$$

and

$$\varepsilon_{11} = C_{11}\sigma_{11} + C_{12}\sigma_{22} + C_{13}\sigma_{33} + C_{14}\,\sigma_{23} + C_{15}\,\sigma_{13} + C_{16}\,\sigma_{12}$$
$$\varepsilon_{22} = C_{21}\sigma_{11} + C_{22}\sigma_{22} + C_{23}\sigma_{33} + C_{24}\,\sigma_{23} + C_{25}\,\sigma_{13} + C_{26}\,\sigma_{12}$$
$$\varepsilon_{33} = C_{31}\sigma_{11} + C_{32}\sigma_{22} + C_{33}\sigma_{33} + C_{34}\,\sigma_{23} + C_{35}\,\sigma_{13} + C_{36}\,\sigma_{12}$$
$$\gamma_{23} = C_{41}\sigma_{11} + C_{42}\sigma_{22} + C_{43}\sigma_{33} + C_{44}\,\sigma_{23} + C_{45}\sigma_{13} + C_{46}\sigma_{12}$$
$$\gamma_{13} = C_{51}\sigma_{11} + C_{52}\sigma_{22} + C_{53}\sigma_{33} + C_{54}\,\sigma_{23} + C_{55}\sigma_{13} + C_{56}\sigma_{12}$$
$$\gamma_{12} = C_{61}\sigma_{11} + C_{62}\sigma_{22} + C_{63}\sigma_{33} + C_{64}\,\sigma_{23} + C_{65}\sigma_{13} + C_{66}\sigma_{12.} \quad (2.38)$$

It can be noted that the subscripts of coefficients have been rearranged systematically: 11→1, 22→2, 33→3, 23→4, 13→5, 12→6, 21→6, etc and $S_{2322} = S_{42,}\ S_{1122} = S_{12,}\ C_{1122} = C_{12,}\ 2C_{2311} = C_{41,}\ 4C_{2323} = C_{44}$, etc.

The elastic stiffness and compliance constants are defined as

$$S_{11} = \frac{\Delta\sigma_1}{\Delta\varepsilon_1},\ S_{44} = \frac{\Delta\sigma_3}{\Delta\gamma_3},\ \text{etc}$$

and

$$C_{11}=\frac{\Delta\varepsilon_1}{\Delta\sigma_1},\ C_{44}=\frac{\Delta\gamma_3}{\Delta\sigma_3},\ \text{etc.}$$

In general, $S_{ij}= S_{ji}$ and $C_{ij}= C_{ji}$ for linear elastic materials. This can be easily shown as follows.

For

$$\frac{\partial\Lambda_0}{\partial\varepsilon_1}=\sigma_{11}=S_{11}\varepsilon_{11}+S_{12}\varepsilon_{22}+S_{13}\varepsilon_{33}+S_{14}\gamma_{23}+S_{15}\gamma_{13}+S_{16}\gamma_{12},$$

the second derivative is given by

$$\frac{\partial^2\Lambda_0}{\partial\varepsilon_1\,\partial\varepsilon_2}=S_{12.} \tag{2.39a}$$

For

$$\frac{\partial\Lambda_0}{\partial\varepsilon_2}=\sigma_{22}=S_{21}\varepsilon_{11}+S_{22}\varepsilon_{22}+S_{23}\varepsilon_{33}+S_{24}\gamma_{23}+S_{25}\gamma_{13}+S_{26}\gamma_{12},$$

another second derivative is given by

$$\frac{\partial^2 \Lambda_0}{\partial \varepsilon_2 \, \partial \varepsilon_1} = S_{21.} \tag{2.39b}$$

Therefore,

$$\frac{\partial^2 \Lambda_0}{\partial \varepsilon_1 \, \partial \varepsilon_2} = \frac{\partial^2 \Lambda_0}{\partial \varepsilon_2 \, \partial \varepsilon_1} = S_{12} = S_{21}. \tag{2.39c}$$

Now we started with 36 elastic constants as given in Equation (2.37), but as a result of analysis, these can be reduced to 21 independent elastic constants.

2.6 Elastic properties dependant on orientation

The elastic properties such as elastic modulus and Poisson's ratio may be characterised by a set of *planes of symmetry* in a particular orientation. Each plane of symmetry is defined as a plane to which elastic properties are symmetric. A material having an infinite number of sets of such planes in any orientation is called an *isotropic* material and otherwise is called an *anisotropic* material.

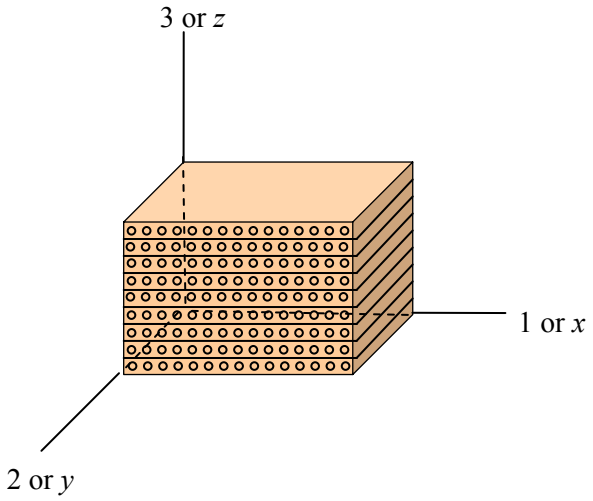

Figure 2.4 Orthotropic material: it has three mutually perpendicular orientations for respective three sets of *planes of symmetry*.

One of the important classes of engineering materials is one that has three mutually perpendicular orientations for respective three sets of *planes of symmetry*. Materials in such a class are called the *orthotropic* materials (see **Figure 2.4**). Examples for orthotropic materials include unidirectional fibre reinforced laminates, highly textured cold rolled metal sheets, etc. For orthotropic materials, constants S_{ij} in Equation (2.37) and C_{ij} in Equation (2.38) reduces to

$$S_{ij} = \begin{bmatrix} S_{11} & S_{12} & S_{13} & 0 & 0 & 0 \\ S_{12} & S_{22} & S_{23} & 0 & 0 & 0 \\ S_{13} & S_{23} & S_{33} & 0 & 0 & 0 \\ 0 & 0 & 0 & S_{44} & 0 & 0 \\ 0 & 0 & 0 & 0 & S_{55} & 0 \\ 0 & 0 & 0 & 0 & 0 & S_{66} \end{bmatrix} \tag{2.40a}$$

and

$$C_{ij} = \begin{bmatrix} C_{11} & C_{12} & C_{13} & 0 & 0 & 0 \\ C_{12} & C_{22} & C_{23} & 0 & 0 & 0 \\ C_{13} & C_{23} & C_{33} & 0 & 0 & 0 \\ 0 & 0 & 0 & C_{44} & 0 & 0 \\ 0 & 0 & 0 & 0 & C_{55} & 0 \\ 0 & 0 & 0 & 0 & 0 & C_{66} \end{bmatrix} \tag{2.40b}$$

respectively. Thus, the stress-strain relations for an orthotropic material are given by

$$\begin{aligned} \varepsilon_{11} &= C_{11}\sigma_{11} + C_{12}\sigma_{22} + C_{13}\sigma_{33} \\ \varepsilon_{22} &= C_{12}\sigma_{11} + C_{22}\sigma_{22} + C_{23}\sigma_{33} \\ \varepsilon_{33} &= C_{13}\sigma_{11} + C_{23}\sigma_{22} + C_{33}\sigma_{33} \\ \gamma_{23} &= C_{44}\,\sigma_{23} \\ \gamma_{13} &= C_{55}\,\sigma_{13} \\ \gamma_{12} &= C_{66}\,\sigma_{12} \end{aligned} \tag{2.41a}$$

or

$$\begin{aligned} \varepsilon_x &= C_{11}\sigma_x + C_{12}\sigma_y + C_{13}\sigma_z \\ \varepsilon_y &= C_{12}\sigma_x + C_{22}\sigma_y + C_{23}\sigma_z \\ \varepsilon_z &= C_{13}\sigma_x + C_{23}\sigma_y + C_{33}\sigma_z \\ \gamma_{yz} &= C_{44}\,\tau_{yz} \\ \gamma_{xz} &= C_{55}\,\tau_{xz} \\ \gamma_{xy} &= C_{66}\,\tau_{xy} \end{aligned} \tag{2.41b}$$

The constants in Equation (2.41) can be related to elastic moduli and Poisson's ratios or directly determined by conducting the tests. For example, stress components for a uni-axial tensile test in the x-direction are given by: $\sigma_x \neq 0$, $\sigma_y = 0$, and $\sigma_z = 0$. From Equation (2.41),

$$\varepsilon_x = C_{11}\sigma_x = \frac{1}{E_x}\sigma_x, \qquad \varepsilon_y = C_{12}\sigma_x, \qquad \varepsilon_z = C_{13}\sigma_x.$$

Accordingly, C_{11} is now determined to be $\frac{1}{E_x}$ and further

$$C_{12} = \frac{\varepsilon_y}{\sigma_x} = \frac{\varepsilon_y}{\varepsilon_x E_x} = -\frac{\nu_{yx}}{E_x}, \text{ and } C_{13} = \frac{\nu_{zx}}{E_x}$$

where $\nu_{zx} = -\frac{\varepsilon_z}{\varepsilon_x}$ and $\nu_{yx} = -\frac{\varepsilon_y}{\varepsilon_x}$. Similar relationships can be obtained by applying stresses in different directions. Therefore,

$$C_{11} = \frac{1}{E_x}, \quad C_{12} = -\frac{\nu_{xy}}{E_y}, \quad C_{13} = -\frac{\nu_{xz}}{E_z}$$

$$C_{12} = -\frac{\nu_{xy}}{E_y}, \quad C_{22} = \frac{1}{E_y}, \quad C_{23} = -\frac{\nu_{yz}}{E_z}$$

$$C_{31} = -\frac{\nu_{zx}}{E_x}, \quad C_{32} = -\frac{\nu_{zy}}{E_y}, \quad C_{33} = \frac{1}{E_z}$$

$$C_{44} = \frac{1}{G_{yz}}$$

$$C_{55} = \frac{1}{G_{xz}}$$

$$C_{66} = \frac{1}{G_{xy}}.$$

Another class of materials are *transversely isotropic*. When two of three sets of symmetry planes for the orthotropic properties become an infinite number of sets, the properties are called *transversely isotropic*. **Figure 2.5** illustrates an example for a *transversely isotropic* material using a unidirectional fibre reinforced composite. Therefore, $E_y=E_z$, $G_{xz}=G_{xy}$, and $\nu_{zy}=\nu_{zx}$.

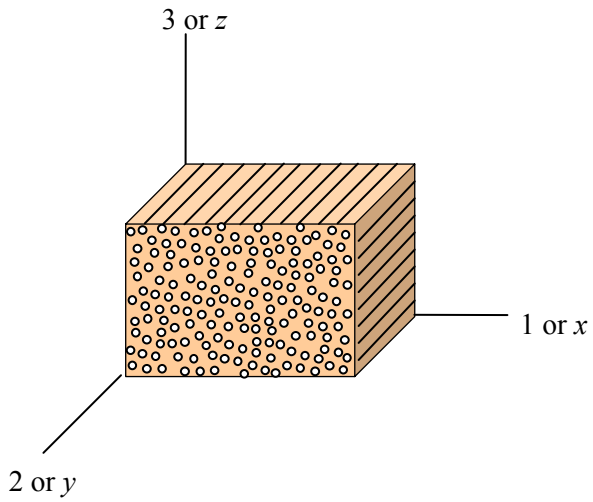

Figure 2.5 Transversely isotropic material.

For isotropic materials, $E_x=E_y=E_z=E$, $G_{yz}=G_{xz}=G_{xy}=G$ and $\nu_{xy}=\nu_{yx}=\nu_{zy}=\nu_{zx}=\nu$. Accordingly, the following equations can be recovered for isotropic materials:

$$\varepsilon_x=\frac{1}{E}\left[\sigma_x-\nu\left(\sigma_y+\sigma_z\right)\right]$$
$$\varepsilon_y=\frac{1}{E}\left[\sigma_y-\nu\left(\sigma_z+\sigma_x\right)\right] \qquad \text{(bis 2.3)}$$
$$\varepsilon_z=\frac{1}{E}\left[\sigma_z-\nu\left(\sigma_x+\sigma_y\right)\right]$$

$$\tau_{xy}=G\gamma_{xy},\quad \tau_{yz}=G\gamma_{yz},\ \tau_{xz}=G\gamma_{xz} \qquad \text{(bis 2.4).}$$

3 Circular Plates

The plates are meant to be subjected to the bending loads. Some examples for the use of plates include pressure vessel end caps and piton heads. An analysis can be conducted for the axi-symmetric loading with the benefit of the circular geometry. The analysis is based on the linear stress distribution across the thickness. For a circular plate (**Figure 3.1**), x in the coordinate system may be exchangeably used with r to indicate the radial direction.

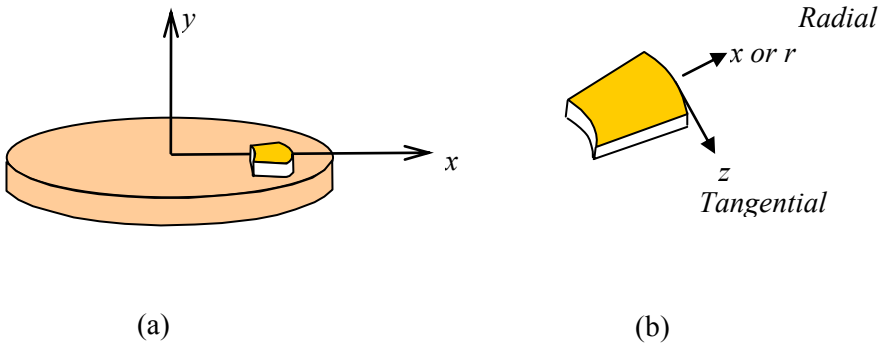

Figure 3.1 (a) A circular plate. (b) An infinitesimal element for directions in the axi-symmetric analysis.

3.1 Stress and strain

The general relations between stresses and strains previously discussed for isotropic materials are applicable:

$$\varepsilon_x = \frac{1}{E}\left[\sigma_x - v\left(\sigma_y + \sigma_z\right)\right]$$
$$\varepsilon_y = \frac{1}{E}\left[\sigma_y - v\left(\sigma_z + \sigma_x\right)\right] \qquad \text{(bis 2.3).}$$
$$\varepsilon_z = \frac{1}{E}\left[\sigma_z - v\left(\sigma_x + \sigma_y\right)\right]$$

The state of *plane stress* is also applicable to the circular plate. The stresses in the radial (x) and tangential directions (z) in the current coordinate system (**Figure 3.1**) are given by:

$$\sigma_x = \frac{E}{1-v^2}\left(\varepsilon_x + v\varepsilon_z\right)$$
$$\sigma_z = \frac{E}{1-v^2}\left(\varepsilon_z + v\varepsilon_x\right) \qquad \text{(bis 2.19)}$$

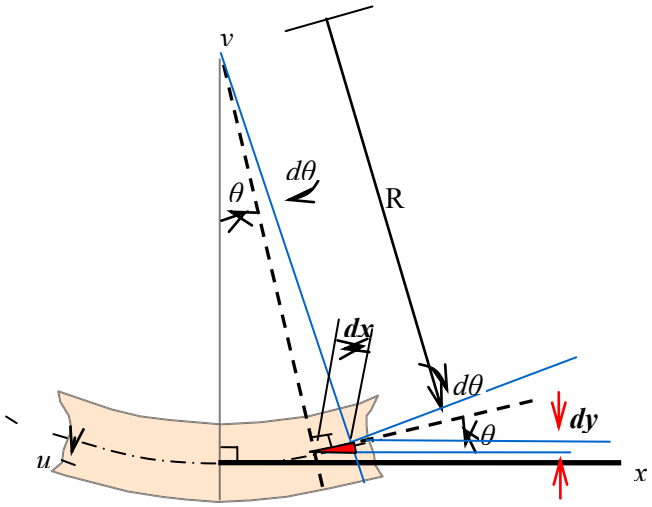

Figure 3.2 Cross section of circular plate.

The following procedure is given for finding strains (ε_x and ε_z) in above equations as functions of slope (θ).

In general, the following relation is applicable to pure bending of an infinitesimal element having a liner strain distribution:

$$\frac{M}{EI} = \frac{1}{R} \tag{3.1}$$

where M is the bending moment, R is the radius of curvature, E is the elastic modulus and I is the second moment of area.

The strain in the x-direction due to pure bending in x-y plane (**Figure 3.2**) is

$$\varepsilon_x = \frac{u}{R_{xy}} \tag{3.2}$$

where u is the distance of any point from the neutral axis.

In general, the curvature ($1/R$) for small deflection (**Figure 3.2**) is given by

$$\frac{1}{R} = \frac{d^2y}{dx^2}, \tag{3.3}$$

and for a small angle,

$$\frac{dy}{dx} = \tan\theta \approx \theta. \tag{3.4}$$

Therefore, the curvature in the x-y plane is given by

$$\frac{1}{R_{xy}} = \frac{d^2y}{dx^2} = \frac{d\theta}{dx} \tag{3.5}$$

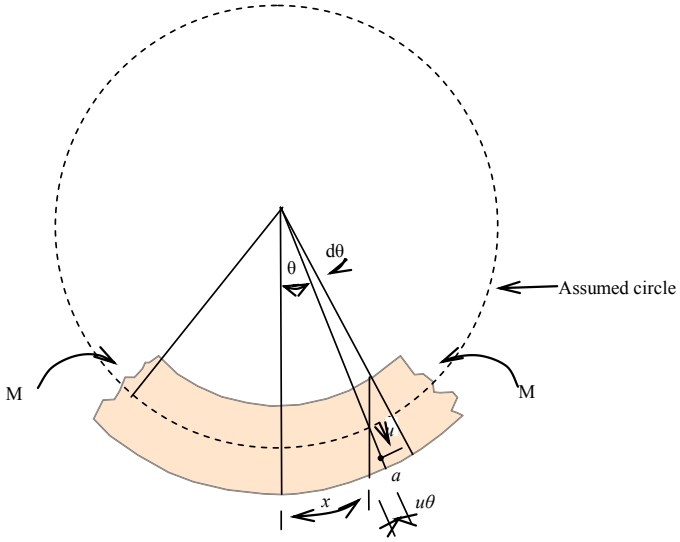

Figure 3.3 An exaggerated cross section of circular plate forming assumed spherical deflection for small deformation when a couple (M) consisting of two equal and opposite forces is applied.

and bending strain in radial direction in the circular plate (ε_x) is given by

$$\varepsilon_x = u\frac{d\theta}{dx}. \tag{3.6}$$

For a plate subjected to a couple (M) consisting two equal and opposite forces is applied (**Figure 3.3**), the circumferential strain (ε_z) at a (= ε_z), to which the distance from the neutral axis is u, due to the pure bending:

$$\varepsilon_z = \frac{x + u\theta - x}{x} = \frac{u\theta}{x}. \tag{3.7}$$

Thus, using the *plane stress* equation, the stresses in the radial (x) and tangential directions (z) are found as functions of slope (θ):

$$\sigma_x = \frac{E}{1-\nu^2}\left(\varepsilon_x + \nu\varepsilon_z\right) = \frac{Eu}{1-\nu^2}\left(\frac{d\theta}{dx} + \nu\frac{\theta}{x}\right) \tag{3.8}$$

and

$$\sigma_z = \frac{Eu}{1-\nu^2}\left(\varepsilon_z + \nu\varepsilon_x\right) = \frac{Eu}{1-\nu^2}\left(\frac{\theta}{x} + \nu\frac{d\theta}{dx}\right). \tag{3.9}$$

Equations (3.8) and (3.9) will be useful for finding stresses when the slope (θ) and its derivative are known.

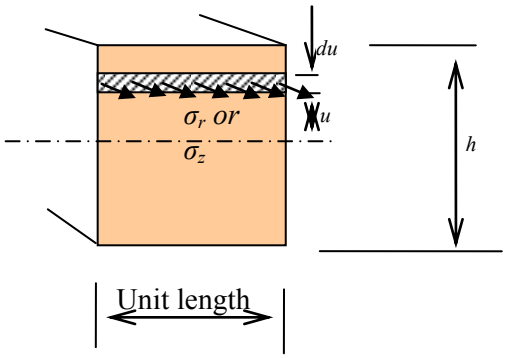

Figure 3.4 A section of the circular plate.

3.2 Bending moment

Let us consider the small section of the circular plate with a unit length (**Figure 3.4**). From the simple bending theory,

$$\frac{M}{I} = \frac{\sigma}{u} \rightarrow M = \frac{\sigma I}{u} = \frac{\sigma h^3}{12u} \tag{3.10}$$

where M is the bending moment per unit length, the bending moment (M_r) due to the stress in the radial direction (σ_x),

$$M_r = \frac{\sigma_x h^3}{12u} = \frac{h^3}{12}\frac{E}{1-v^2}\left(\frac{d\theta}{dx} + v\frac{\theta}{x}\right) = D\left(\frac{d\theta}{dx} + v\frac{\theta}{x}\right) \tag{3.11}$$

where $D = \frac{h^3}{12}\frac{E}{1-v^2}$

Similarly, the bending moment (M_z) due to the stress in the tangential direction (σ_z),

$$M_z = D\left(\frac{\theta}{x} + v\frac{d\theta}{dx}\right) \tag{3.12}$$

where $D = \frac{h^3}{12}\frac{E}{1-v^2}$.

It is useful to know that, unlike beams, the bending moments (M_r and M_z) here will be eliminated rather than calculated.

3.3 Slope and deflection without boundary conditions

Consider an infinitesimal element in **Figure 3.5** to relate deformation with the shear force (Q) and then external forces such as concentrated force and pressure.

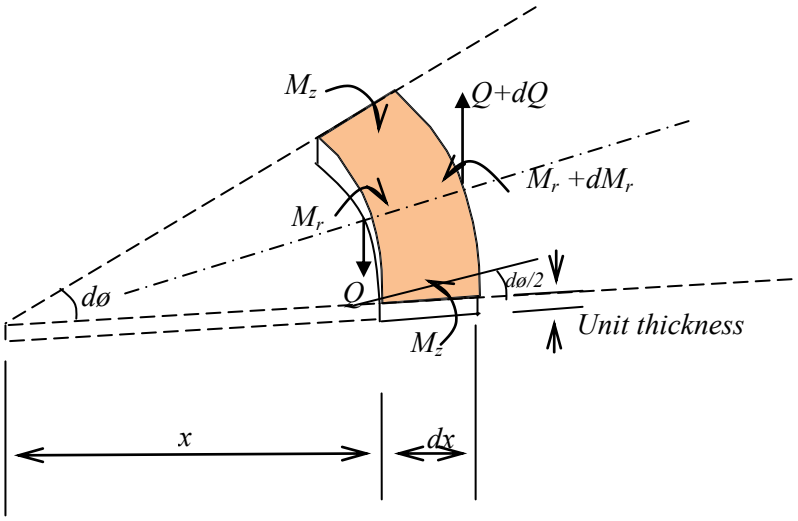

Figure 3.5 An infinitesimal element of circular plate.

The moments in the radial and tangential directions per unit length are M_r and M_z respectively and Q is the shear force per unit thickness.

Taking the moments about the outside edge under the equilibrium:

$$(M_r + dM_r)(x + dx)d\phi - M_r x d\phi - 2M_z dx \sin(\frac{1}{2}d\phi) + Qxd\phi dx = 0. \tag{3.13}$$

Neglecting small quantities, this reduces to

$$M_r dx + dM_r x - M_z dx + Qxdx = 0. \tag{3.14}$$

and rearranging,

$$M_r + x\frac{dM_r}{dx} - M_z = -Qx. \tag{3.15}$$

To eliminate moments, substituting

$$M_r = D\left(\frac{d\theta}{dx} + v\frac{\theta}{x}\right) \text{ and } M_z = D\left(\frac{\theta}{x} + v\frac{d\theta}{dx}\right) \tag{bis 3.11 \& 3.12}$$

into Equation (3.15) yields,

$$\frac{d^2\theta}{dx^2} + \frac{1}{x}\frac{d\theta}{dx} - \frac{\theta}{x^2} = -\frac{Q}{D} \tag{3.16}$$

or

$$\frac{d}{dx}\left(\frac{1}{x}\frac{d(x\theta)}{dx}\right)=-\frac{Q}{D}. \tag{3.17}$$

For a circular plate, it is convenient to replace x with r so that

$$\frac{d}{dr}\left(\frac{1}{r}\frac{d}{dr}(r\frac{dy}{dr})\right)=-\frac{Q}{D}. \tag{3.18}$$

Note that $\frac{dy}{dr}$ and y in equation above are the slope (θ) and the deflection respectively. The following section will show how to relate Equation (3.18) with external forces.

3.4 A general axi-symmetric case where a circular plate is subjected to combined uniformly distributed load (*p*) and central concentrated load (F)

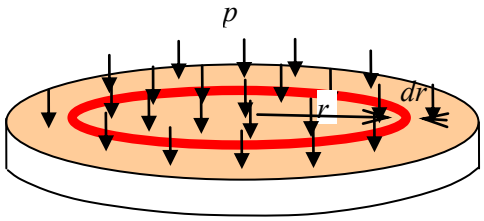

Figure 3.6 A circular plate subjected to pressure (p).

A general axi-symmetric case where the *pressure* (p) is applied uniformly on the circular plate is given in **Figure 3.6** without boundary conditions yet. The *shear force per unit length* (Q) may be found from the equilibrium at any radius (r):

$$Q\times 2\pi r = p\times \pi r^2 \rightarrow Q=\frac{pr}{2} \tag{3.19}$$

so that Equation (3.18) is related with an external load, pressure (p),

$$\frac{d}{dr}\left(\frac{1}{r}\frac{d}{dr}(r\frac{dy}{dr})\right)=-\frac{Q}{D}. \tag{3.20}$$

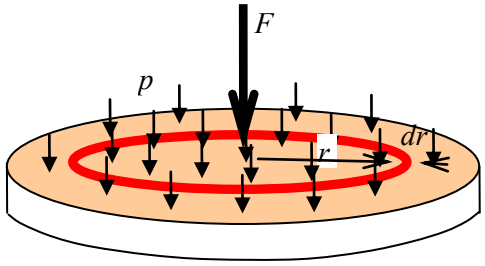

Figure 3.7 A circular plate subjected to pressure p and point force F.

Similarly, for the case (**Figure 3.7**) where both *pressure* (p) and *central concentrated load* (F) on the circular plate are applied, the shear force per unit length (Q):

$$Q \times 2\pi r = p \times \pi r^2 + F \rightarrow Q = \frac{pr}{2} + \frac{F}{2\pi r} \tag{3.21}$$

so that

$$\frac{d}{dr}\left(\frac{1}{r}\frac{d}{dr}(r\frac{dy}{dr})\right) = \left[-\frac{pr}{2} - \frac{F}{2\pi r}\right]\frac{1}{D}. \tag{3.22}$$

To find the slope ($\frac{dy}{dr}$) and the deflection (y), this equation may be integrated,

$$\frac{d}{dr}(r\frac{dy}{dr}) = -\frac{1}{D}\int\left[\frac{pr}{2} + \frac{F}{2\pi r}\right]dr = -\frac{1}{D}\left[\frac{pr^3}{4} + \frac{Fr}{2\pi}\ln r\right] + C_1 r \tag{3.23}$$

where C_1 is an integration constant. Integrating again,

$$\theta = \frac{dy}{dr} = -\frac{pr^3}{16D} - \frac{Fr}{8\pi D}(2\ln r - 1) + \frac{C_1 r}{2} + \frac{C_2}{r}. \tag{3.24}$$

Then,

$$y = -\frac{pr^4}{64D} - \frac{Fr^2}{8\pi D}(\ln r - 1) + \frac{C_1 r^2}{4} + C_2 \ln r + C_3 \tag{3.25}$$

The integration constants can be determined according to the boundary conditions as will be introduced for different cases.

3.5 A case where a circular plate with edges clamped is subjected to a pressure (*p*)

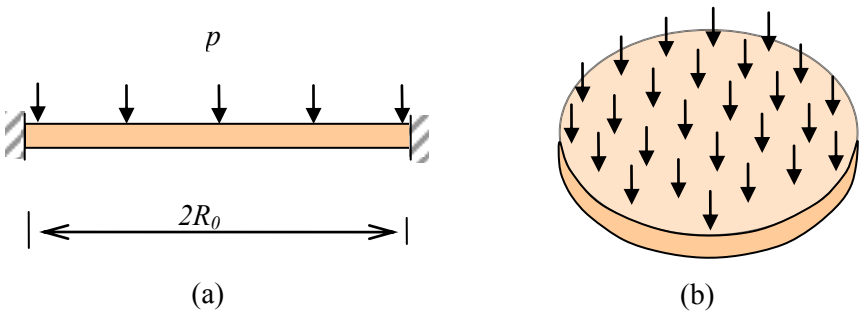

Figure 3.8 Circular plate with edges clamped: (a) cross sectional view; and (b) perspective view of plate.

To determine the integration constants in Equations (3.24) and (3.25) for the case where a circular plate with edges clamped is subjected to a pressure (p) with $F=0$ (**Figure 3.8**):

$$\theta = -\frac{pr^3}{16D} + \frac{C_1 r}{2} + \frac{C_2}{r}. \tag{3.26a}$$

and

$$y = -\frac{pr^4}{64D} + \frac{C_1 r^2}{4} + C_2 \ln r + C_3. \tag{3.26b}$$

The slope (θ) is zero at r =0, then, C_2 should be *zero* if the slope θ is not to approach infinity near the centre of the plate. If the centre of the circular plate is taken as the origin, deflection $y = 0$ at r = 0, and then C_3=0. At the clamped edge where $r = R_0$, $\theta = dy/dr$=0, from Equation (3.26a),

$$\theta = -\frac{pr^3}{16D} + \frac{C_1 r}{2} + \frac{C_2}{r} = -\frac{pR_0^3}{16D} + \frac{C_1 R_0}{2} = 0$$

$$\rightarrow C_1 = \frac{pR_0^2}{8D}. \tag{3.27a}$$

Therefore, the three integration constants are determined.

The maximum deflection (y_{max}) of the plate occurs at $r = R_0$:

$$y_{\max} = -\frac{pR_0^4}{64D} + \frac{pR_0^2}{8D}\frac{R_0^2}{4} = \frac{pR_0^4}{64D} \tag{3.27b}$$

To determine stresses (σ_x and σ_r) using Equations (3.8) and (3.9), the slope (θ) is determined first,

$$\theta = -\frac{pr^3}{16D} + \frac{C_1 r}{2} + \frac{C_2}{r} = -\frac{pr}{16D}(r^2 - R_0^2) \tag{3.27c}$$

and then,

$$\frac{d\theta}{dr} = -\frac{p}{16D}(3r^2 - R_0^2). \tag{3.27d}$$

Therefore,

$$\sigma_r = \sigma_x = \frac{Eu}{1-v^2}\left(\frac{d\theta}{dx} + v\frac{\theta}{x}\right) = \frac{Eu}{1-v^2}\left(-\frac{pr^2}{16D}(3+v) + \frac{pR_0^2}{16D}(1+v)\right) \tag{3.28a}$$

and

$$\sigma_z = \frac{Eu}{1-v^2}\left(\frac{\theta}{r} + v\frac{d\theta}{dr}\right) = \frac{Eu}{1-v^2}\left(-\frac{pr^2}{16D}(1+3v) + \frac{pR_0^2}{16D}(1+v)\right). \tag{3.28b}$$

The maximum stress (σ_{rmax}) will occur at the edge at which $r = R_0$ and at the surface where $u = h/2$,

$$\sigma_{r\max} = -\frac{3}{4}\frac{pR_0^2}{h^2} \tag{3.28c}$$

and σ_{zmax} takes place at $r=0$ so that

$$\sigma_{z\max} = \frac{3pR_0^2}{8h^2}(1+v). \tag{3.28d}$$

3.6 A case where a circular plate with edges clamped is subjected to a centrally concentrated load (F)

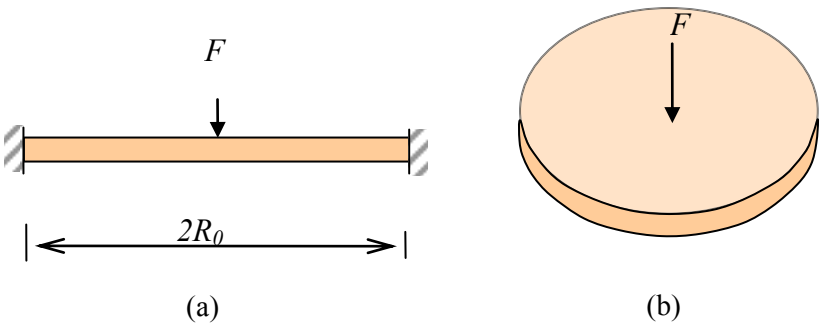

Figure 3.9 Circular plate with a radius of R_0, subjected to a centrally concentrated load (F), where edges of the plate are clamped: (a) cross sectional view; and (b) perspective view.

To determine the integration constants in Equations (3.24) and (3.25) for a case where a circular plate with edges clamped is subjected to a centrally concentrated load (F) as given in **Figure 3.9**, the slope (θ) at the centre is zero at r=0 so that C_2=0. If the origin of the coordinate system is taken as the centre of the plate, y = 0 at r = 0, therefore, C_3=0. Also, to determine C_1, a boundary condition is θ = 0 at r=R_0, therefore, from Equation (3.24),

$$\frac{Fr}{8\pi D}(2\ln r - 1) = \frac{C_1 r}{2} \rightarrow C_1 = \frac{F}{\pi D}\left(\frac{\ln R_0}{2} - \frac{1}{4}\right) \tag{3.29}$$

The maximum deflection (y_{max}) will occur at r =R_0, according to the current coordinate system, From Equation (3.25),

$$y_{\max} = \frac{FR_0^{\,2}}{16\pi D} \tag{3.30a}$$

or

$$y_{\max} = \frac{3FR_0^{\,2}}{4\pi Eh^3}(1-\nu^2)\,. \tag{3.30b}$$

To determine σ_r at r = R_0, the slope (θ) and its derivative need to be determined first:

$$\theta = \frac{dy}{dr} = -\frac{pr^3}{16D} - \frac{Fr}{8\pi D}(2\ln r - 1) + \frac{C_1 r}{2} + \frac{C_2}{r} \tag{bis 3.24}$$

$$= \left(-\frac{Fr}{4\pi D} \ln r + \frac{Fr}{8\pi D} \right) + \frac{Fr}{8\pi D} (2 \ln R_0 - 1), \tag{3.31a}$$

$$\frac{d\theta}{dr} = -\frac{F}{8\pi D} (2 \ln r + 2 - 2 \ln R_0) = -\frac{2F}{8\pi D} (\ln \frac{r}{R_0} + 1) \tag{3.31b}$$

and

$$\nu \frac{\theta}{r} = \left(-\frac{\nu F}{4\pi D} \ln r \right) + \frac{\nu F}{4\pi D} \ln R_0 = \frac{\nu F}{4\pi D} (\ln R_0 - \ln r). \tag{3.31c}$$

Therefore, from Equations (3.8) and (3.9),

$$\sigma_r = \frac{Eu}{1-\nu^2} \left(\frac{d\theta}{dr} + \nu \frac{\theta}{r} \right) = \frac{F}{4\pi D} \frac{Eu}{1-\nu^2} \left(-(\ln \frac{r}{R_0} + 1) + \nu (\ln R_0 - \ln r) \right) \tag{3.32a}$$

and

$$\sigma_z = \frac{Eu}{1-\nu^2} \left(\frac{\theta}{r} + \nu \frac{d\theta}{dr} \right) = \frac{F}{4\pi D} \frac{Eu}{1-\nu^2} \left((\ln R_0 - \ln r) - \nu (\ln \frac{r}{R_0} + 1) \right). \tag{3.32b}$$

The stress distribution according to Equation (3.32a) is shown in **Figure 3.10**.

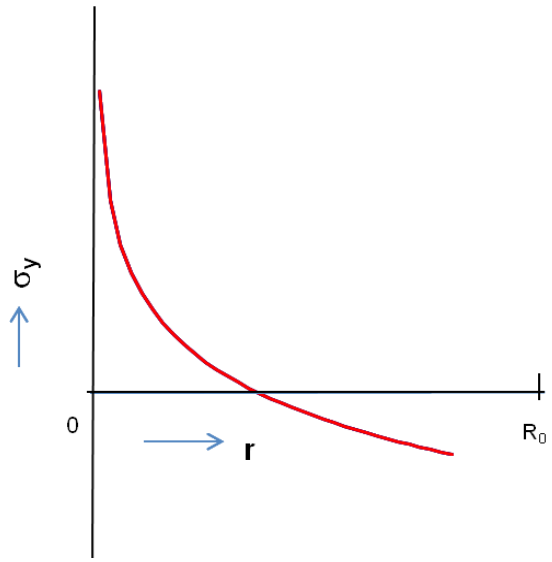

Figure 3.10 Stress distribution in the radial direction.

Accordingly, the stresses are found at $r = R_0$ and $u = \frac{h}{2}$ with $D = \frac{h^3}{12} \frac{E}{1-\nu^2}$:

$$\sigma_{r=R_0} = \frac{Eu}{1-\nu^2} \left(\frac{d\theta}{dr} + \nu \frac{\theta}{r} \right) = -\frac{3F}{2\pi h^2} \tag{3.33a}$$

and

$$\sigma_{z=R_0} = \frac{Eu}{1-\nu^2}\left(\frac{d\theta}{dr} + \nu\frac{\theta}{r}\right) = -\frac{3\nu F}{2\pi h^2}. \tag{3.33b}$$

3.7 A case where a circular plate with edges freely supported is subjected to a pressure (*p*)

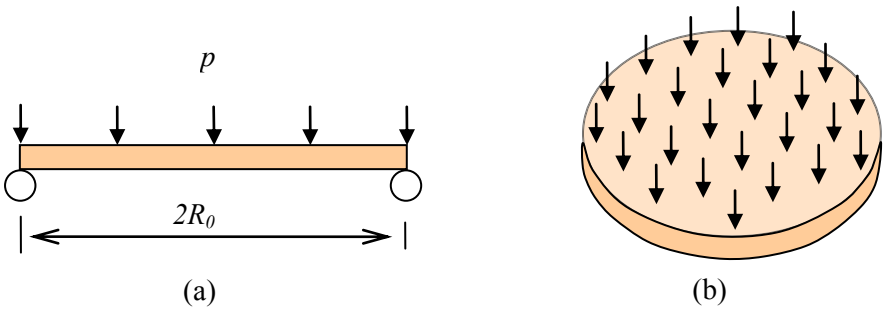

Figure 3.11 Circular plate with edges freely supported: (a) cross sectional view; and (b) perspective view.

To determine the integration constants in Equations (3.24) and (3.25) for a case where a circular plate with edges freely supported is subjected to a pressure (p) as given in **Figure 3.11**, the boundary conditions may be considered with:

$$\theta = \frac{dy}{dr} = -\frac{pr^3}{16D} - \frac{Fr}{8\pi D}(2\ln r - 1) + \frac{C_1 r}{2} + \frac{C_2}{r}, \tag{bis3.24}$$

$$y = -\frac{pr^4}{64D} - \frac{Fr^2}{8\pi D}(\ln r - 1) + \frac{C_1 r^2}{4} + C_2 \ln r + C_3. \tag{bis3.25}$$

At r=0, the slope (θ) at the centre is zero and therefore $C_2 = 0$ if the slope (θ) is not to approach infinity near the centre of the plate.

Again, if the centre of the circular plate is taken as the origin of the coordinate system, deflection $y = 0$ at $r = 0$ and therefore C_3=0.

To determine C_1, we consider that the bending moment (M_r) is zero at any free support ($r = R_0$). From

$$M_r = D\left(\frac{d\theta}{dr} + \nu\frac{\theta}{r}\right) = 0, \tag{bis3.11}$$

we find,

$$\frac{d\theta}{dr} = -\nu\frac{\theta}{r}. \tag{3.34}$$

Using Equations (3.34) and (3.24), we find,

$$\left.\begin{aligned}\frac{d\theta}{dr} &= -\frac{3pr^2}{16D} + \frac{C_1}{2} \\ \frac{\theta}{r} &= -\frac{pr^2}{16D} + \frac{C_1}{2}\end{aligned}\right] \rightarrow -\frac{3pr^2}{16D} + \frac{C_1}{2} = -\nu\left(-\frac{pr^2}{16D} + \frac{C_1}{2}\right) \tag{3.35a}$$

and

$$C_1 = \left(\frac{pR_0^2}{8D}\right)\frac{(3+\nu)}{(1+\nu)}. \tag{3.35b}$$

The maximum deflection (y_{max}) occurs at $r = R_0$ if we use the current coordinate system:

$$y_{\max} = \left(\frac{pR_0^4}{64D}\right)\frac{(5+\nu)}{(1+\nu)} \tag{3.35c}$$

with $D = \frac{h^3}{12}\frac{E}{1-\nu^2}$, or

$$y_{\max} = \frac{3pR_0^4}{16Eh^3}(5+\nu)(1-\nu). \tag{3.35d}$$

To determine stresses (σ_r and σ_z) using Equations (3.8) and (3.9), we need to determine the slope (θ) and $\frac{d\theta}{dr}$ first:

$$\theta = -\frac{pr^3}{16D} - \frac{Fr}{8\pi D}(2\ln r - 1) + \frac{C_1 r}{2} + \frac{C_2}{r} = -\frac{pr^3}{16D} + \frac{r}{1}\left(\frac{pR_0^2}{16D}\right)\frac{(3+\nu)}{(1+\nu)}, \tag{3.36a}$$

$$\nu\frac{\theta}{r} = -\nu\frac{pr^2}{16D} + \nu\left(\frac{pR_0^2}{16D}\right)\frac{(3+\nu)}{(1+\nu)}, \tag{3.36b}$$

and

$$\frac{d\theta}{dr} = -\frac{3pr^2}{16D} + \left(\frac{pR_0^2}{16D}\right)\frac{(3+\nu)}{(1+\nu)}. \tag{3.36c}$$

Therefore, the radial stress (σ_r) is found,

$$\sigma_r = \frac{Eu}{1-\nu^2}\left(\frac{d\theta}{dr} + \nu\frac{\theta}{r}\right) = \frac{Eu}{1-\nu^2}\left(-\frac{pr^2}{16D}(1+\nu) + \left(\frac{pR_0^2}{16D}\right)(3+\nu)\right). \tag{3.37a}$$

The maximum stress σ_{rmax} occurs at $r = 0$,

$$\sigma_{r\max} = \frac{Eu}{1-\nu^2}\left(-\frac{pr^2}{16D}(3+\nu) + \left(\frac{pR_0^2}{16D}\right)(3+\nu)\right) = \frac{Eh/2}{1-\nu^2}\left(\frac{pR_0^2}{16D}\right)(3+\nu) \tag{3.37b}$$

with $D = \frac{h^3}{12}\frac{E}{1-\nu^2}$, or

$$\sigma_{r\max} = \left(\frac{3pR_0^2}{8h^2}\right)(3+\nu) \tag{3.38a}$$

Similarly, the maximum stress in the tangential direction occurs at $r = 0$ and

$$\sigma_{z\max} = \sigma_{r\max} = \left(\frac{3pR_0^2}{8h^2}\right)(3+\nu). \tag{3.38b}$$

3.8 A case where a circular plate with edges freely supported is subjected to a central concentrated load (F)

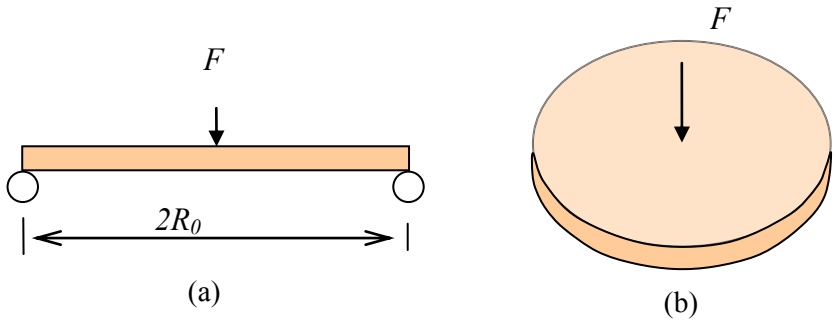

Figure 3.12 Cross section of a circular plate with a radius of R_0, subjected to a point force (F), where edges are freely supported: (a) cross sectional view; and (b) perspective view.

To determine the integration constants in Equations (3.24) and (3.25) for a case where a circular plate with edges freely supported is subjected to a central concentrated load (F) as given in **Figure 3.12**, the boundary conditions may be considered with:

$$\theta = \frac{dy}{dr} = -\frac{pr^3}{16D} - \frac{Fr}{8\pi D}(2\ln r - 1) + \frac{C_1 r}{2} + \frac{C_2}{r}, \qquad \text{(bis 3.24)}$$

$$y = -\frac{pr^4}{64D} - \frac{Fr^2}{8\pi D}(\ln r - 1) + \frac{C_1 r^2}{4} + C_2 \ln r + C_3. \qquad \text{(bis 3.25)}$$

At r=0, the slope (θ) at the centre is zero and therefore $C_2 = 0$ if the slope (θ) is not to approach infinity near the centre of the plate.

Again, if the centre of the circular plate is taken as the origin of the coordinate system, deflection $y = 0$ at $r = 0$ and therefore C_3=0.

To determine C_1, we consider that the bending moment (M_r) is zero at any free support ($r = R_0$). As before, from,

$$M_r = D\left(\frac{d\theta}{dr} + \nu\frac{\theta}{r}\right) = 0, \qquad \text{(bis 3.11)}$$

we find,

$$\frac{d\theta}{dr} = -\nu\frac{\theta}{r}. \qquad \text{(bis 3.34)}$$

Using Equations (3.34) and (3.24) again,

$$\frac{d\theta}{dr} = -\frac{F}{8\pi D}\left(2\ln r + 2r\frac{1}{r} - 1\right) + \frac{C_1}{2} = -\frac{2F}{8\pi D}\left(\ln r + \frac{1}{2}\right) + \frac{C_1}{2} \qquad \text{(3.39a)}$$

and

$$-\nu\frac{\theta}{r}=\frac{\nu F}{8\pi D}(2\ln r-1)-\frac{C_1\nu}{2}. \tag{3.39b}$$

Equating these two equations with $r = R_0$

$$C_1=\frac{F}{4\pi D}\left(2\ln R_0+\frac{1-\nu}{1+\nu}\right). \tag{3.39c}$$

The maximum deflection (y_{max}) occurs at the supports ($r = R_0$), if we use the current coordinate system. From Equation (3.25), ($p = 0$, $C_2 = C_3 = 0$)

$$y_{\max}=\frac{FR_0^{\,2}}{16\pi D}\frac{3+\nu}{1+\nu} \tag{3.39d}$$

with $D=\frac{h^3}{12}\frac{E}{1-\nu^2}$ or

$$y_{\max}=\frac{FR_0^{\,2}}{16\pi D}\frac{3+\nu}{1+\nu}=\frac{FR_0^{\,2}}{16\pi}\frac{3+\nu}{1+\nu}\frac{12(1-\nu^2)}{Eh^3}=\frac{3FR_0^{\,2}}{4\pi Eh^3}(3+\nu)(1-\nu). \tag{3.39e}$$

This maximum deflection is approximately 2.5 times that of the plate with the clamped edge for Poisson's ratio ν = 0.3.

To determine stresses (σ_r and σ_z) using Equations (3.8) and (3.9), we need to determine the slope (θ) and $\frac{d\theta}{dr}$ first. From Equation (3.24),

$$\theta = -\frac{F}{8\pi D}\left(2r\ln r - r\right) + \frac{C_1 r}{2} \quad (C_2 = 0,\ p = 0) \tag{3.40a}$$

$$\frac{d\theta}{dr} = \frac{F}{4\pi D}\left(\ln\frac{R_0}{r} - \frac{\nu}{1+\nu}\right), \tag{3.40b}$$

and

$$\nu\frac{\theta}{r} = \frac{\nu F}{4\pi D}\left(\frac{1}{1+\nu} + \ln\frac{R_0}{r}\right). \tag{3.40c}$$

Accordingly,

$$\sigma_r = \frac{Eu}{1-\nu^2}\left(\frac{d\theta}{dr} + \nu\frac{\theta}{r}\right) = \frac{Eu}{1-\nu^2}\left[\frac{F}{4\pi D}\left((1+\nu)\ln\frac{R_0}{r}\right)\right] \tag{3.41a}$$

with $D = \frac{h^3}{12}\frac{E}{1-\nu^2}$ or

$$\sigma_r = \frac{3F(1+\nu)}{2\pi h^2}\ln\frac{R_0}{r}. \tag{3.41b}$$

Note that σ_r is zero at the edge and infinite at the centre. In practice, the concentrated load is on a finite area.

The stress in the z-direction,

$$\sigma_z = \frac{Eu}{1-\nu^2}\left(\frac{\theta}{r} + \nu\frac{d\theta}{dr}\right) \tag{3.41c}$$

$$= \frac{Eu}{1-\nu^2}\left[\frac{F}{4\pi D}\left((1+\nu)\ln\frac{R_0}{r} + (1-\nu)\right)\right]$$

with $D = \frac{h^3}{12}\frac{E}{1-\nu^2}$ or

$$\sigma_z = \frac{3F}{2\pi h^2}\left[\left((1+\nu)\ln\frac{R_0}{r} + (1-\nu)\right)\right]. \tag{3.41d}$$

3.9 A case where a circular plate with edges freely supported is subjected to a load (F) round a circle

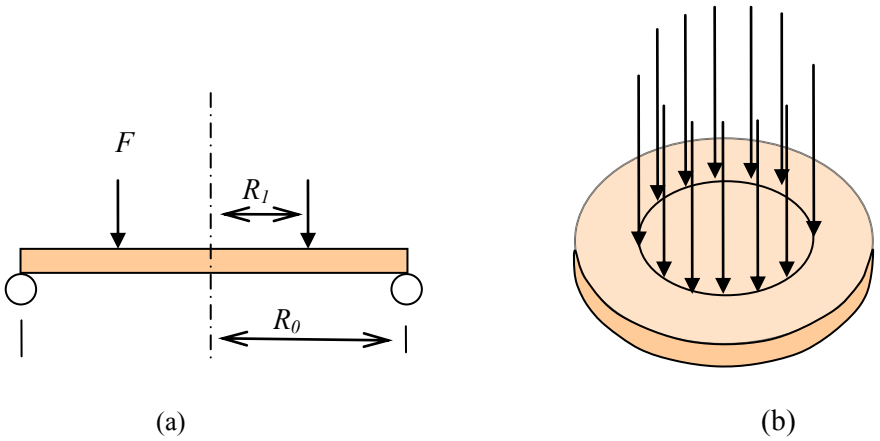

Figure 3.13 Circular plate with a radius of R_0, subjected to a load round a circle (F), where edges are freely supported: (a) cross-section (b) perspective view.

To determine the integration constants in Equations (3.24) and (3.25) for a case where a circular plate with edges freely supported is subjected to a load (F) round a circle as given in **Figure 3.13**, the boundary conditions may be considered with:

$$\theta = \frac{dy}{dr} = -\frac{pr^3}{16D} - \frac{Fr}{8\pi D}(2\ln r - 1) + \frac{C_1 r}{2} + \frac{C_2}{r}, , \qquad \text{(bis3.24)}$$

$$y = -\frac{pr^4}{64D} - \frac{Fr^2}{8\pi D}(\ln r - 1) + \frac{C_1 r^2}{4} + C_2 \ln r + C_3 . . \qquad \text{(bis3.25)}$$

There will be two sets of integration constants because of the discontinuity between two parts. For the inner part of the circular plate, $r < R_1$, $p = F = 0$. From Equation (3.25), the deflection (y) is found to be

$$y = \frac{C_1 r^2}{4} + C_2 \ln r + C_3 \qquad (3.42a)$$

and from Equation (3.24), the slope (θ) is found as

$$\theta = \frac{C_1 r}{2} + \frac{C_2}{r} . \qquad (3.42b)$$

If the centre of the circular plate is taken as the origin of the coordinate system, deflection $y = 0$ at $r = 0$ and therefore C_3=0. For non-infinite slope at the centre, C_2=0.

Thus, the deflection (y) for the inner part of the circular plate ($r < R_1$),

$$y = \frac{C_1 r^2}{4} \qquad (3.43a)$$

and

$$\theta = \frac{C_1 r}{2}. \tag{3.43b}$$

The constant C_1 is to be determined later.

For the outer part of the circular plate, $r \geq R_1$, another set of integration constants (C_1' , C_2' , and C_3') may be introduced and Equations (3.24) and (3.25) reduce respectively to

$$\theta = \frac{dy}{dr} = -\frac{Fr}{8\pi D}(2\ln r - 1) + \frac{C_1' r}{2} + \frac{C_2'}{r} \tag{3.44a}$$

and

$$y = -\frac{Fr^2}{8\pi D}(\ln r - 1) + \frac{C_1' r^2}{4} + C_2' \ln r + C_3'. \tag{3.44b}$$

Now, four constants (C_1 , C_1' , C_2' , and C_3') need to be determined and we need to find four simultaneous equations. Inner and outer plate parts are common at $r = R_1$ for deflection (y) and slope (θ). Accordingly, equating Equation (3.43a) to Equation (3.43b), and Equation (3.43b) to Equation (3.44b), two of the four simultaneous equations are found:

$$\frac{C_1 R_1}{2} = -\frac{F R_1}{8\pi D}\left(2\ln R_1 - 1\right) + \frac{C_1' R_1}{2} + \frac{C_2'}{R_1} \tag{3.45a}$$

and

$$\frac{C_1 R_1^{\,2}}{4} = -\frac{F R_1^{\,2}}{8\pi D}\left(\ln R_1 - 1\right) + \frac{C_1' R_1^{\,2}}{4} + C_2' \ln R_1 + C_3'. \tag{3.45b}$$

Also, using

$$M_r = D\left(\frac{d\theta}{dr} + \nu\frac{\theta}{r}\right), \tag{bis 3.11}$$

with the common M_r at $r = R_1$, two more equations can be found .

For the inner part (F=0, $r<R_1$) using Equation (3.42b),

$$\theta = \frac{C_1 r}{2} \tag{3.46a}$$

then,

$$\frac{d\theta}{dr} = \frac{C_1}{2} \tag{3.46b}$$

and

$$\frac{\theta}{r} = \frac{C_1}{2}. \tag{3.46c}$$

For outer part ($F\neq 0$, $r\geq R_2$), using Equation (3.44a),

$$\frac{d\theta}{dr} = -\frac{F}{8\pi D}\left(2\ln r + 2r\frac{1}{r} - 1\right) + \frac{C_1'}{2} - \frac{C_2'}{r^2} \tag{3.47a}$$

and for $r = R_1$,

$$\left(\frac{d\theta}{dr}\right)_{r=R_1} = -\frac{F}{8\pi D}\left(2\ln R_1 + 1\right) + \frac{C_1'}{2} - \frac{C_2'}{R_1^{\,2}}. \tag{3.47b}$$

Also,

$$\frac{\theta}{r} = -\frac{F}{8\pi D}\left(2\ln r - 1\right) + \frac{C_1'}{2} + \frac{C_2'}{r^2} \tag{3.47c}$$

and for $r = R_1$,

$$\left(\frac{\theta}{r}\right)_{r=R_1} = -\frac{F}{8\pi D}\left(2\ln R_1 - 1\right) + \frac{C_1'}{2} + \frac{C_2'}{R_1^{\,2}}. \tag{3.47d}$$

Substituting Equations (3.46) and (3.47) into Equation (3.11) and then equating resulting two equations:

$$\frac{C_1}{2}(1+\nu) = -\frac{F}{8\pi D}\left(2\ln R_1(1+\nu)+(1-\nu)\right)+\frac{C_1'}{2}(1+\nu)-\frac{C_2'}{R_1^{\,2}}(1-\nu). \tag{3.48}$$

This is the third equation of the four simultaneous equations.

For one more simultaneous equation, we may use $M_r = 0$ at the outside edge ($r = R_0$) with Equation (3.11),

$$-\frac{F}{8\pi D}\left(2\ln R_1(1+\nu)+(1-\nu)\right)+\frac{C_1'}{2}(1+\nu)-\frac{C_2'}{R_1^{\,2}}(1-\nu)=0. \tag{3.49}$$

Thus, four simultaneous Equations (3.45a), (3.45b), (3.48), and (3.49) have been found for four unknowns. The solution yields

$$C_1 = \frac{F}{4\pi D}(1+2\ln\frac{R_0}{R_1}+\frac{(1-\nu)(R_0^2-R_1^2)}{(1+\nu)R_0^2}-R_1), \tag{3.50a}$$

$$C_1' = \frac{F}{4\pi D}\left(2\ln R_0+\frac{(1-\nu)(R_0^2-R_1^2)}{(1+\nu)R_0^2}\right), \tag{3.50b}$$

$$C_2' = -\frac{FR_1^2}{8\pi D}, \tag{3.50c}$$

and

$$C_3' = \frac{FR_1^2}{8\pi D}(\ln R_1 - 1). \tag{3.50d}$$

The deflection (y) for the outer part of the circular plate, $r \geq R_1$ with the origin of the current coordinate system at the centre of the plate, Equation (3.44b) yields:

$$y = -\frac{Fr^2}{8\pi D}\left(\ln r-1\right)+\frac{C_1'r^2}{4}+C_2'\ln r+C_3'$$

$$= -\frac{Fr^2}{8\pi D}\left(\ln r-1\right)+\frac{r^2}{4}\frac{F}{4\pi D}\left(2\ln R_0+\frac{(1-\nu)(R_0^2-R_1^2)}{(1+\nu)R_0^2}\right)-\frac{FR_1^2}{8\pi D}\ln r+\frac{FR_1^2}{8\pi D}(\ln R_1-1). \tag{3.51}$$

The maximum deflection (y_{max}) occurs at the supports ($r = R_0$) and is given by

$$y_{\max} = y_{r=R_0} = \frac{F}{8\pi D}\left[\left(\frac{3-\nu}{2(1+\nu)}\right)(R_0^2-R_1^2)-R_1^2\ln\frac{R_0}{R_1}\right]. \tag{3.52}$$

The stress σ_{rmax} for this case occurs at $r = R_1$. Using Equation (3.8),

$$\sigma_{r\max} = \frac{3F}{4\pi h^2}\left\{2(1+\nu)\ln\frac{R_0}{R_1}+(1-\nu)\frac{R_0^2-R_1^2}{R_0^2}\right\}. \tag{3.53}$$

3.10 A case where an annular ring with edges freely supported is subjected to a load round a circle ($p = 0$)

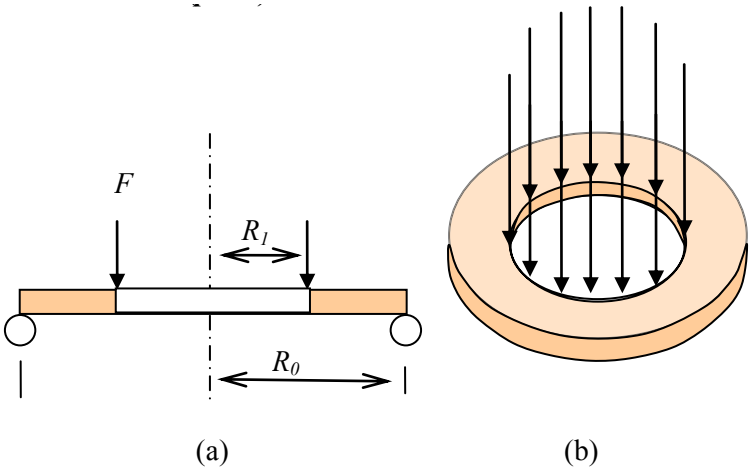

Figure 3.14 Annular ring with a radius of R_0, subjected to a load round a circle (F), where edges are freely supported:(a) cross-section; and (b) perspective view.

The plate subjected to a load round a circle ($p = 0$) shown in **Figure 3.14** is an annular ring with edges freely supported. The following equations derived previously for the outer part of the circular plate in **Figure 3.13** is directly applicable for the annular ring:

$$\theta = \frac{dy}{dr} = -\frac{Fr}{8\pi D}(2\ln r - 1) + \frac{C_1' r}{2} + \frac{C_2'}{r} \qquad \text{(bis 3.44a)}$$

and

$$y = -\frac{Fr^2}{8\pi D}(\ln r - 1) + \frac{C_1' r^2}{4} + C_2' \ln r + C_3'. \qquad \text{(bis 3.44b)}$$

To determine constants in equation above, we may use $M_r = 0$ at both $r = R_1$ and $r = R_0$ with

$$M_r = D\left(\frac{d\theta}{dr} + \nu\frac{\theta}{r}\right). \qquad \text{(bis 3.11)}$$

Differentiating Equation (3.44a),

$$\frac{d\theta}{dr} = -\frac{F}{8\pi D}\left(2\ln r + 2r\frac{1}{r} - 1\right) + \frac{C_1'}{2} - \frac{C_2'}{r^2}, \qquad (3.54a)$$

then,

$$\left(\frac{d\theta}{dr}\right)_{r=R_1} = -\frac{F}{8\pi D}(2\ln R_1 + 1) + \frac{C_1'}{2} - \frac{C_2'}{R_1^2} \qquad (3.54b)$$

and

$$\left(\frac{d\theta}{dr}\right)_{r=R_0} = -\frac{F}{8\pi D}(2\ln R_0 + 1) + \frac{C_1'}{2} - \frac{C_2'}{R_0^2}. \qquad (3.54c)$$

Using Equation (3.44a),

$$\frac{\theta}{r} = -\frac{F}{8\pi D}(2\ln r - 1) + \frac{C_1'}{2} + \frac{C_2'}{r^2}, \qquad (3.54d)$$

$$\left(\nu\frac{\theta}{r}\right)_{r=R_1} = -\frac{\nu F}{8\pi D}(2\ln R_1 - 1) + \frac{C_1'\nu}{2} + \frac{C_2'\nu}{R_1^2} \qquad (3.54e)$$

and

$$\left(\nu\frac{\theta}{r}\right)_{r=R_0} = -\frac{\nu F}{8\pi D}(2\ln R_0 - 1) + \frac{C_1'\nu}{2} + \frac{C_2'\nu}{R_0^2}. \qquad (3.54f).$$

Setting Equation (3.11) to zero for $r = R_1$,

$$-\frac{F}{8\pi D}\{2(1+\nu)\ln R_1 + (1-\nu)\} + \frac{C_1'}{2}(1+\nu) - \frac{C_2'}{R_1^2}(1-\nu) = 0 \qquad (3.55)$$

and for $r = R_0$,

$$-\frac{F}{8\pi D}\{2(1+\nu)\ln R_0 + (1-\nu)\} + \frac{C_1'}{2}(1+\nu) - \frac{C_2'}{R_0^2}(1-\nu) = 0. \qquad (3.56)$$

From the two simultaneous Equations (3.55) and (3.56), two of the three integration constants are found to be

$$C_2' = -\frac{F}{4\pi D}\frac{(1+\nu)}{(1-\nu)}\frac{{R_0}^2{R_1}^2}{{R_1}^2-{R_0}^2}\ln\frac{R_0}{R_1} \tag{3.57a}$$

and

$$C_1' = \frac{F}{4\pi D}\left\{\frac{(1-\nu)}{(1+\nu)} - \frac{2(R_0^2-R_1^2)}{R_0^2-R_1^2}\ln\frac{R_0}{R_1}\right\}. \tag{3.57b}$$

If we use the same coordinate system, $y = 0$ at $r = R_1$,

$$C_3' = \frac{F{R_1}^2}{8\pi D}\left\{1+\frac{1}{2}\frac{(1+\nu)}{(1-\nu)} - \frac{R_0^2}{R_0^2-R_1^2}\ln\frac{R_0}{R_1}\right\}. \tag{3.57c}$$

More cases with different boundary conditions are shown in **Figure 3.15**. The maximum stress ($\sigma_{\max}$) for all those cases can be in a generalised form given by

$$\sigma_{\max} = \frac{k_1 pR_0^2}{h^2} \tag{3.58a}$$

or

$$\sigma_{\max} = \frac{k_1 F}{h^2} \tag{3.58b}$$

where k_1 is a factor dependant on the boundary condition, Poisson's ratio, and $\frac{R_0}{R_1}$. Likewise, the maximum deflection ($y_{\max}$) for the same cases is given by

$$y_{\max} = \frac{k_2 pR_0^2}{Eh^2} \tag{3.58c}$$

or

$$y_{\max} = \frac{k_2 FR_0^2}{Eh^2} \tag{3.58d}$$

where k_2 is a factor dependant on the boundary condition, Poisson's ratio, and $\frac{R_0}{R_1}$.

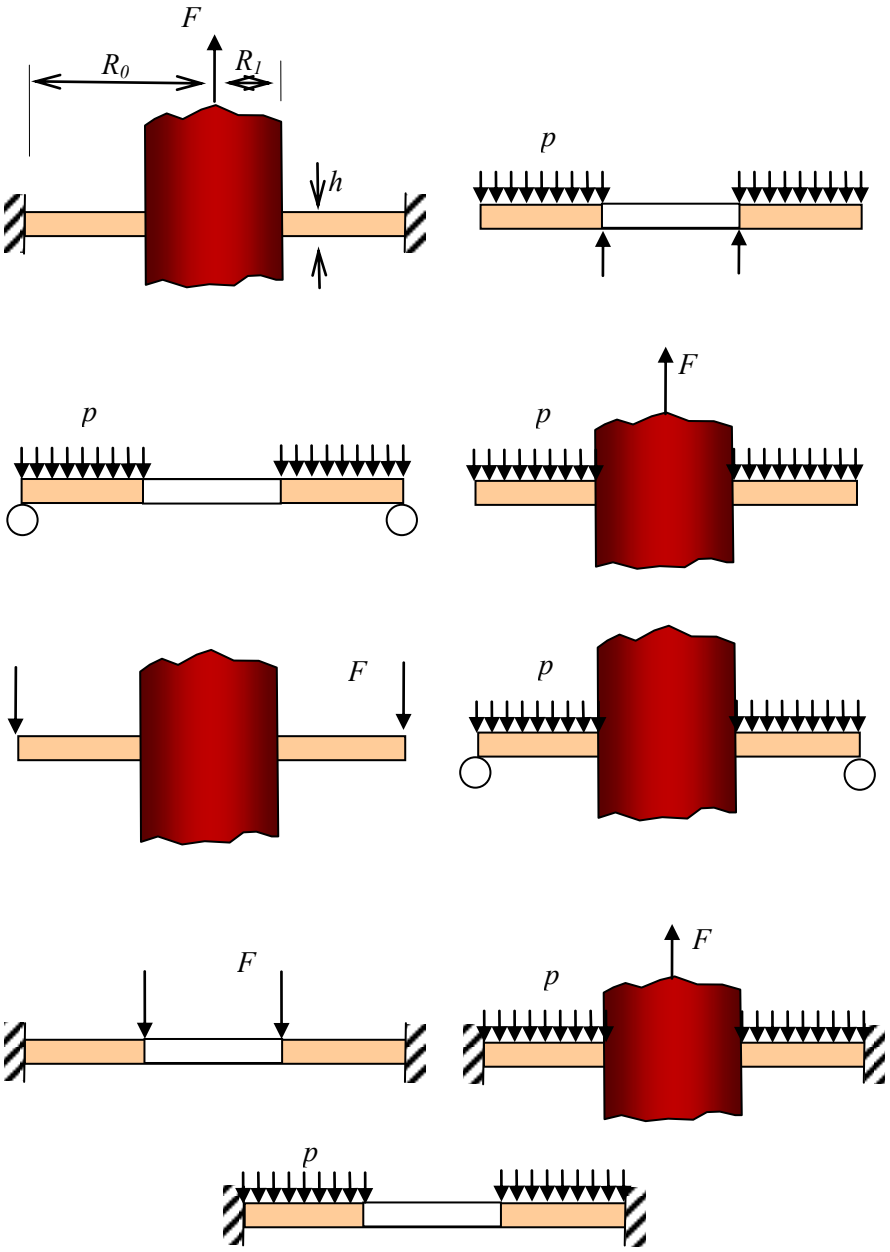

Figure 3.15 Cross sections of various cases for different boundary conditions.

4 Fundamentals For Theory Of Elasticity

In the elementary mechanics of solids, assumptions are used for simplification before arriving at solutions. For example, a linear stress distribution is assumed for a beam or a shaft. In the theory of elasticity, however, the stress distribution is to be found by satisfying the equilibrium equations, compatibility equations, and boundary conditions without such assumptions. It is a mathematical process.

4.1 Equilibrium and compatibility equations

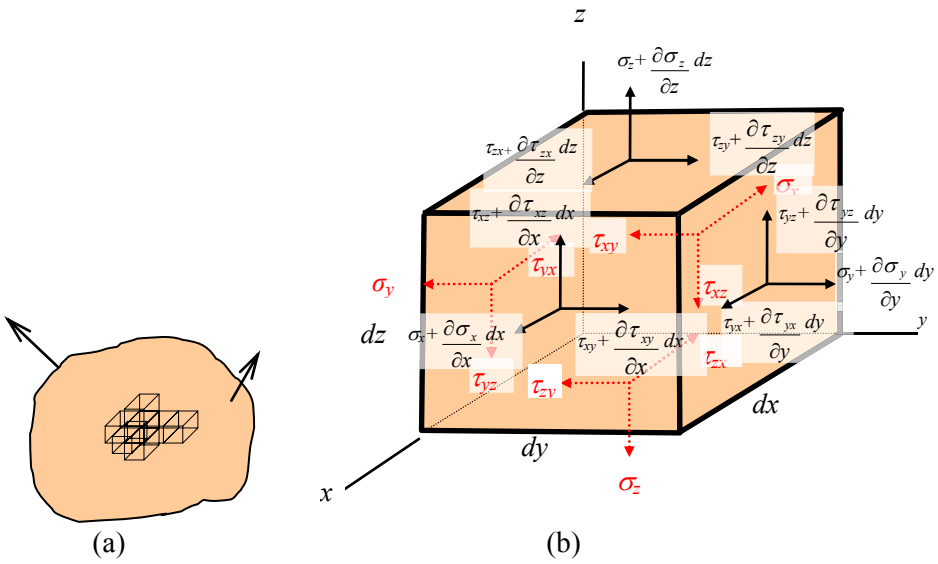

Figure 4.1 (a) A body subjected to external forces.
(b) One of the elements where stress varies from one face to another.

For the stress variation within a elastic body [**Figure 4.1(a)**], let us consider one of the stress elements given in **Figure 4.1(b)**. To find the equilibrium equations, we need to consider the *forces* acting on the element. The *forces* are found by multiplying the stress on any face by the surface area. Also, we need to consider a body force though the centroid of the element and having components X, Y, Z per unit volume. Taking the summation of *forces* in the x, y and z directions results in the following differential equations of equilibrium:

for x-direction,

$$\frac{\partial \sigma_x}{\partial x} + \frac{\partial \tau_{yx}}{\partial y} + \frac{\partial \tau_{zx}}{\partial z} + X = 0; \tag{4.1}$$

for *y*-direction,

$$\frac{\partial \sigma_y}{\partial y} + \frac{\partial \tau_{xy}}{\partial x} + \frac{\partial \tau_{zy}}{\partial z} + Y = 0; \tag{4.2}$$

for *z*-direction,

$$\frac{\partial \sigma_z}{\partial z} + \frac{\partial \tau_{yz}}{\partial y} + \frac{\partial \tau_{xz}}{\partial x} + Z = 0. \tag{4.3}$$

Also, the body forces are given by

$$X = -\frac{\partial \Omega}{\partial x}, \tag{4.4}$$

$$Y = -\frac{\partial \Omega}{\partial y}, \tag{4.5}$$

$$Z = -\frac{\partial \Omega}{\partial z} \tag{4.6}$$

where Ω is called the *potential function*. The *body forces* are to deal with gravitational forces, magnetic forces and/or inertia forces. The force of one body acting on another by a direct contact is the *surface force*. It may be noted that the equilibrium Equations (4.1–4.3) do not provide a relationship between the stresses and the external loads, although they give the rate of change of the stresses at any point in the body. One of the requirements to establish such a relationship is that the deformation continuity of each element must be preserved. This means that the displacement in components must be continuous and single-valued functions. Certain relationships between the strain components must be satisfied to meet the requirement. These relationships are called the *equations of compatibility*. The relationship between the stresses and the external loads is required to also satisfy the boundary conditions.

To derive the *equations of compatibility*, let us consider the strain-displacement relations previously given in Equation (1.18):

$$\varepsilon_x = \frac{\partial u}{\partial x}, \tag{a}$$

$$\varepsilon_y = \frac{\partial v}{\partial y}, \tag{b}$$

$$\varepsilon_z = \frac{\partial w}{\partial z}, \tag{c}$$

$$\gamma_{xy} = \frac{\partial u}{\partial y} + \frac{\partial v}{\partial x}, \tag{d}$$

$$\gamma_{xz} = \frac{\partial u}{\partial z} + \frac{\partial w}{\partial x}, \tag{f}$$

$$\gamma_{yz} = \frac{\partial v}{\partial z} + \frac{\partial w}{\partial y}. \tag{g}$$

To eliminate the displacements from the above equations, we differentiate Equation (a) twice with respect to y and Equation (b) twice with respect to x and Equation (d) once with respect to x and then once with respect to y results in the following *compatibility equation*,

$$\frac{\partial^2 \varepsilon_x}{\partial y^2} + \frac{\partial^2 \varepsilon_y}{\partial x^2} = \frac{\partial^2 \gamma_{xy}}{\partial x \partial y}. \tag{4.7}$$

Thus, the *compatibility equations* are to establish relationships between different strain components as well.

Two additional *compatibility equations* may be obtained in a similar way:

$$\frac{\partial^2 \varepsilon_y}{\partial z^2} + \frac{\partial^2 \varepsilon_z}{\partial y^2} = \frac{\partial^2 \gamma_{yz}}{\partial y \partial z}, \tag{4.8}$$

$$\frac{\partial^2 \varepsilon_z}{\partial x^2} + \frac{\partial^2 \varepsilon_x}{\partial z^2} = \frac{\partial^2 \gamma_{xz}}{\partial x \partial z}. \tag{4.9}$$

The following equations may be found from Equation (1.18) for more *compatibility equations*:

$$\frac{\partial \varepsilon_x}{\partial y \partial z} = \frac{\partial^3 u}{\partial x \partial y \partial z}, \tag{4.10}$$

$$\frac{\partial^2 \gamma_{xy}}{\partial x \partial z} = \frac{\partial^3 u}{\partial x \partial y \partial z} + \frac{\partial^3 v}{\partial^2 x \partial y}, \tag{4.11}$$

$$\frac{\partial^2 \gamma_{xz}}{\partial x \partial y} = \frac{\partial^3 u}{\partial x \partial y \partial z} + \frac{\partial^3 w}{\partial^2 x \partial y}, \tag{4.12}$$

$$\frac{\partial^2 \gamma_{yz}}{\partial x^2} = \frac{\partial^3 v}{\partial x^2 \partial z} + \frac{\partial^3 w}{\partial^2 x \partial y}. \tag{4.13}$$

We may add Equation (4.11) and Equation (4.12) together and then subtract Equation (4.11) to get

$$\frac{\partial^2 \gamma_{xy}}{\partial x \partial z} + \frac{\partial^2 \gamma_{xz}}{\partial x \partial y} - \frac{\partial^2 \gamma_{yz}}{\partial x^2} = 2\frac{\partial^3 u}{\partial x \partial y \partial z}. \tag{4.14}$$

From Equation (4.10) and Equation (4.14), we find a *compatibility equation*,

$$2\frac{\partial^2 \varepsilon_x}{\partial y \partial z} = \frac{\partial}{\partial x}\left(-\frac{\partial \gamma_{yz}}{\partial x} + \frac{\partial \gamma_{xz}}{\partial y} + \frac{\partial \gamma_{xy}}{\partial z}\right). \tag{4.15}$$

Similarly, *two more compatibility equations* can be found:

$$2\frac{\partial^2 \varepsilon_y}{\partial x \partial z} = \frac{\partial}{\partial y}\left(-\frac{\partial \gamma_{xz}}{\partial y} + \frac{\partial \gamma_{xy}}{\partial z} + \frac{\partial \gamma_{yz}}{\partial x}\right) \tag{4.16}$$

$$2\frac{\partial^2 \varepsilon_z}{\partial x \partial y} = \frac{\partial}{\partial z}\left(-\frac{\partial \gamma_{xy}}{\partial z} + \frac{\partial \gamma_{yz}}{\partial x} + \frac{\partial \gamma_{xz}}{\partial y}\right). \tag{4.17}$$

4.2 Airy's stress function

As discussed, to find equations for stress distribution on a solid body, any candidate equations are required to satisfy the boundary conditions, equilibrium equations and compatibility equations. This procedure can be simplified using the *Airy's stress function* (Φ) which is defined by the following three equations:

$$\sigma_x = \frac{\partial^2 \Phi}{\partial y^2} + \Omega \tag{4.18}$$

$$\sigma_y = \frac{\partial^2 \Phi}{\partial x^2} + \Omega \tag{4.19}$$

$$\tau_{xy} = -\frac{\partial^2 \Phi}{\partial x \partial y}. \tag{4.20}$$

The three equations above containing the *Airy stress function* (Φ) satisfy the equilibrium equations for two dimensional cases. Thus, the procedure for finding equations for stress distribution involves finding the Airy stress function (Φ) and satisfying the compatibility equations. The compatibility equations and Airy stress function (Φ) will be further discussed in relation with *plane stress* and *plane strain*.

4.2.1 Plane stress

Equations (4.18) – (20) are substituted into the following equations for *plane stress* ($\sigma_z = \tau_{xz} = \tau_{yz} = 0$),

$$\varepsilon_x = \frac{1}{E}\left(\sigma_x - \nu\sigma_y\right) \tag{bis 2.19a}$$

$$\varepsilon_y = \frac{1}{E}\left(\sigma_y - \nu\sigma_x\right) \tag{bis 2.19b}$$

$$\varepsilon_z = -\frac{\nu}{E}\left(\sigma_x - \sigma_y\right) \tag{bis 2.19c}$$

$$\gamma_{xy} = \frac{1}{G}\tau_{xy} = \frac{2(1+\nu)}{E}\tau_{xy} \tag{bis 2.4 & 2.8}$$

and then into the compatibility equation (4.7) to obtain

$$\frac{\partial^4 \Phi}{\partial x^4} + 2\frac{\partial^4 \Phi}{\partial x^2 \partial y^2} + \frac{\partial^4 \Phi}{\partial y^4} = -(1-\nu)\left(\frac{\partial^2 \Omega}{\partial x^2} + \frac{\partial^2 \Omega}{\partial y^2}\right). \tag{4.21}$$

The symbol ∇ is called *del operator* and ∇^4 is called the *biharmonic operator* defined as

$$\nabla^4 = \frac{\partial^4}{\partial x^4} + 2\frac{\partial^4}{\partial x^2 \partial y^2} + \frac{\partial^4}{\partial y^4} \tag{4.22}$$

and ∇^2 is called the *Laplacian operator* defined as

$$\nabla^2 = \frac{\partial^2}{\partial x^2} + \frac{\partial^2}{\partial y^2}. \tag{4.23}$$

Thus, Equation (4.21) becomes

$$\nabla^4\Phi = -(1-\nu)\nabla^2\Omega \tag{4.24a}$$

Note that no use has been made of the remaining five *compatibility equations*. Two of these vanish because of the stress field here is independent of z but the other three will not be satisfied. However, the stresses above are known to be good approximations. For the case of zero body forces Equation (4.24a) reduces to the so called the *biharmonic equation*:

$$\nabla^4\Phi = 0. \tag{4.24b}$$

4.2.2 Plane strain

We employ the same *Airy stress function* $\Phi(x, y)$ [see Equations (4.18)–(4.20)] as for the *plane stress* case in conjunction with the following relations for *plane strain* ($\varepsilon_z = 0$):

$$\sigma_z = \nu(\sigma_x + \sigma_y) \tag{bis 2.20b}$$

$$\varepsilon_x = \frac{1-\nu^2}{E}\left(\sigma_x - \frac{\nu}{1-\nu}\sigma_y\right) \tag{bis 2.20c}$$

$$\varepsilon_y = \frac{1-\nu^2}{E}\left(\sigma_y - \frac{\nu}{1-\nu}\sigma_x\right). \qquad \text{(bis 2.20d)}$$

For the *plane strain* case, five of the *compatibility equations* are satisfied, leaving only Equation (4.7), $\frac{\partial^2 \varepsilon_x}{\partial y^2} + \frac{\partial^2 \varepsilon_y}{\partial x^2} = \frac{\partial^2 \gamma_{xy}}{\partial x \partial y}$, to be considered. If we consider the compatibility Equations (4.15), (4.16) and (4.17), we obtain

$$\nabla^4 = -\frac{1}{1-\nu}\nabla^2\Omega. \qquad \text{(4.24c)}$$

When there are no body forces, the same *biharmonic equation* as that for *plane stress* is obtained as

$$\nabla^4 \Phi = 0. \qquad \text{(4.24d)}$$

Therefore, to find the equation for a stress distribution, we need to find an Airy's stress function with the *biharmonic equation* satisfied.

The following is an example for using the Airy stress function to find equations for stress distribution. A case is given in **Figure 4.2**, in which the pressure p varies along the bar. The stress function $\Phi = By^3$ may be considered for it (B is a constant). It is found that The stress function satisfies the *biharmonic equation* ($\nabla^4 \Phi=0$) and therefore produces the following equations for stress distribution:

$$\sigma_x = \frac{\partial^2 \Phi}{\partial y^2} = 6By, \qquad \text{(4.25a)}$$

$$\sigma_y = \frac{\partial^2 \Phi}{\partial x^2} = 0 \text{ , and} \qquad \text{(4.25b)}$$

$$\tau_{xy} = -\frac{\partial^2 \Phi}{\partial x \partial y} = 0. \qquad \text{(4.25c)}$$

To determine the constant (B), boundary conditions are used:

$\sigma_x = p_A = 0$ at $y=0$

and

$\sigma_x = 6Bl = p_B$ at $y=l$.

Accordingly, $B = \frac{p_B}{6l}$ and therefore the stress distribution is described by

$$\sigma_x = \frac{\partial^2 \Phi}{\partial y^2} = 6By = p_B \frac{y}{l} \tag{4.25d}$$

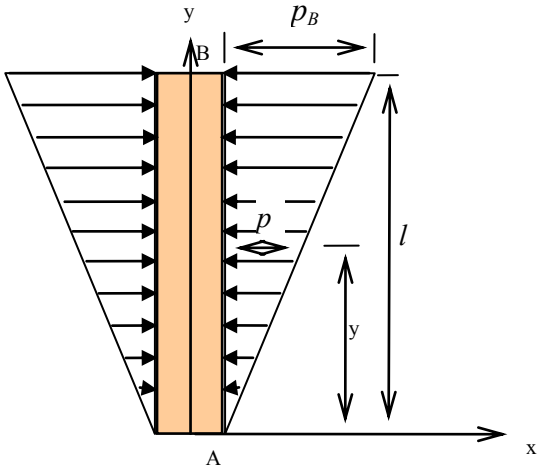

Figure 4.2 A bar subjected to a linear stress distribution.

For many problems, the stress function may be possible to be in the form of the following polynomial expression:

$$\begin{aligned} \Phi &= Ax^2 + Bxy + Cy^2 \\ &+ Dx^3 + Ex^2 y + Fxy^2 + Gy^3 \\ &+ Hx^4 + Jx^3 y + Kx^2 y^2 + Lxy^3 + My^4 \\ &+ Nx^5 + Px^4 y + Qx^3 y^2 + Rx^2 y^3 + Sxy^4 + Ty^5 + \ldots \end{aligned} \tag{4.26}$$

Terms containing *x* or *y* up to the third power satisfy the *biharmonic equation*. However, terms containing higher powers remain in the *biharmonic equation*. Those terms can be sometimes vanished by relating associated coefficients.

4.3 Application of equilibrium equations in photo-elastic stress analysis

The *equilibrium equations* may be useful for photo-elastic stress analysis.

For example,

$$\frac{\partial \sigma_x}{\partial x} + \frac{\partial \tau_{yx}}{\partial y} + \frac{\partial \tau_{zx}}{\partial z} + X = 0 \tag{bis 4.1}$$

can be rewritten for plane stress as

$$\frac{\partial \sigma_x}{\partial x} + \frac{\partial \tau_{yx}}{\partial y} = 0 \tag{4.27a}$$

and rearranging,

$$d\sigma_x = -\frac{\partial \tau_{yx}}{\partial y} dx. \tag{4.27b}$$

Therefore, the normal stress in the x-direction may be obtained by integration

$$\sigma_x = -\int \frac{\partial \tau_{yx}}{\partial y} dx + c \tag{4.27c}$$

where c is an integration constant.

Accordingly, a stress difference ($\Delta\sigma_x$) between any two points (x_0 and x) is found to be,

$$\Delta\sigma_x = -\int_{x_0}^{x} \frac{\partial \tau_{yx}}{\partial y} dx. \tag{4.27d}$$

For numerical calculation, if a stress at the point x_0, $(\sigma_x)_{x=x_0}$ is known, then the stress at the point x (σ_x) can be translated into

$$\sigma_x = (\sigma_x)_{x=x_0} - \sum_1^n \frac{\Delta \tau_{yx}}{\Delta y} \Delta x \,. \tag{4.27e}$$

Equation (4.27e) may be practically useful in conjunction with photo-elastic stress analysis for finding stress values.

Photoelasticity has been used as an experimental method for finding stress distributions on various geometries. It is based on a material property called birefringence (double refraction) which reacts to stresses. In practice, there are two types of patterns on the model for stress analysis may be used – *isoclinic* and *isochromatic*. As shown in **Figure 4.3**(a), an *isochromatic* is the locus of the points, along which the difference between major and minor principal stresses is constant while an *isoclinic* is a locus of points at which the principle stresses are all in the same direction.The loci appear on the photoelastic model in a form of lines called *fringes – isoclinics appear* in black and *isochromatics* in other colours as shown in **Figure 4.3**(b).

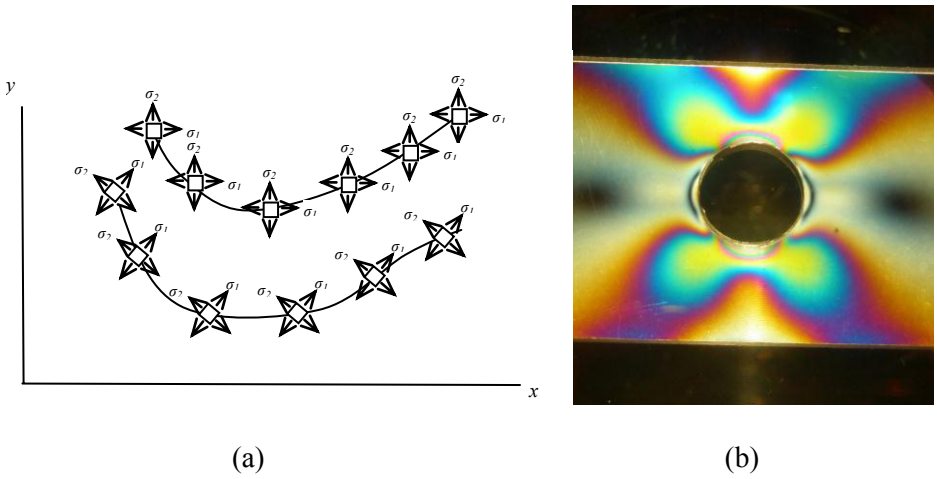

Figure 4.3 (a) Isoclinics with the principle stress directions – the principle stress directions of each point are inclined at a constant angle to *x* and *y* axes. (b) Fringes on a plate with a hole.

When a ray of plane polarized light pass through a photo-elastic material model, it resolves along the two principal stress directions and each of these components experiences different refractive indices as they travel at different velocities within the model. When the light comes through the analyzer (**Figure 4.4)**, the phase difference or relative retardation (R) in wave lengths between the two resolved rays is given by[3]

$$R = Ct(\sigma_1 - \sigma_2) = 2Ct\tau_{\max} \tag{4.28a}$$

where C is a constant known as the stress optic coefficient, t is the thickness of the model plate, and σ_1 and σ_2 are major and minor the principal stresses.

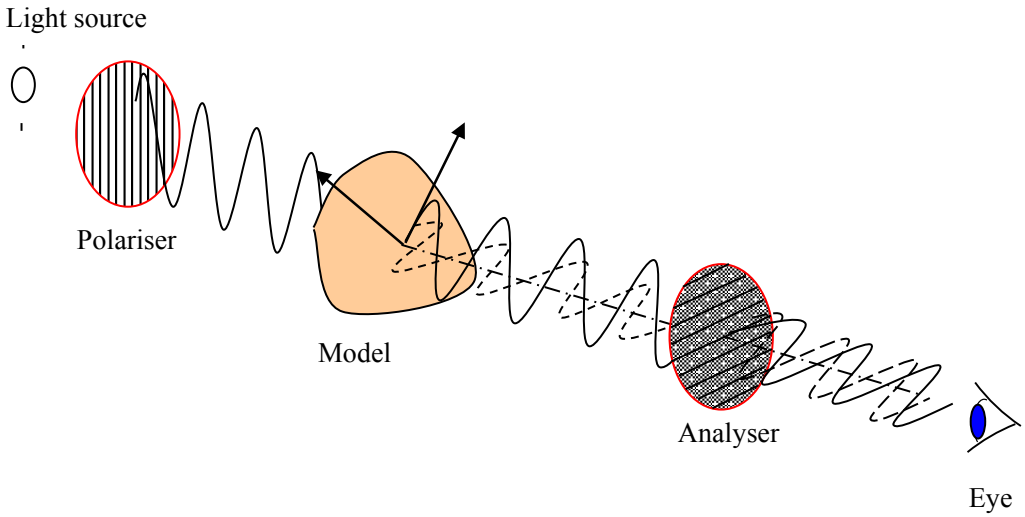

Figure 4.4 A photoelasticity arrangement to view a fringe pattern on the model. The fringe pattern viewed is due to the *plane polarized* light. Each fringe is a locus of *isochromatic* points at which the difference between two principal stresses or the maximum shear stress is constant.

When a material of birefringence is stressed, fringes are created. Fringes for stress may be similar to contour lines on a map where a close spacing between contour lines indicates a high slope and vice versa. Each fringe line is a locus of points of constant difference between the major (σ_1) and minor (σ_2) principal stresses and can be used for stress calculation using

$$\sigma_1 - \sigma_2 = \frac{nf}{t} \tag{4.28b}$$

where n is the *fringe number* or *fringe order*, f is the model material fringe value, and t is the *model thickness*.

Equation (4.28b) can be used for finding shear stress (τ_{yx}) with the stress relation in **Figure 4.5**.

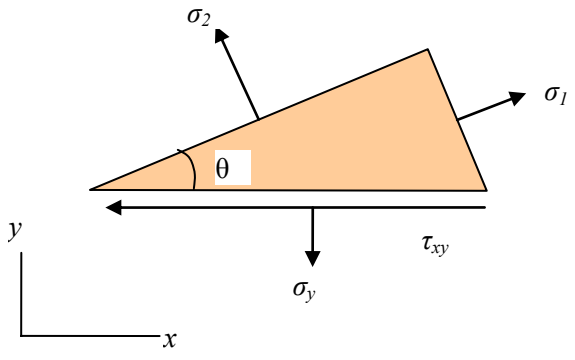

Figure 4.5 Principal stresses with other stress components.

A relation according to the equilibrium in the x-direction (**Figure 4.5**) is

$$\sigma_1 \sin\theta\cos\theta - \tau_{xy} - \sigma_2 \cos\theta\sin\theta = 0 \tag{4.28c}$$

so that

$$\tau_{xy} = \frac{\sigma_1 - \sigma_2}{2}\sin 2\theta. \tag{4.28d}$$

In practice, the variables in Equation (4.28d) can be measured from the photo-elastic experiment and then stress at any point can be calculated according to Equation (4.27e).

Further, the stress distribution for a three- dimensional model or real component can be obtained using the same theory if reflective surface and photo-elastic coating are used as shown in **Figure 4.6**.

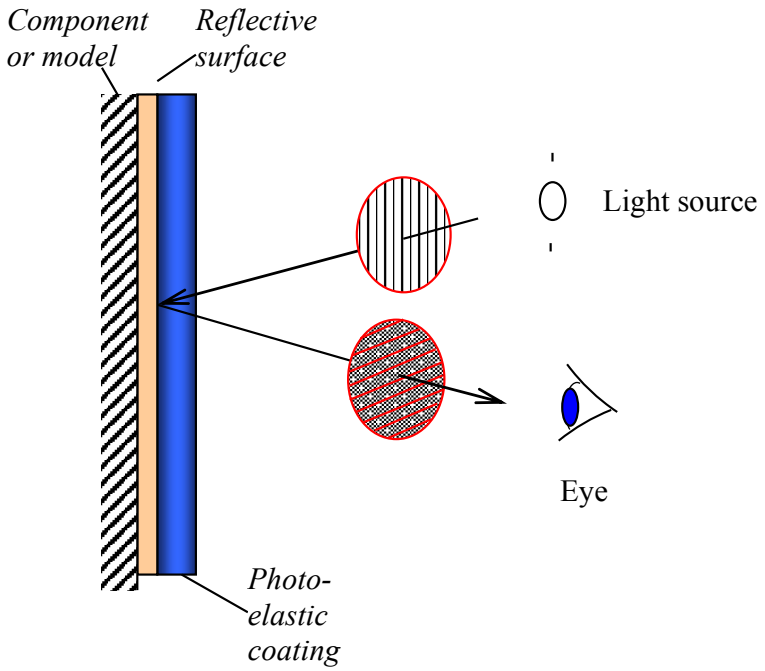

Figure 4.6 A photoelasticity arrangement for a three dimensional component or model.

4.4 Stress distribution in polar coordinates

The polar coordinate system is useful for some particular geometries such as cylinder and circular plates. Stress components on an infinitesimal element in polar coordinates are given in **Figure 4.7**.

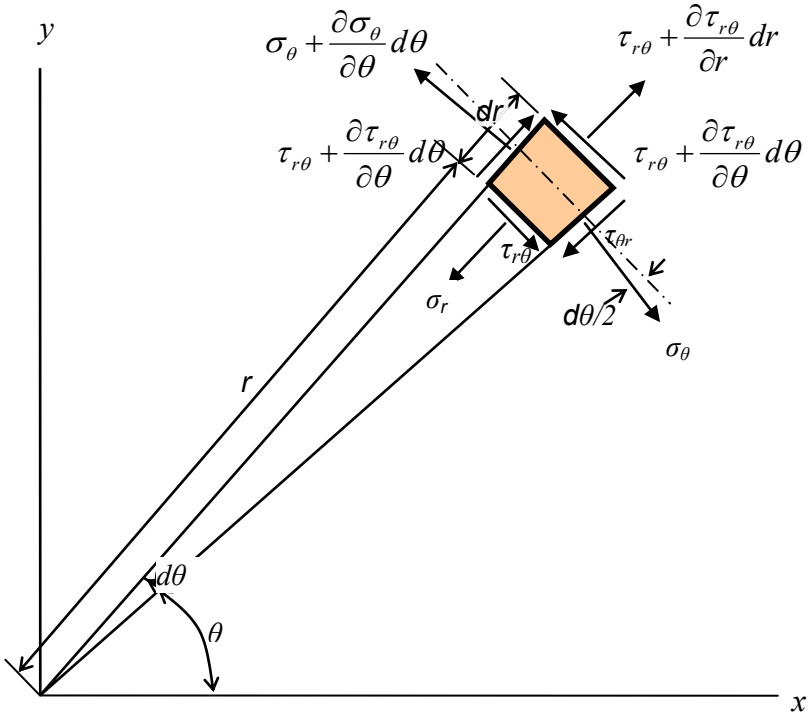

Figure 4.7 Stress components on an infinitesimal element in the polar coordinate system.

The *equilibrium equations* in radial and tangential directions are given by

$$\frac{\partial \sigma_r}{\partial r}+\frac{1}{r}\frac{\partial \tau_{r\theta}}{\partial \theta}+\frac{\sigma_r-\sigma_\theta}{r}+R=0 \tag{4.29}$$

$$\frac{1}{r}\frac{\partial \sigma_\theta}{\partial \theta}+\frac{\partial \tau_{r\theta}}{\partial r}+2\frac{\tau_{r\theta}}{r}+T=0 \tag{4.30}$$

where R is a radial body force and T is a tangential body force.

The normal stress distributions in radial and tangential directions and shear stress are given by

$$\sigma_r=\frac{1}{r}\frac{\partial \Phi}{\partial r}+\frac{1}{r^2}\frac{\partial^2 \Phi}{\partial \theta^2}, \tag{4.31}$$

$$\sigma_\theta=\frac{\partial^2 \Phi}{\partial r^2}, \tag{4.32}$$

$$\tau_{r\theta}=\frac{1}{r^2}\frac{\partial \Phi}{\partial \theta}+\frac{1}{r}\frac{\partial^2 \Phi}{\partial r\partial \theta}=-\frac{\partial}{\partial r}\left(\frac{1}{r}\frac{\partial \Phi}{\partial \theta}\right) \tag{4.33}$$

where Φ is the Airy stress function.

The *biharmonic equation* without the body force is

$$\nabla^2(\nabla^2)\Phi=\left(\frac{\partial^2}{\partial r^2}+\frac{1}{r}\frac{\partial}{\partial r}+\frac{1}{r^2}\frac{\partial^2}{\partial \theta^2}\right)\left(\frac{\partial^2 \Phi}{\partial r^2}+\frac{1}{r}\frac{\partial \Phi}{\partial r}+\frac{1}{r^2}\frac{\partial^2 \Phi}{\partial \theta^2}\right)=0 \tag{4.34}$$

4.4.1 Thick walled cylinder

The Airy stress function for the general continuous axi-symmetric stress distributions independent of θ can be found by solving the *biharmonic equation* (4.34). The *biharmonic equation* independent of θ is given by

$$\nabla^2(\nabla^2)\Phi=\left(\frac{\partial^2}{\partial r^2}+\frac{1}{r}\frac{\partial}{\partial r}\right)\left(\frac{\partial^2 \Phi}{\partial r^2}+\frac{1}{r}\frac{\partial \Phi}{\partial r}\right)=0 \tag{4.35}$$

or

$$\nabla^2(\nabla^2)\Phi=\left(\frac{\partial^4 \Phi}{\partial r^4}+\frac{2}{r}\frac{\partial^3 \Phi}{\partial r^3}-\frac{1}{r^2}\frac{\partial^2 \Phi}{\partial r^2}+\frac{1}{r^3}\frac{\partial \Phi}{\partial r}\right)=0. \tag{4.36}$$

Solving the differential equation,

$$\Phi = A + B\ln r + Cr^2 + D(\ln r)r^2 . \tag{4.37}$$

Consequently, the normal stress distributions in radial and tangential directions and shear stress are given by

$$\sigma_r = \frac{B}{r^2} + 2C , \tag{4.38}$$

$$\sigma_\theta = \frac{-B}{r^2} + 2C \tag{4.39}$$

$$\tau_{r\theta} = 0 . \tag{4.40}$$

The stress distributions for a thick walled cylinder shown in **Figure 4.8** may be determined using the following boundary conditions when pressures exist both internally (p_i) and externally (p_o):

$\sigma_r = -p_i$ at $r = r_i$

$\sigma_r = -p_o$ at $r = r_0$

$\tau_{r\theta} = 0$ at both $r = r_i$ and $r = r_0$.

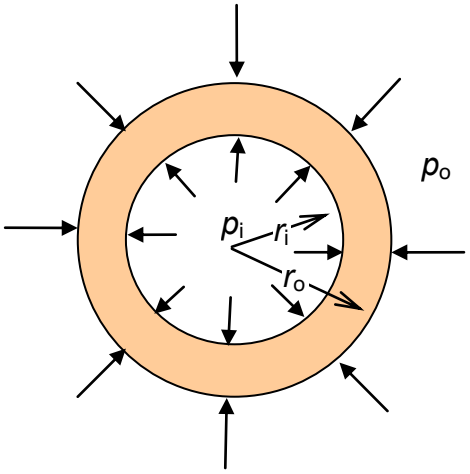

Figure 4.8 Thick walled cylinder cross section with an internal pressure (p_i) and an external pressure (p_o).

Therefore,

$$\sigma_r = \frac{B}{r^2} + 2C = \frac{(p_i - p_o)r_o^{\,2}r_i^{\,2}}{r^2(r_i^{\,2} - r_o^{\,2})} + \frac{p_o r_o^{\,2} - p_i r_i^{\,2}}{(r_i^{\,2} - r_o^{\,2})} \tag{4.41}$$

and

$$\sigma_\theta = -\frac{B}{r^2} + 2C = -\frac{(p_i - p_o)r_o^{\,2}r_i^{\,2}}{r^2(r_i^{\,2} - r_o^{\,2})} + \frac{p_o r_o^{\,2} - p_i r_i^{\,2}}{(r_i^{\,2} - r_o^{\,2})}. \tag{4.42}$$

4.4.2 Stress distribution for an infinitely large thin plate with a small circular hole

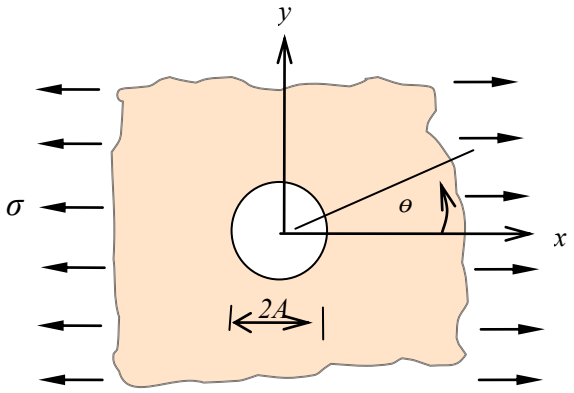

Figure 4.9 An infinitely large thin plate with a small circular hole.

The Airy stress function Φ for the stress distribution for an infinitely large thin plate with a small circular hole (**Figure 4.9**) is found to be

$$\Phi = \frac{\sigma}{4}\left\{r^2 - 2A^2 \ln r - \frac{(r^2 - A^2)^2}{r^2}\cos 2\theta\right\} \tag{4.43}$$

where σ is a uni-axial tensile stress applied in a remote place. Accordingly, the stress distributions are given by

$$\sigma_r = \frac{1}{r}\frac{\partial \Phi}{\partial r} + \frac{1}{r^2}\frac{\partial^2 \Phi}{\partial \theta^2} = \frac{\sigma}{2}\left\{1 - \frac{A^2}{r^2} + (1 - \frac{4A^2}{r^2} + \frac{3A^4}{r^4})\cos 2\theta\right\} \tag{4.44a}$$

$$\sigma_\theta = \frac{\partial^2 \Phi}{\partial r^2} = \frac{\partial^2}{\partial r^2}[\frac{\sigma}{4}\left\{r^2 - 2A^2 \ln r - \frac{(r^2 - A^2)^2}{r^2}\cos 2\theta\right\}] \tag{4.44b}$$

$$\tau_{r\theta} = -\frac{\partial}{\partial r}\left(\frac{1}{r}\frac{\partial \Phi}{\partial \theta}\right) = \frac{\sigma}{2}\left(1 - \frac{2A^2}{r^2} + \frac{3A^4}{r^4}\right)\sin 2\theta \tag{4.44c}$$

where A is the radius of the hole.

4.4.3 Stress distribution acting on a straight boundary of a semi-infinite plate subjected to a normal line force (*P*)

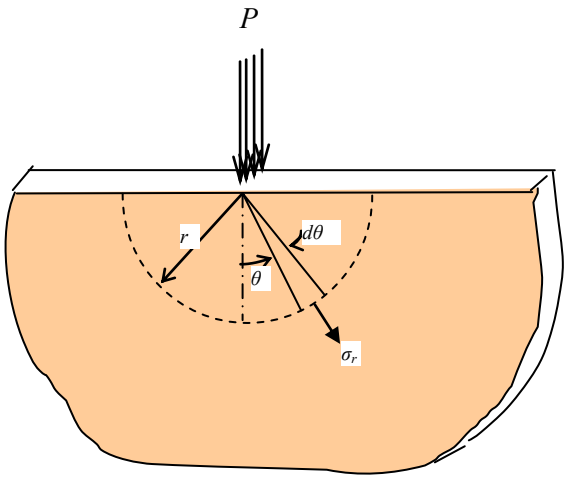

Figure 4.10 A semi-infinite plate subjected to a normal line force (*P*).

The Airy stress function Φ for the stress distribution due to a concentrated normal force (P) acting on a straight boundary of a semi-infinite plate (see **Figure 4.10**) is given by

$$\Phi = Ar\,\theta \sin\theta \tag{4.45a}$$

so that

$$\sigma_r = \frac{1}{r}\frac{\partial \Phi}{\partial r} + \frac{1}{r^2}\frac{\partial^2 \Phi}{\partial \theta^2} = -2A\frac{\cos\theta}{r} \tag{4.45b}$$

$$\sigma_\theta = \frac{\partial^2 \Phi}{\partial r^2} = \frac{\partial^2 (Ar\theta \sin\theta)}{\partial r^2} = 0 \tag{4.45c}$$

$$\tau_{r\theta} = -\frac{\partial}{\partial r}\left(\frac{1}{r}\frac{\partial \Phi}{\partial \theta}\right) = 0 \tag{4.45d}$$

where A is a constant. The radial stress (σ_r) appears to be a principal stress in the absence of shear stress ($\tau_{r\theta} = 0$). The constant A is determined according to the equilibrium of forces acting on any cylindrical surfaces of radius r so that

$$\sigma_r = -\frac{2P}{\pi}\frac{\cos\theta}{r}. \tag{4.46a}$$

A locus for a constant radial principle stress (σ_r) for a given load (P) may be found by eliminating θ, given that 4 cos $\theta = r$ in the circle with a diameter (d) shown in **Figure 4.10**, which is given by

$$\sigma_r = -\frac{2P}{\pi d}. \tag{4.46b}$$

In other words, the principle stress direction constantly varies along the circle although the radial stress ($\sigma_r \sigma_r$) is constant.

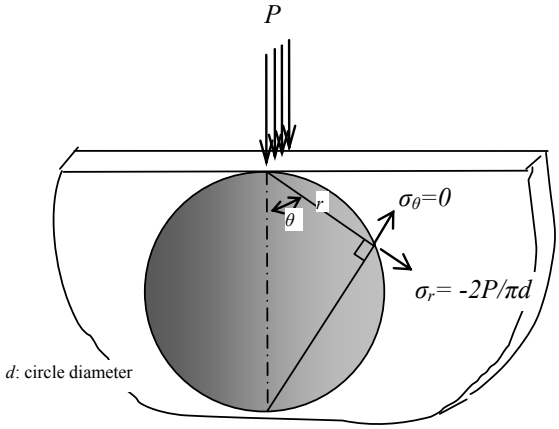

Figure 4.11 A locus of radial stress (σ_r) for a given load (P).

4.4.4 Stress distribution in a circular disk

In order to obtain the stress distribution for a finite circular disk subjected to a force (P), the stress distribution in the semi-infinite plate may be used. If two equal tensile radial stresses ($\sigma_r = \frac{2P}{\pi d}$) with another force P are added on the circle circumference in **Figure 4.11**, then, the radial compressive stresses are offset and, as a result, no stress exists on the circumferential surface and the circle is equivalent to a finite disk as shown in **Figure 4.12**. Therefore, the stress distribution within the disk can be calculated by superimposing the two equal tensile radial stresses on the previous stress distribution in the circle.

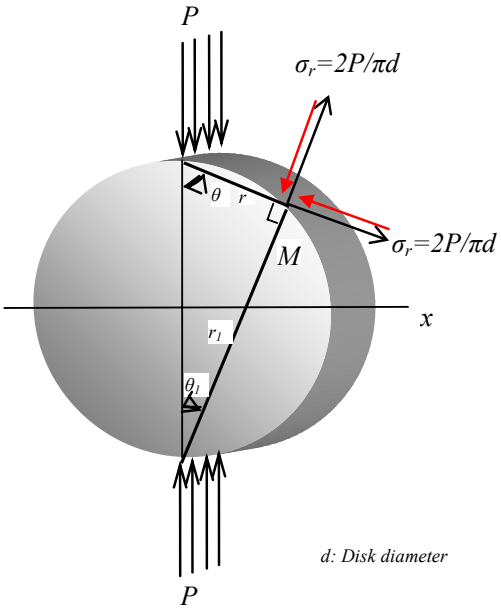

Figure 4.12 A circle is isolated from the semi-infinite plate subjected to the force *P* and then two equal tensile radial stresses ($\sigma_r = \frac{2P}{\pi d}$) with another force *P* are added on the circle circumference to offset the compressive stresses. As a result, no stress exists on the circumferential surface and the circle is equivalent to a finite disk.

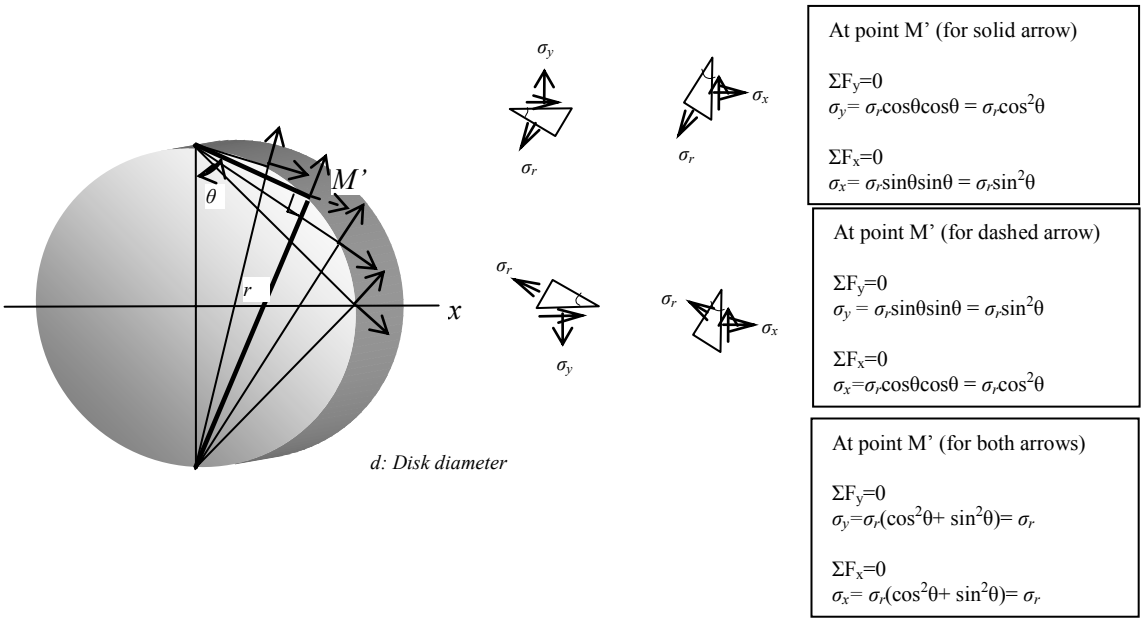

Figure 4.13 The stress distribution caused by the tensile stresses added along the circumference is uniform within the disk i.e. $\sigma_x=\sigma_y=\sigma_r$ without force P.

Before we obtain the stress distribution for a finite circular disk, we need to know that the two equal tensile radial stresses ($\sigma_r = \frac{2P}{\pi d}$) added along the circumference causes a uniform stress distribution where $\sigma_x = \sigma_y = \frac{2P}{\pi d}$ within the disk as shown in **Figure 4.13**.

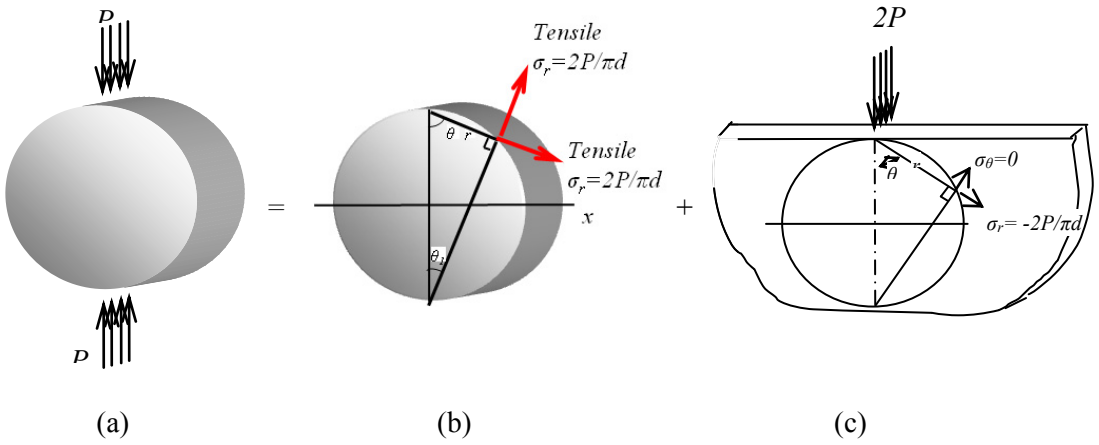

Figure 4.14 A finite disk with a diameter of *d* subjected to line force P.

Accordingly, we use the superposition as shown in **Figure 4.14** to find the stress distribution on the horizontal diametral section of the circular disk subjected to a force *P* [**Figure 4.14(a)**]. The stress in the *y*-direction (σ_y) on the horizontal diametral section where the stress directions are symmetric [**Figure 4.14(c)**] is given by

$$\sigma_y = 2\sigma_r \cos^2\theta = -\frac{4P}{\pi}\frac{\cos^3\theta}{r} \tag{4.47a}$$

and the stress in the *y*-direction (σ_y) due to the two equal tensile radial stresses at any point in **Figure 4.13(b)** is given by

$$\sigma_y = \frac{2P}{\pi d}. \tag{4.47b}$$

Superimposing these together,

$$\sigma_y = -\frac{4P}{\pi}\frac{\cos^3\theta}{r} + \frac{2P}{\pi d}. \tag{4.47c}$$

The maximum compressive stress (= minor principal stress) along the horizontal diameter occurs at the center of the disk (θ=0) and is found to be

$$\sigma_{y\max} = -\frac{6P}{\pi d}. \tag{4.47d}$$

Similarly, the stress in the *x*-direction along the horizontal diameter (σ_x) is given by

$$\sigma_x = (-\frac{4P}{\pi}\frac{\cos\theta}{r})\sin^2\theta + \frac{2P}{\pi d} \tag{4.47e}$$

and the stress at the center of the disk (= major principal stress) is found to be

$$\sigma_{x\max} = \frac{2P}{\pi d}. \tag{4.47f}$$

It follows that

$$\sigma_x - \sigma_y = \sigma_1 - \sigma_2 = \frac{8P}{\pi d}, \tag{4.47g}$$

which may be useful for the *photo-elasticity calibration*.

5 Linear Elastic Stress Field In Cracked Bodies

5.1 Introduction

Most engineering materials contain small cracks or defects produced during service or manufacturing. When an engineering component is fractured, new surfaces are created. They are caused by the rupture of atomic bonds due to high local stresses. The phenomenon of fracture may be approached at different scales. As the crack size decreases, smaller scale analyses would be required. At a small scale for some cases, the phenomena of interest may be considered within distances of the order of 10^{-7} cm so that the problem is studied using the concepts of uncertainty. However, as the crack size increases, the material behaviour based on continuum mechanics may be more appropriate. The complex nature of cracking behaviour prohibits a unified approach of the problem, and the existing theories deal with the subject from either the microscopic or the macroscopic point of view. In this chapter, the linear elastic stress analysis for cracked bodies will be introduced as part of the continuum mechanics.

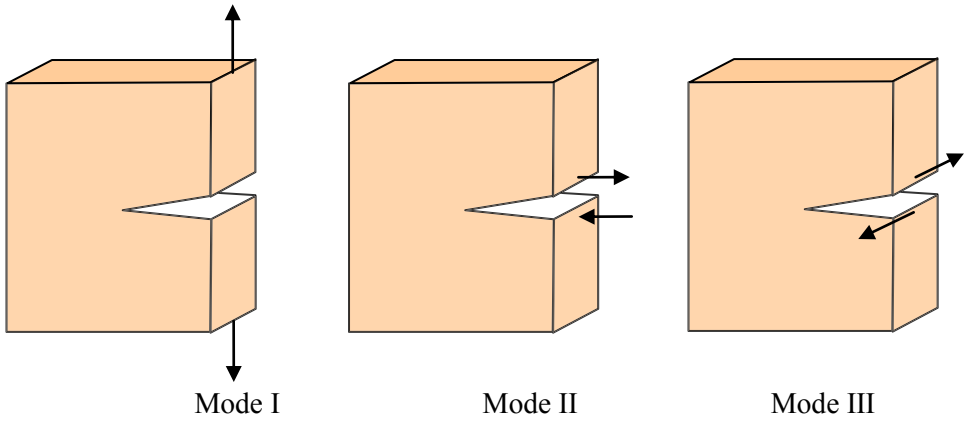

Figure 5.1 The three modes of cracking.

When we consider a two-dimensional crack extending through the thickness of a flat plate, three different cracking modes need to be defined by the loading position and direction. These three basic modes are illustrated in **Figure 5.1**, which presents three types of relative displacements of the crack upper and lower surfaces. Mode I, mode II and mode III are also called *opening mode*, *shearing mode* and *tearing mode* respectively. Some practical loading examples of testing for such modes are given in **Figure 5.2**.

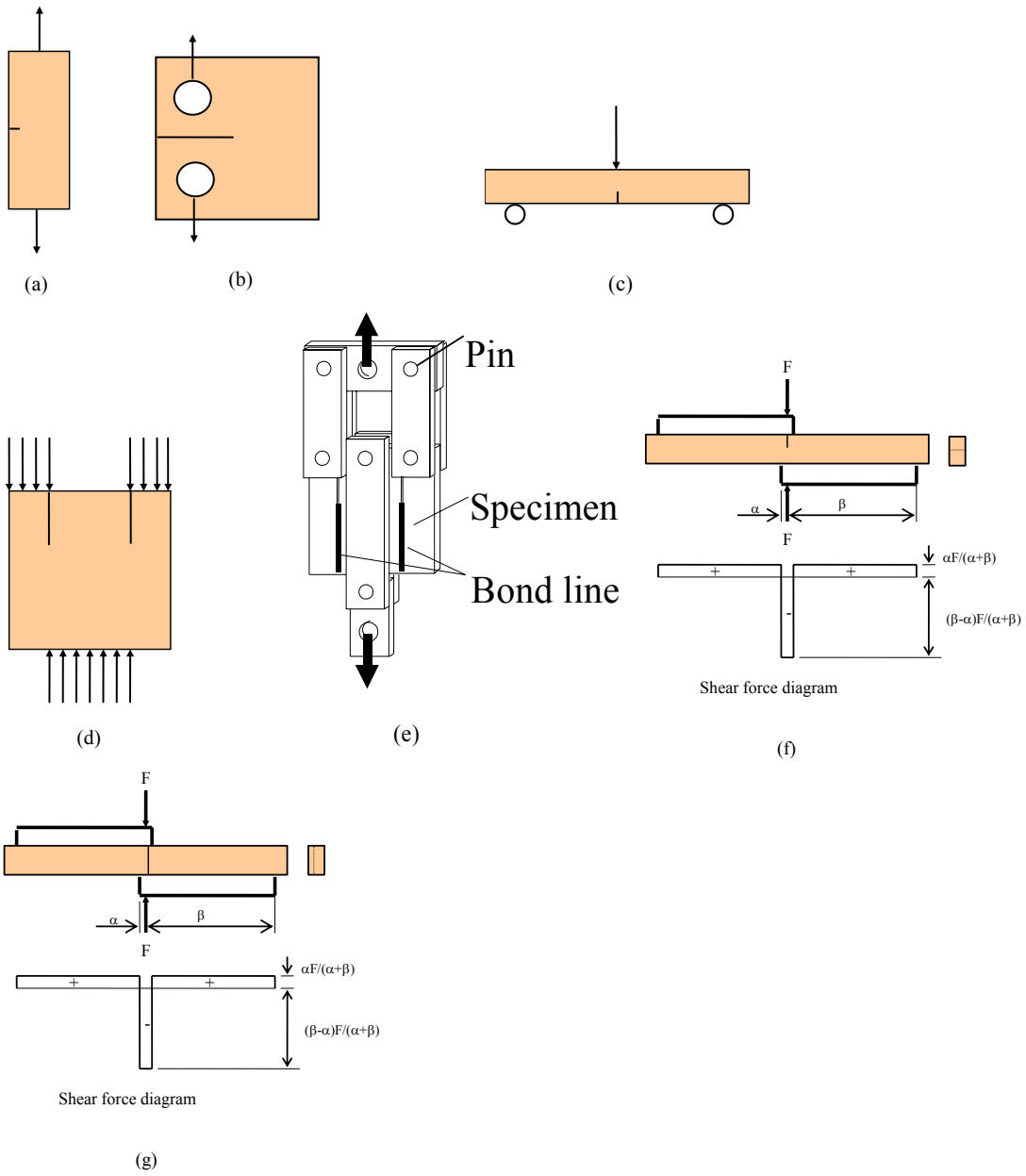

Figure 5.2 Practical loading examples of testing for different modes:
(a) mode I, (b) mode I, (c) mode I, (d) mode II, (e) mode II [after Kim and Ma, 1998][4], (f)[1] mode II, and (g) mode III.

5.2 Complex stress function

The stress field around a crack tip can be found mathematically using the equations with the *Airy's stress function* (Φ) as discussed previously:

$$\sigma_x = \frac{\partial^2 \Phi}{\partial y^2} + \Omega \qquad \text{(bis 4.18)}$$

$$\sigma_y = \frac{\partial^2 \Phi}{\partial x^2} + \Omega \qquad \text{(bis 4.19)}$$

$$\tau_{xy} = -\frac{\partial^2 \Phi}{\partial x \partial y}. \qquad \text{(bis 4.20)}$$

The complex function is defined as

$$Z(z) = \mathrm{Re}\, Z + i\, \mathrm{Im}\, Z \qquad (5.1)$$

where $z = x + iy$.

The Cauchy-Riemann conditions for the complex function are given by

$$\mathrm{Re}\frac{dZ}{dz} = \frac{\partial \mathrm{Re}\, Z}{\partial x} = \frac{\partial \mathrm{Im}\, Z}{\partial y} \qquad (5.2)$$

$$\mathrm{Im}\frac{dZ}{dz} = \frac{\partial \mathrm{Im}\, Z}{\partial x} = -\frac{\partial \mathrm{Re}\, Z}{\partial y} \quad \left(\text{or} \quad \mathrm{Im}\frac{d\bar{Z}}{dz} = \frac{\partial \mathrm{Im}\, \bar{Z}}{\partial x} = -\frac{\partial \mathrm{Re}\, \bar{Z}}{\partial y}\right). \qquad (5.3)$$

The Airy's stress function[5] is given by

$$\Phi = \mathrm{Re}\,\bar{\bar{Z}} + y\,\mathrm{Im}\,\bar{Z} \tag{5.4}$$

where $\frac{d\bar{\bar{Z}}}{dz} = \bar{Z}$, $\frac{d\bar{Z}}{dz} = Z$ and $\frac{dZ}{dz} = Z'$.

Therefore, the stresses are found:

$$\sigma_x = \mathrm{Re}\,Z - y\,\mathrm{Im}\,Z' \tag{5.5}$$

$$\sigma_y = \mathrm{Re}\,Z + y\,\mathrm{Re}\,Z' \tag{5.6}$$

$$\tau_{xy} = -y\,\mathrm{Re}\,Z'. \tag{5.7}$$

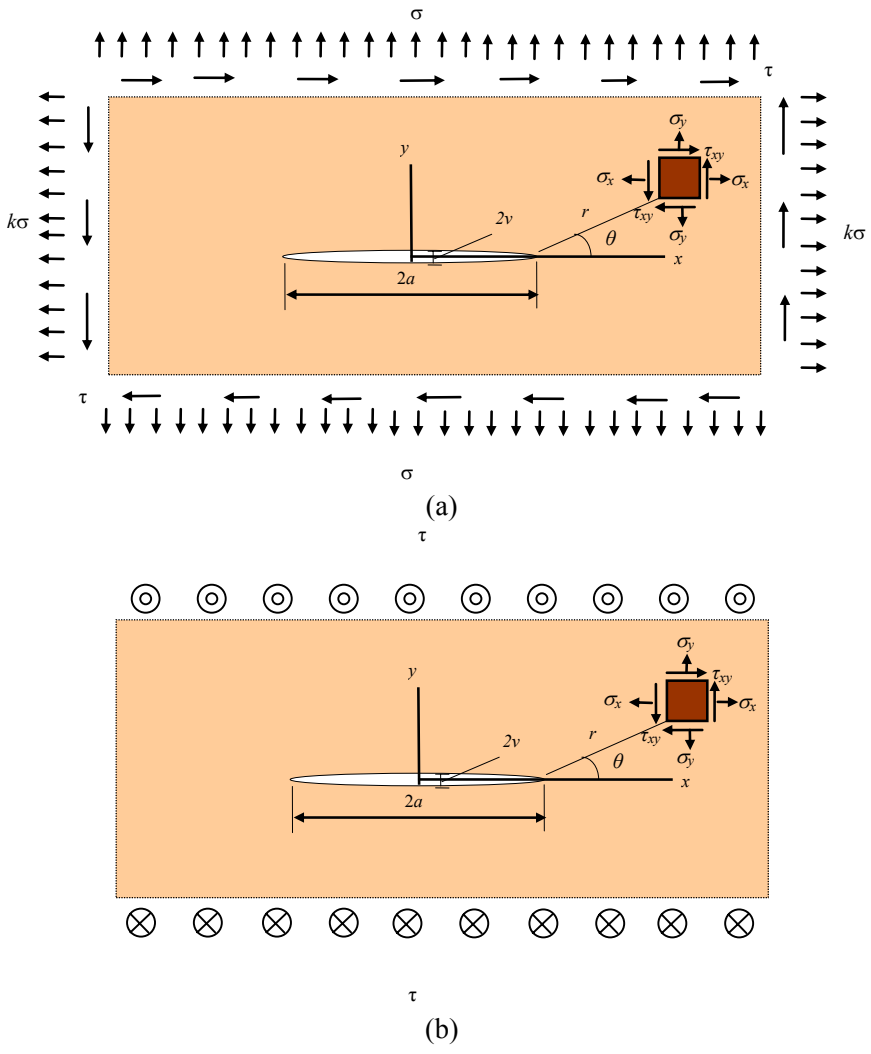

Figure 5.3 Crack in an infinite plate: (a) mode I and II; and (b) mode III.

5.3 The stress around a crack tip

Let us consider mode I crack problem when k =1 in **Figure 5.3** with a crack length of 2a in an infinite plane under biaxial stresses. The boundary conditions of the problem at infinity and on the crack surface may be stated as:

$$\sigma_x = \sigma_y = \sigma \text{ and } \tau_{xy} = 0 \text{ for } |z| = |x + iy| = \sqrt{x^2 + y^2} \to \infty$$

and along the crack face $\sigma_y = 0$ and $\tau_{xy} = 0$ for y=0, $-a<x<a$.

The stress function for symmetric crack problems satisfying the boundary conditions is

$$Z = \frac{\sigma z}{\sqrt{z^2 - a^2}} \ . \tag{5.8}$$

The equation is analytic except for $-a \le x \le a$ at $y = 0$.

To move the origin of the coordinate system to the crack tip ($z = a$) from the middle of the crack, z is replaced by $z + a$:

$$Z = \frac{\sigma z}{\sqrt{z^2 - a^2}} = \frac{\sigma(z+a)}{\sqrt{2az}}\left\{1 - \frac{1}{2}\frac{z}{2a} + \frac{1}{2}\frac{3}{4}\left(\frac{z}{2a}\right)^2 - \frac{1}{2}\frac{3}{4}\frac{5}{6}\left(\frac{z}{2a}\right)^3 + \ldots.\right\}. \tag{5.9}$$

For small $|z|$,

$$Z_I = \frac{K_I}{\sqrt{2\pi z}} \text{ where } K_I = \sigma\sqrt{\pi a} \ . \tag{5.10}$$

Using the polar coordinates with $z = r(\cos\theta + i \sin\theta) = re^{i\theta}$, the stresses near the crack tip are obtained for mode I:

$$\sigma_x = \frac{K_I}{\sqrt{2\pi r}}\cos\frac{\theta}{2}\left(1 - \sin\frac{\theta}{2}\sin\frac{3\theta}{2}\right) - (1-k)\sigma \tag{5.11a}$$

$$\sigma_y = \frac{K_I}{\sqrt{2\pi r}}\cos\frac{\theta}{2}\left(1 + \sin\frac{\theta}{2}\sin\frac{3\theta}{2}\right) \tag{5.11b}$$

$$\tau_{xy} = \frac{K_I}{\sqrt{2\pi r}}\cos\frac{\theta}{2}\sin\frac{\theta}{2}\cos\frac{3\theta}{2} \tag{5.11c}$$

$$\sigma_z = \nu(\sigma_x + \sigma_y) \text{ for plain strain} \tag{5.11d}$$

where $K_I = \sigma\sqrt{\pi a}$.

The last term $(1-k)\sigma$ in the equation for σ_x is obtained separately for $k \neq 1$ by the superposition principle.

Also, the vertical displacement (v) along the crack:

$$\left.\begin{aligned} v &= \frac{2\sigma}{E}\left(1-\nu^2\right)\sqrt{a^2-x^2} \quad \text{for plane strain} \\ v &= \frac{2\sigma}{\mathrm{E}}\sqrt{a^2-x^2} \qquad\quad \text{for plane stress} \end{aligned}\right\} . \tag{5.12}$$

The stresses around the crack tip for Mode II are given by:

$$\sigma_x = \frac{-K_{II}}{\sqrt{2\pi r}}\sin\frac{\theta}{2}\left[2+\cos\frac{\theta}{2}\cos\frac{3\theta}{2}\right] \tag{5.13a}$$

$$\sigma_y = \frac{K_{II}}{\sqrt{2\pi r}}\sin\frac{\theta}{2}\cos\frac{\theta}{2}\cos\frac{3\theta}{2} \tag{5.13b}$$

$$\tau_{xy} = \frac{K_{II}}{\sqrt{2\pi r}} \cos\frac{\theta}{2}\left[1 - \sin\frac{\theta}{2}\sin\frac{3\theta}{2}\right] \tag{5.13c}$$

$$\sigma_z = \nu\left(\sigma_x + \sigma_y\right) \text{ for plain strain} \tag{5.13d}$$

where $K_{III} = \tau\sqrt{\pi a}$.

The stresses around the crack tip for Mode III are given by:

$$\left.\begin{aligned} \begin{bmatrix}\tau_{xz}\\ \tau_{yz}\end{bmatrix} &= \frac{K_{III}}{\sqrt{2\pi r}}\begin{bmatrix}\sin\theta/2\\ \cos\theta/2\end{bmatrix}\\ \sigma_x = \sigma_y &= \tau_{xy} = 0 \end{aligned}\right\} \tag{5.14}$$

where $K_{III} = \tau\sqrt{\pi a}$.

The stress intensity factors (K_I, K_{II} and K_{III}) given above are for an infinity body. Obviously, the finite size of the cracked body is expected to have an influence upon crack tip stress field. Accordingly, the expressions for the stress intensity factor have to be modified to account for this effect. A more general expression for the stress intensity factor may take the form:

$$K = Y\sigma\sqrt{\pi a} \tag{5.15}$$

where Y is a factor which accounts for geometric effect and $Y = 1$ for an infinite plate. Some authors do not incorporate $\sqrt{\pi}$ in the expression. Mode I is the usual one for fracture toughness tests and a critical value of stress intensity factor (K_{Ic}) determined for this mode would be $K_{Ic} = Y\sigma_c\sqrt{\pi a}$.

5.4 Stress intensity factor determination

The stress intensity factors may be determined for various loading cases using the stress intensity factor for a case given in **Figure 5.4** with the superposition principle.

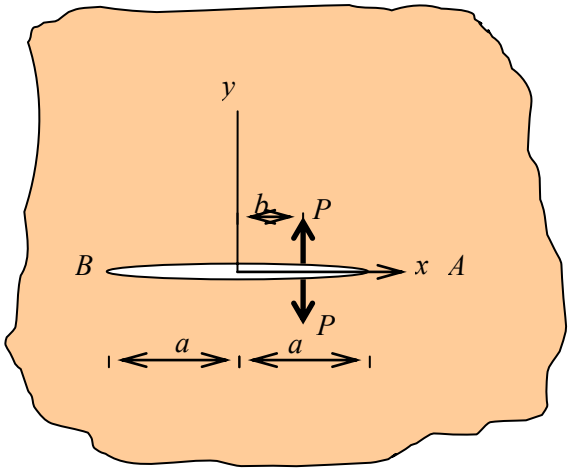

Figure 5.4 Crack subjected to a point forces *P*.

Figure 5.4 shows a plate containing a crack subjected to point forces (P) at crack surfaces, which may resemble a practical case where a crack originates at a bolt or rivet hole under loading. The stress function satisfying the *boundary conditions* is given by

$$Z = \frac{P}{\pi(z-b)}\left(\frac{a^2-b^2}{z^2-a^2}\right)^{1/2} \tag{5.16}$$

and, accordingly, the stress intensity factors for A and B sides are found [6] to be

$$K_{IA} = \frac{P}{B\sqrt{\pi a}}\sqrt{\frac{a+b}{a-b}} \tag{5.17a}$$

and

$$K_{IB} = \frac{P}{B\sqrt{\pi a}}\sqrt{\frac{a-b}{a+b}} \tag{5.17b}$$

where B is the thickness, and (K_{IA} and K_{IB}) denote the stress intensity factors for A and B sides respectively. When $b = 0$ for a centrally located point force (P), the equations reduce to

$$K_{IA} = K_{IB} = \frac{P}{B\sqrt{\pi a}}. \tag{5.18}$$

Equation (5.18) descirbes that the stress intensity factor decreases for increasing crack size at a constant P. It is therefore possible that a crack can be arrested after some growth when its stress intensity factor falls below a critical value (K_{Ic}).

The superposition principle can be used to calculate the stress intensity factor if the same stress field equations are applicable for mode I cases or mode II cases or mode III cases. However, it is not permitted for a combination of different fracture modes because of different stress fields.

As an example for the calculation of a stress intensity factor, let us consider the case of a crack with an internal pressure. **Figure 5.5(a)** shows a plate without a crack under uni-axial tension and hence the stress intensity factor $K_{Ia} = 0$. The stress distribution in **Figure 5.5(a)** may be equivalent to a case given in **Figure 5.5(b)** where a crack with a length of *2a* is made at the centre of the plate and an external stresses (σ) are applied to the crack edges.

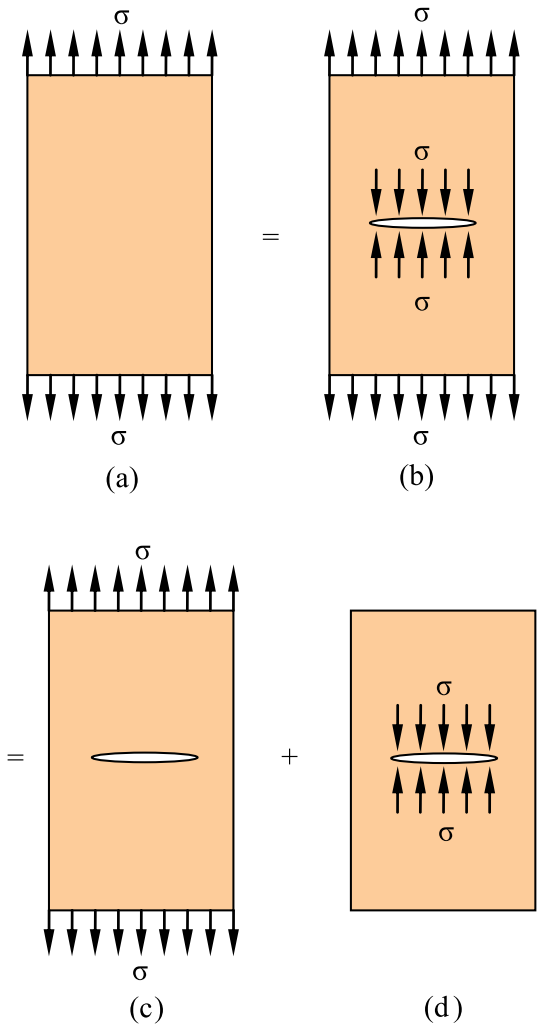

Figure 5.5 Illustration of superposition principle.

Case (b) in **Figure 5.5** is a case where a plate given in Case (c) with a central crack under uni-axial tensile stress (σ) is superimposed with a plate given in Case (d) with a crack having uniformly distributed stress (σ) along its edges. Accordingly, the stress intensity factor for Case (c) is found

$$K_{Ic}+K_{Id}=K_{Ib}=0 \text{ or } K_{Ic}=-K_{Id}=-\sigma\sqrt{\pi a} \tag{5.19}$$

A case where a crack is subjected to an internal pressure p is equivalent to the case in **Figure 5.5(d)** except the pressure acting in an opposite direction to σ. If the sign of K in Equation (5.19) is reversed, the stress intensity factor for a crack with internal pressure is found to be

$$K_I = p\sqrt{\pi a}\,. \tag{5.20}$$

Further examples for the determination of stress intensity factor will follow. For cracks emanating from a loaded rivet hole (**Figure 5.6**), it can now be derived using the superposition principle. The hole is assumed to be small with respect to the crack. The case given in **Figure 5.6(a)** is broken up into components **(b)**, **(d)** and **(e)**. The components **(b)** and **(d)** can be obtained first with satisfied equilibrium conditions, and then component **(e)** is found to take away the stress (σ) and force (P) used for the equilibrium in **(b)** and **(d)** respectively. Accordingly, the stress intensity factor (K_{Ia}) is given by:

$$K_{Ia} = K_{Ib} + K_{Id} - K_{Ie} \tag{5.21}$$

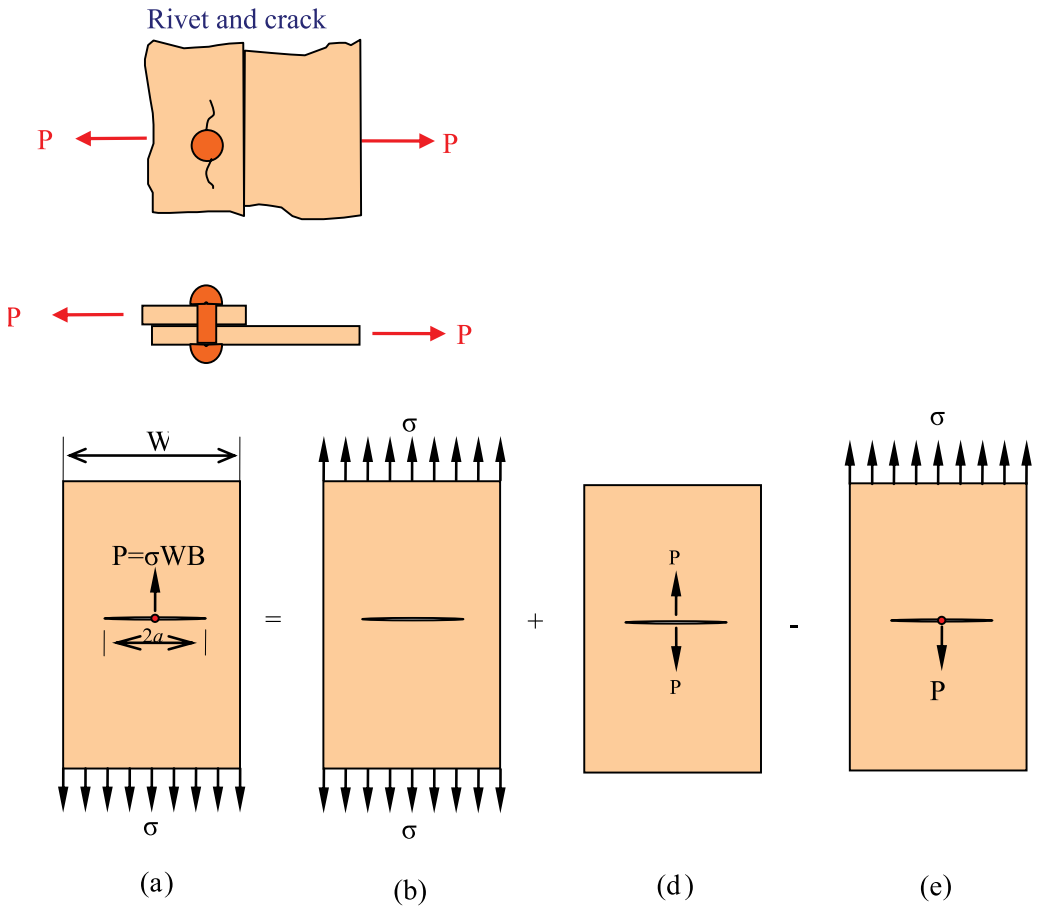

Figure 5.6 Cracks emanating from loaded rivet hole and superposition.

and, given that $K_{Ia} = K_{Ie}$:

$$K_{Ia} = \frac{1}{2}(K_{Ib} + K_{Id}) = \frac{1}{2}\sigma\sqrt{\pi a} + \frac{\sigma W}{2\sqrt{\pi a}}. \tag{5.22}$$

The internal pressure (p) [Equation (5.20)] is equivalent to a series of evenly distributed point forces. This allows us to use Equation (5.17) for determining stress intensity factors by integration for various cases. For example, Equation (5.19) can be found by integration:

$$K_I = \frac{p}{\sqrt{\pi a}} \int_o^a \left\{ \sqrt{\frac{a+x}{a-x}} + \sqrt{\frac{a-x}{a+x}} \right\} dx$$

$$= 2p\sqrt{\frac{a}{\pi}} \int_o^a \frac{dx}{\sqrt{a^2 - x^2}}$$

$$= -\left[2p\sqrt{\frac{a}{\pi}} \cos^{-1}\frac{x}{a} \right]_0^a = p\sqrt{\pi a} \tag{5.23}$$

Thus, the two methods validate each other.

5.5 Stress intensity factor with crazing

Crazing is a phenomenon which occurs in polymers when crack-like discontinuities are formed, in which fibrils connect the two faces of the crack. The restraining of the faces may be described by a uniform stress $-\sigma_c$ over the crack faces [**Figure 5.7 (a)**] and from Equation (5.19) we have:

$$K_I' = -\sigma_c\sqrt{\pi a} \tag{5.24}$$

where $2a$ is the length of the craze and K_I' is the stress intensity factor due to the crazing. The applied stress σ at infinity also gives rise to a stress intensity factor (K_I''),

$$K_I'' = \sigma\sqrt{\pi a} \tag{5.25}$$

so that the net stress intensity factor (K_I) is given by

$$K_I = K_I'' + K_I' = (\sigma - \sigma_c)\sqrt{\pi a}. \tag{5.26}$$

This is illustrated in **Figure 5.7** using the superposition principle.

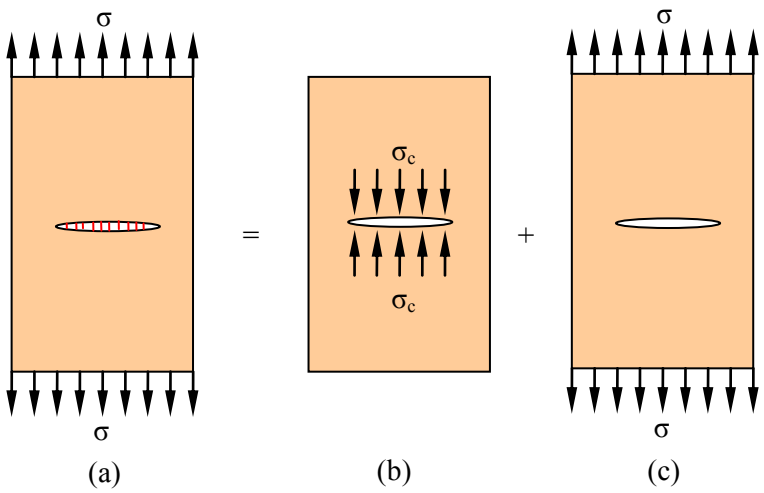

Figure 5.7 Superposition with crazing: (a) fully crazed to resist applied stress; (b) σ_c represents resisting stress by crazing; and (c) a crack subjected to stress, σ.

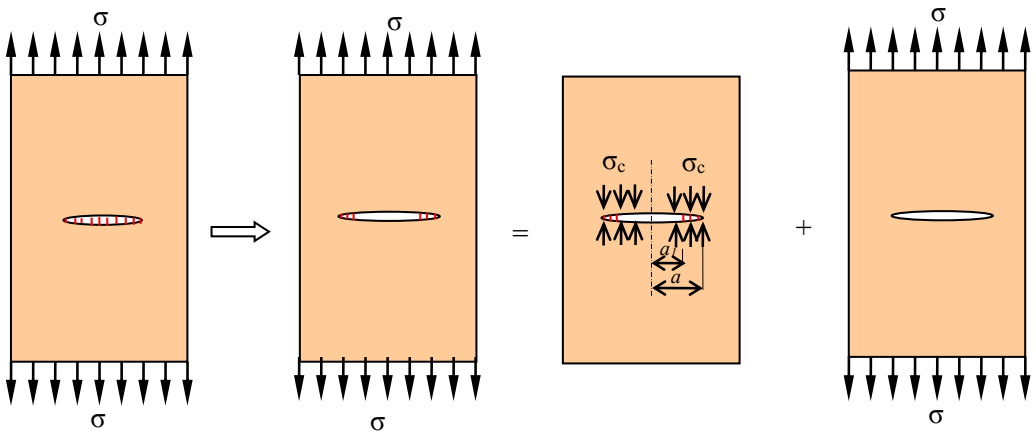

Figure 5.8 Craze development and superposition of stress intensity factors for crazing: (a) fully crazed to resist applied stress; (b) partial craze breakage; c) σ_c represents resisting stress due to crazing at the tips; and (d) a crack subjected to stress, σ.

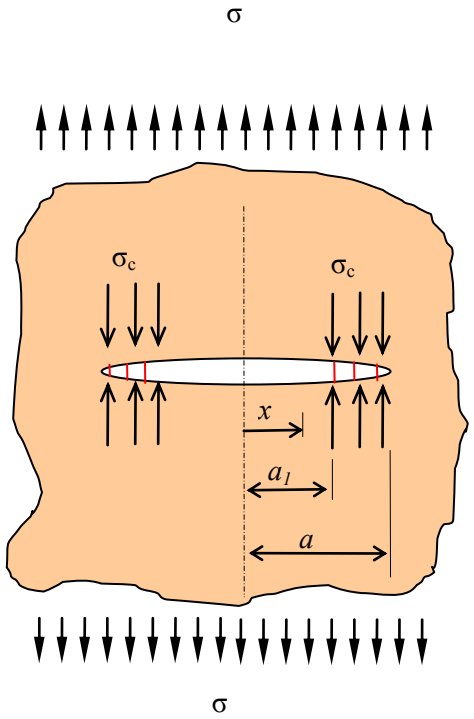

Figure 5.9 Stresses in a craze.

As the applied stress (σ) increases, the crack length increases and becomes partially crazed as illustrated in **Figure 5.8**. The stress intensity factor due to the craze [**Figure 5.8(c)**] may be derived:

$$K_I' = \frac{2\sqrt{a}}{\sqrt{\pi}} \int_{a_1}^{a} \frac{-\sigma_c dx}{\sqrt{\left(a^2 - x^2\right)}} \tag{5.27}$$

i.e.

$$K_I' = -\frac{2\sqrt{a}}{\sqrt{\pi}} \sigma_c \cos^{-1}\left(\frac{a_1}{a}\right). \tag{5.28}$$

The stress intensity factor (K_I'') due to the applied stress (σ) is the same as before and hence the net value of the stress intensity factor (K_I) for the case given in **Figure5.8(b)** or **Figure 5.9** is given by:

$$K_I = K_I'' + K_I' = \sigma\sqrt{\pi a}\left[1 - \frac{2}{\pi}\frac{\sigma_c}{\sigma}\cos^{-1}\frac{a_1}{a}\right]. \tag{5.29}$$

To calculate the craze zone size (r_p) or a plastic zone size in the case of metals using the model given in **Figure 5.9**, we need to find a condition for it. It can be supposed that the crazes grow as the load increases but cease to grow at a stage where no further craze stress increases i.e. the craze stress and length remain constant at σ_c. Therefore, the critical condition is found to be $K_I = 0$. Accordingly, setting Equation (5.29) to zero leads to

$$\frac{\sigma}{\sigma_c} = \frac{2}{\pi}\cos^{-1}\frac{a_1}{a}. \tag{5.30}$$

If we consider small values of stress, i.e. $\sigma << \sigma_c$ and $r_p = (a - a_1) < a$ for approximation, we find,

$$\frac{a_1}{a} = \cos\frac{\pi\sigma}{2\sigma_c} \approx 1 - \frac{1}{2}\frac{\pi^2\sigma^2}{4\sigma_c^2}. \tag{5.31}$$

Therefore, the craze size (r_p) becomes

$$r_p = \frac{\sigma^2\pi^2 a}{8\sigma_c^{\,2}}. \tag{5.32}$$

If we let $K_I = \sigma\sqrt{\pi a}$, then,

$$r_p = \frac{\pi}{8}\left(\frac{K_I}{\sigma_c}\right)^2. \tag{5.33}$$

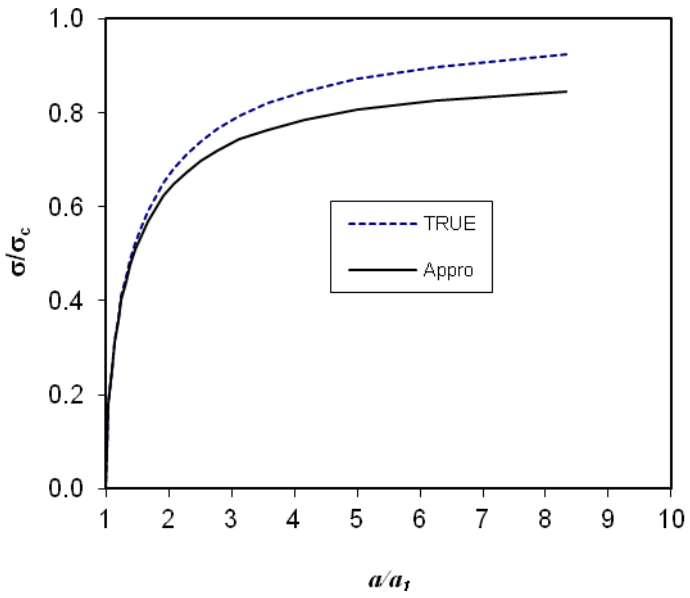

Figure 5.10 Comparison between true and approximated approaches.

The relationship between applied stress and craze length at the critical condition is shown in **Figure 5.10** for both approximated and true values. There is very rapid change in a for σ greater than about $0.8\sigma_c$. Dugdale[7] conducted an experiment and found that there is a good agreement between experimental data and theory for a steel.

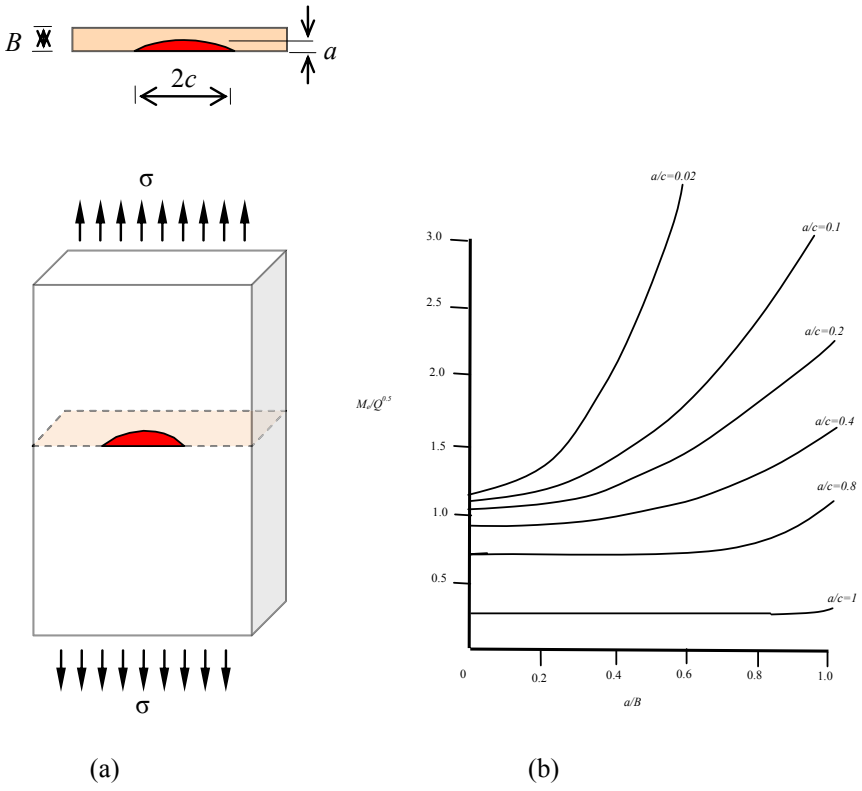

Figure 5.11 (a) A surface crack subject to uniaxial tension and (b)[8] the associated elastic magnification factors on stress intensity.

5.6 Semi-elliptical crack

The semi-elliptical crack resembles a surface crack occurring in practice **(Figure 5.11**). A three-dimensional geometry is useful involving crack depth (a), crack length ($2c$) and thickness of plate (B) to model a semi-elliptical part-through crack. An empirical stress intensity factor[9] subjected to a remote stress (σ) is given by

$$K_I = \sigma\sqrt{\pi a}\left(M_e / \sqrt{Q}\right) \tag{5.34}$$

where M_e, is called an elastic magnification factor on stress intensity, and Q is an elastic shape factor for an elliptical crack. M_e and Q are functions of a/B and a/c; plots of the factor $M_e/\sqrt{Q}$ are given in **Figure 5.11**(b). It is found that long, shallow cracks have high $M_e/\sqrt{Q}$ values increasing with a/B whereas short, deep cracks have essentially constant low $M_e/\sqrt{Q}$ values. Equation (5.34) may be useful in the design of pressure vessels.

5.7 'Leak-before-burst' criterion

The safety may be one of the most important factors for consideration in the pressure vessel design. There are two different possibilities in pressure vessel failure process. When the fracture toughness of a material chosen is sufficiently high and the growing surface crack reaches the other external surface, the pressure vessel starts to leak before it bursts (**Figure 5.12 (a)**). However, if the fracture toughness is low and the growing crack reaches its critical value (K_{IC}) before it leaks, the pressure vessel would burst.

We may consider crack geometry and fracture toughness for 'leak before burst' design. One of the conditions to be satisfied for design is

$$a > B$$

as given in **Figure 5.12 (b)**. Another condition is that fracture toughness should be sufficiently high. We can find a 'leak before burst' criterion from Equation (5.34) satisfying the conditions:

$$K_{IC} > \sigma\sqrt{\pi B}\left(M_e / \sqrt{Q}\right). \tag{5.35}$$

Note that the crack depth (a) is replaced with the thickness (B).

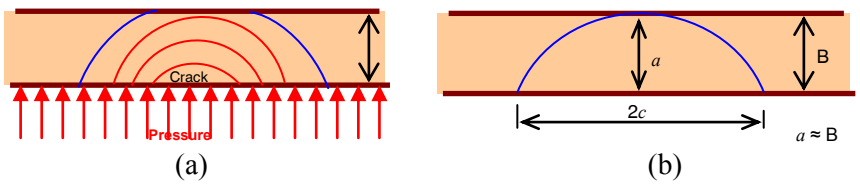

Figure 5.12 Cross section of pressure vessel: (a) different stages of semi-elliptical crack growth; and (b) assumed crack geometry for 'leak before burst'.

5.8 Relation between energy release rate G and K_I

Consider an infinite plate (for plane stress) with fixed ends containing a crack size a as shown in **Figure 5.13**. Two different stages are shown – before and after crack length increment over a distance Δa. If we want to close the crack over an infinitesimal distance Δa, the strain energy for the closure ($\Delta\Lambda$) is calculated as:

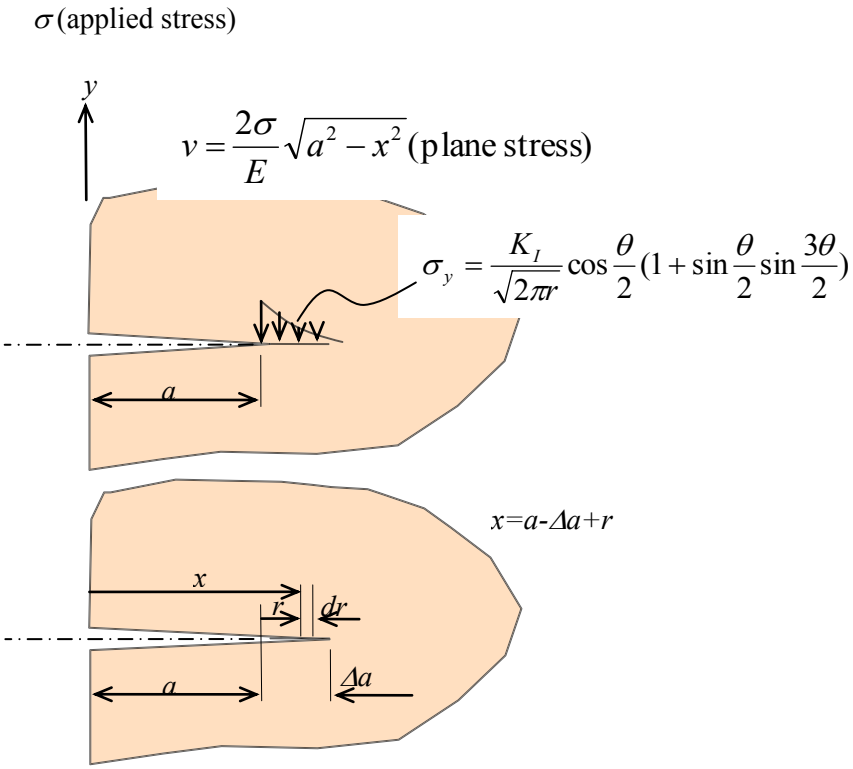

Figure 5.13 Before and after crack length increment over a distance (Δa).

$$\Delta\Lambda = 2B\int_0^{\Delta a}\frac{\sigma_y v}{2}dr = \frac{BK_I^2}{E}\Delta a \tag{5.36}$$

where B is the thickness. When the crack length (a) increases, the strain energy ($\Delta\Lambda$) will be released and its release rate, G_I (strain energy release rate), is defined as,

$$G_I = \frac{\Delta\Lambda}{B\Delta a}. \tag{5.37}$$

Combining Equations (5.36) and (5.37) yields:

$$G_I = \frac{K_I^2}{E} \text{ (plane stress)} \tag{5.38}$$

and

$$G_I = \frac{K_I^2}{E}(1-\nu^2) \text{ (plane strain).} \tag{5.39}$$

5.9 Fracture criteria for mixed mode loading

In mechanics of solids, various criteria are used for yielding, failure, and fracture. The fracture criteria to be introduced here are those involving the stress intensity factor for mode I and mode II.

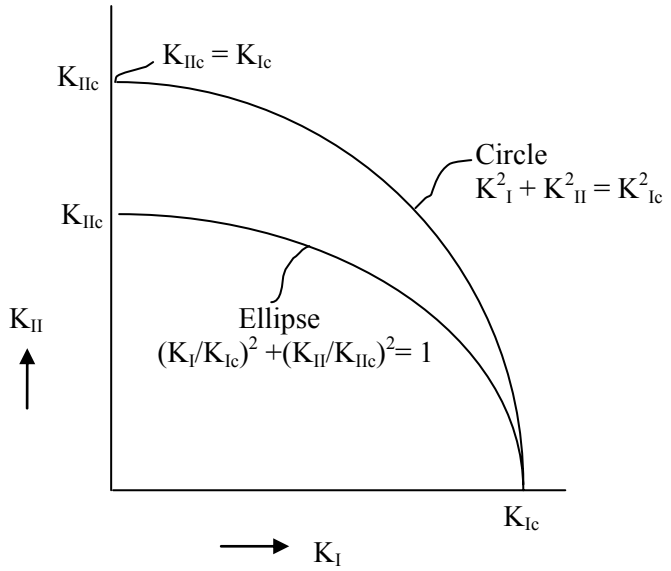

Figure 5.14 Fracture criterion based on the energy balance for combined loading.

The stress fields under mode I and mode II loading can be characterised by stress intensity factors $K_I = \sigma\sqrt{\pi a}$ and $K_{II} = \tau\sqrt{\pi a}$ respectively. When the stress intensity factors increase under mixed mode loading, fracture must be assumed to occur when a certain combination of the two stress intensity factors reaches a critical value.

One of the fracture criteria is based on an energy balance principle. According to the energy conservation, the total energy release rate (G_t) is the sum of individual contributions for I – II mixed mode loading and assumed to be a constant:

$$G_t = G_I + G_I = \text{constant} \tag{5.40}$$

where $G_I = (1-\nu^2)K_I^2/E$ (for plane stress), $G_I = \frac{K_I^2}{E}$ (for plane stress), $G_{II} = (1-\nu^2)K_{II}^2/E$ (for plane strain) and $G_{II} = \frac{K_{II}^2}{E}$. Alternatively, the fracture condition would be:

$$K_I^2+K_I^2 = \text{constant}. \tag{5.41}$$

According to Equation (5.41), when $K_{II} = 0$ for mode I cracking, $K_I^2 = K_{Ic}^2 =$ constant, and, when $K_I = 0$ for mode II cracking, $K_{II}^2 = K_{IIc}^2$. Consequently,

$$K_I^2+K_{II}^2 = K_{Ic}^2 = K_{IIc}^2 \tag{5.42}$$

This is depicted in **Figure 5.14**. However, Equation (5.42) is problematic if $K_{Ic} \neq K_{IIc\cdot c}$. In practice, unfortunately $K_{Ic} \neq K_{IIc\cdot}$ is the case, indicating the energy consumption for creating fracture surfaces under mode I loading is different from that under mode II loading. Also, it is usually observed that crack extension under mode II loading takes place at an angle with respect to the original crack direction. The fracture condition is then empirically modified to satisfy the condition $K_{Ic} \neq K_{IIc\cdot}$:

$$\left(\frac{K_I}{K_{Ic}}\right)^2 + \left(\frac{K_{II}}{K_{IIc}}\right)^2 = 1. \tag{5.43}$$

As shown in **Figure 5.14**, it is elliptical.

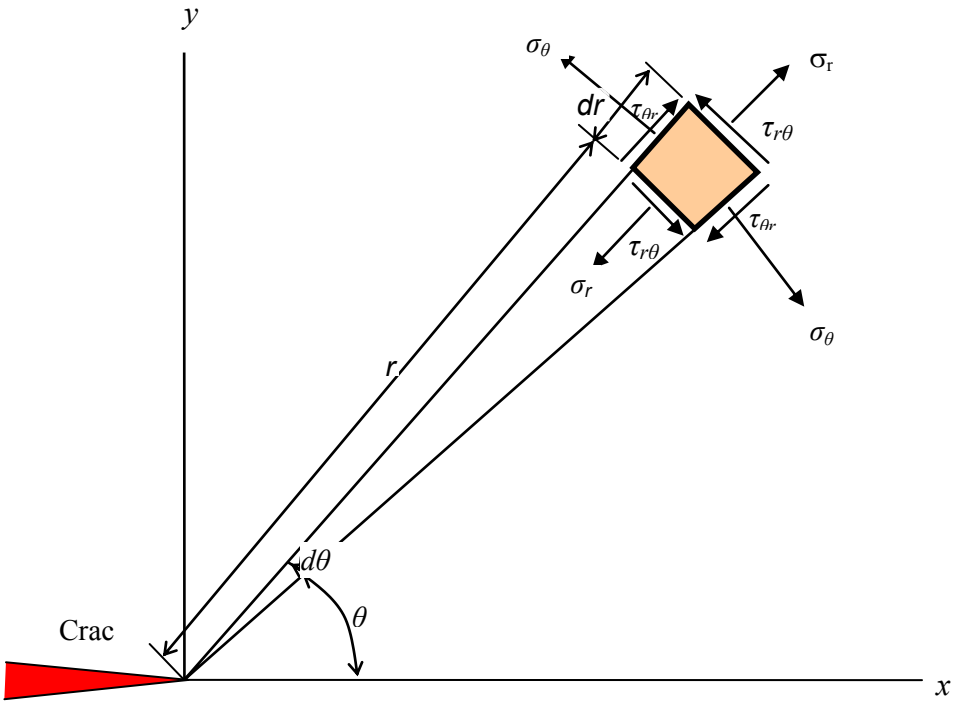

Figure 5.15 Stress components in the polar coordinate system.

Another criterion proposed by Erdogan and Sih[10] is based on the postulation that crack growth occurs in a direction perpendicular to the maximum principal stress to derive the fracture condition under mixed loading.

It is convenient to use the polar coordinate system for analysis (**Figure 5.15**). The stresses in the polar coordinate system are given by

$$\sigma_r = \frac{K_I}{\sqrt{2\pi r}}\cos\frac{\theta}{2}\left(1+\sin^2\frac{\theta}{2}\right)+\frac{K_{II}}{\sqrt{2\pi r}}\sin\frac{\theta}{2}\left(1-3\sin^2\frac{\theta}{2}\right) \tag{5.44a}$$

$$\begin{aligned}\sigma_\theta &= \frac{K_I}{\sqrt{2\pi r}}\cos^3\frac{\theta}{2}-\frac{K_{II}}{\sqrt{2\pi r}}3\sin\frac{\theta}{2}\cos^2\frac{\theta}{2}\\ &= \frac{1}{\sqrt{(2\pi r)}}\cos\frac{\theta}{2}\left[K_I\cos^2\frac{\theta}{2}-\frac{3}{2}K_{II}\sin\theta\right]\end{aligned} \tag{5.44b}$$

$$\begin{aligned}\tau_{r\theta} &= \frac{K_I}{\sqrt{2\pi r}}\sin\frac{\theta}{2}\cos^2\frac{\theta}{2}+\frac{K_{II}}{\sqrt{2\pi r}}\cos\frac{\theta}{2}\left(1-3\sin^2\frac{\theta}{2}\right)\\ &= \frac{1}{2\sqrt{(2\pi r)}}\cos\frac{\theta}{2}\left[K_I\sin\theta+K_{II}\left(3\cos\theta-1\right)\right]\end{aligned} \tag{5.44c}$$

Note that the stress fields around the crack tip are obtained by superimposing the stress fields from mode I and mode II.

The cracking angle (θ_m) with respect to the x-direction can be found if the major principal stress direction is known. The stress σ_θ will be the principal stress (σ_1) if $\tau_{r\theta}=0$ as we readily find that a mode I crack extends along θ = 0. Accordingly, setting Equation (5.44b) to zero:

$$K_I \sin\theta_m + K_{II}\left(3\cos\theta_m - 1\right) = 0 . \tag{5.45}$$

Equation (5.45) can be rewritten using $\cos^2\frac{\theta_m}{2}+\sin^2\frac{\theta_m}{2}=1$ and $\cos\theta_m = 1-2\sin^2\frac{\theta_m}{2}$ as

$$2K_I \sin\frac{\theta_m}{2}\cos\frac{\theta_m}{2}+3K_{II}\left(\cos^2\frac{\theta_m}{2}-\sin^2\frac{\theta_m}{2}\right)-K_{II}\left(\sin^2\frac{\theta_m}{2}+\cos^2\frac{\theta_m}{2}\right)=0 \tag{5.46}$$

which yields a quadratic equation

$$2K_{II}\tan^2\frac{\theta_m}{2}-K_I\tan\frac{\theta_m}{2}-K_{II}=0 . \tag{5.47}$$

Solving this equation, the cracking angle (θ_m) is found to be

$$\left(\tan\frac{\theta_m}{2}\right)_{1,2}=\frac{1}{4}\frac{K_I}{K_{II}}+\frac{1}{4}\sqrt{\left(\frac{K_I}{K_{II}}\right)^2+8} \tag{5.48a}$$

or

$$\left(\tan\frac{\theta_m}{2}\right)_{1,2}=\frac{1}{4}\frac{K_I}{K_{II}}-\frac{1}{4}\sqrt{\left(\frac{K_I}{K_{II}}\right)^2+8} . \tag{5.48b}$$

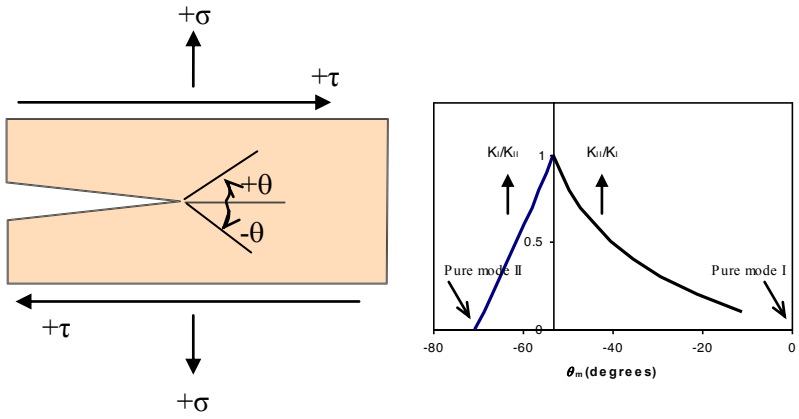

Figure 5.16 Sign convention and theoretical crack extension angle according to Equation (5.48b)

Accordingly, the principal stress (σ_1) is also found as

$$\sigma_1=\sigma_\theta\left(\theta=\theta_m\right)=\frac{K_I}{\sqrt{2\pi r}}\cos^3\frac{\theta_m}{2}-\frac{K_{II}}{\sqrt{2\pi r}}3\sin\frac{\theta_m}{2}\cos^2\frac{\theta_m}{2} . \tag{5.49}$$

A sign convention and theoretical crack extension angle as a function of K_{II}/K_I according to Equation (5.48b) are given in **Figure 5.16**. According to the sign convention, the crack propagation angle under mode II loading is negative.

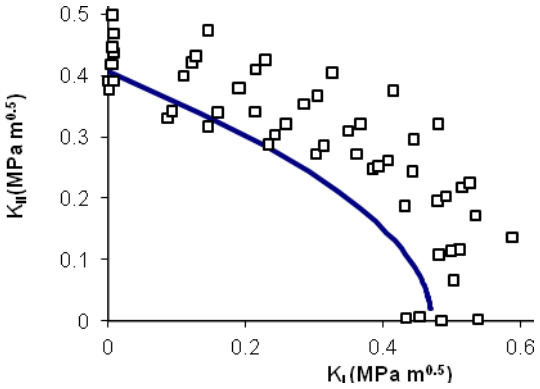

Figure 5.17[11] Comparison between theory [Equation (5.51)] and experimental data for PMMA.

To find the fracture condition under mixed loading, we postulate that the crack extension takes place if σ_1 under mixed loading has the same value as σ_1 at fracture under mode I loading. The principal stress for pure mode I at fracture is given by

$$\sigma_1 = \frac{K_{Ic}}{\sqrt{(2\pi r)}} \quad (\theta = 0) \tag{5.50}$$

from

$$\sigma_y = \frac{K_I}{\sqrt{2\pi r}} \cos\frac{\theta}{2}\left(1 + \sin\frac{\theta}{2}\sin\frac{3\theta}{2}\right). \tag{bis 5.11b}$$

The fracture condition under mixed loading, then, is found by equating Equations (5.49) and (5.50):

$$K_{Ic} = K_I \cos^3\frac{\theta_m}{2} - 3K_{II}\sin\frac{\theta_m}{2}\cos^2\frac{\theta_m}{2}. \tag{5.51}$$

A comparison between theory [Equation (5.51)] and experimental data for PMMA is shown in **Figure 5.17**. The theoretical prediction appears to be conservative compared to experimental data.

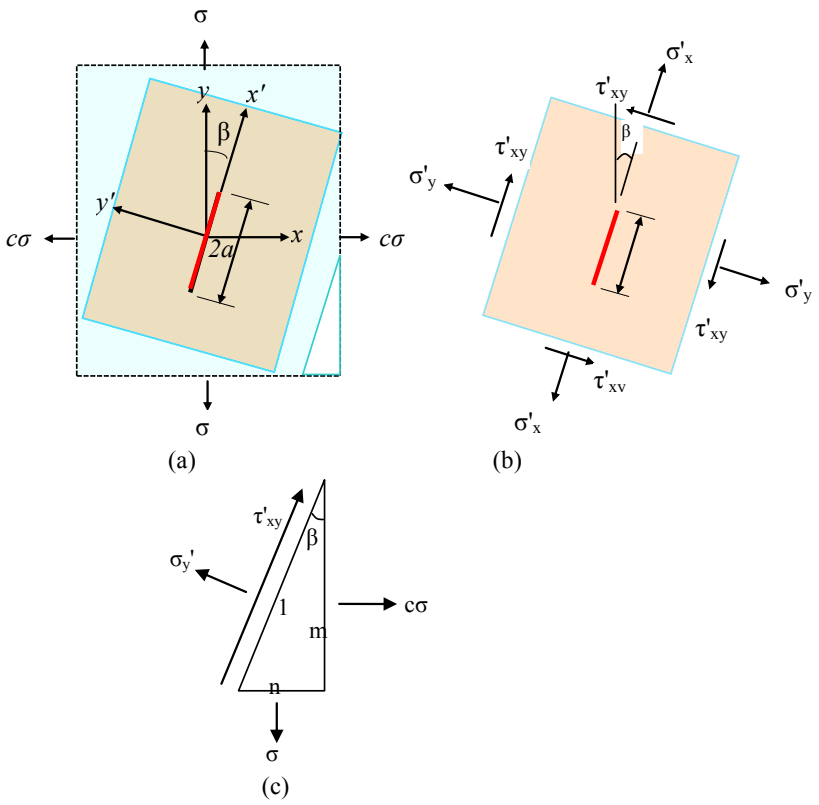

Figure 5.18 (a) An infinite plate subjected to remote stresses s and cs biaxially. (b) Applied stresses at a different angle to find separate mode I and mode II. (c) Stress components in equilibrium.

Let us consider an infinite plate containing a crack of length 2*a* at an angle (β) to the *y* direction as shown in **Figure 5.18(a)**. It is subjected to stresses σ and $c\sigma$ in the *y*- and *x*-directions respectively at infinity. We need to find stresses for mode I and mode II to use the fracture criterion under mixed mode loading. To this end, we need to find the stress components defined in **Figure 5.18(b)** in relation with those in **Figure 5.18(a)** using the equilibrium condition as shown in **Figure 5.18(c)**. Consequently, the stress intensity factors for this case are obtained as

$$K_I = (1/2)\left[c+1+(c-1)\cos 2\beta\right]\sigma\sqrt{\pi a} \tag{5.52}$$

and

$$K_{II} = -\frac{c-1}{2}\sin 2\beta\,\sigma\sqrt{\pi a} \tag{5.53}$$

for mode I and mode II respectively.

Example) A thin walled cylindrical pressure vessel with a large radius of *R* and a wall thickness of *B* contains a through-the-thickness crack oriented at an angle β with the circumferential direction as shown in **Figure 5.19**. Determine the stress intensity factors of the crack when the vessel is subjected to an internal pressure, *p*. Assume the geometry factor is 1.

Solution) The hoop σ_h and longitudinalσ_l stresses for the cylindrical vessel are

$\sigma_l = \frac{pR}{2B}$ and $\sigma_h = \frac{pR}{B}$ respectively. The ratio *c*=1/2 in Equations (5.52) and (5.53). Thus, the stress intensity factors due to hoop and longitudinal stresses are given by

$$K_{Is} = 0.5\left[0.5+1+(0.5-1)\cos 2\beta\right]\frac{pR}{B}\sqrt{\pi a} = 0.5\left[1+\sin^2\beta\right]\frac{pR}{B}\sqrt{\pi a} \tag{5.54a}$$

and

$$K_{IIs} = -\frac{0.5-1}{2}(\sin 2\beta)\quad\frac{pR}{B}\sqrt{\pi a} = 0.5(\sin 2\beta)\quad\frac{pR}{2B}\sqrt{\pi a}\,. \tag{5.54b}$$

The stress intensity factors due to pressures over the cracked surfaces are

$K_{Ip} = p\sqrt{\pi a}$ and $K_{IIp} = 0$. Therefore, the total stress intensity factors by superposition are

$$K_I = p\left[\left(1+\sin^2\beta\right)\frac{R}{2B}+1\right]\sqrt{\pi a} \text{ and } K_{II} = (\sin 2\beta)\,\frac{pR}{4B}\sqrt{\pi a}\,.. \tag{5.54c}$$

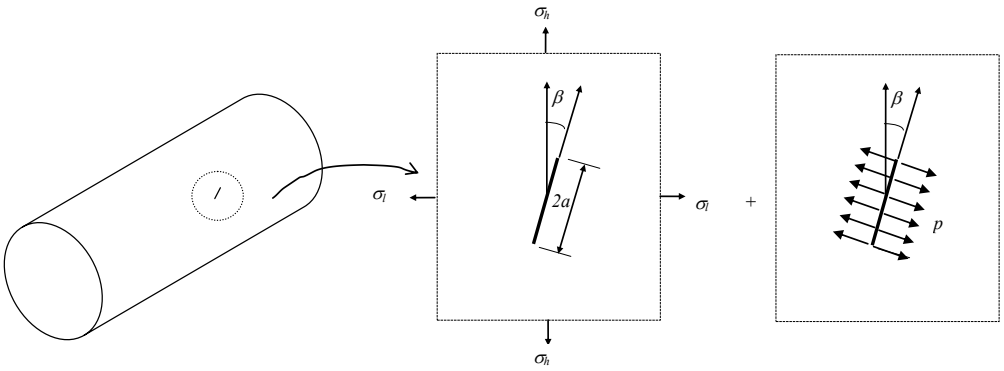

Figure 5.19 A cylindrical pressure vessel with an inclined 'through the thickness' crack and superposition.

6 Plastic Deformation Around A Crack Tip

6.1 One-dimensional plastic zone size estimation

The elastic stress field around the crack tip is very high so that a cracked body is usually accompanied by plastic deformation and non-linear effects. There are, however, cases where the extent of plastic deformation and the non-linear effects are very small compared to the crack size. In such cases, the linear elastic theory is still validly used to address the problem of stress distribution in the cracked body. The elastic stress field solutions discussed in the previous chapter show a stress singularity exists at the tip of a crack i.e. the stress approaches infinity. However, the stress in the vicinity of a crack tip, in reality, is limited to a yield stress when subjected to loading, and deform plastically. A simplistic estimate of the size of the plastic zone can be made, whether in plane strain or in plane stress. Let us consider first a plane stress case for a one-dimensional horizontal extent of plastic zone, which occurs on the surface of a plate.

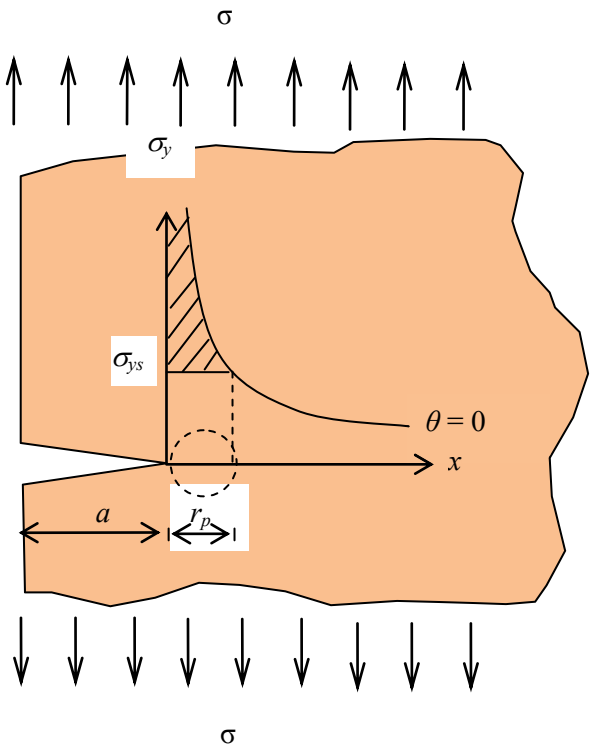

Figure 6.1 One-dimensional plastic zone with stress distribution of σ_y and yield stress (σ_{ys}).

The stress distribution of σ_y on a plate with a yield stress of σ_{ys} for $\theta = 0$ when subjected to an applied stress (σ) is shown in **Figure 6.1** according to Equation (5.11b),

$$\sigma_y = \frac{K_I}{\sqrt{2\pi r}} \cos\frac{\theta}{2}\left(1 + \sin\frac{\theta}{2}\sin\frac{3\theta}{2}\right). \qquad \text{(bis 5.11b)}$$

One can realise that the stress (σ_y) cannot increases in a real material beyond the yield stress (σ_{ys}). Accordingly, the corresponding distance from the crack tip (r_p) to the yield stress (σ_{ys}) may be used as a simplistic estimate for the plastic zone size. Substituting $\theta = 0$, $\sigma_y = \sigma_{ys}$ and $r = r_p$ into Equation (5.11b), we find

$$r_p = \frac{K_I^2}{2\pi\sigma_{ys}^2} = \frac{\sigma^2 a}{2\sigma_{ys}^2}. \tag{6.1a}$$

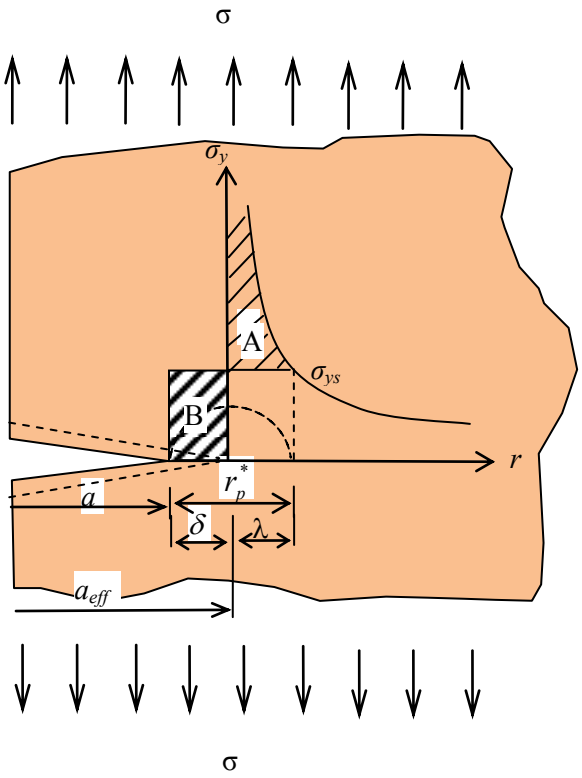

Figure 6.2 Modified one-dimensional plastic zone size

In this calculation, though, the hatched area in **Figure 6.1** is ignored. If we compensate for the loss of the hatched area, the actual plastic zone size must be larger than r_p [see Equation (6.1a)]. Such shortcomings may be reduced if the material immediately ahead of the plastic zone (r_p) is allowed to carry some more stress by introducing an *effective crack size* (a_{eff})[12] which is longer than the physical crack length (a). To this end, the crack tip position can be shifted for calculation. Then, the *effective crack size* becomes $a_{eff} = a+\delta$ where δ is the length contributed by the hatched area as shown in **Figure 6.2**. Accordingly, the plastic zone is calculated by adding λ and δ together. The distance λ is found by replacing a with $a+\delta$ in calculation using Equation (5.11b):

$$\sigma_y = \frac{K_I}{\sqrt{2\pi r}} (\text{when } \theta = 0) \rightarrow \sigma_{ys} = \frac{\sigma\sqrt{\pi(a+\delta)}}{\sqrt{2\pi r}} \tag{6.1b}$$

or

$$\sigma_{ys} \approx \frac{\sigma\sqrt{a}}{\sqrt{2\lambda}} \tag{6.1c}$$

for δ <<*a*. Therefore, for small plastic deformation,

$$\lambda = \frac{\sigma^2 a}{2\sigma_{ys}^2} = r_p . \tag{6.1d}$$

The distance δ is obtained by equating area A to area B in **Figure 6.2**:

$$\int_0^{\lambda} \sigma_y dr - \lambda\sigma_{ys} = \int_0^{\lambda} \frac{K_I}{\sqrt{2\pi r}} dr - \lambda\sigma_{ys} = \int_0^{\lambda} \frac{\sigma\sqrt{\pi a_{eff}}}{\sqrt{2\pi r}} dr - \lambda\sigma_{ys} \tag{6.1e}$$

$$= \frac{\sigma\sqrt{(a+\delta)}}{\sqrt{2}} \int_0^{\lambda} \frac{1}{\sqrt{r}} dr - \lambda\sigma_{ys} = \delta\sigma_{ys}$$

so that, for δ <<*a*,

$$\delta \approx \frac{\sigma^2 a}{2\sigma_{ys}^2} = \frac{K_I^2}{2\pi\sigma_{ys}^2} . \tag{6.1f}$$

Accordingly, it is found that

$$\delta = r_p \tag{6.2}$$

and that the modified plastic zone size (r_p^*) is given by

$$r_p^* = \lambda + \delta = 2r_p . \tag{6.3}$$

The size of the plastic zone (r_p^*) calculated according to the second model (**Figure 6.2**) appears twice as large as the one calculated according to the first model (**Figure 6.1**).

6.2 Two dimensional shape of plastic zone

The two dimensional shape can be obtained by examining the yield condition around the crack tip. Either the Tresca criterion or the Von Mises criterion may be adopted. The Von Mises yield criterion, in terms of the principal stresses, is given by

$$2\sigma_{ys}^2 = (\sigma_1 - \sigma_2)^2 + (\sigma_2 - \sigma_3)^2 + (\sigma_3 - \sigma_1)^2 \tag{bis 2.28}$$

where σ_{ys} in the uniaxial yield stress.

The crack tip stress field equations in terms of principal stresses can be found by substituting the following equations [for the case where k=1],

$$\sigma_x = \frac{K_I}{\sqrt{2\pi r}} \cos\frac{\theta}{2}\left(1 - \sin\frac{\theta}{2}\sin\frac{3\theta}{2}\right) - (1-k)\sigma \tag{bis 5.11a}$$

$$\sigma_y = \frac{K_I}{\sqrt{2\pi r}} \cos\frac{\theta}{2}\left(1 + \sin\frac{\theta}{2}\sin\frac{3\theta}{2}\right) \tag{bis 5.11b}$$

$$\tau_{xy} = \frac{K_I}{\sqrt{2\pi r}} \cos\frac{\theta}{2}\sin\frac{\theta}{2}\cos\frac{3\theta}{2} \tag{bis 5.11c}$$

$\sigma_z = \nu(\sigma_x + \sigma_y)$ for plain strain (bis 5.11d)

into Equation (6.4) for two dimensional principal stresses (σ_1 and σ_2),

$$\sigma_1 \text{ or } \sigma_2 = \frac{\sigma_x + \sigma_y}{2} \pm \left[\left(\frac{\sigma_x - \sigma_y}{2}\right)^2 + \tau_{xy}^2\right]^{1/2} \tag{6.4}$$

yielding,

$$\sigma_1 = \frac{K_I}{\sqrt{2\pi r}} \cos\frac{\theta}{2}\left(1 + \sin\frac{\theta}{2}\right) \tag{6.5a}$$

$$\sigma_2 = \frac{K_I}{\sqrt{2\pi r}} \cos\frac{\theta}{2}\left(1 - \sin\frac{\theta}{2}\right) \tag{6.5b}$$

$$\sigma_3 = \nu(\sigma_1 + \sigma_2) = 2\nu\frac{K_I}{\sqrt{2\pi r}} \cos\frac{\theta}{2} \quad \text{(plane strain)} \tag{6.5c}$$

or

$$\sigma_3 = 0 \quad \text{(plane stress)}\,. \tag{6.5d}$$

The two-dimensional plastic zone (r_p) as a function of θ can be obtained by substituting Equation (6.5) into *distortion energy criterion* (or Von Mises criterion) Equation (2.28):

$$r_p = \frac{K_I^{\,2}}{4\pi\sigma_{ys}^{\,2}}\left[\frac{3}{2}\sin^2\theta + (1-2\nu)^2(1+\cos\theta)\right] \text{ for plane strain} \tag{6.6}$$

and

$$r_p = \frac{K_I^{\,2}}{4\pi\sigma_{ys}^{\,2}}\left[1 + \frac{3}{2}\sin^2\theta + \cos\theta\right] \text{ for plane stress.} \tag{6.7}$$

Substituting θ = 0 in Equation (6.7) for plane stress, we recover the one-dimensional estimate:

$$r_p = \frac{K_I^{\,2}}{2\pi\sigma_{ys}^{\,2}}\,. \tag{bis 6.1a}$$

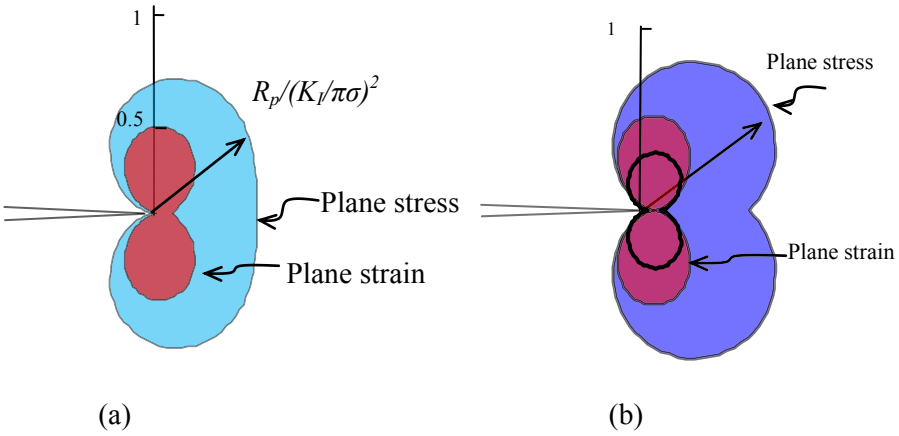

Figure 6.3 Plastic zone shapes calculated according to Von Mises and Tresca yield criteria: (a) Von Mises criterion; (b) Tresca criterion.

The two-dimensional shape can be shown by plotting Equations (6.6) and (6.7) as shown non-dimensionally in **Figure 6.3(a)**. It is seen that the plastic zone in plane strain is smaller than that in plane stress.

Similarly, the *Tresca yield* (or *maximum shear stress*) *criterion* may be employed for the two-dimensional plastic zone. As already discussed, the Tresca yield criterion assumes that yielding occurs when the maximum shear stress $\tau_{\max} = \frac{\sigma_1 - \sigma_3}{2}$ or $\tau_{\max} = \frac{1}{2}(\sigma_1 - \sigma_2)$, whichever is the largest, reaches its yielding point. In the case of uni-axial loading, the maximum principle stress (σ_1) reaches its yielding point (σ_{yz}) so that $\sigma_1 = \sigma_{yz}$, $\sigma_2 = \sigma_3 = 0$. Accordingly, the maximum shear stress is given by

$$\tau_{\max} = \frac{\sigma_1 - \sigma_3}{2} = \frac{\sigma_1 - 0}{2} = \frac{\sigma_{ys}}{2}. \qquad \text{(bis 1.6)}$$

By substituting Equation (6.5) into the maximum shear stress ($\tau_{\max}$) or the *maximum shear stress criterion* (or *Tresca yield criterion*), we obtain

$$r_p = \frac{K_I^2}{2\pi\sigma_{ys}^2}\left[\cos\frac{\theta}{2}\left(1+\sin\frac{\theta}{2}\right)\right]^2 \text{ for plane stress} \qquad (6.8)$$

and the larger of

$$r_p = \frac{K_I^2}{2\pi\sigma_{ys}^2}\cos^2\frac{\theta}{2}\left[1-2\nu+\sin\frac{\theta}{2}\right]^2 \text{ and } \quad r_p = \frac{K_I^2}{2\pi\sigma_{ys}^2}\sin^2\theta \text{ for plane strain.} \qquad (6.9)$$

The two-dimensional shape then can be shown by plotting Equations (6.8) and (6.9) as shown non-dimensionally in **Figure 6.3(b)**. The difference is seen between Von Mises and Tresca plastic zone shapes and sizes. The Tresca plastic zone size appears slightly larger than Von Mises plastic zone size.

Similar calculations are made for modes II and III and plastic zone shapes based on the Von Mises yield criterion are shown in **Figure 6.4**.

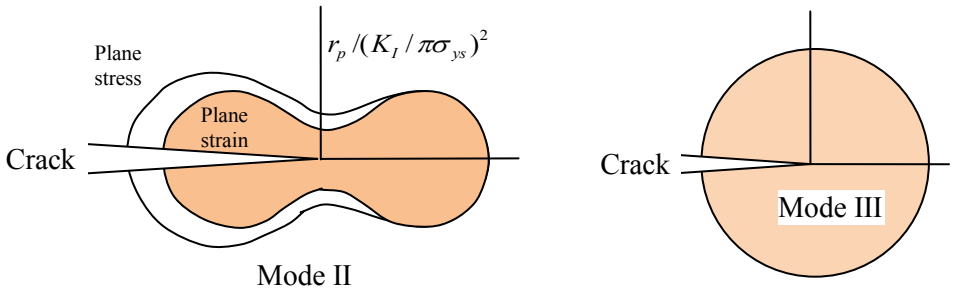

Figure 6.4 Plastic zone shapes based on Von Mises for modes II and III.

Figure 6.5 shows a plastic deformation zone obtained experimentally on a steel using an etching technique. We can find some similarities in plastic zone profile. The etching response is sensitive to grain orientations. Nonetheless, it offers a good guide for understanding the simple theoretical calculations. It is noted that the plastic zone size has been shown to be proportional to K_I^2/σ_{ys}^2 regardless of the different calculation methods, which may be a basis for developing a valid practical testing method of fracture toughness.

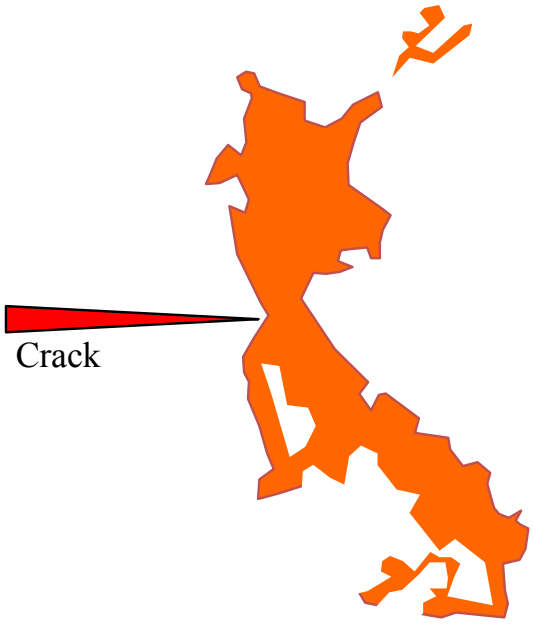

Figure 6.5 Plastic zone around a crack tip, boundaries of which were traced out from an experimental plastic deformation image obtained by an etching technique. [Hahn et al, 1971][13].

6.3 Three dimensional shape of plastic zone

The three dimensional plastic zone around a crack tip may be theoretically estimated when the plane strain condition exists for a thick plate. The plane stress condition is, also, applicable depending on how far the location of interest is away from the plate surface. The plane stress exists at the surface of the plate if the surface is free from stresses ($\sigma_z = \sigma_3 = 0$). In contrast, plane strain prevails in the interior of the plate because the stress σ_3 gradually increases from zero at the surface towards the middle of the plate. The three dimensional plastic zone is illustrated schematically in **Figure 6.6** using the previous calculations based on the Von Mises yield criterion.

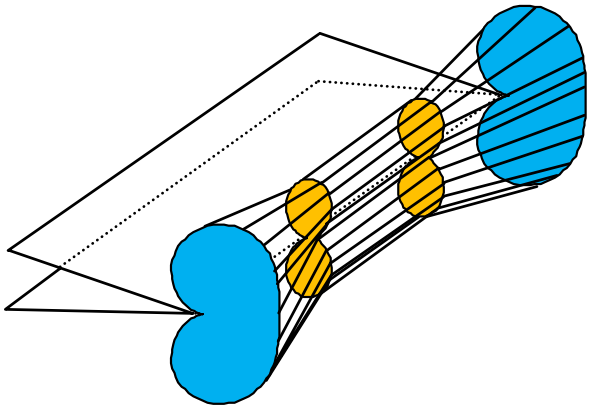

Figure 6.6 Three-dimensional plastic zone shape based on the Von-Mises yield criterion.

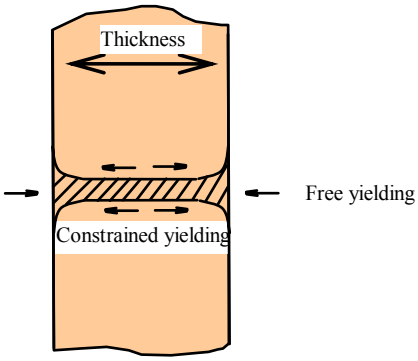

Figure 6.7 Yielding at different states of stress.

Figure 6.7 shows a cross section schematically of the three dimensional plastic zone shown in **Figure 6.6**. The plastic deformation at the surface takes place more freely than that in the interior because of plane stress condition. Concurrently, the plastic deformation in the interior is much more constrained than that at the surface because of plane strain condition ($\varepsilon_z = 0$). Therefore, more hydrostatic component than deviatoric stress component prevails internally, resulting in the smaller plastic zone and more brittleness. Such different stress conditions may be shown using the Mohr's circles and stress elements under mode I loading in **Figure 6.8**. For $\theta \approx 0$, the stresses σ_y, σ_x and σ_z near the crack tip correspond to the principal stresses σ_1, σ_2 and σ_3 respectively according to Equation (6.5). In the case of plane stress, the maximum shear stress (τ_{max}) occurs at planes inclined at angles of 45° to the directions of σ_2, and σ_3 as shown on the stress element in the figure. In the case of plane strain, σ_1 and σ_2 have the same magnitude as that in plane stress but $\sigma_3 = \nu(\sigma_1 + \sigma_2)$ is acting in the *z*-direction. The Mohr's circles represent such a difference between plane stress and plane strain for $\nu = 0.5$. Accordingly, the hydrostatic stress (σ_m)

$$\sigma_m = \frac{I_1}{3} = \frac{\sigma_x + \sigma_y + \sigma_z}{3} = \frac{\sigma_1 + \sigma_2 + \sigma_3}{3} \qquad \text{(bis 1.7)}$$

is not only higher in plane strain than in plane stress but also the maximum shear stresses (τ_{max}) occurs at planes inclined at angles of 45° to σ_1 and σ_2 directions (**Figure 6.8**).

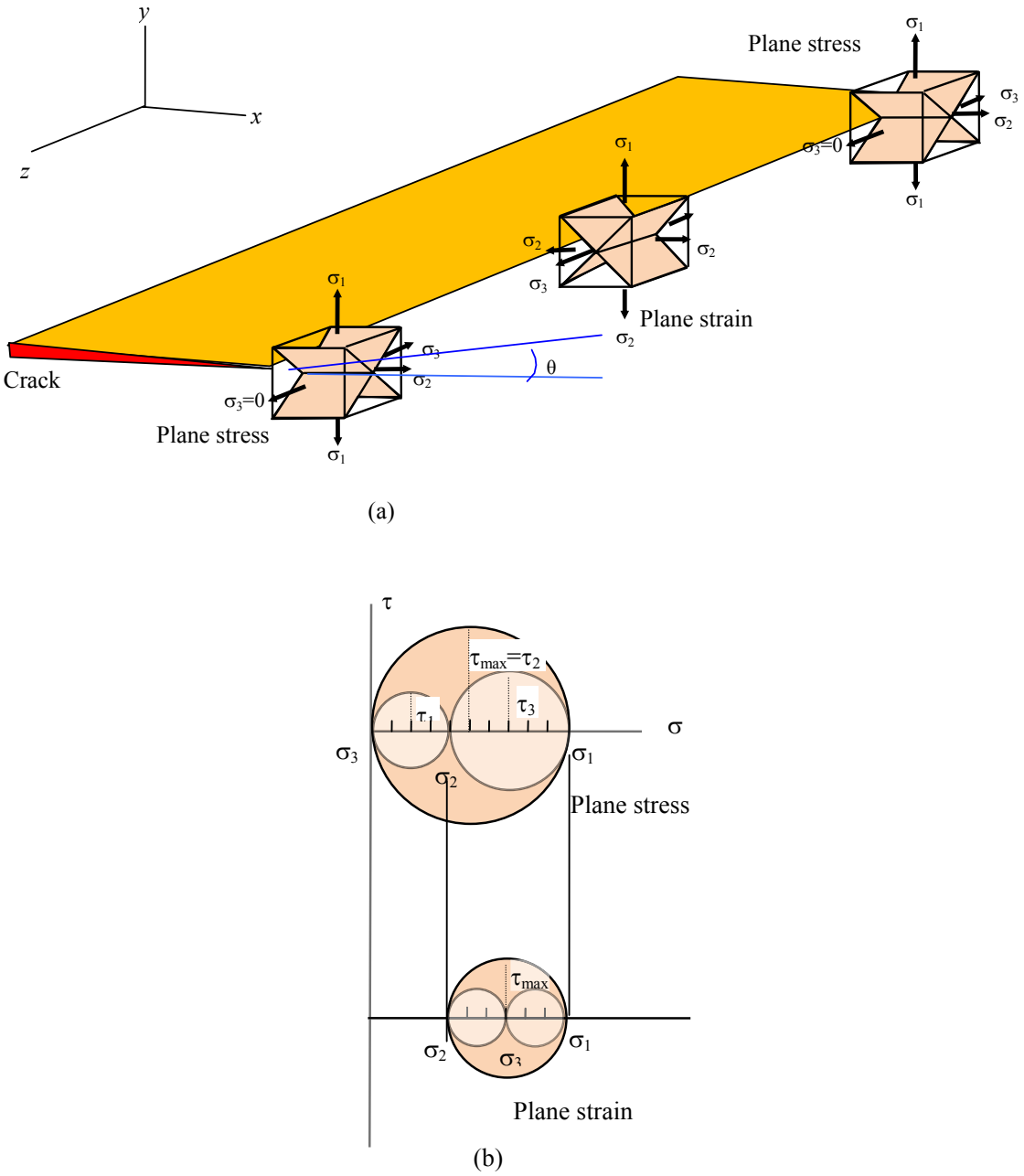

Figure 6.8 (a) Planes of maximum shear stresses near the crack tip for θ ≈ 0; and (b) Mohr's circle representation for plane stress and plane strain.

Such maximum shear stress planes manifest themselves in a form of slip bands as depicted graphically in **Figure 6.9**. The 45˚ slip bands appear internally at the cross section perpendicular to the specimen surface in the case of plane stress while they appear also, in the case of plane strain, internally on the cross section but parallel with the specimen surface. In the plane strain case, the 45 ˚ slip bands constantly varies as a function of θ because the principal stress directions for σ_1 and σ_2 varies although the principal stress direction for σ_3 is always in the z direction. **Figure 6.10** shows sketches of experimental slip bands with plastic deformation on the specimen surface in plane stress.

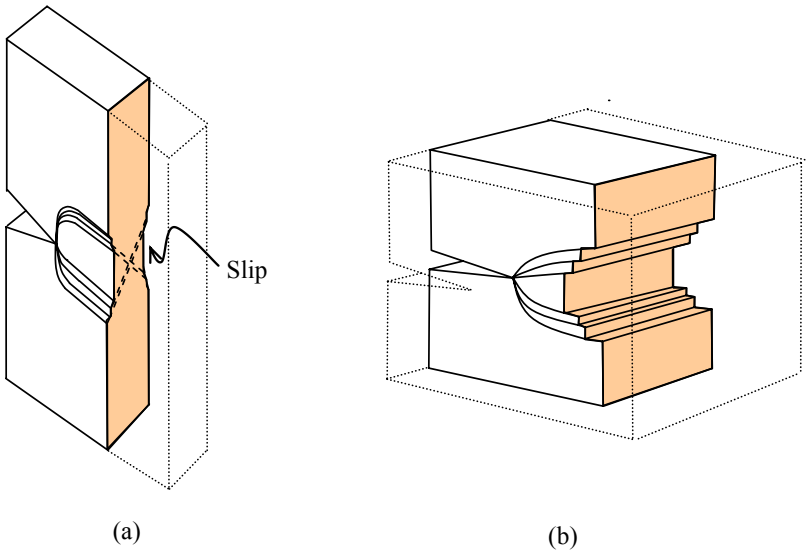

Figure 6.9 Deformation patterns around the crack tip: (a) 45° shear planes in plane stress; and (b) hinge type deformation in plane strain in the middle section.

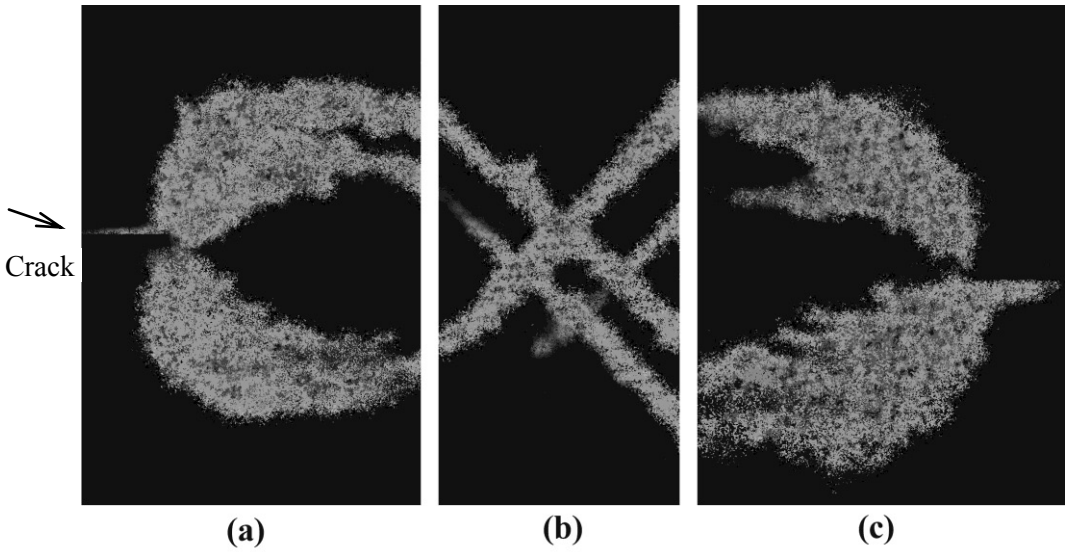

Figure 6.10 Experimental plastic zones in plane stress[14]: (a) front surface section, (b) cross section normal to the front and back sections, and (c) back surface section. [Sketches were provided by Haleh Allameh Haery.]

(a)

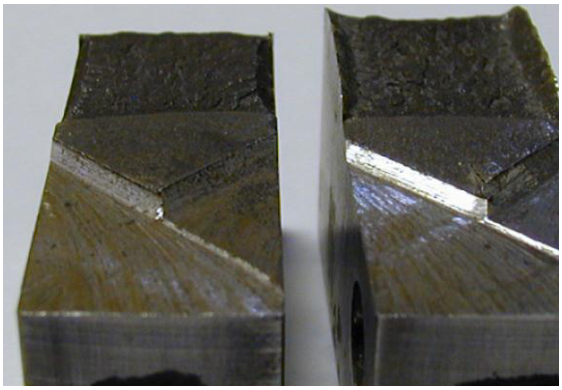

(b)

Figure 6.11 Compact tension specimen after fracture: (a) depression along the crack; and (b) flat fracture surface in the middle section and slant fracture along the edges.

Also, the plane stress and plane strain deformations affect the failure mode as shown in **Figure 6.11**. The slant regions so called 'shear lips' are formed on the specimen surfaces along the edges and the flat fracture surfaces are created in the middle section [**Figure 6.11(b)**]. The shear lips coincide with the 45° shear planes indicating that their formation is associated with the ductile failure mode. However, the flat fracture surfaces do not coincide with the shear planes but appear to be caused directly by the maximum principal stress involving the brittle failure mode.

6.4 Plastic constraint factor

The yielding behaviour in the vicinity of a crack tip is affected by plane thickness. For instance, the plane strain plastic zone is significantly smaller than the plane stress plastic zone. Such a difference is caused by different constraints. A plastic constraint factor (p.c.f.) may be introduced for quantification defined as

$$\text{p.c.f.} = \frac{\sigma_1}{\sigma_{ys}} \tag{6.10}$$

where σ_1 is the maximum principal stress. To relate σ_1 with other principal stress components, let

$$\sigma_2 = n\sigma_1 \text{ and } \sigma_3 = m\sigma_1$$

From the Von Mises yield criterion,

$$2\sigma_{ys}^2 = (\sigma_1 - \sigma_2)^2 + (\sigma_2 - \sigma_3)^2 + (\sigma_3 - \sigma_1)^2 \qquad \text{(bis 2.28)}$$

the following relation is found:

$$\left[(1-n)^2 + (n-m)^2 + (1-m)^2\right]\sigma_1^2 = 2\sigma_{ys}^2 . \qquad (6.11)$$

Therefore,

$$\text{p.c.f.} = \frac{\sigma_{\max}}{\sigma_{ys}} = \frac{\sigma_1}{\sigma_{ys}} = \left(1 - n - m + n^2 + m^2 - mn\right)^{-\frac{1}{2}}. \qquad (6.12)$$

From the stress field equations,

$$\sigma_1 = \frac{K_I}{\sqrt{2\pi r}} \cos\frac{\theta}{2}\left(1 + \sin\frac{\theta}{2}\right) \qquad \text{(bis 6.5a)}$$

$$\sigma_2 = \frac{K_I}{\sqrt{2\pi r}} \cos\frac{\theta}{2}\left(1 - \sin\frac{\theta}{2}\right) \quad \text{(bis 6.5b)}$$

$$\sigma_3 = \nu(\sigma_1 + \sigma_2) = 2\nu \frac{K_I}{\sqrt{2\pi r}} \cos\frac{\theta}{2} \quad \text{(plane strain)} \quad \text{(bis 6.5c)}$$

or

$$\sigma_3 = 0 \quad \text{(plane stress)} \quad \text{(bis 6.5d)}$$

we found,

$$n = (1 - \sin\theta/2)(1 + \sin\theta/2) \quad (6.13)$$

and

$$m = 2\nu / (1 + \sin\theta / 2) \text{ (for plane strain)} \quad (6.14a)$$

$$m = 0 \text{ (for plane stress).} \quad (6.14b)$$

Accordingly, we found p.c.f = 1 for plane stress when θ = 0, and p.c.f. = 3 (and n = 1, m = 2ν=0.67) for plane strain when θ = 0 and ν = 1/3. The maximum stress in plane strain appears as high as three times the uni-axial yield stress.

A comparison of approximate stress distribution between plane stress and plane strain based on the calculations is shown in **Figure 6.12**. In the case of plane strain, the stress continues to rise beyond σ_{ys} until it becomes $3\sigma_{ys}$ around the crack tip.

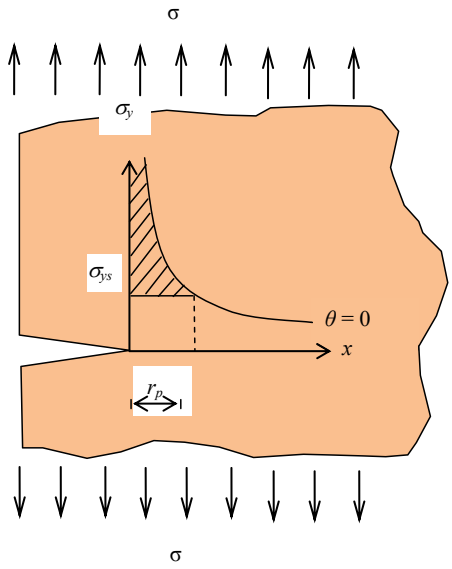

(a)

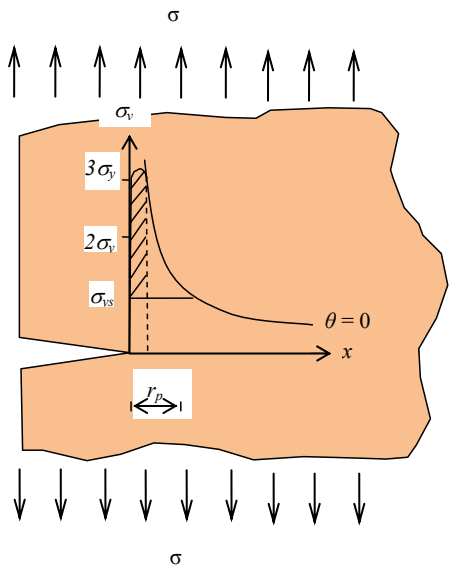

(b)

Figure 6.12 Comparison of approximate stress distribution between plane stress and plane strain in relation with yield stress (σ_{ys}): (a) plane stress; and (b) plane strain.

6.5 The thickness effect

As discussed, the failure mode (e.g. ductile mode) is affected by plastic deformation and hence by the thickness of specimen. Therefore, the fracture behaviour is ultimately affected by the specimen thickness until it reaches a point where the plane stress condition is negligibly small. The transition from plane stress dominant deformation to plane strain dominant deformation is graphically illustrated in **Figure 6.13**. **Figure 6.13(a)** shows a thin specimen with plastic zone shape and size according to the Von Mises yield criterion. As the thickness (B) increases, the proportion of plastic deformation governed by plane stress is maintained until it reaches a stage where the plastic deformation occurs with plane stress slip planes as shown in **Figure 6.13(b)**. Eventually, the thickness reaches another stage [**Figure 6.13(c)**] where the plastic deformation occurs with slip planes generated by both plane stress and plane strain.

The maximum depth (r_p^h) of the zone can be shown to be at about 80° and to have a value:

$$r_p^h = 2.59\left(r_p\right)_{\theta=0} \tag{6.15a}$$

and is given by

$$r_p^h = B_{crit} \tag{6.15b}$$

at the transitional stage [**Figure 6.13(b)**]. Therefore, the critical thickness (B_{crit}) is found:

$$B_{crit}=\frac{2.59}{2\pi}\left(\frac{K_I}{\sigma_{ys}}\right)^2=0.41\left(\frac{K_I}{\sigma_{ys}}\right)^2 \tag{6.16}$$

According to the ASTM standard, the minimum specimen thickness requirement for plane strain fracture toughness test is given by

$$B \geq 2.5\left(\frac{K_{IC}}{\sigma_{ys}}\right)^2 . \tag{6.17}$$

A higher stress intensity and a lower yield stress give rise to a larger plastic zone. As a result, a larger thickness is required for the plane strain fracture toughness test.

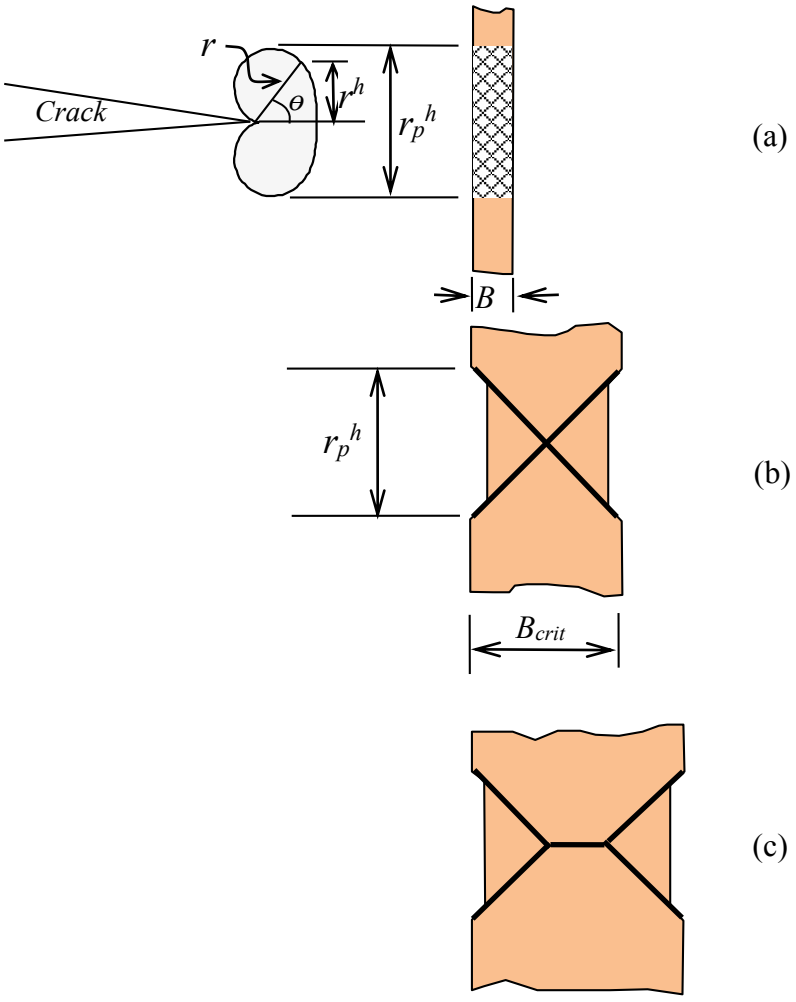

Figure 6.13[15] Graphical representation of plastic deformation transition from plane stress to plane strain at the back face of the specimen as the specimen thickness increases: (a) plane stress; (b) at the transition; and (c) plain strain deformation in addition to that of plane stress. The plastic zone shape in '(a)' is based on the Von Mises yield criterion.

The dependence of K_{1c} on thickness is illustrated given in **Figure 6.14**. (The critical stress intensity for cracking is usually denoted by K_c, but the notation K_{1c} will be adopted here to indicate mode I cracking for both plane stress and plane strain.) The figure shows also cross sections for shear lips and flat fracture surface regions corresponding to K_{1c}. The curve suggests that, beyond a certain thickness (B_s), a state of plane strain prevails and toughness reaches the plane strain toughness value (K_{Ic}) practically independent of thickness for B> B_s. It also suggests there is an optimum thickness B_0 where the toughness reaches its highest level. In the transitional region between B_0 and B_s, the toughness has intermediate values. For thicknesses below B_0, it is possible that there is not much material available for the plastic flow before the fracture, resulting in low values of K_{1c} as the thickness decreases.

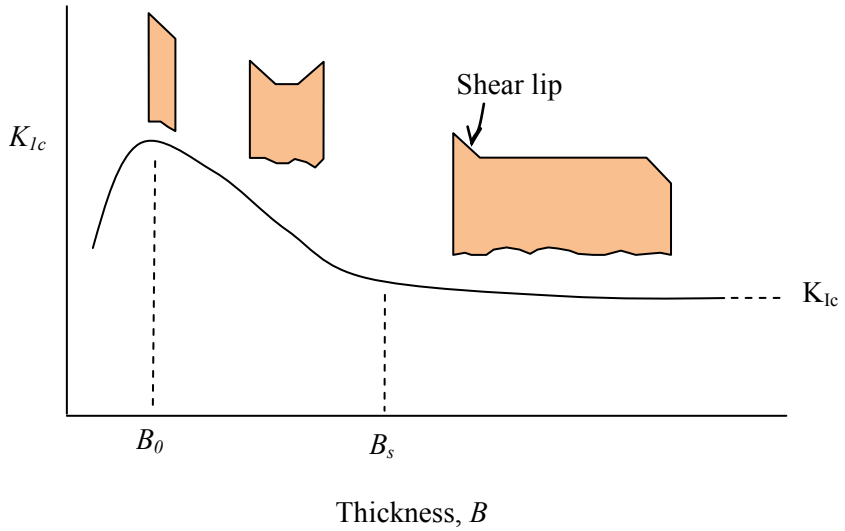

Figure 6.14 Toughness as a function of thickness and cross sections of specimens with different thicknesses.

6.6 Thickness of adhesive layer

The adhesion between different components is important for the integrity of engineering structure made of composites. The thickness of adhesive layer significantly affects the fracture toughness (G_{Ic}) of adhesively jointed section although, for highly brittle adhesives, this parameter may be not as much significant. **Figure 6.15** shows the fracture toughness as a function of adhesive layer thickness for both toughened and un-toughened epoxies.

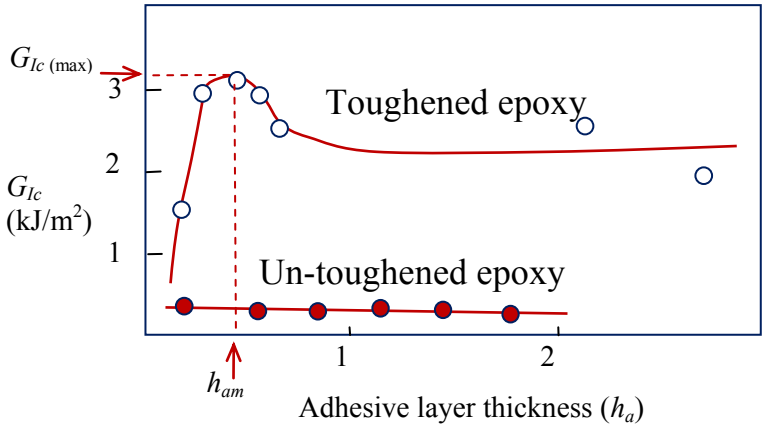

Figure 6.15 Adhesive fracture energy (G_{Ic}) as a function of thickness (h_a) of the adhesive layer for joints consisting of steel bonded with a rubber-toughened or un-toughened epoxy. [After Kinloch and Shaw, 1981][16]

A relatively complex behaviour with toughened adhesives arises from the plastic deformation in the vicinity of the crack tip, which is highly constrained with high modulus and high yield strength substrates such as steel or aluminium alloy. The constraint of adhesive joint may be higher than that of an adhesive without substrates. It may restrict the full volume development of the plastic zone in the adhesive layer ahead of the crack tip (**Figure 6.16**). Since the toughness is largely derived from the energy required for forming the plastic zone, the adhesive fracture energy (G_{Ic}) steadily increases as the adhesive layer thickness (h_a) increases up to a certain value. The maximum toughness, $G_{Ic(\max)}$ occurs when the adhesive layer thickness and the plastic-zone height (r_p^h), are similar to each other (**Figure 6.15**). Accordingly, the following equation based on plastic zone size calculation [see Equation (6.6)] would provide a good guidance for the adhesive thickness (h_{am}) at $G_{Ic(\max)}$:

$$h_{am} \approx r_p^h \left(\approx \frac{1}{\pi} \frac{EG_{Ic}(\text{control})}{\sigma_{ys}^2} \right) \tag{6.18}$$

where E is the elastic modulus and σ_{ys} is the yield stress. **Table 6.1** lists some experimental results.

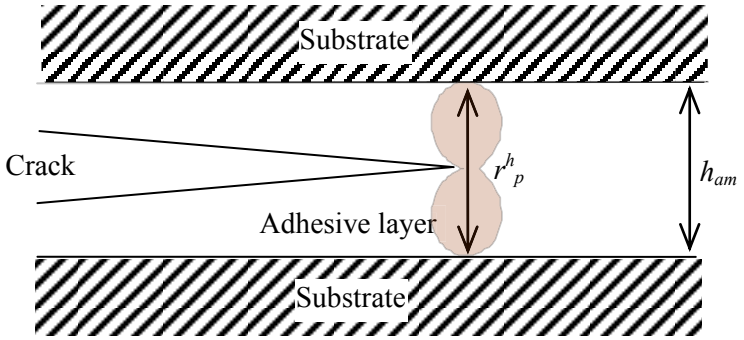

Figure 6.16 Elastic-plastic model for plastic deformation zone at a crack tip in the adhesive layer with high yield stress (elastic) substrates.

Temperature (^oC)	Log (rate of test) (m/s)	G_{Ic} (Control) (kJ/m^2)	$G_{Ic(\max)}$ (Joint) (kJ/m^2)	h_{am} (mm)	r_p^h (mm)
20	-6.08	2.10	3.90	1.0	0.85
20	-4.78	1.85	3.65	0.8	0.70
20	-3.78	1.55	3.55	0.55	0.49
20	-3.08	1.50	3.15	0.4	0.43
50	-4.66	4.70	2.95	1.1	1.6
37	-4.66	3.75	2.85	0.9	1.16
25	-4.66	2.70	3.85	0.6	0.57
0	-4.66	1.65	3.00	0.5	0.39
-20	-4.66	1.00	3.15	0.25	0.15
-40	-4.66	0.75	2.50	0.1	0.05

Table 6.1 Comparison of measured adhesive layer thickness (h_{am}) at maximum adhesive fracture energy (G_{Icm}) and calculated plastic zone diameter (r_p^h). [After Kinloch and Shaw, 1981][17]

6.7 Experimental determination of K_{Ic}

The experimental determination of plane strain fracture toughness (K_{Ic}) is based on the theories discussed up to now to obtain reproducible values of K_{Ic} under the conditions of maximum constraint. The plastic zone size in the vicinity of a crack tip must be very small relative to the specimen dimensions. The procedure for measuring K_{Ic} has been standardised by the American Society for Testing and Materials (ASTM) to meet the requirements. In this section, the salient points of the ASTM standard test method will be introduced.

6.7.1 Test specimen dimensions

The dimensions of specimens are specified for the minimum thickness (B) for a valid plane strain fracture toughness (K_{Ic}) is given by

$$B \geq 2.5\left(\frac{K_{Ic}}{\sigma_{ys}}\right)^2 \tag{6.17 bis}$$

and the crack length (a) is given by

$$a \geq 2.5\left(\frac{K_{Ic}}{\sigma_{ys}}\right)^2 . \tag{6.19}$$

The ASTM E 399 describes many pre-cracked test specimens such as three-point bend specimen, compact tension specimen, arc-shaped specimen, and disk-shaped compact specimen. The three-point bend specimen and compact tension specimen are shown in **Figures 6.17** and **6.18**. The stress intensity factor expressions[18] for the standard specimens are:

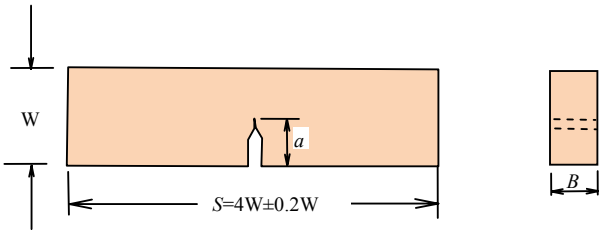

Figure 6.17 Three-point bend specimen.

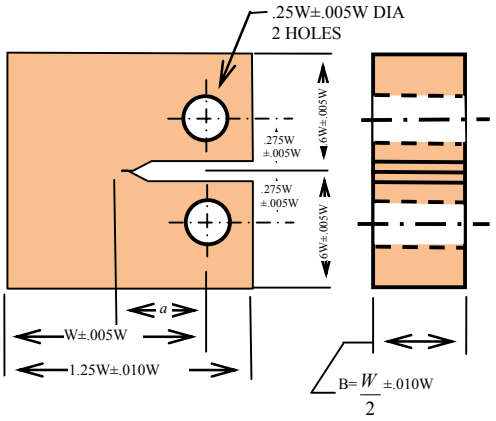

Figure 6.18 Compact tension specimen.

$$K_I = \frac{PS}{BW^{3/2}} \frac{3\left(\frac{a}{W}\right)^{1/2}\left[1.99 - \frac{a}{W}\left(1-\frac{a}{W}\right)\left(2.15 - 3.93\frac{a}{W} + 2.7\frac{a^2}{W^2}\right)\right]}{2\left(1+2\frac{a}{W}\right)\left(1-\frac{a}{W}\right)^{3/2}} \tag{6.20}$$

for three point bend specimen, and

$$K_I = \frac{P}{BW^{1/2}} \frac{\left(2+\frac{a}{W}\right)\left[0.886 + 4.64\frac{a}{W} - 13.32\left(\frac{a}{W}\right)^2 + 14.72\left(\frac{a}{W}\right)^3 - 5.6\left(\frac{a}{W}\right)^4\right]}{\left(1-\frac{a}{W}\right)^{3/2}} \tag{6.21}$$

for compact tension specimen. The dimensions a, W and B are shown in **Figures 6.17** and **6.18**. The P in equations is a measure of the load, and S is the distance between the points of support of the beam in **Figure 6.17**. Equation (6.20) is accurate within ±0.25 per cent, over the entire range of a/W ($a/W < 1$). Equation (6.21) is also accurate within ±0.25 per cent for $0.2 < a/W < 1$.

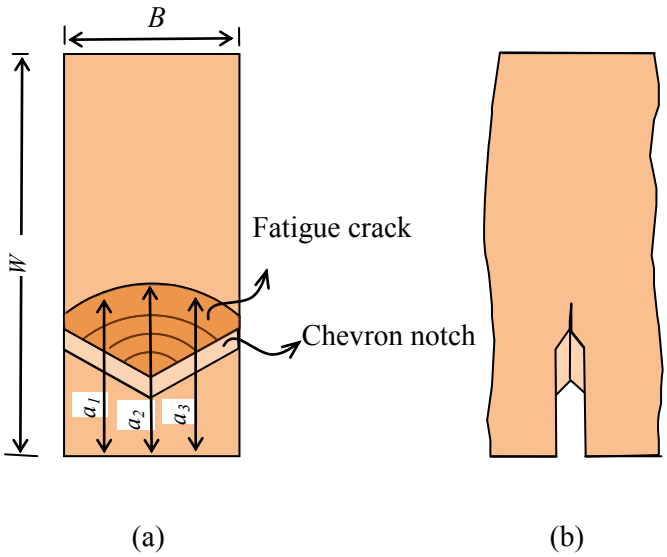

Figure 6.19 Chevron Notch: (a) Cracked surface with different crack lengths; and (b) side view. (see **Figure 6.11**)

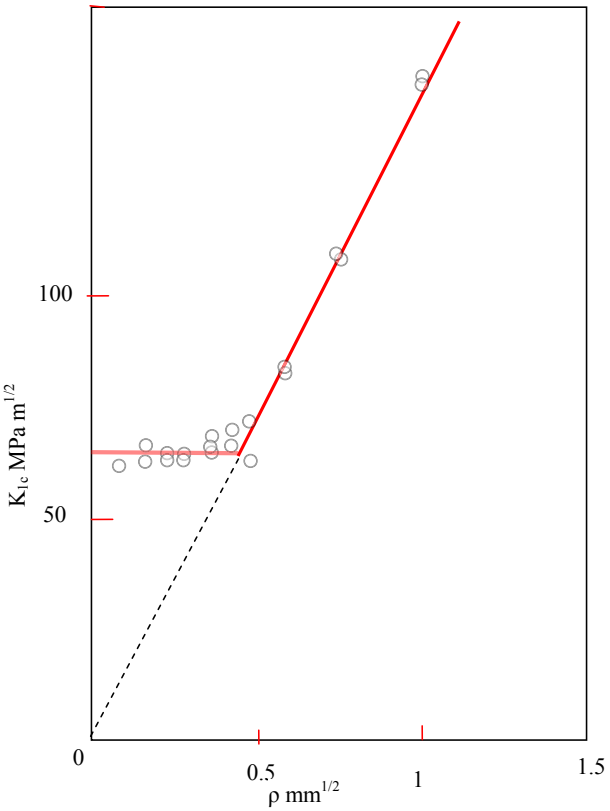

Figure 6.20 Effect of notch radius (ρ) on the critical stress intensity factor K_{1c}. [After Irwin, 1964][19]

6.7.2 Precrack

The precrack of test specimen is made of mechanical and fatigue cracks as shown in **Figure 6.19**. The mechanical crack is first machined for a chevron starter notch and then a fatigue crack follows. There is an advantage of using the chevron notch in that it forces crack initiation into the centre so that a reasonable symmetric crack front is obtained before testing. If the initial machined notch front is straight, the subsequent fatigue crack tends to initiate from a corner. The prepared crack front may be not straight so that an average of three crack lengths is used. One of the crack lengths is measured in the centre of the crack front, and the other two lengths are measured in the midway between the centre and the end of the crack front, giving $a=\frac{a_1+a_2+a_3}{3}$. The reason for using the fatigue crack is that the crack tip radius should be sufficiently small. The effect of the notch radius (ρ) on the stress intensity factor (K_{1c}) is shown in **Figure 6.20**. The stress intensity factor (K_{1c}) decreases with decreasing notch radius (ρ) until a transitional point is reached, and then a plateau value is found. The fatigue loading should satisfy some requirements to achieve such a small radius of crack tip and consistent results. The maximum stress intensity factor during fatigue cycling should not exceed 60% of K_{Ic}.

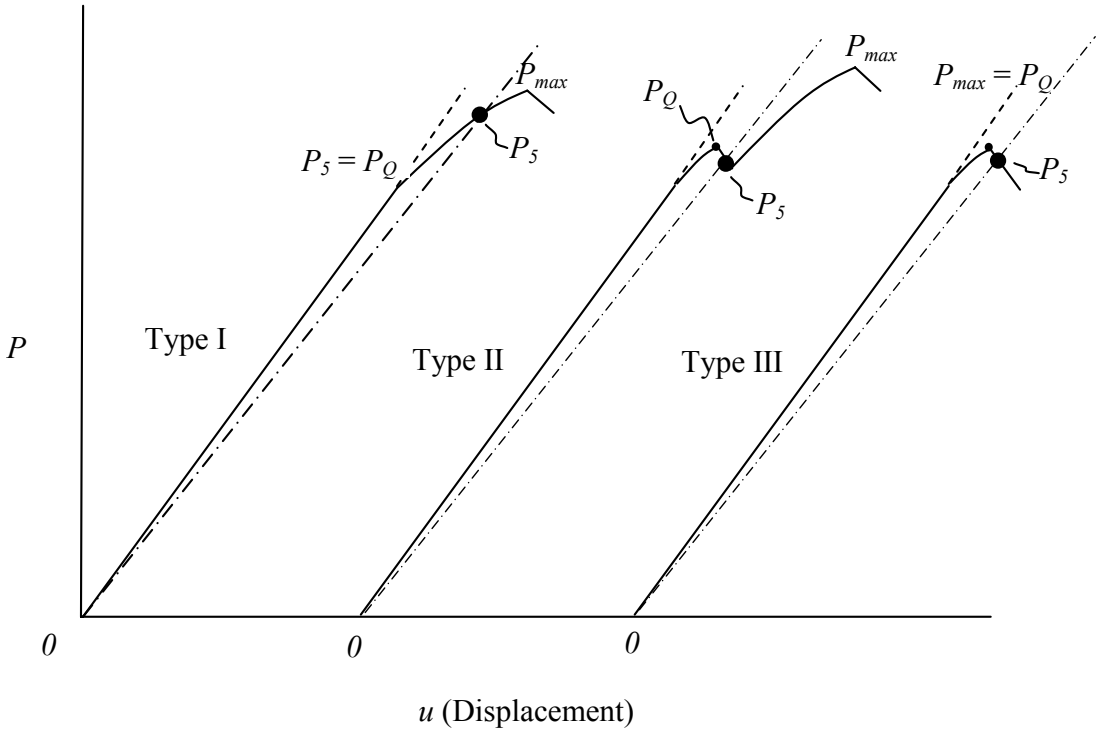

Figure 6.21 Determination of P_Q for three types of load-displacement response according to ASTM standards.

6.7.3 Interpretation of test record and calculation of K_{Ic}

The procedure for conducting the test is straightforward. A typical instrumentation for measurement requires a clip gauge to produce a load-displacement curve. A typical record of load-displacement for metallic materials would look like one of the three curves shown in **Figure 6.21**. Type I represents nonlinear behaviour involving a large plastic deformation, type III dominantly linear response and type II reflects the phenomenon of 'pop-in'. From the output record, three values P_Q, P_5 and P_{max} are extracted – P_Q is the load for calculation of the fracture toughness [see Equations (6.20) and (6.21)], P_5 is the limit of allowable plastic or non-linear deformation, and P_{max} is the maximum load. To identify the three different loads, a secant line $0P_5$ is drawn through the origin with a slope equal to 0.95 of the slope of the tangent to the initial linear part of the record. The load P_5 corresponds to the intersection of the secant with the test record. The load P_Q is then determined as follows. If the load at every point on the record between the initial tangent line and a secant line $0P_5$ is lower than P_Q as in Type I, then $P_Q = P_5$. If, however, there is a load higher than P_5 between the initial tangent line and a secant line $0P_5$, then P_Q is equal to this higher load as in Types II and III. Furthermore, the test is not valid if P_{max}/P_Q is greater than 1.10, where P_{max} is the maximum load the specimen was able to resist. When a test is invalid, it is necessary to use a larger specimen to determine K_{Ic}.

7 Crack Growth Based On The Energy Balance

The theories of crack growth based on the energy conservation for fracture will be introduced in this chapter. They not only complement various methods based on the linear stress analysis for the fracture toughness determination but also are capable of dealing with non-linear materials behaviour. Also, the equivalence of the energy conservation approach to that based on the linear stress analysis will be found. The energy principles, thus, provides further benefits for understanding the fracture behaviour of materials.

7.1 Energy conservation during crack growth

The fracture process is associated with the energy conservation. The energy is supplied to the structural system by the externally applied load, and is simultaneously consumed when the rupture of atomic bonds of a material takes place for a new crack surface formation, for elastic and plastic deformations, and for kinetic behaviour. Let us consider a cracking body creating a cracked area A [= thickness (B) × crack length (a)]. According to the law of conservation of energy, we have,

$$\dot{W}=\dot{\Lambda}+\dot{K}+\dot{\Gamma} \tag{7.1}$$

where W is the work performed per unit time by the applied load, Λ and K are the rates of change for the strain energy and kinetic energy of the body respectively, and Γ is the energy per unit time for increasing the crack area. (A dot over a letter denotes differentiation with respect to time.)

The strain energy Λ can be broken up into two parts i.e. one for elastic work and the other for plastic work,

$$\Lambda = \Lambda^e + \Lambda^p \tag{7.2}$$

where Λ^e is the elastic strain energy and Λ^e the plastic strain energy.

If the crack grows slowly in a stable manner, the kinetic term K is negligible and can be omitted. Since all the changes with respect to time are caused by change in crack size, we find that

$$\frac{\partial}{\partial t}=\frac{\partial A}{\partial t}\frac{\partial}{\partial A}=\dot{A}\frac{\partial}{\partial A} \qquad A \geq 0 \tag{7.3}$$

and Equation (7.1) becomes

$$\frac{\partial W}{\partial A}=\left(\frac{\partial \Lambda^e}{\partial A}+\frac{\partial \Lambda^p}{\partial A}\right)+\frac{\partial \Gamma}{\partial A}. \tag{7.4}$$

Equation (7.4) describes the energy balance during the crack growth. In other words, the work rate supplied to the cracking body by the applied load is balanced with the rate of the elastic strain work, the rate of plastic strain work, and the energy consumption rate for crack surface creation. From Equation (7.4), the *potential energy* (Π) in the system may be defined as

$$-\frac{\partial \Pi}{\partial A} = \frac{\partial \Lambda^p}{\partial A} + \frac{\partial \Gamma}{\partial A} \tag{7.5}$$

where

$$\Pi = \Lambda^e - W \,. \tag{7.6}$$

Equation (7.5) describes that the rate of potential energy reduction during the crack growth is balanced with the rate of energy consumed for plastic deformation and crack surface creation.

7.2 Griffith's approach[20]

The energy consumed for plastic deformation in an ideally brittle material is negligibly small and can be omitted from Equation (7.4). Then, Equation (7.4) is rewritten as

$$G = \frac{\partial W}{\partial A} - \frac{\partial \Lambda^e}{\partial A} = \frac{\partial \Gamma}{\partial A}. \tag{7.7}$$

The symbol G is introduced in the equation and represents the *crack driving force* involving W and Λ^e. Equation (7.7) describes that the *crack driving force* is balanced with the *resistance* of the material having a characteristic value of Γ.

Two limiting loading cases may be considered in practice – one is the *constant displacement* with varying load and the other is the *constant loading* with varying displacement. In the case of *constant displacement*, $\frac{\partial W}{\partial A} = 0$ in Equation (7.7). Therefore, we find,

$$G = \frac{-\partial \Lambda^e}{\partial A}. \tag{7.8}$$

Equation (7.8) describes the energy release rate when the energy stored in material is released for crack growth. Hence, the symbol G is usually referred to as the *elastic strain energy release rate*. In the case of *constant loading*, the work performed by the constant load is approximately twice the increase of elastic strain energy $\left(\partial W / \partial A = 2\partial \Lambda^e / \partial A\right)$. Consequently, Equation (7.7) becomes,

$$G = \frac{\partial \Lambda^e}{\partial A}. \tag{7.9}$$

In this case, the energy required for crack surface creation is supplied by the external load.

Thus, G is found to be independent of the loading method and Equations (7.8) and (7.9) can be put in the form for ideally brittle materials:

$$G = \frac{\partial \Pi}{\partial A} \tag{7.10}$$

where the potential Π energy is defined in Equation (7.6). Also, the energy balance in general may be written as

$$\frac{\partial(\Pi + \Gamma)}{\partial A} = 0. \tag{7.11}$$

The elastic strain energy (Λ^e) can be calculated using the stress field and displacement (v) around a crack tip. Let us consider a line crack of length $2a$ in an infinite plate subjected to a uniform stress (σ), perpendicular to the crack (**Figure 7.1**). The change in elastic strain energy ($\Delta\Lambda$) due to the crack length increment (Δa) is found:

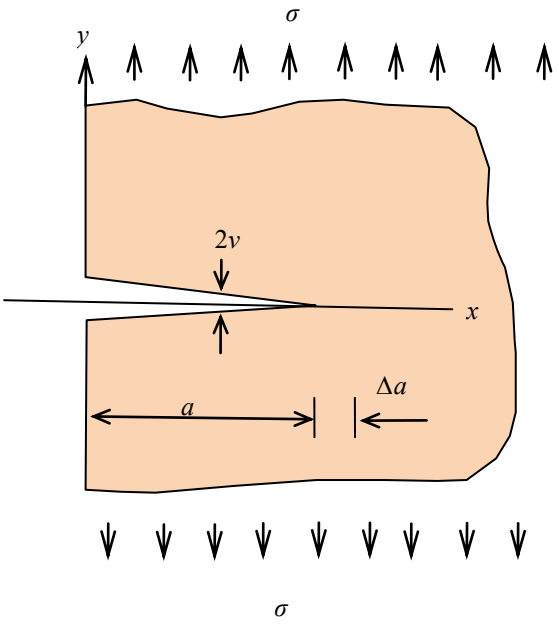

Figure 7.1 An infinite plate with a thickness (*B*) and a crack length (*a*) subjected to a remote stress (σ).

$$\Delta\Lambda = 2B\int_0^{\Delta a}\frac{\sigma_y v}{2}dr = \frac{B\pi a\sigma^2}{E}\Delta a \text{ for plane stress.} \qquad \text{(bis 5.36)}$$

According to the following definition for a critical energy release rate (G_c),

$$G_c = \frac{\Delta\Lambda}{B\Delta a} \qquad (7.12)$$

the critical stress (σ_c) required for crack growth is given by

$$\sigma_c = \sqrt{\frac{EG_c}{\pi a}} \qquad (7.13)$$

for plane stress, and

$$\sigma_c = \sqrt{\frac{EG_c}{\pi a\left(1-\nu^2\right)}} \qquad (7.14)$$

for plane strain. One of conclusions drawn by Griffith (1921) is as follows:

> "The breaking load of thin plate of glass having in it a sufficiently long straight crack normal to the applied stress, is inversely proportional to the square root of the length of the crack. The maximum tensile stress in the corners of the crack is more than ten times as great as the tensile strength of the material, as measured in an ordinary test."

7.3 Graphical representation of the energy release rate

The graphical representation of the energy balance for crack growth is useful for interpretation of experimental results for finding the energy release rate. The load-displacement response of cracked plate as can be obtained from a testing machine will be discussed for three different cases: (a) constant displacement, (b) constant load, and (c) generalised case of changing both the load and the displacement.

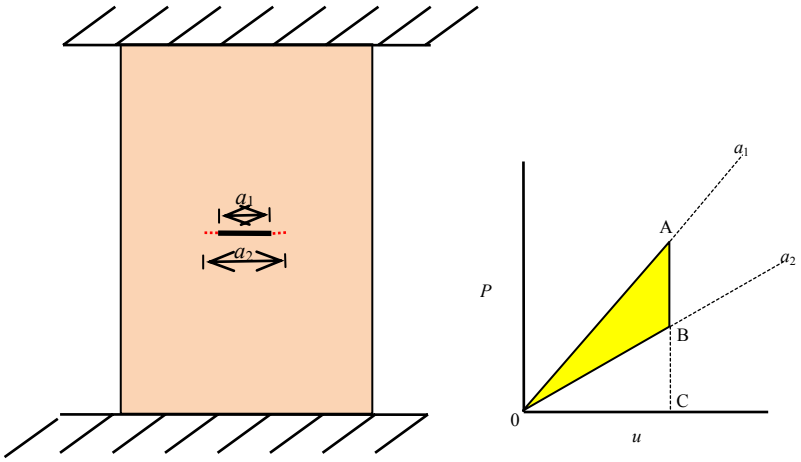

Figure 7.2 Load-displacement response of a cracked plate to a crack length change from length a_1 to a_2 under constant displacement.

7.3.1 Constant displacement case

The load-displacement response of a cracked plate is represented in **Figure 7.2**. Two different crack lengths (a_1 and a_2) are shown for $a_2 > a_1$. The straight line OA is a linear response of the cracked plate with a crack length of a_1 and the other straight line OB is that with a crack length of a_2. It is noted that the cracked plate with a shorter crack is stiffer than that with a longer crack. The magnitudes of strain energy stored at point A and point B are represented by area OAC and area OBC respectively. If the crack length changes from a_1 to a_2, the load drops from point A to point B and hence the strain energy in the cracked plate is reduced by a magnitude represented by area OAB. Therefore, the elastic energy release rate (G) equivalent to Equation (7.8) is graphically obtained as:

$$G = \frac{\text{area}\,(0AB)}{B\Delta a} \tag{7.15}$$

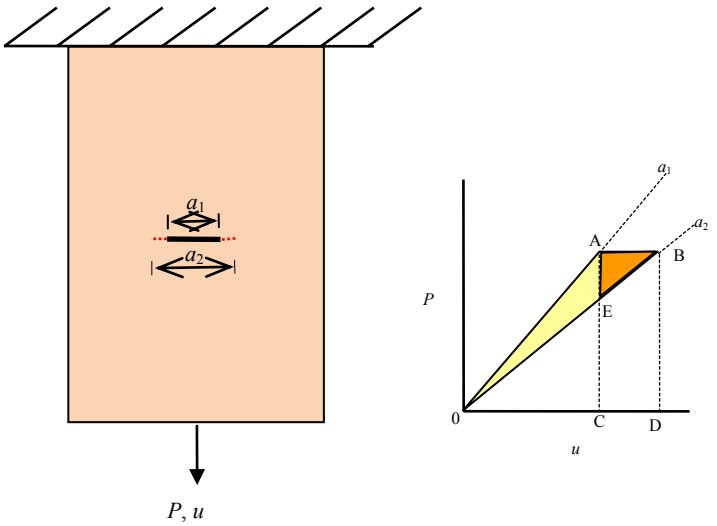

Figure 7.3 Load-displacement response of a cracked plate to a crack length change from a_1 to a_2 under constant load.

7.3.2 Constant load case

The load-displacement response of a cracked plate is represented in **Figure 7.3**. Two different crack lengths (a_1 and a_2) are again shown for $a_2 > a_1$. The straight line 0A is a linear response of the cracked plate with a crack length of a_1 and the other straight line 0B is that with a crack length of a_2 as before. The strain energy stored in the cracked plate at point A is represented by area 0AC. If the crack length changes from a_1 to a_2, the displacement (u) increases from point A to point B. At this point, the total energy supplied by the load (P) is represented by area 0ABD and the strain energy stored in the cracked plate is represented by area 0BD. Thus, the strain energy released from the cracked plate due to the crack length change is represented by

area 0BD – area 0AC

Also, the total energy lost from the total energy supplied due to the crack length change is represented by area 0AB. However,

area 0AB ≈ area 0BD – area 0AC

because area ABE diminishes as the crack length change Δa approaches zero. Therefore, the elastic energy release rate (G) equivalent to Equation (7.9) is graphically obtained as:

$$G = \frac{\text{area}\,(0AB)}{B\Delta a}. \tag{7.16}$$

7.3.3 Generalized case

The previous two cases are the limiting ones and the crack growths cannot be produced directly by the load (P) without assistance. The different crack lengths (a_i) in the generalised case shown in **Figure 7.4** are, however, directly produced by the applied load. The crack length a_1 is the initial crack length and $a_1 < a_2 < a_3 < a_4 < a_5$. As the crack length increases during quasi static crack growth, the stiffness of a cracked plate decreases but displacement (u) increases. Therefore, the elastic energy release rate (G) equivalent to Equation (7.8) or (7.9) is graphically obtained as

$$G = \frac{\text{area}\left(0A_{i+1}A_i\right)}{B\left(a_{i+1} - a_i\right)} \tag{7.17}$$

with i =1, 2, 3, etc.

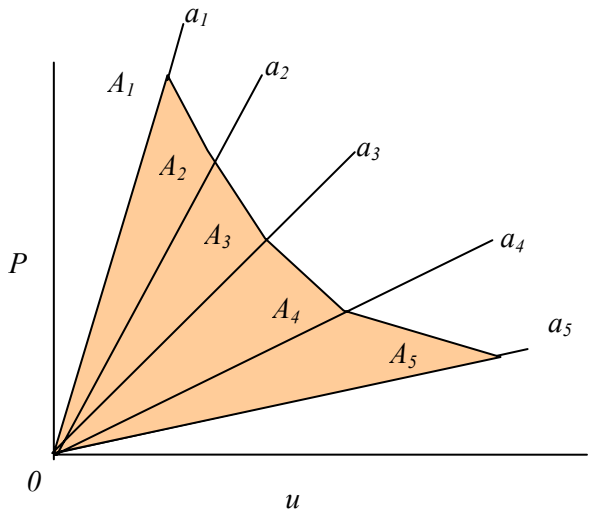

Figure 7.4 Load-displacement response of a cracked plate to crack propagation with crack lengths $a_1 < a_2 < a_3 < a_4 < a_5$.

In an experimental determination of G, the locations of different crack lengths are recorded on the P-u output and the corresponding radial stiffness lines $0A_i$ are drawn for finding areas. The linear elastic behaviour of the cracked plate is verified by unloading if P-u follows the radial stiffness lines.

7.3.4 $G - a$ representation

The elastic energy release rate (G) may be represented as a function of crack length (a) as shown in **Figure 7.5**. It is given by [see Equation (13) and (14)]

$$G = \frac{\pi a \sigma^2}{E} k \tag{7.18}$$

where $k=1-\nu^2$ for plane strain and $k=1$ for plane stress. **Figure 7.5** shows three different stresses $\sigma_3>\sigma_2>\sigma_1$ for various crack lengths. According to Equation (7.18) at a given stress σ_1, G linearly increases with increasing crack length and reaches a critical point for fracture ($G= G_c$). At a lower stresses (σ_2 and σ_3), though, longer crack lengths are required to reach the same critical point for fracture ($G= G_c$).

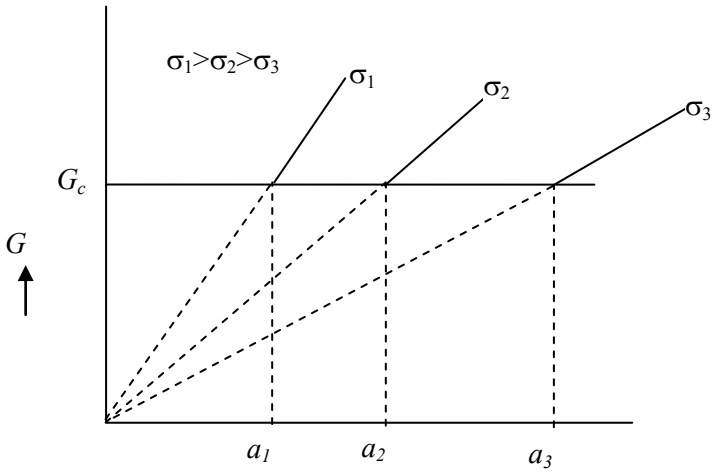

Figure 7.5 The elastic energy release rate (G) versus crack length (a) for a crack of length $2a$ in an infinite plate subjected to a uniform stress σ, perpendicular to the crack axis.

7.4 Analytical Approach

The analytical approach is based on the energy balance principles. From Equation (7.7)

$$G = \frac{\partial W}{\partial A} - \frac{\partial \Lambda^e}{\partial A} = \frac{\partial \Gamma}{\partial A} \qquad \text{(bis 7.7)}$$

we find that

$$Pdu = d\Lambda + GdA\,. \qquad (7.19)$$

The Λ without the subscript e denotes the elastic strain energy unless otherwise stated. The Pdu in Equation (7.19) represents dW, the infinitesimal amount of external work done, during the crack area growth (dA), and ($d\Lambda$ + GdA) the internal work done for strain energy and crack growth. Equation (7.19) is the basis for the following derivations.

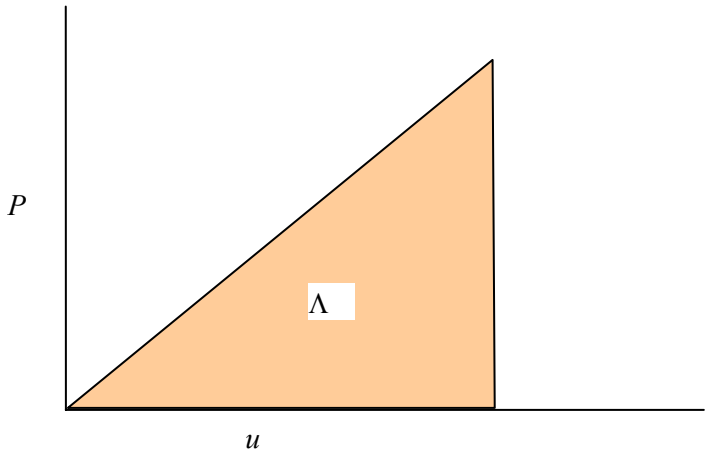

Figure 7.6 Stain energy in a linear elastic system.

In a linear elastic system, the strain energy (Λ) is the triangular area under a given stiffness line (**Figure 7.6**) so that

$$d\Lambda = d\left(\tfrac{1}{2} Pu\right). \qquad (7.20a)$$

Thus, from Equation (7.19) for the applied force P and associated displacement u, we find,

$$Pdu = \tfrac{1}{2}\left(Pdu + udP\right) + GdA \qquad (7.20b)$$

or

$$Pdu - udP = 2GdA\,. \qquad (7.20c)$$

Dividing both sides by P^2, we have

$$\frac{d(u/P)}{dA}=\frac{2G}{P^2} \tag{7.21a}$$

or

$$G=\frac{P^2}{2}\frac{d\left(\frac{u}{P}\right)}{dA} \tag{7.21b}$$

Equation (7.21) is practically useful for the fracture toughness determination. The derivative $\frac{d\left(\frac{u}{P}\right)}{dA}$ in the equation is the rate of change of (u/P) with respect to crack area. In other words it represents the slopes of the curve in **Figure 7.7 (b)**. It can be found experimentally using multiple specimens for a series of different crack lengths as shown for sequence in **Figure 7.7**. The specific work of fracture (R) is equal to G_c for linear elastic fracture and given by

$$R = G_c = \frac{P_c^2}{2}\left[\frac{d\left(\frac{u}{P}\right)}{dA}\right]_{P=P_c} \tag{7.21c}$$

where P_c is the fracture load at a crack length a_6 (**Figure 7.7**).

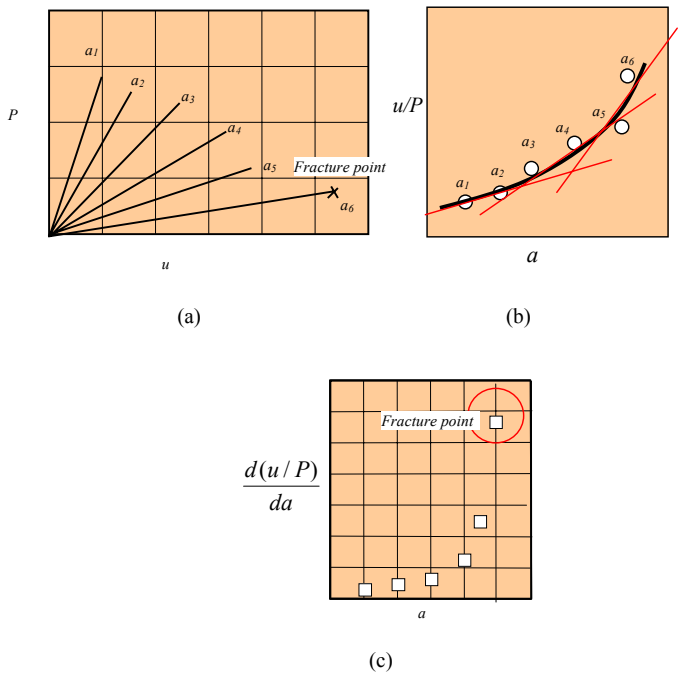

Figure 7.7 Analysis for experimental results from multiple specimens for different crack lengths: (a) a series of stiffness lines for different crack lengths; (b) compliance (u/P) versus crack length; and then (c) $d\left(\frac{u}{P}\right)/dA$ versus crack length with a critical value at fracture.

More analytical expressions can be derived from Equation (7.19) for quasi static linear elastic cracking. They are

$$u_c^{\,2} = \frac{-2R}{\left[\dfrac{d\left(P/u\right)}{dA}\right]_{P=P_c}} \tag{7.22a}$$

$$R = \frac{P_c}{2}\left[\frac{\partial u}{\partial A}\right]_{P=P_c} \tag{7.22b}$$

$$R = -\frac{u_c}{2}\left[\frac{\partial P}{\partial A}\right]_{u=u_c} \tag{7.22c}$$

$$R = \left[\frac{\partial\left(\frac{1}{2}Pu\right)}{\partial A}\right]_{P=P_c} = \frac{P_c}{2}\left[\frac{du}{dA}\right]_{P=P_c} \tag{7.22d}$$

$$R = \left[\frac{-\partial\left(\frac{1}{2}Pu\right)}{\partial A} \right]_{u=u_c} = -\frac{u_c}{2}\left[\frac{dP}{dA}\right]_{u=u_c}. \tag{7.22e}$$

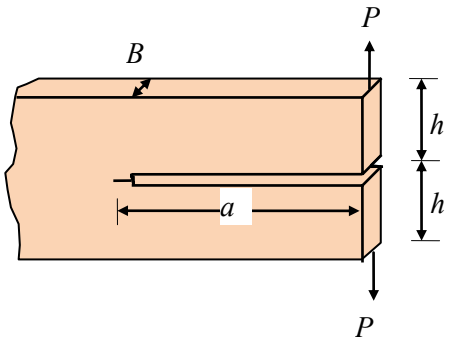

Figure 7.8 DCB Specimen

If the compliance (u/P) is theoretically known, a single specimen instead of multiple specimens may be sufficient for the fracture toughness determination. For example, the compliance of a double cantilever beam (DCB) specimen shown in **Figure 7.8** is determined using the deflection formula for a cantilever beam. The theoretical compliance is given by

$$\frac{u}{P} = \frac{a^3}{3EI} \times 2 \tag{7.23a}$$

so that

$$\frac{d(u/P)}{dA} = \frac{2a^2}{EIB}. \tag{7.23b}$$

Using Equation (7.21c), we find the critical fracture load (P_c) as

$$P_c^2 = \frac{REIB}{a^2}. \tag{7.23c}$$

7.5 Non-linear elastic behaviour

The non-linear elastic behaviour may be analyzed using the same energy principles. The symbol J is commonly used for non-linear rate of change of potential energy with respect to crack area to be distinguished from G (strain energy release rate) for linear behaviour. When quasi-static fracture occurs, J or G has the critical value J_C or G_C which exactly matches the specific work of fracture given by R. Accordingly,

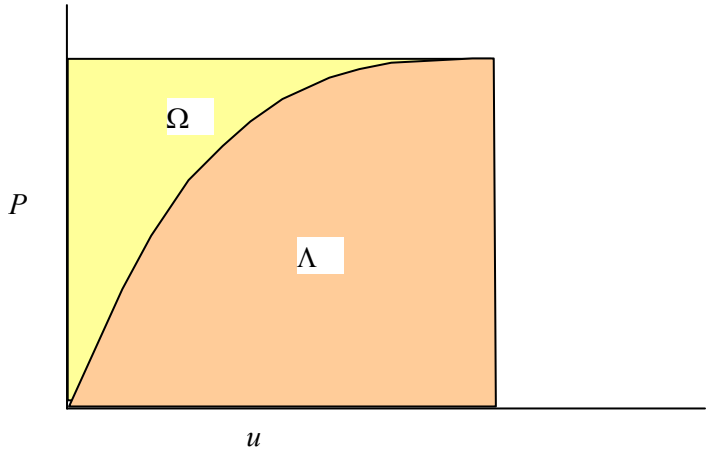

Figure 7.9 The strain energy (Λ) and complementary strain energy (Ω).

$$Pdu = d\Lambda + GdA \tag{bis 7.19}$$

is rewritten as

$$Pdu = d\Lambda + JdA \tag{7.24}$$

for non-linear elastic cracked bodies. The strain energy (Λ) for a non-linear elastic cracked body (**Figure 7.9**) is given by

$$\Lambda = \int Pdu \tag{7.25}$$

and the complementary strain energy (Ω) is given by

$$\Omega = \int udP\,. \tag{7.26}$$

From W = Pu – Λ and Equation (7.24), we have

$$udP = d\Omega - JdA \tag{7.27}$$

From Equations (7.27) and (7.24), we have

$$J = \left(\frac{\partial \Omega}{\partial A}\right)_{P=const} \tag{7.28a}$$

and

$$J = -\left(\frac{\partial \Lambda}{\partial A}\right)_{u=const} \tag{7.28b}$$

respectively.

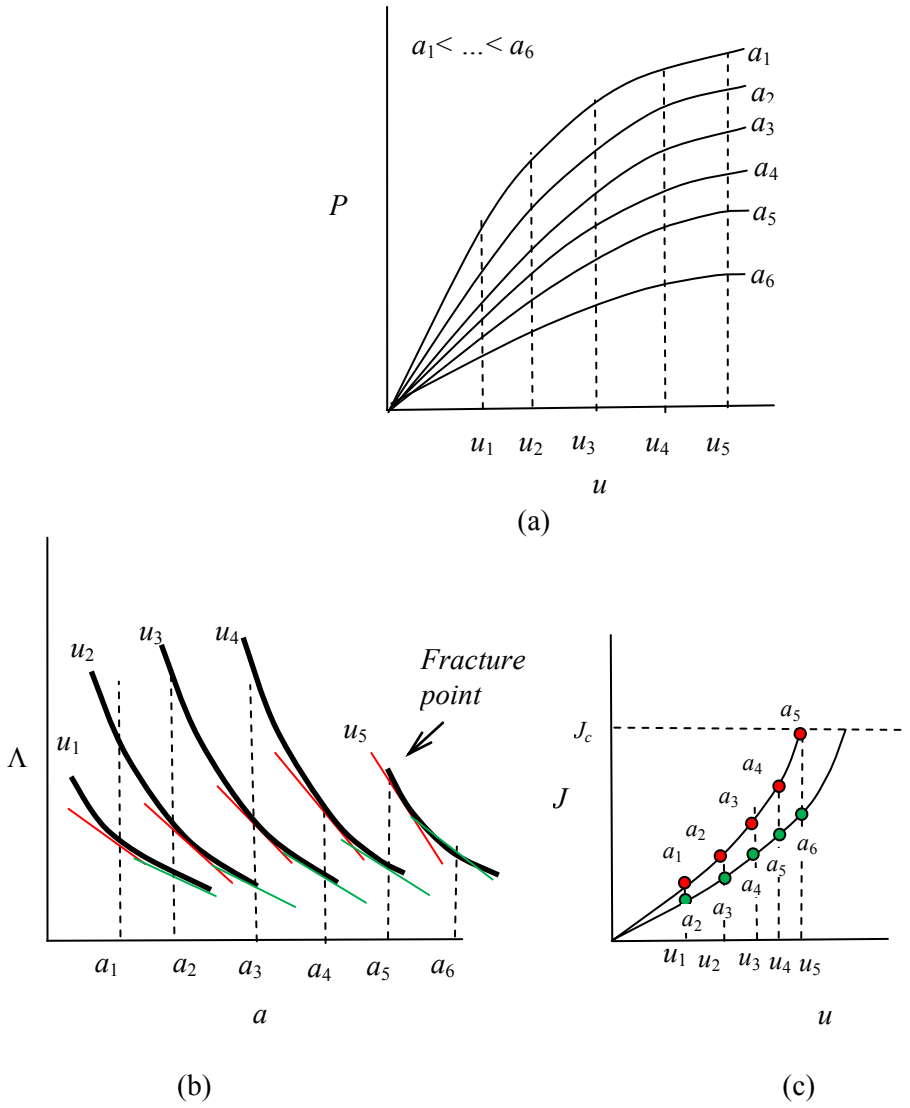

Figure 7.10 Analysis for experimental results from multiple specimens for different crack lengths: (a) a series of curves for strain energy from different crack lengths; (b) strain energy versus crack length; and then (c) *J* versus displacement (*u*) with a critical value at fracture (J_c).

Equation (7.28) form the basis for the experimental determination of *J* and *Jc*. The quantity of $\frac{\partial \Lambda}{\partial A}$ in Equation (7.28b) is the rate of change of strain energy with respect to crack area ($A=Ba$). Accordingly, the strain energy (Λ) is obtained from *P*-*u* curves [**Figure 7.10(a)**] for a constant displacement (u) to construct a strain energy versus crack length (a) diagram shown in **Figure 7.10(b)**. Then, the values for $\frac{\partial \Lambda}{\partial a}$ is plotted as shown in **Figure 7.10(c)**. The value of J_c corresponds to the point of fracture.

If the non-linear elastic behaviour can theoretically be characterized by a power relation

$$C_n = \frac{u^n}{P} \tag{7.29a}$$

where n is a constant, the strain energy (Λ) is given by

$$\Lambda = \int P du = \int \frac{U^n}{C_n} du \tag{7.29b}$$

Also, from Equation (7.24), we find,

$$J = \frac{1}{1+n}\left[nP\frac{du}{dA} - u\frac{dP}{dA}\right] \tag{7.30}$$

and we have J in terms of C_n,

$$J = \frac{1}{1+n} P^{(1+n)/n} C_n^{1/(1-n)} \frac{dC_n}{dA} = \frac{1}{1+n}\frac{u^{1+n}}{C_n^2}\frac{dC_n}{dA}. \tag{7.31}$$

For n = 1, we recover the linear elastic parameter (G),

$$G = \frac{P^2}{2}\frac{d\left(\frac{u}{P}\right)}{dA}. \tag{bis 7.21b}$$

7.6 Crack growth resistance curve (*R-curve*)

It is possible that, as the crack grows under loading, much more energy is consumed in the plastic deformation under plane stress than under plain strain condition. Also, such a plastic deformation takes place as the crack grows. The crack resistance (R) curve is useful for describing the crack growth involving a relatively large plastic deformation. The theoretical basis is found from Equation (7.5) and R is defined as

$$R = \frac{\partial \Gamma}{\partial A} + \frac{\partial \Lambda^p}{\partial A}. \tag{7.32}$$

The crack resistance (R) consists of the energy consumption rate for crack surface creation and the rate of plastic strain work as previously discussed.

In the case of plane strain or small plastic deformation,

$$R = G_c \left(= \frac{\partial W}{\partial A} - \frac{\partial \Lambda^e}{\partial A} \right) \tag{7.33}$$

and G_c or R is a constant as shown in **Figure 7.11(a)**. Otherwise, R increases non-linearly as shown in **Figure 7.11(b)**. The R-curve is known as a unique property independent of the initial crack size and the geometry of the specimen.

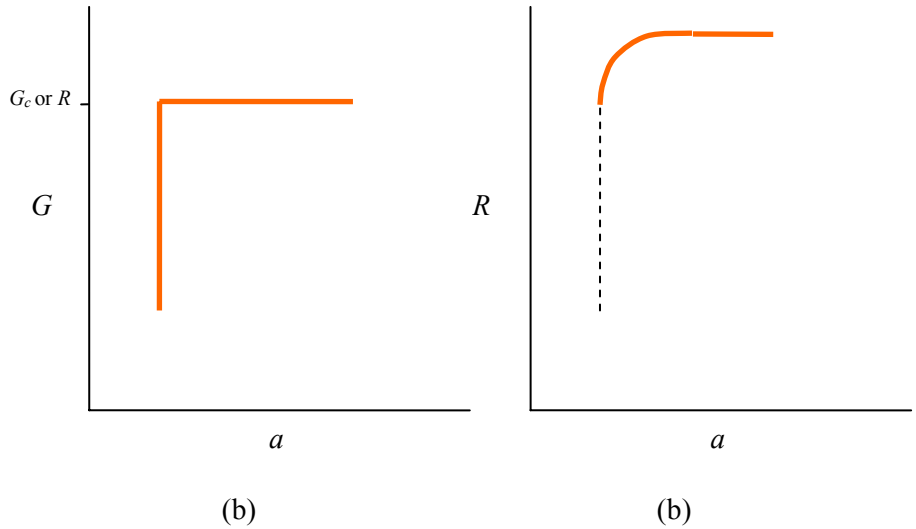

Figure 7.11 Typical load (P)-crack length (a) curves for: (a) plane strain and (b) plane stress.

7.6 *R*-Curve and stability

The rate at which strain energy may be released depends on the geometry of a cracked body and the conditions of loading. **Figure 7.12** shows an *R*-curve and a set of radial lines of slope $\left(\frac{\partial G}{\partial a}\right)_\sigma = \tan^{-1}\left(\frac{\pi\sigma^2}{E}\right)$ for the geometry of a small crack in a large sheet for which $G = \frac{\pi\sigma^2 a}{E}$ is applicable. (The radial lines for some cracked body geometri es would not necessarily be straight if a geometry factor is considered.) The slope increases as the applied stress (σ) increases. As the stress increases from zero, the available G increases from point A to point B without the crack growth. The point B represents the minimum fracture toughness of the material before any subsequent increase in R along the R-curve. Cracking can thus commence at point B stably. We may compare the set of radial lines of slopes represented by $\left(\frac{\partial G}{\partial a}\right)_\sigma$ with the other set of slopes represented by $\frac{dR}{da}$ which is independent of the initial crack length (a_0). At point B, and we see that

$$\frac{dR}{da} > \left(\frac{\partial G}{\partial a}\right)_{\sigma=\sigma_B} . \tag{7.34a}$$

As the R increases, the slope $\left(\frac{\partial G}{\partial a}\right)_\sigma$ also increases. As the crack further grows quasi-statically under increasing load, point C is reached. At point C, we find that

$$\frac{dR}{da} = \left(\frac{\partial G}{\partial a}\right)_{\sigma=\sigma_c} . \tag{7.34b}$$

The crack growth between point B and point C is stable because of the balance between energy consumption rate and energy supply rate. However, beyond point C along the R-curve, we find that

$$dR/da < \left(\partial G/\partial a\right)_\sigma \tag{7.34c}$$

representing an instability condition because of the higher energy supply rate than the energy consumption rate. The part of the R curve beyond C at which and $a = a_c$ is not observable with the given geometry unless a longer initial crack (a_0) or a stable geometry is used.

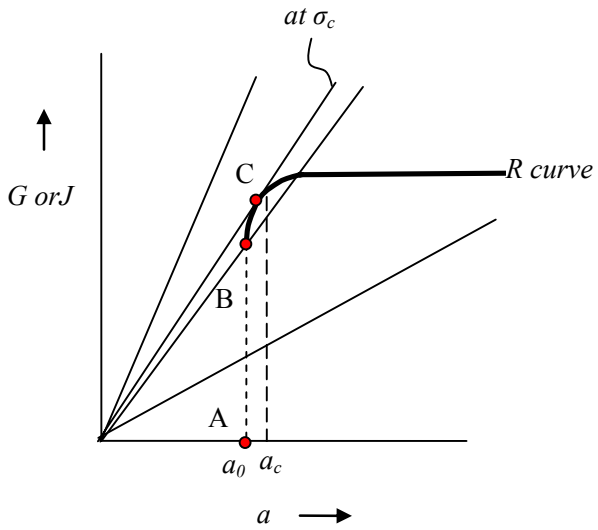

Figure 7.12 *G* versus *a* curve for constant applied stress σ; *R* versus *a* curve is also superimposed.

7.7 Geometric stability factors in elastic fracture

The cracking stability is also dependent on the testing machine type because the testing machine itself stores the strain energy and/or the energy balance is not exactly maintained unless a special control circuitry is used for controlling a crosshead. In practice, there are two typical types of testing machines viz displacement controlled machines and load controlled machines (**Figure 7.13**). The increment of the crosshead (*du*) in a displacement controlled machine is always positive because it does not reverse the loading direction during testing. In a load controlled machine, on the other hand, the increment of load (*dP*) is always positive.

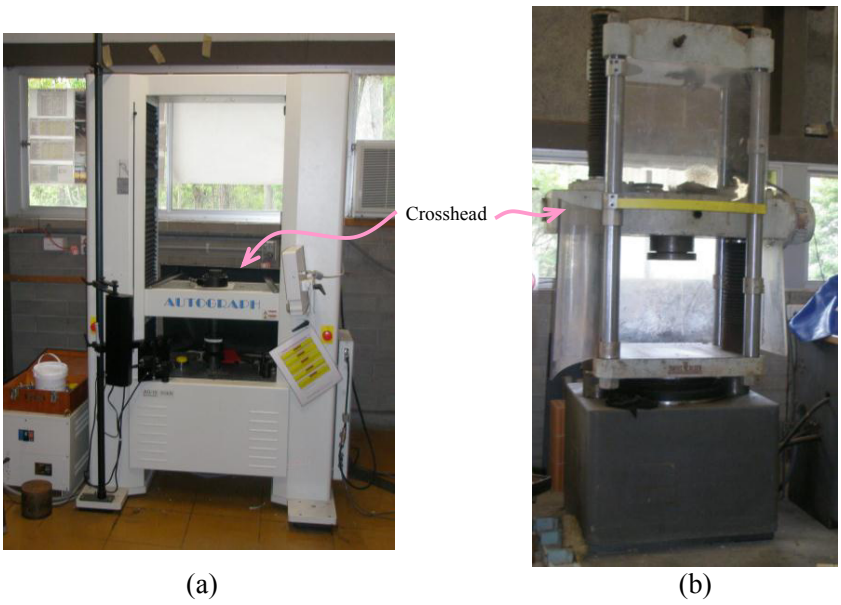

Figure 7.13 Testing machines: (a) Displacement controlled; and (b) load controlled.

We may consider the following equation for a linear elastic cracked plate,

$$P_c^2 = \frac{2R}{\dfrac{d\left(\dfrac{u}{P}\right)}{dA}}. \qquad \text{(bis 7.21c)}$$

Since R may vary during the crack propagation, the variation of R with respect to incremental input P and output A (thickness × crack length a) is obtained by differentiating Equation (7.21c) to have

$$\frac{2}{P}\left(\frac{dP}{dA}\right) = \frac{1}{R}\frac{dR}{dA} - \frac{\dfrac{d^2(u/P)}{dA^2}}{\dfrac{d(u/P)}{dA}}. \qquad (7.35)$$

For stability in a *load controlled testing machine*, the condition $dP > 0$ applies so that

$$\frac{1}{R}\frac{dR}{dA} \geq \frac{\dfrac{d^2(u/P)}{dA^2}}{\dfrac{d(u/P)}{dA}} = \frac{\dfrac{d^2(P/u)}{dA^2}}{\dfrac{d(P/u)}{dA}} - 2\frac{\dfrac{d(P/u)}{dA}}{(P/u)}. \qquad (7.36)$$

Similarly, from Equation (7.22a)

$$u^2 = \frac{2G}{\frac{d\left(\frac{P}{u}\right)}{dA}} \qquad \text{(bis 7.22a)}$$

for stability in a *displacement controlled testing machine* (du > 0), we find

$$\frac{1}{R}\frac{dR}{dA} \geq \frac{\frac{d^2(P/u)}{dA^2}}{\frac{d(P/u)}{dA}} = \frac{\frac{d^2(u/P)}{dA^2}}{\frac{d(u/P)}{dA}} - 2\frac{\frac{d(u/P)}{dA}}{(u/P)}. \qquad (7.37)$$

In the equation, $\frac{d(P/u)}{dA}$ is negative if the stiffness decreases with increasing crack length. In the right hand sides of Inequalities (7.36) and (7.37), $\frac{1}{R}\frac{dR}{dA}$ is called the *geometry stability factor* (*GSF*) of a test specimen. It can be calculated for the stability. For example, for a DCB specimen is calculated to have $d/dA(P/u) = -9EI/2a^4B$ and $d^2/dA^2(P/u) = 36EI/2a^5B^2$ to give

$$\frac{1}{R}\frac{dR}{dA} > \frac{4}{A}$$

for stability in a displacement controlled testing machine. If R is constant in this condition, *GSF* becomes zero and accordingly the stability condition becomes $0 > -4/A$. Therefore, the DCB specimen satisfies the stability condition. If a test specimen does not satisfy the stability condition, instability of cracking is expected. Sometimes it may be possible that test specimens with satisfied stability conditions have instabilities if the crack front is blunt.

Also, the *GSF* can be calculated using a stress intensity factor relation with G ($G_I = K_I^2/E$) for plane stress. From Equation (7.21b), we obtain

$$K_I^2 = EG_I = \left(\frac{EP^2}{2B}\right)\frac{d(u/P)}{da} = Y^2\sigma^2\pi a \qquad (7.38)$$

where Y is the geometry factor. Accordingly, for displacement controlled machine

$$\frac{1}{R}\frac{dR}{da} \geq \frac{1}{a}\left(1 + \frac{2aY'}{Y}\right) - \frac{2Y^2 a}{\int_0^a Y^2 a\, da} \qquad (7.39a)$$

and for load controlled machine

$$\frac{1}{R}\frac{dR}{da} \geq \frac{1}{a}\left(1 + \frac{2aY'}{Y}\right) \qquad (7.39b)$$

where $Y' = dY/da$.

7.8 Testing machine stiffness

The total deflection (u^*) of the system including test specimen and testing machine is given by

$$u^* = u + CP \tag{7.40}$$

where C is the compliance of testing machine. It is found that

$$\frac{d\left(\frac{u^*}{P}\right)}{dA} = \frac{d\left(\frac{u}{P}\right)}{dA} \tag{7.41a}$$

and

$$\frac{d^2\left(\frac{u^*}{P}\right)}{dA^2} = \frac{d^2\left(\frac{u}{P}\right)}{dA^2} \ . \tag{7.41b}$$

Therefore, it follows from Equation (7.36) that the stability of test specimen in the load controlled machine is unaffected by the flexibility of the testing machine. However, the situation is different under $du > 0$ for displacement controlled machine, as $P/u \neq P/u^*$. Now, we have for, $du > 0$,

$$P/u^* = \frac{(P/u)}{1 + C(P/u)} \tag{7.41c}$$

so that

$$\frac{d(P/u^*)}{dA} = \frac{\frac{d(P/u)}{dA}}{[1+C(P/u)]^2} \tag{7.41d}$$

and

$$\frac{d^2(P/u^*)}{dA^2} = \frac{[1+C(P/u)]\frac{d^2(P/u)}{dA^2} - 2C\left[\frac{d(P/u)}{dA}\right]^2}{[1+C(P/u)]^3} \ . \tag{7.41e}$$

Therefore,

$$\frac{1}{R}\frac{dR}{dA} > \frac{\frac{d^2(P/u)}{dA^2}}{\frac{d(P/u)}{dA}} - \frac{2C\frac{d(P/u)}{dA}}{1+C(P/u)} \ . \tag{7.42}$$

Inequality (7.42) may be compared with Inequality (7.37) for testing machine stiffness effect on the stability. For increasing crack length, $\frac{d(P/u)}{dA}$ is negative and hence the value of right hand side of the Inequality (7.42) increases due to the additional term. Therefore, the stability is decreased by the flexibility of the testing machine.

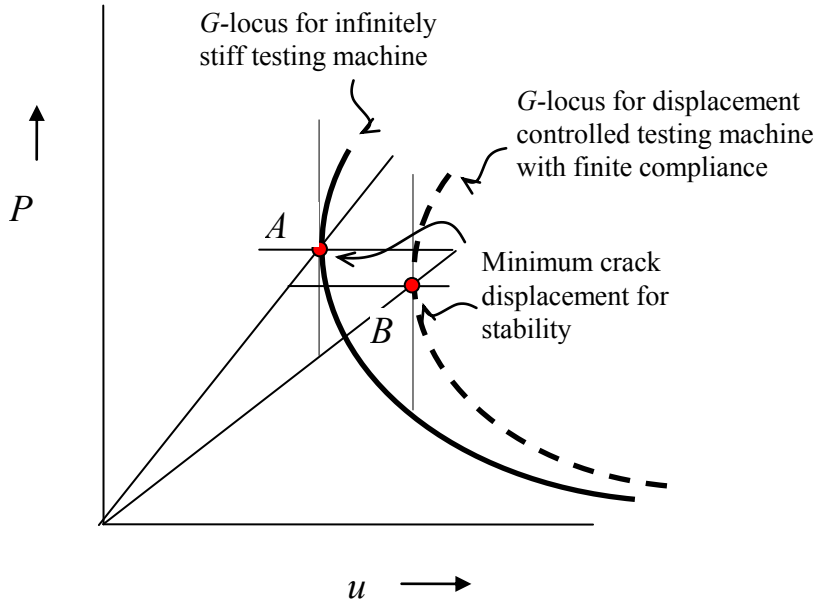

Figure 7.14 Effect of machine stiffness on load -deflection diagram and on *R*-locus.

The testing machine stiffness effect is illustrated in load (P)-displacement (u) diagram given in **Figure 7.14**. Two G-loci are shown: one for infinitely stiff testing and the other for displacement controlled testing machine with a finite compliance. Points A and B indicate the transition between crack lengths for stability in infinitely stiff testing machine and displacement controlled testing machine respectively. They also indicate the minimum crack displacements. Point B lies on a longer crack length with a lower load for transition than point A. It is noted that, for a constant load, the energy stored in a testing machine with a finite compliance is larger than that with infinitely stiff testing machine.

7.9 Essential work of energy

Resistance to tear is one of important mechanical properties of flexible materials such as thin polymer sheets, rubbers, etc. The trousers test under mode III loading has drawn attention for material evaluation since Rivlin and Thomas[21] considered trouser tear criterion for rubbers. Joe and Kim[22] analysed the load–displacement records to determine the critical J-integral (or just J) value and crack resistance (R). The determination of the critical J value, however, requires the detection of the crack initiation which is not an easy task for highly deformable materials. Alternatively, the resistance to tear may be evaluated using the essential work of fracture (EWF) approach which was first developed for mode I fracture of ductile metals[23]. The EWF approach was further developed by Mai and Cotterell[24] for elasto-plastic fracture of thin metal sheets under mode III loading using trouser specimens with various widths, taking into account the work done in plastic bending and unbending of the trousers. Muscat-Fenech and Atkins[25] expanded this Mai and Cotterell's work for a wide range of specimen dimensions and geometric change. For tearing of polymer sheets, however, the work for plastic bending and un-bending of the trousers is negligible due to their low stiffness, and deformation reflected in the model for metals cannot be translated into that for the tearing of thin polymer sheets.

Wong et al.[26] proposed a two-zone model for deformation and tearing behaviour of thin polymer sheets under mode III loading. In the first zone, which is called zone A in their paper and is adjoining the initial crack tip, the outer plastic zone height lineally increases with the torn ligament and thus the zone is of triangular shape. At the end of zone A, the deformation enters zone B. The height of the zone B remains constant with further increase of torn ligament length. The zone A, though, did not consider plastic deformation caused by loading prior to tearing (which is referred to as initial plastic zone in the paper). The two-zone model hence would lead to overestimation of EWF if tearing is the case where increasing height of the initial plastic zone does not coincide with that of subsequently following zone B. In the light of the deficiency, Kim and Karger-Kocsis[27] developed a three-zone model for tear fracture under mode III loading to include the initial plastic deformation and analysis based on the EWF approach for prediction of overall tear resistance. In tearing of thin ductile polymeric sheets, mode III fracture mode is expected at the beginning of loading but the mode tends to be mode I later so that tearing becomes virtually mixed mode. In this section, the three-zone model for tear fracture under mode III loading will be introduced.

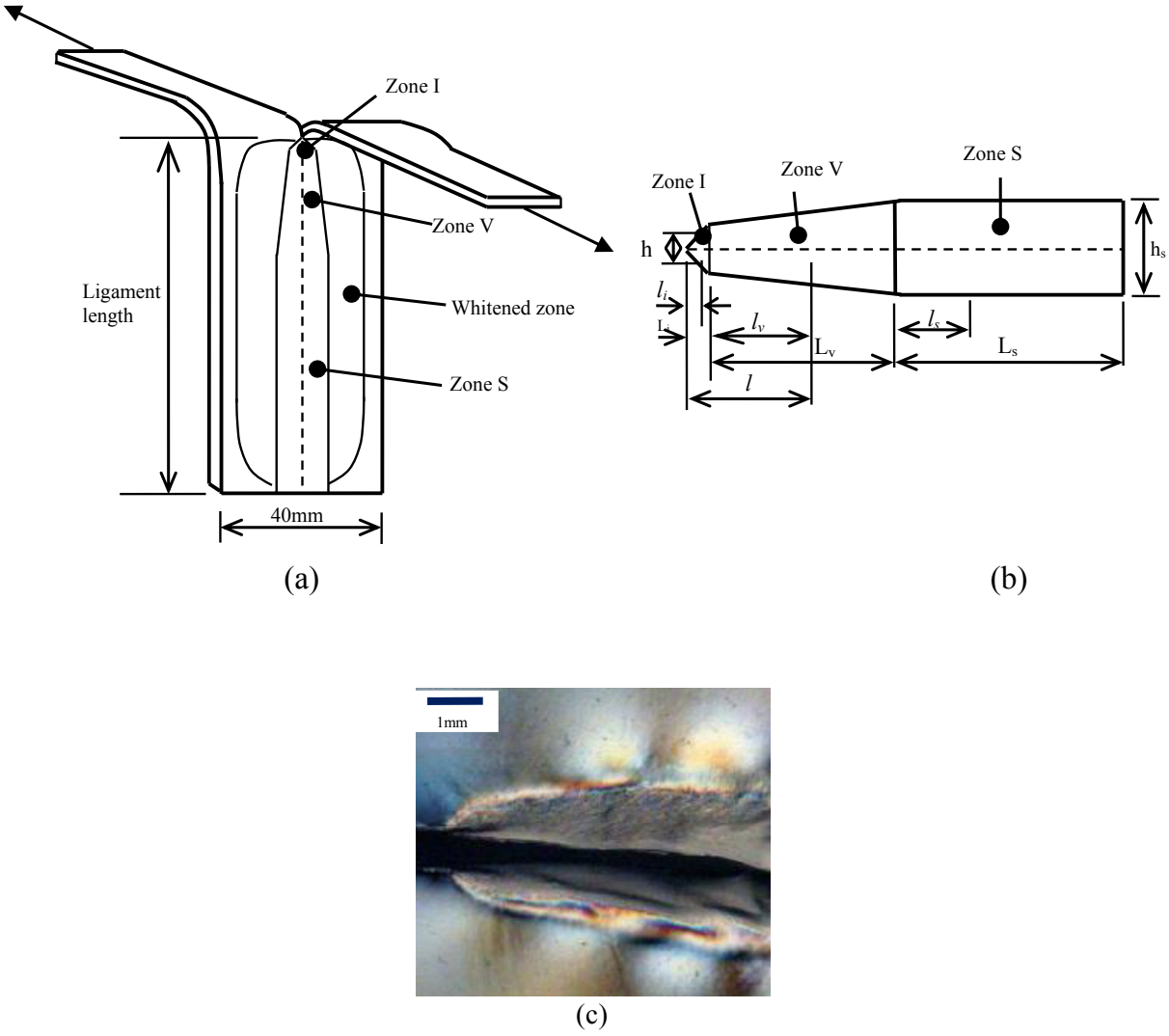

Figure 7.15 (a) Configuration of trousers test. (b) Plastic zone model consisting of zones I, V and S for tear specimens with sufficiently long ligaments. (c) Polarised light microscopic image for plastic deformation in PET (0.25 mm thick) near the crack tip showing zones I and V. [After Kim and Karger-Kocsis, 2004][28]

As schematically indicated for a specimen with sufficiently long ligament in **Figure 7.15** (if the ligament is not long enough, only partial deformation occurs), generally two different types of deformation appear along the torn ligament after tearing. One is plastic deformation and the other characterized by whitening. The whitening, accompanied by a weak change of transparency, is found in some polymers and is of non-plastic deformation as seen in a polarized image along the torn ligament – note photo-elastic fringe pattern does not appear in plastic deformation. Also it did not cause any visible change in the surface texture of the specimens. This indicates that its deformation energy would be small compared to the plastic deformation which requires relatively large deformation energy as expected.

Therefore, the whitened zone is not included in the model formulation despite its considerable size. The plastic zone is found to have three distinctive zones as detailed in **Figure 7.15**. The three zones will be referred to as: zone I (initial), zone V (v-shape) and zone S (saturation). Zone I is initially formed as loading increases prior to the crack propagation. After zone I fully developed, the following events took place sequentially to form zone V: (a) change of specimen configuration as a result of further lining up of the trouser legs with increasing load; (b) change in the fracture mode from mode III to mode I to include more mode I component due to rotation of the area around the crack tip; and (c) gradual increase in duration of straining applied to the plastic zone around the crack tip as a result of increase in plastic deformation size as the tear progresses at an almost constant speed (e.g. material at $l = L_v$ is subjected longer straining time than that at $l = L_i$ because material at $l = L_v$ is strained and plastically deformed more ahead in time before the crack tip arrives at it than material at $l = L_i$). Thus, the zone V is the result of an evolutionary process before it saturates. The height (h) of zone V continues to extend as the crack propagates until it reaches zone S where the plastic deformation is stabilized and thus the height (h) becomes constant. Based on the deformation described above, the following analysis is given. The total work of fracture (W_f) for a pre-cracked test specimen can be generally divided into two components:

$$W_f = W_e + W_p \tag{7.43}$$

where W_e is the energy for yielding and tearing of the inner fracture process zone, which is referred to as the essential work, and W_p is the work for the outer plastic deformation zone which is geometry dependant, non-essential work.

For $0 < l_i < L_i$,

the total work of fracture (W_{if}) for a specimen with a ligament length of l_i is given for zone I as

$$W_f = W_{if} = W_{ie} + W_{ip} = w_{ie} l_i t + w_{ip} A_i t \tag{7.44a}$$

where subscript 'i' indicates zone I, w_{ie} is the specific EWF, w_{ip} is the specific non-EWF, t is the thickness and A_i is the outer plastic deformation zone area given by

$$A_i = l_i h/2 = l_i^2 . \tag{7.44b}$$

This equation considers the fact that the profile of the initial plastic zone is inclined approximately 45° to the tear path. Although different materials might have different angles, it appears reasonable for approximation. Thus,

$$W_{if} = w_{ie} l_i t + w_{ip} l_i^2 t \tag{7.44c}$$

or

$$w_f = w_{if} = \frac{W_{if}}{l_i t} = w_{ie} + w_{ip} l_i \tag{7.44d}$$

where w_{if} is the specific total work of fracture. In practice, it is difficult to use this equation for determination of w_{ie} because l_i is often too small to be varied in test specimens. The total work of fracture (W_{vf}) for a specimen with a ligament length of ($L_i + l_v$) can similarly be written for zone V as

$$W_f = W_{vf} = W_{ve} + W_{vp} = w_{ve}(L_i + l_v)t + w_{vp} A_v t \tag{7.45a}$$

for $0 < l_v < L_v$ where subscript 'v' indicates zone V and the outer plastic zone area (A_v) is obtained as

$$A_v = L_i^2 + 2L_i l_v + \alpha l_v^2 \tag{7.45b}$$

where α is the taper angle given by

$$\alpha = \frac{h_s - 2L_i}{L_v} \tag{7.45c}$$

where h_s and L_i would be directly measured from specimens after testing or L_v can be estimated from a plot of specific total work of fracture versus ligament length of specimen if it is difficult to be identified under a microscope. The specific total work of fracture (w_{vf}) in this case becomes

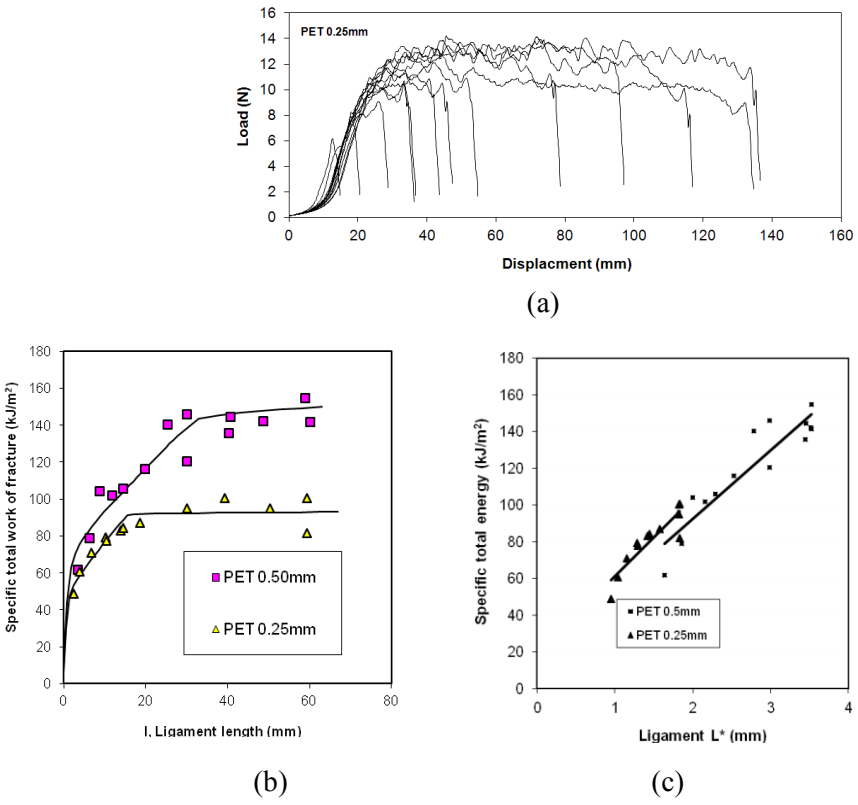

Figure 7.16 PET with a thickness of 2.5 mm for essential work of fracture: (a) load-displacement curves; (b) specific total work of fracture as a function of torn ligament length obtained from both experiments and predictions based on Equations (7.44d), (7.45e) and (7.46b); and (c) linear plots with the least square lines for data shown in '(a)' using L^* which is $(L_i^2+2L_il_v+al_v^2)/(L_i+l_v)$ for V zone data or $(L_i^2+2L_iL_v+aL_v^2+h_sl_s)/(L_i+L_v+l_s)$ for S zone data. [After Kim and Karger-Kocsis, 2004]

$$w_f = w_{vf} = \frac{W_{vf}}{(L_i + l_v)t} = w_{ve} + \frac{w_{vp}(L_i^2 + 2L_i l_v + \alpha l_v^2)}{L_i + l_v} \tag{7.45d}$$

where w_{vp} and w_{ve} can be found by the linear regression analysis using a plot of w_{vf} versus $(L_i^2 + 2L_i l_v + \alpha l_v^2)/(L_i + l_v)$. For $l = L_i$ or $l_v = 0$, this equation becomes

$$w_{vf} = w_{ve} + w_{vp} L_i \,. \tag{7.45e}$$

The total work of fracture (W_{vf}) for a specimen with a ligament length of ($L_i + L_v + l_s$) can similarly be given for zone S as

$$A_s = L_i^2 + 2L_i L_v + \alpha L_v^2 + h_s l_s \tag{7.46a}$$

so that

$$w_f = w_{sf} = \frac{W_f}{(L_i + L_v + l_s)t} = w_{se} + w_{sp} \frac{L_i^2 + 2L_i L_v + \alpha L_v^2 + h_s l_s}{L_i + L_v + l_s} \tag{7.46b}$$

where w_{sp} and w_{ve} can be found by linear regression analysis using experimental data from specimens with ligament length longer than ($L_i + L_v$) for a plot of w_{sf} versus $\frac{L_i^2 + 2L_i L_v + \alpha L_v^2 + h_s l_s}{L_i + L_v + l_s}$ but preferably the data can be combined with those for $0 < l_v < L_v$ if a full range of data is used. The intercepts and slopes can be used for w_e ($=w_{se} = w_{ve}$) and w_p ($=w_{sp} = w_{vp}$) respectively in a linear plot (see **Figure 7.16**).

7.10 Impact fracture toughness

Structural materials used for functioning components are very likely subjected to impact loading. Accordingly, impact strength is often the deciding factor in materials selection for such an application. The impact test methods in general may fall into two categories according to the relative amounts of energy between striker and specimen viz: (a) *limiting energy methods*, in which the striker energy is adjusted until a set damage to specimen is found; and (b) *excess energy methods*, in which the kinetic energy of the striker is always greater than the energy required to break the specimens. The falling weight test falls into the first category, and the Charpy, Izod and tensile impact tests typically fall into the second.

The conventional test methods have the advantages of being easily and rapidly performed. However, their results are dependent on the notch size. The problem of specimen geometry dependence can be approached in different ways based on the fracture mechanics. One of the ways is to obtain force (P) – displacement (u) curves from a single specimen test with instrumented striker. The other way is to make variations in notch depth with a sharp radius for multiple specimens.

In the Charpy test (**Figure 7.17**), a bar specimen is placed on horizontal supports attached to up right pillars for central striking. The impact energy is an amount lost from the kinetic energy of striker for breaking a specimen. The energy measurement in the Izod test is based on the same principle as for the Charpy test. The difference between two tests is that the lower half of a specimen in the Izod test is clamped for cantilever loading. The clamping, though, generates the complex stress field around a notch tip, making it difficult for analysis. In this section, a theory and method based on fracture mechanics for the Charpy impact test will be introduced.

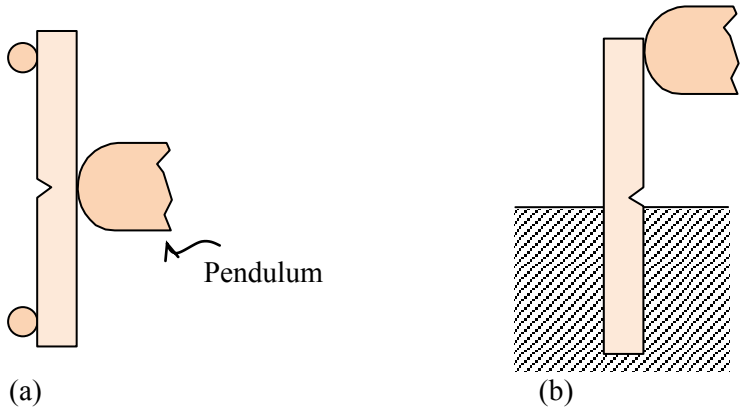

Figure 7.17 Impact test type: (a) Charpy test; and (b) Izod test.

The impact specimen breaks and flies away after being struck by the striker, involving kinetic energy of specimen. The impact energy (Λ_E) measured is hence the sum of elastic strain energy (Λ^e) and kinetic energy of specimen (K_s), i.e.

$$\Lambda_E = \Lambda^e + K_s. \tag{7.47}$$

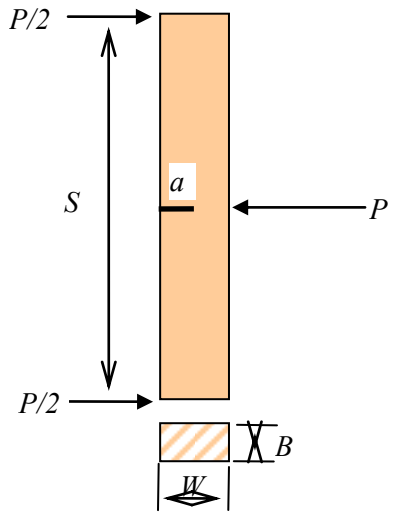

Figure 7.18 Impact specimen with a crack length *a*.

The elastic strain energy (Λ^e) is given by

$$\Lambda^e = \frac{Pu}{2} = \frac{P^2}{2}\frac{u}{P}. \tag{7.48}$$

On the other hand, from the elementary beam theory with the section modulus (Z) and bending moment (M),

$$\sigma = \frac{M}{Z} = \frac{\frac{P}{2}\frac{S}{2}}{\frac{BW^2}{6}} \tag{7.49a}$$

We find that

$$P = \frac{2}{3}\frac{\sigma B W^2}{S}. \tag{7.49b}$$

We know

$$G = \frac{K_I^2}{E}(1-\nu^2) = \frac{Y^2\sigma^2\pi a}{E}(1-\nu^2) = \frac{9\pi}{4}Y^2\frac{P^2S^2a}{B^2W^4E}(1-\nu^2) \tag{7.49c}$$

where Y is a geometry factor. For the three point bend specimen with S=4W:

$$Y\sqrt{\pi} = 1.93 - 3.07\left(\frac{a}{W}\right) + 14.53\left(\frac{a}{W}\right)^2 - 25.11\left(\frac{a}{W}\right)^3 + 25.80\left(\frac{a}{W}\right)^4.$$

In instrumented tests, the peak force P_c is measured and G_{Ic} is found directly from Equation (7.49c). Otherwise, for non-instrumented tests with varying notch depth (**Figure 7.18**), we obtain from

$$G = \frac{P^2}{2}\frac{d\left(\frac{u}{P}\right)}{dA}, \tag{bis 7.21b}$$

that

$$\frac{d\left(\frac{u}{P}\right)}{dA}=\frac{2G_{Ic}}{P_c^2}=\frac{9}{2}\frac{S^2Y^2\pi a}{B^2W^4E}(1-\nu^2) \tag{7.49d}$$

and

$$\frac{u}{P}=\int d\left(\frac{u}{P}\right)+C=\frac{9\pi}{2}\frac{S^2}{B^2W^4E}(1-\nu^2)\int Y^2a+C\,. \tag{7.49e}$$

To determine the integration constant, we use the deflection formula of a simply supported beam for $a = 0$,

$$C=\frac{u}{P}=\frac{1}{4}\frac{S^3}{EBW^3}\,. \tag{7.49f}$$

Substituting Equations (7.49b) and (7.49e) into Equation (7.48), we find a practical formula for an impact test:

$$\Lambda_E=BW\phi G_{IC}+K_s \tag{7.50a}$$

where the factor ϕ can be obtained experimentally or can be calculated from

$$\phi=\frac{\frac{SW}{18}+\pi\int Y^2ada}{Y^2aW}\,. \tag{7.50b}$$

The specific energy release rate (G_{Ic}) is obtained from the slope for a linear regression line as shown in **Figure 7.19**.

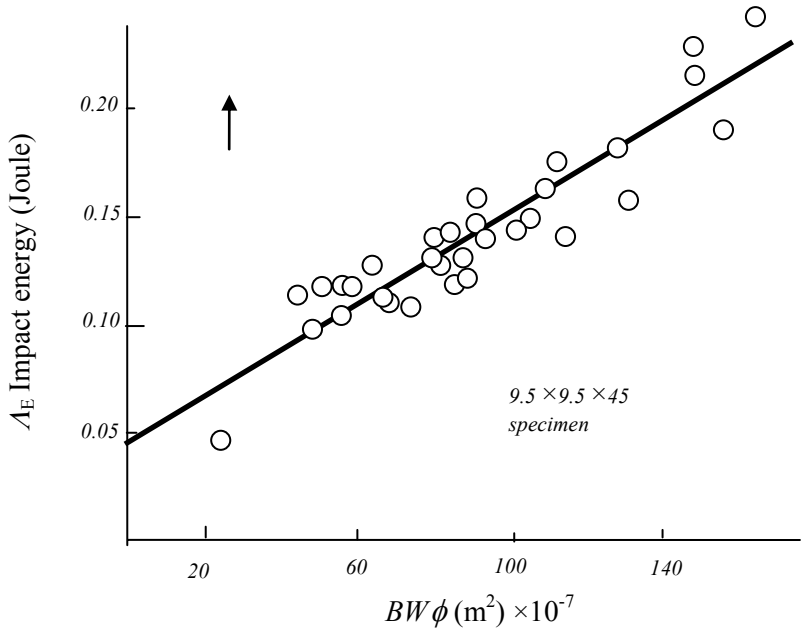

Figure 7.19 Measured energy versus $BW\,\phi$. [After Marshall et al, 1973][29]

8 Fatigue

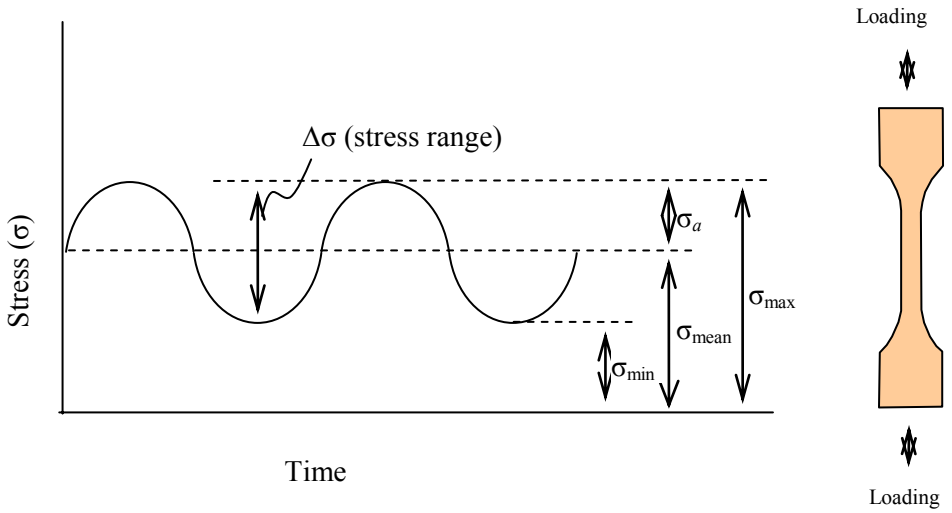

Figure 8.1 Cyclic loading and definitions of terms for applied stress.

Fatigue is the most common cause of service failure in mechanical components and structures. It is a type of damage caused by cracking and deformation. The fatigue failure takes place when subjected to cyclic loading. The stress at the failure is much lower than the static strength. The theories with fatigue have largely been founded on the empiricism with phenomenological analysis since Wohler curve[30] was introduced in 1870. There are two approaches for the fatigue problems viz the stress-life (S-N) curve approach to treat multiple cracks collectively and the stress intensity factor approach to treat cracking individually.

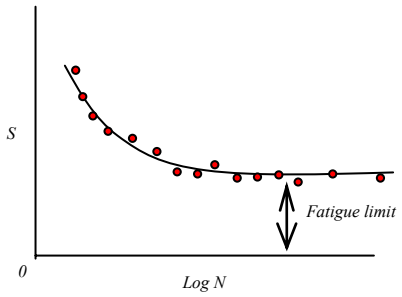

Figure 8.2 Schematic S-N curve.

8.1 Stress-life (S-N) curve approach for un-notched specimen

The fatigue life is measured in a laboratory using parameters such as stress range ($\Delta\sigma$), mean stress (σ_{mean}), minimum stress (σ_{min}), and maximum stress (σ_{max}) as shown in **Figure 8.1**. The test results on unnotched specimens consist of a series of data points obtained from multiple specimens at different stresses. The data points represent a range of different values of σ_{max} or $\Delta\sigma$ corresponding to respective numbers of loading cycles to failure (N) forming a curve known as the S-N curve (**Figure 8.2**). If the S-N curve has a plateau value at a low stress, the stress is called the *fatigue limit* or *endurance limit*. Below the *fatigue limit* if exists, it is considered that the material would last for an infinite number of cycles without failure.

The S-N curve can be affected by various factors such as material surface roughness, applied mean stress, residual stresses, specimen size, loading method (e.g. bending, tension-tension), and temperature. If a S-N curve is used for the life prediction or design of notched components, the notch sensitivity should be taken into account.

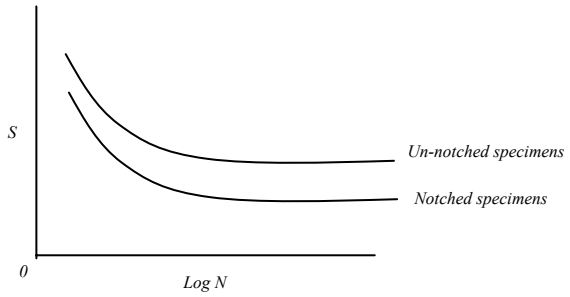

Figure 8.2 Schematic S-N curves for un-notched and notched specimens.

The stress concentration factor (K_t) is defined as

$$K_t = \frac{\text{Maximum stress}}{\text{Average stress}} > 1 \tag{8.1}$$

and can be theoretically obtained. The difference between un-notched specimens and notched specimens for the fatigue limit is schematically shown in **Figure 8.2**. Note that the *average stress* is used for the S-N curve for notched specimens. Now, the *fatigue limit reduction factor* (K_f) due to a notch is defined as

$$K_f = \frac{\text{Fatigue limit for unnotched specimens}}{\text{Fatigue limit for notched specimens}} > 1 \tag{8.2}$$

for the effect of the notch in decreasing the fatigue limit. It is generally observed that K_t is always greater than K_f and therefore the ratio of K_f/K_t is in a range between zero and one i.e.

$$K_t > K_f \tag{8.3a}$$

$$0 < \frac{K_f}{K_t} < 1. \tag{8.3b}$$

The ratio $\frac{K_f}{K_t} = 1$ or notch root radius (r) = ∞ represents a limiting case where no difference between two factors is found allowing us to theoretically obtain the fatigue limit using the stress concentration factor (K_t). The ratio $\frac{K_f}{K_t} = 0$ or the notch root radius (r) = 0 represents another limiting case where the stress concentration factor (K_t) is irrelevant but taken over by the stress intensity factor. However, the two values from the two limiting cases do not necessarily reflect a material property. Therefore, it may be convenient that the notch sensitivity of a material in fatigue is expressed by

$$q = \frac{K_f - 1}{K_t - 1} \tag{8.4}$$

and is called the *notch-sensitivity factor* (q) to have a range of values between zero and one. When a material experiences no change at all in fatigue limit due to the presence of a notch, K_f=1 and q = 0 (insensitive, which is good) for any different values of K_t. On the other hand, when a material has its full theoretical effect, K_f= K_t and q = 1 (sensitive). It should be noted, however, that q is not a material constant but is dependant on the geometry of specimen and notch, and the loading type.

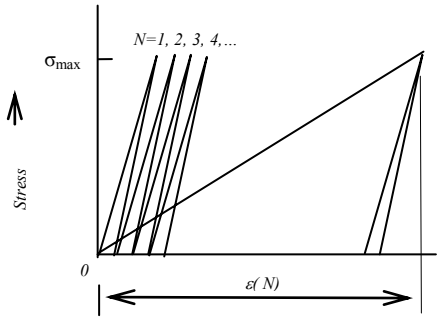

Figure 8.3 Fatigue modulus.

8.2 Fatigue damage and life prediction

Mechanical properties of materials such as fibre reinforced plastics are susceptible to fatigue damage so that their resultant stiffness decreases under cyclic loading. In this situation, the fatigue modulus may be useful to quantify such damage. The fatigue modulus[31] is defined as

$$E_{fi} = \frac{\sigma_{\max}}{\varepsilon(N)} \tag{8.5}$$

where σ_{max} is the maximum applied stress and $\varepsilon(N)$ is the resultant fatigue strain at Nth cycle (see **Figure 8.3**).

Figure 8.4 shows examples of fatigue moduli measured for a glass reinforced composite in comparison with stiffness. **Figure 8.4 (a)** shows one at a maximum stress of 436 MPa and failed at 926 cycles; and **Figure 8.4 (b)** at a stress of 266 MPa and failed at 5.66×10^5 cycles to failure. It is seen that low applied stress tends to produce more variation in the fatigue modulus than high stress does.

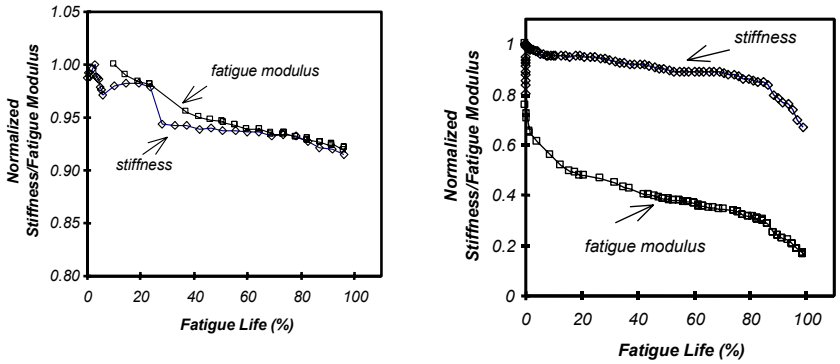

Figure 8.4 Normalised stiffness and fatigue modulus measured as a function of life for glass fibre reinforced vinyl ester: (a) maximum applied stress = 436 MPa and N = 926 cycles; and (b) maximum applied stress = 266 MPa and N = 566377 cycles. [After Kim and Zhang 2001][32]

Fatigue damage may be defined as any permanent change due to fatigue loading. The damage (D) is a function of a number of parameters at least, N, $\Delta\sigma$, R and f :

$$D = f\,(N,\ \Delta\sigma,\ R,\ f) \tag{8.6a}$$

where N is the number of loading cycles, $\Delta\sigma$ is the applied stress range, R is the stress ratio and f is the loading frequency.

The damage may be quantified by a normalized fatigue modulus:

$$D = (1 - \frac{E_{fa}}{E_0}) \tag{8.6b}$$

where E_{fa} is the fatigue modulus at Nth fatigue cycle and E_0 is the initial modulus before fatigue loading. There is a boundary condition in Equation (8.6b) for an undamaged coupon i.e. $D=D_0=0$ when $E_{fa} = E_0$. The initial modulus can be determined in a monotonic tensile test using

$$E_0 = \frac{\sigma_u}{\varepsilon_u} \tag{8.6c}$$

where σ_u is the ultimate stress and ε_u is the ultimate strain. As cycling progresses, E_0 reduces to E_{fa}. It is assumed that failure occurs when the fatigue resultant strain reaches the static ultimate strain, $\varepsilon(N) = \varepsilon_u$. Then, E_{fa} at failure (E^f_{fa}) is

$$E^f_{fa} = \frac{\sigma_{\max}}{\varepsilon_u} \tag{8.6d}$$

To predict a S-N curve, damage D is required to be a function of applied stress. Substituting Equations (8.5) and (8.6c) into Equation (8.6b) yields

$$D = (1 - \frac{\varepsilon_u}{\varepsilon(N)} \frac{\sigma_{\max}}{\sigma_u}) \tag{8.7}$$

and the damage accumulated to failure [$\varepsilon(N) = \varepsilon_u$] becomes

$$D_f = (1 - \frac{\sigma_{\max}}{\sigma_u}) . \tag{8.8}$$

If a non-linearity exists between damage and cycling for a given stress range, generally

$$\frac{dD}{dN} \neq \frac{dD_f}{dN_f} \tag{8.9}$$

where $N = N_f$ at failure, but always

$$\frac{dD_f}{dN_f} \approx \frac{\Delta D_{fi}}{\Delta N_{fi}} \tag{8.10}$$

where the subscript i = 1, 2, 3 … which indicate different applied stress ranges, ΔD_{fi} (= $|D_0 - D_f|$) is the damage to failure and ΔN_{fi} is the number of cycles to failure at a given stress range. The right hand side of the equation is associated with the experimental S-N curve while the left hand side is associated with a theoretical S-N curve. We can determine ΔN_{fi} experimentally by measuring the number of cycles to failure. If we want to determine it theoretically using the stiffness change, the following relation needs to be established:

$$\frac{dD}{dN} = f(E_{fa}) . \tag{8.11a}$$

Further from Equation (8.6b)

$$dD = -\frac{1}{E_0} dE_{fa} . \tag{8.11b}$$

From these two equations,

$$\Delta N_{fi} = \int_{E_0}^{E^f_{fa}} \frac{dD}{f(E_{fa})} = \frac{-1}{E_0} \int_{E_0}^{E^f_{fa}} \frac{1}{f(E_{fa})} dE_{fa} . \tag{8.12}$$

The potential of this equation lies in its capacity to predict residual fatigue life at a given stress by choosing appropriate integration limits.

Now, for a S-N curve prediction it is required to establish the damage rate as a function of applied stress range ($\Delta\sigma$) for a given set of conditions:

$$\frac{dD_f}{dN_f} = f(\Delta\sigma) \tag{8.13}$$

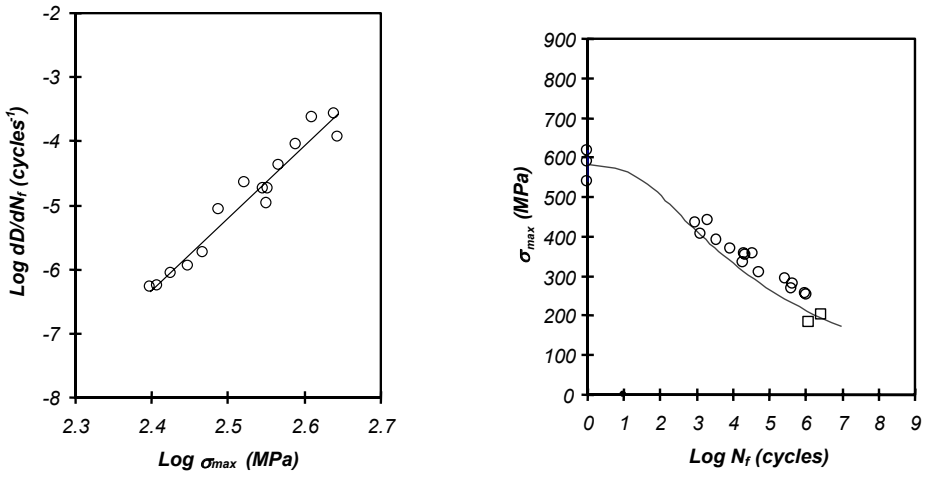

(a) (b)

Figure 8.5 (a) Log damage rate obtained as a function of applied maximum stress. Correlation coefficient = 0.96. Stress ratio =0. (b) Experimental results for maximum applied stress versus log number of cycles obtained at 1.5 Hz and a stress ratio of zero. The curve represents prediction based on Equation (8.15). Square symbols represent run-outs. [After Kim and Zhang 2001][33]

If the damage rate follows a power law:

$$\frac{dD_f}{dN_f} = \alpha\sigma_{\max}^{\beta} \tag{8.14a}$$

where constants α and β are found from the least square line for damage data as shown in **Figure 8.5(a)**. Then, we find

$$N_f = \int_{\sigma_u}^{\sigma_{\max}} dN_f = \int_{\sigma_u}^{\sigma_{\max}} \frac{dD_f}{\alpha\sigma_{\max}^{\beta}} \tag{8.14b}$$

for a stress ratio $(R = \sigma_{min}/\sigma_{max})$ of zero. From Equation (8.8), $dD_f = -\frac{d\sigma_{\max}}{\sigma_u}$. Therefore the fatigue life (N_f) or a S-N curve can be calculated as:

$$N_f = \frac{\sigma_u^{-\beta}}{\alpha(\beta-1)}\left[1-\left(\frac{\sigma_{\max}}{\sigma_u}\right)^{1-\beta}\right]. \tag{8.15}$$

The prediction based on Equation (8.15) is shown in comparison with experimental data in **Figure 8.5(b)**. A good agreement between the prediction and experimental data is seen.

8.3 Effect of mean stress on fatigue

The fatigue life (N) generally increases as the mean stress (σ_{mean}) or stress ratio (R) increases at a constant stress amplitude (σ_a). Also, we know that a material breaks when the maximum stress (σ_{max}) reaches the ultimate strength (σ_u). (Assume σ_u is equal to yield stress.) It is useful to use a σ_a – σ_{mean} plane for a relation between the variables. On the σ_a – σ_{mean} plane (**Figure 8.6**), it is easily found that there are two limiting cases in which two breaking points A and B are at σ_a =0 for σ_{mean}= σ_u and at σ_{mean}= 0 for σ_a = σ_u. If we connect the two points, a straight line (which is a locus of breaking points at the 1st cycle) is found for a constant life at the same maximum stress but at different stress ratios. The same principle for a constant life may be applied to different stress amplitudes at R=-1. Then, another point C at a lower stress may be found from an experiment for another constant fatigue life line CB but for a longer fatigue life. The point B is used for all other stress levels because it is a known condition for any stress ratios. If a fatigue limit is available from a S-N curve for R=-1, the fatigue limit line DB may be found. As a result, it is possible from a single S-N curve to predict a series of different values of σ_{mean} and σ_a for different stress ratios for each constant fatigue life. On the other hand, the dash-dot line in **Figure 8.6** represents a constant stress ratio for different fatigue lives for a given stress ratio (R), and its slope is

$$\frac{\sigma_a}{\sigma_{mean}} = \frac{1-R}{1+R} \tag{8.16a}$$

and the stress ratio (R) is given by

$$R = \frac{\sigma_{\min}}{\sigma_{\max}} = \frac{\sigma_{mean} - \sigma_a}{\sigma_{mean} + \sigma_a}. \tag{8.16b}$$

(8.16a)

In this way, series of constant fatigue life lines and constant stress ratio lines can be drawn for predicting various parameters. If the constant fatigue life lines are not linear, they may be generalized by

$$\sigma_a = (\sigma_a)_{R=-1}\left[1-\left(\frac{\sigma_{mean}}{\sigma_u}\right)^x\right] \tag{8.17a}$$

where x = 1 for linearity (Goodman model[34]). For a fatigue limit $(\sigma_a)_o$ at R=-1 the constant fatigue life line is given by

$$\sigma_a = (\sigma_a)_o\left[1-\left(\frac{\sigma_{mean}}{\sigma_u}\right)^x\right]. \tag{8.17b}$$

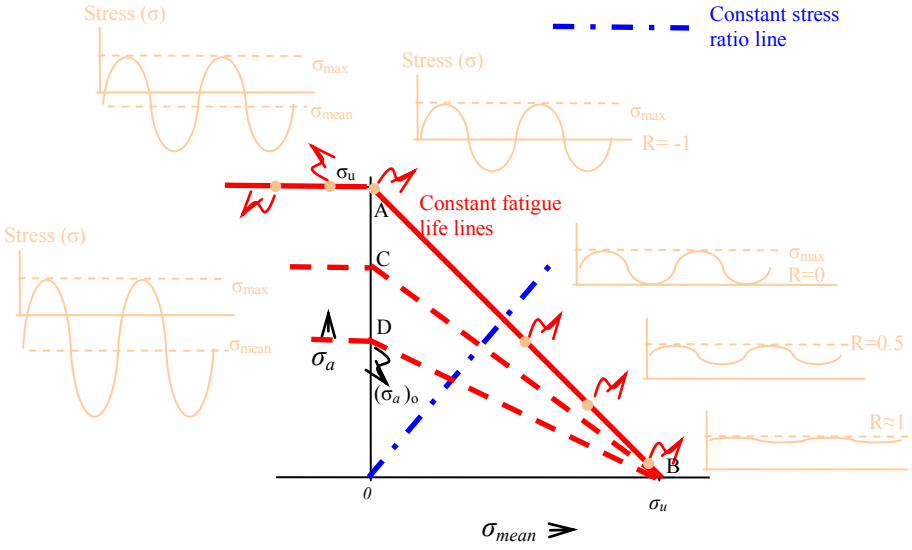

Figure 8.6 Stress amplitude (σ_a) versus mean stress (σ_{mean}).

If compressive mean stresses are considered, horizontal lines from points A, C, and E are for the expected constant fatigue lives, given that that the portions of compressive stresses do not affect the cracking damage.

If the ultimate strength (σ_u) is not equal to the yield stress (σ_{ys}), another straight line CD (which is a locus of yield points at the 1st cycle) is found in addition to the line of breaking points AB as shown in **Figure 8.7**. As a result, two parallel lines can be drawn. Accordingly, the intersects on line CD with other possible constant fatigue life lines provide the yield limits as the stress ratio (R) increases on a constant fatigue life line.

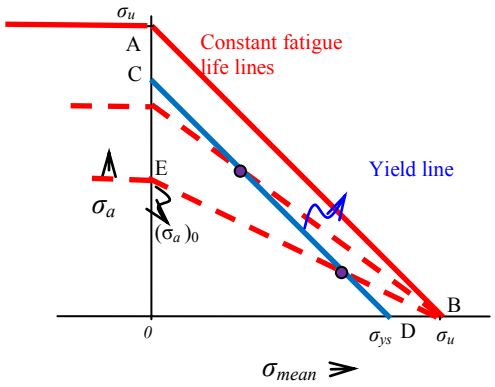

Figure 8.7 Stress amplitude (σ_a) versus mean stress (σ_{mean}) for $\sigma_u \neq \sigma_{ys}$.

8.4 Cumulative damage

When a structural component is subjected to a series of different stress amplitudes, It may be assumed that the total fatigue life is the sum of each fraction of life (N_i/N_{fi}) consumed at a particular applied stress:

$$\sum_{i=1}^{k} \frac{N_i}{N_f} = 1 \text{ or } \frac{N_1}{N_{f1}} + \frac{N_2}{N_{f2}} + \cdots + \frac{N_k}{N_{fk}} = 1 \tag{8.18}$$

where N_i is the number of cycles of operation at a stress and N_{fi} is the fatigue life at each corresponding stress. Equation (8.18) has been known as the *cumulative damage rule* or Palmgren[35]-Miner[36] rule, which may be used for the calculation of the total fatigue life. Deviations from the rule are possible for some materials. The fatigue life estimation for random cyclic loading due to variation of mean stress (σ_{mean}) and stress range ($\Delta\sigma$) may be made using the rule in conjunction with Goodman model.

> **Example) Figure 8.8** represents the stress fluctuation pattern taking place every 15 seconds on an alloy component. A S-N curve with a fatigue limit of 120 MPa obtained experimentally at R=-1 is given in **Figure 8.9**. The alloy component has an ultimate strength (σ_u) of 500 MPa. Estimate the fatigue life using the cumulative damage rule and Goodman's model. Assume that ultimate strength is equal to yield strength. Ignore the notch sensitivity.

Solution) The fatigue life estimation may be conducted according to the following procedure:

a) locate the ultimate strength (σ_u) of 500 MPa on σ_{mean} axis in **Figure 8.10**;
b) find values of stress amplitude (σ_a) and mean stress (σ_{mean}) individually from **Figure 8.8** as listed in **Table 8.1**;
c) plot data points on $\sigma_{mean} - \sigma_a$ plane to find stress amplitude at R=-1 as shown in **Figure 8.10** and then to use the S-N curve (**Figure 8.9**) for finding corresponding number of cycles (N_{fi}) and
d) use the cumulative damage rule $\sum_{i=1}^{k} \frac{N_i}{N_f} = 1$ for the life estimation as follows. The values of N_{fi} are found from the S-N curve.

$$\frac{N_a}{N_{fa}} = \frac{2}{\infty} = 0, \quad \frac{N_b}{N_{fb}} = \frac{1}{\infty} = 0, \quad \frac{N_c}{N_{fc}} = \frac{4}{\infty} = 0$$

$$\frac{N_d}{N_{fd}} = \frac{2}{10^{5.75}} = 3.556 \times 10^{-6}$$

$$\frac{N_e}{N_{fe}} = \frac{4}{10^{4.55}} = 1.127 \times 10^{-4}$$

$$\frac{N_f}{N_{ff}} = \frac{1}{10^{3.1}} = 7.943 \times 10^{-4}$$

A fraction of fatigue life spent by the pattern (15 seconds) shown:

$$\frac{N_a}{N_a} + \ldots + \frac{N_f}{N_f} = 3.556 \times 10^{-6} + 1.127 \times 10^{-4} + 7.943 \times 10^{-4}$$

$$= 910.56 \times 10^{-6} < 1.$$

Therefore, the total fatigue life estimate $= \frac{15 \sec}{910.56 \times 10^{-6}.} = 16{,}473$ cycles.

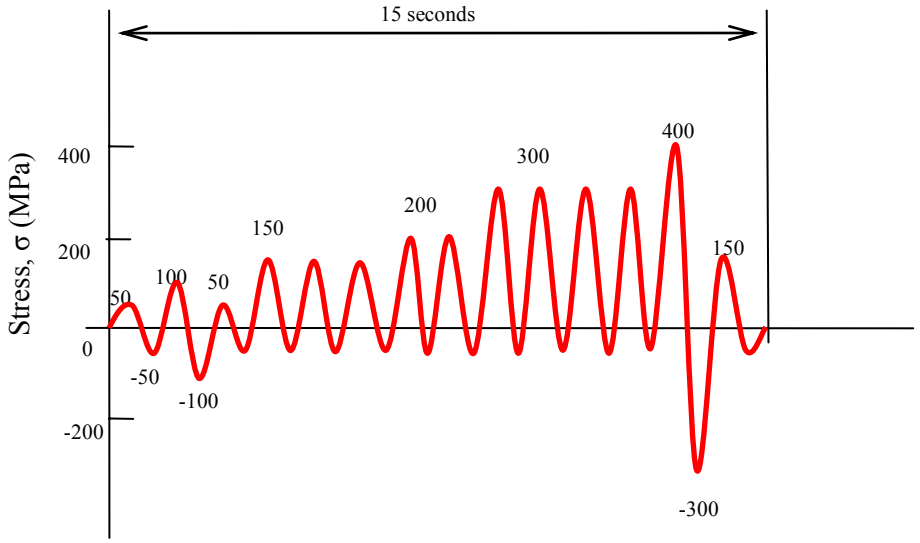

Figure 8.8 A stress fluctuation pattern taking place every 15 seconds.

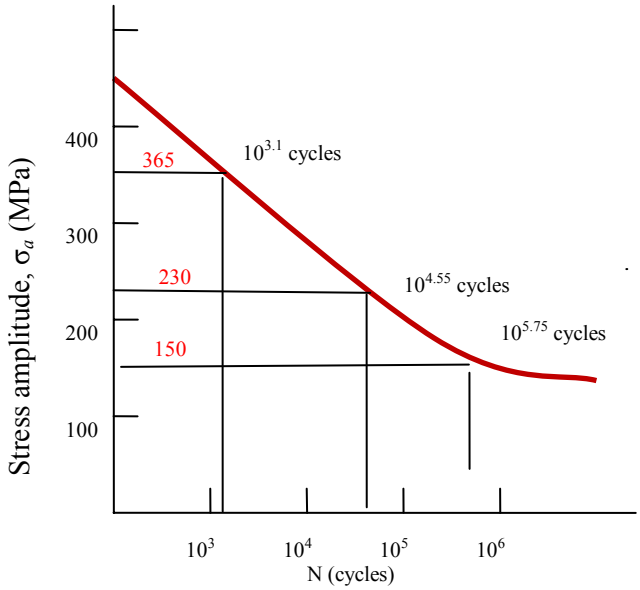

Figure 8.9 A S-N curve obtained experimentally at R = -1.

Designation	σ_{max} (MPa)	σ_{mean} (MPa)	σ_a (MPa)	Number of loads (*n*)	Comment
a	50	0	50	2	Lower than fatigue limit
b	100	0	100	1	Lower than fatigue limit
c	150	(150-50)/2=50	100	4	Lower than fatigue limit
d	200	(200-50)/2=75	125	2	Counted
e	300	(300-50)/2=125	175	4	Counted
f	400	(400-300)/2=50	350	1	Counted

Table 8.1 Data collected.

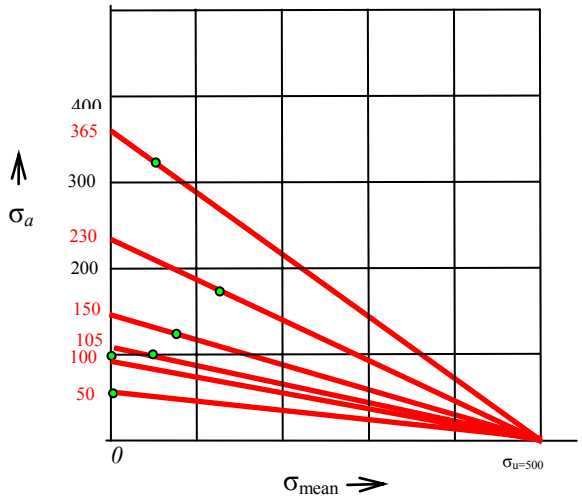

Figure 8.10 Stress amplitude (σ_a) versus mean stress (σ_{mean}).

8.5 Single crack approach for fatigue

The S-N curve approach in fatigue does not account for the details of a crack although it is useful to deal with a case where the failure is caused by the multiple cracks. A single crack approach provides another aspect of fundamental understanding of the fatigue phenomenon by modelling the fatigue crack initiation and propagation processes. The fatigue initiation may be analysed at a smaller scale while the fatigue crack propagation at a larger scale. When a component is subjected to cyclic loading, energy is consumed in the neighbourhood of inherent small defects, which grow and coalesce, for forming a crack to be large enough to be analysed by the principles of continuum mechanics. The crack propagation leading to the catastrophic failure is more predictable than the initiation of a fatigue crack.

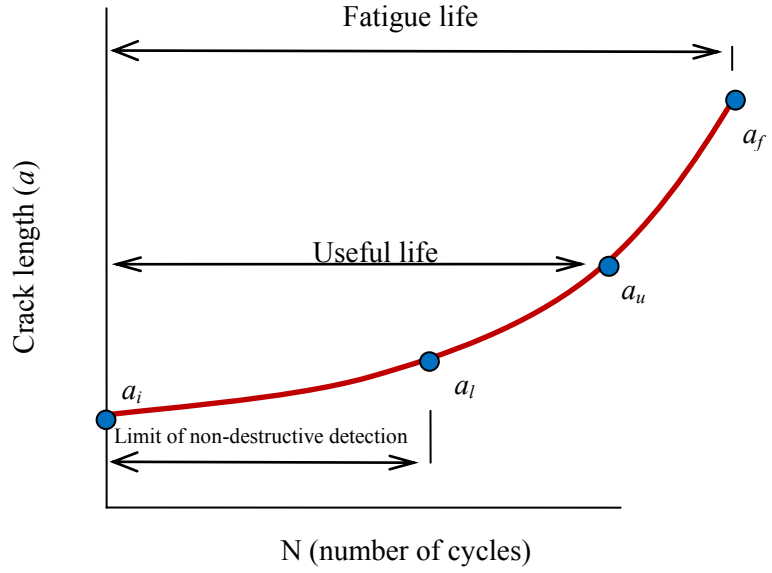

Figure 8.11 Typical form of crack size versus number of cycles curve for constant amplitude loading.

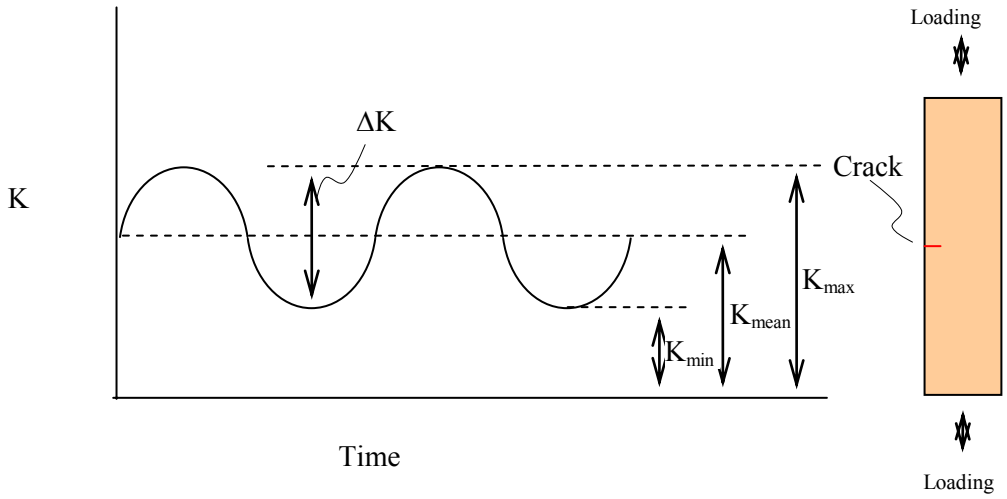

Figure 8.12 A sinusoidal load with a constant amplitude and frequency for stress intensity factor (*K*).

Figure 8.11 illustrates some characteristic crack lengths (a) dependant on number of loading cycles (N). There are relative four different crack lengths. The smallest crack length (a_i) represents the one that is big enough for fracture mechanics to apply but too small to be detected by the non-destructive inspection technology until it grows to a_i. The crack length further grows to reach the limit of useful life (a_u) before the catastrophic failure takes place (a_f).

Fatigue crack propagation data at a stress ratio ($R= K_{min}/K_{max} = \sigma_{min}/\sigma_{max}$) are obtained from experiments on precracked specimens subjected to cyclic loading, and the change in crack length (a) is recorded as a function of loading cycles (N). The crack growth rates (da/dN) are then numerically calculated for corresponding stress intensity factor ranges (ΔK) from the raw data. The experimental results are usually plotted in a log (ΔK) versus log (da/dN) diagram. The load is usually sinusoidal with constant amplitude and frequency (**Figure 8.12**).

A typical plot of a log (ΔK) – log (da/dN) curve is shown in **Figure 8.13**. Three characteristic Stages may be identified. In Stage I, da/dN diminishes rapidly to a vanishingly small level, and for some materials there might be a threshold of the stress intensity factor range (ΔK_{th}), below which no crack propagation takes place. In Stage II, a linear log (ΔK) – log (da/dN) relation is usually found. As da/dN further increases, it reaches Stage III in which the crack growth rate (da/dN) curve rapidly rises and the maximum stress intensity factor (K_{max}) in the fatigue cycle becomes equal to the critical stress intensity factor (K_c) leading to catastrophic failure. Experimental results indicate that the fatigue crack growth rate curve depends on the stress ratio (R), and is shifted towards higher da/dN values as R increases. The Stage I has been known to be sensitive to variations of mean stress, microstructure and environment as expected at low stress intensity factor values and extremely slow crack growths. Stage II is not as sensitive as Stage III to mean stress and specimen thickness because of relatively small plastic zone sizes at low stress intensity factors compared to those in Stage III. Also, it represents a wide range of ΔK.

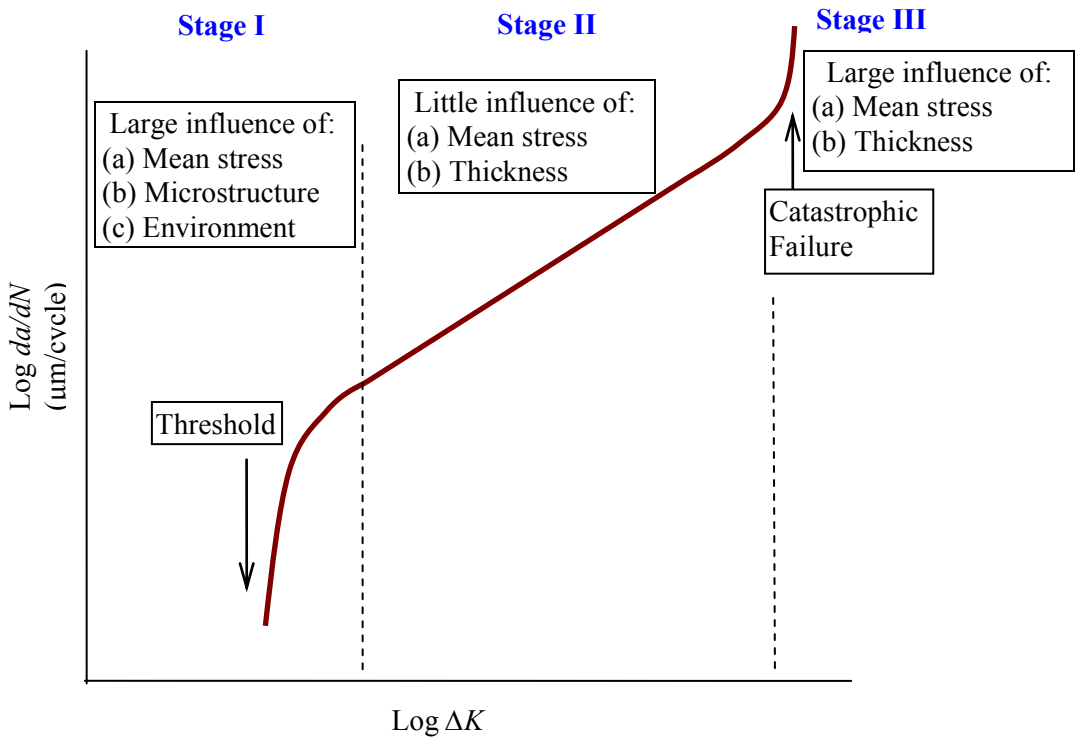

Figure 8.13 Typical form of the fatigue crack growth rate curve.

One of the most widely used fatigue crack propagation empirical models for Stage II is proposed by Paris and Erdogan[37] and will be referred to as the *Paris equation*. It has the form

$$\frac{da}{dN} = C(\Delta K)^m \tag{8.19}$$

where $\Delta K = K_{max} - K_{min}$, and C and m are constants for materials. Equation (8.19) represents a linear relationship between log (ΔK) and log (da/dN) and is used to determine the constants C and m for the effects of mean stress, frequency, and temperature variation. Equation (8.19) does not, however, describe the crack growth rates in Stages I and III. At high ΔK values in Stage III, as approaches the critical level K_c, the crack growth rate approaches infinity. Stages II and III can be represented by a modification of the Paris Equation, i.e.

$$\frac{da}{dN} = \frac{C(\Delta K)^n}{1-(K_{max}/K_c)^n} = \frac{C(\Delta K)^n}{1-\left\{\frac{\Delta K}{K_c(1-R)}\right\}^n} \tag{8.20}$$

where $R = K_{min}/K_{max}$ and C and n are material constants. The fatigue crack growth rate (da/dN) in Equation (8.20) approaches infinity if $K_{max} = K_c$, satisfying the requirement of the curve.

8.6 Temperature and frequency effects on fatigue crack growth

Materials such as polymers are readily influenced by temperature variation. The fatigue crack growth rate (da/dN) generally increases with increasing temperature although some materials display a different response. Arrhenius[38] proposed an expression to account for the influence of temperature on the rate (k) of inversion of sucrose:

$$k = A_1 \exp\left(\frac{-\Delta H}{RT}\right) \tag{8.21a}$$

where A_1 is a quantity independent of, or varies relatively little, with temperature, ΔH is the activation energy (kJ/mol), R(= 8.31J/mol K) is the universal gas constant and T is the absolute temperature (K).

Krausz and Krausz[39] related the rate constant (k) to a crack velocity based on an atomistic model as

$$\frac{da}{dt} = A_2 k \tag{8.21b}$$

allowing us to relate this to k

$$\frac{da}{dt} = A_2 \exp\left(\frac{-\Delta H}{RT}\right) \tag{8.21c}$$

and

$$\frac{da}{dN} = \frac{da}{dt}\frac{dt}{dN} = \frac{da}{dt}\frac{1}{f} \tag{8.21d}$$

where f is the cyclic load frequency. The fatigue crack process is affected not only by temperature but also by the stress intensity in the vicinity of a crack. We see that the higher activation energy (ΔH) the slower crack growth – ΔH is an energy barrier – but the higher stress intensity factor the faster crack growth is expected. Accordingly, an apparent activation energy (ΔH_a) may be used to account for this and we find a term $\gamma \log \Delta K$ satisfying the Paris equation for the energy barrier reduction:

$$\Delta H_a = \Delta H - \gamma \log \Delta K \tag{8.21e}$$

where γ is a constant and ΔK is the stress intensity factor range. Then, the fatigue crack growth rate (da/dN)[40] takes the final form for the temperature effect,

$$\frac{da}{dN} = B \exp\left(\frac{-\Delta H_a}{RT}\right) = B \exp\left(\frac{-\left(\Delta H - \gamma \log \Delta K\right)}{RT}\right) \tag{8.22}$$

where B is an approximate constant.

The time (t) dependence for polymers may be expressed as

$$E = E_0\, t^{-k} \tag{8.23a}$$

where E is the tensile modulus, E_0 is the unit time modulus (at time), and $-k = \frac{d\ln E}{d\ln t}$. Although Marshall et al41 indicated that k decreases at extremes of rate or temperature, the constant (k) is assumed to be approximately constant in a certain range for any visco-elastic process. Williams42 related da/dN to frequency (f) based on the line zone model by the following relationship

$$\frac{da}{dN} \propto f^{-km} \tag{8.23b}$$

where m is the Paris equation exponent which is insensitive to temperature and frequency for many polymers so that km may be an approximately constant.

To accommodate both temperature and frequency in one equation, the following procedure is conducted[43]. Taking log in Equation (8.23b), we have

$$\log\left(\frac{da}{dN}\right) \propto -km \log f\ . \tag{8.23c}$$

Accordingly, a series of straight lines with a slope of -km for a given ΔK, one line for each temperature, can be obtained in a plot of log (da/dN) against log f.

Since the fatigue crack growth rate as influenced by temperature at a given frequency can be described by Equation (8.22), it allows us to relate frequency to temperature by

$$-km = \frac{\log a_T}{\log a_f} \tag{8.23d}$$

where a_T

$$a_T = \frac{\left(\frac{da}{dN}\right)}{\left(\frac{da}{dN}\right)_r} = \frac{B\exp\left[\frac{-(\Delta H - \gamma \log \Delta K)}{RT}\right]}{\left(B\exp\left[\frac{-(\Delta H - \gamma \log \Delta K)}{RT}\right]\right)_r}$$

and $a_f = \frac{f}{f_r}$. The subscript, r, denotes an arbitrarily chosen reference point in the coordinate system. Therefore, we obtain fatigue crack growth rate (da/dN) as

$$\frac{da}{dN} = \left(\frac{f}{f_r}\right)^{-km}\left(B\exp\left[-\frac{\Delta H - \gamma \log \Delta K}{RT}\right]\right)_r \tag{8.24}$$

Since Equation (8.24) has been developed for the Stage II governed by the Paris equation it can be equated to the Paris equation. Taking logs on both equations, the following relations are obtained

$$m = \frac{\gamma_r}{2.303\,RT} \tag{8.25a}$$

and

$$\log A = \log f^{-km} + \log C - \frac{\Delta H}{2.303RT} \tag{8.25b}$$

where C is B_r / f_r^{-km}. It should be noted that the constant B is dependent on frequency. However, the constant C here is independent of frequency and temperature. Also, Equation (8.25a) indicates γ_r, is independent of frequency and temperature. Hence, Equation (8.24) can be simplified to

$$\frac{da}{dN} = f^{-km} C \exp\left[-\frac{\Delta H - \gamma \log \Delta K}{RT} \right] \tag{8.26}$$

This equation expresses the combined effects of frequency and temperature on the fatigue crack growth rate. Equations (8.23d) and (8.25) can be used to plot experimental data and determine the constants in Equation (8.26). Equation (8.22) is recovered from Equation (8.26) for a constant frequency, $B = f^{-km} C$.

8.7 Fatigue crack life calculations

The fatigue crack life or a number of load cycles (N) required for a crack to grow one-dimensionally from a certain initial crack size a_o to the maximum permissible crack length a_c is easily calculated using the Paris equation.

Consider a fatigue crack of length (a_0) in a plate subjected to a uniform stress σ perpendicular to the plane of the crack (**Figure 8.14**). The stress intensity factor (K_I) is given by

$$K_I = Y\sigma\sqrt{\pi a} \tag{5.15 bis}$$

where Y is a geometry factor and a function of a/W.

Integrating dN of the Paris equation, we find

$$N = \int_{a_o}^{a_c} \frac{d}{C(\Delta K)^m} = \int_{a_o}^{a_c} \frac{d}{C\left[Y\Delta\sigma\sqrt{\pi a}\right]^m}. \tag{8.27}$$

Usually Y varies with the crack length a and the integration cannot be performed directly but by a numerical method. However, we may assume for estimation that Y is an approximately constant if the initial and final crack lengths are very small compared to the width (W). The crack length a_c is calculated from K_{Ic}.

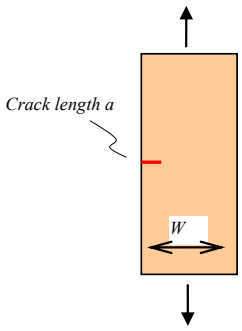

Figure 8.14 Fatigue specimen geometry.

8.8 Overload retardation and crack closure

The fatigue crack propagation discussed so far has been concerned with constant amplitude loads. It is one of types. Another type is of variable amplitude loads. In the case of constant amplitude loads, the crack growth is more predictable. In other words, a higher fatigue crack growth rate is expected when subjected to higher amplitude of stress intensity factor. However, when a single overload is applied as shown in **Figure 8.15**, the crack length does not increase as same rate as expected. Surprisingly, its rate is, in fact, lower than it would have been under constant amplitude loading. This effect is shown schematically in **Figure 8.15**. The crack retardation takes place when a tensile overload follows a constant amplitude cyclic load. An explanation of the crack retardation phenomenon may be obtained by examining the stress distribution in the wake of the plastic zone formation ahead of the crack tip. The plastic deformation creates a compressive residual stress field reducing mode I stress intensity factor for any subsequent lower load. The compressive residual stress tends to close the crack. The overload leaves a larger plastic zone size than the subsequent regular constant amplitude load. The reduction of mode I stress intensity factor depends on the difference between the overload and the regular constant amplitude load. Accordingly, the crack propagates after overloading at a decreased rate into the zone of residual compressive stresses. Once it passes through the plastic zone created by the overload, its expected growth rate is recovered as the residual stress diminishes.

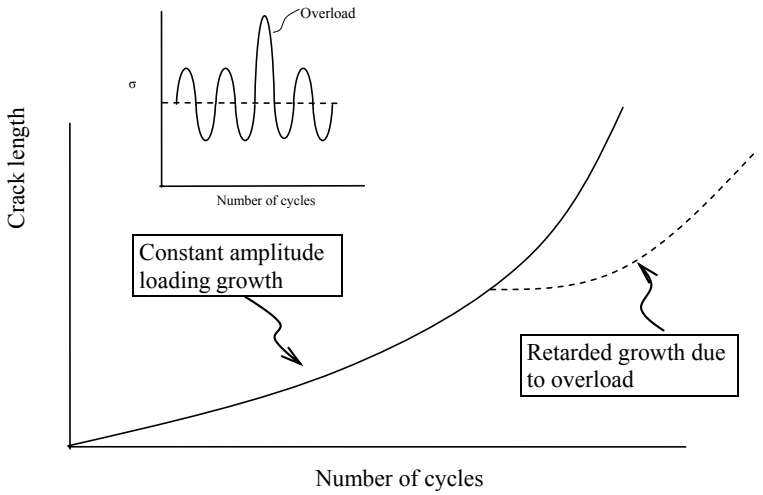

Figure 8.15 Typical form of crack length versus number of cycles curve for constant amplitude loading and constant amplitude plus overloading.

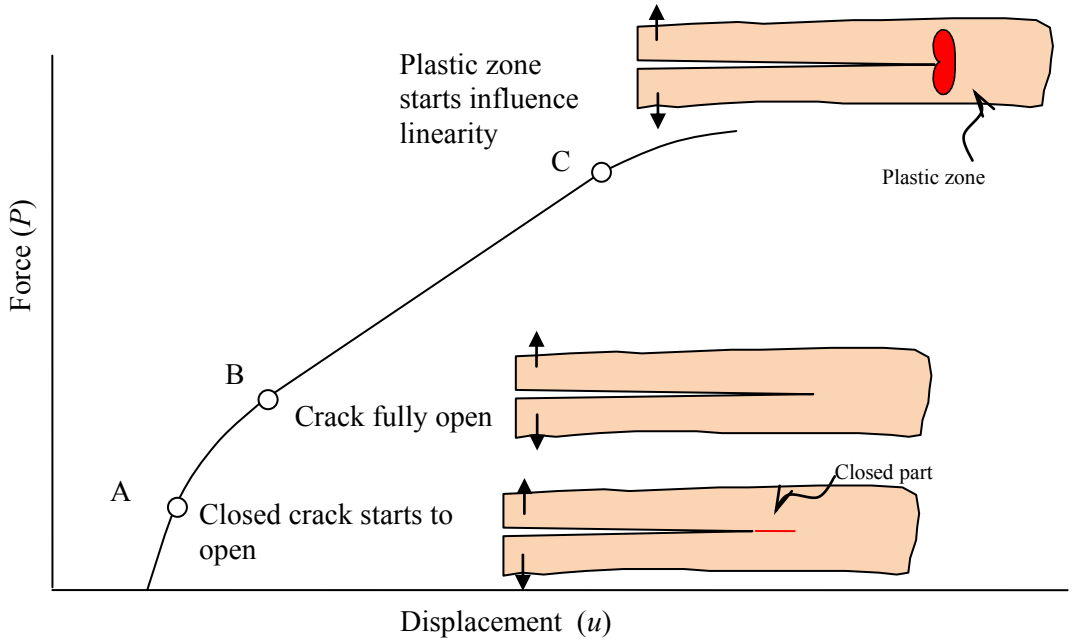

Figure 8.16 Force-displacement diagram showing the non-linearity caused by configuration change and plastic zone formation.

The crack closure and plastic zone formation can be detected on the force-displacement (*P-u*) diagram as Elber[44] suggested. Since the non-linearity of a linear elastic material on a force-displacement diagram can only be caused by two reasons – change of geometric configuration, and material plasticity, as illustrated in **Figure 8.16**. When an elastic body with a closed crack is under loading, it displays a linear behaviour until the closed-crack starts to open at point A. As the crack opens, the crack length increases, causing the change in geometrical configuration. Accordingly, non-linearity continues from point A until point B at which the crack is fully open. The linearity remains from point B to point C at which the plastic deformation sufficiently large to change the linear behaviour again.

A retardation factor[45] may be defined using plastic zones in the wake of overloading. Let us consider a crack-tip plastic zone of length (r_{po}) (**Figure 8.17)** at a crack length (a_0) by an overload of stress (σ_o) given by

$$r_{p0}=\frac{K_I^2}{2\pi\sigma_{ys}^2}=C\frac{\sigma_0^2 a_0}{\sigma_{ys}^2} \tag{8.28a}$$

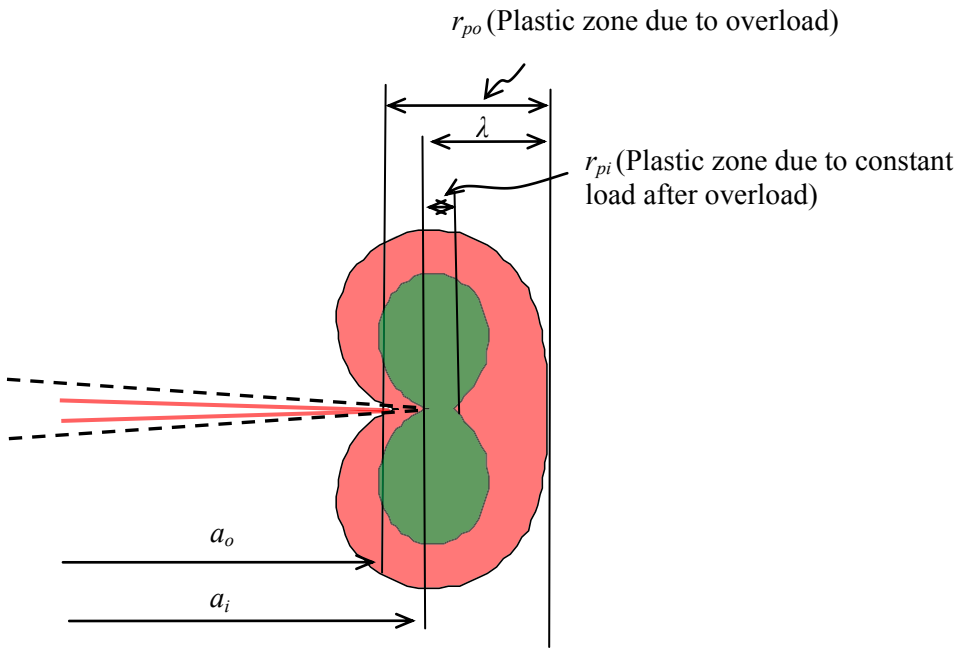

Figure 8.17 Plastic zones: small one produced by constant amplitude and large one by overload.

and another plastic zone size (r_{pi}) when the crack has propagated to a length a_i at a stress (σ_i) is calculated as

$$r_{pi}=C\frac{\sigma_i^2 a_i}{\sigma_{ys}^2} \tag{8.28b}$$

where C is a constant. The plastic zone (r_{pi}) due to the stress (σ_i) is within the overload plastic zone (r_{po}). The retardation is due to the difference ($=\lambda - r_{pi}$) and a retardation factor is given by

$$\phi=\left(\frac{r_{pi}}{\lambda}\right)^m \tag{8.28c}$$

where $\lambda = a_0 + r_{po} - a_i$ and m is an empirical parameter. Then, the retarded crack growth rate $\left(\frac{da}{dN}\right)_R$ for $a_i + r_{pi} < a_0 + r_{po}$ is given by

$$\left(\frac{da}{dN}\right)_R = \phi\left(\frac{da}{dN}\right) \tag{8.28d}$$

where da/dN is the constant amplitude crack growth rate unaffected by the overload. We see that, when the crack has propagated through the overload plastic zone, the crack length $a_i + r_{pi}$ becomes greater than $a_0 + r_{po}$ and the retardation factor also becomes $\phi = 1$.

Elber[46] introduced a model based on the crack closure for stress ratio (R) effect on fatigue crack growth.

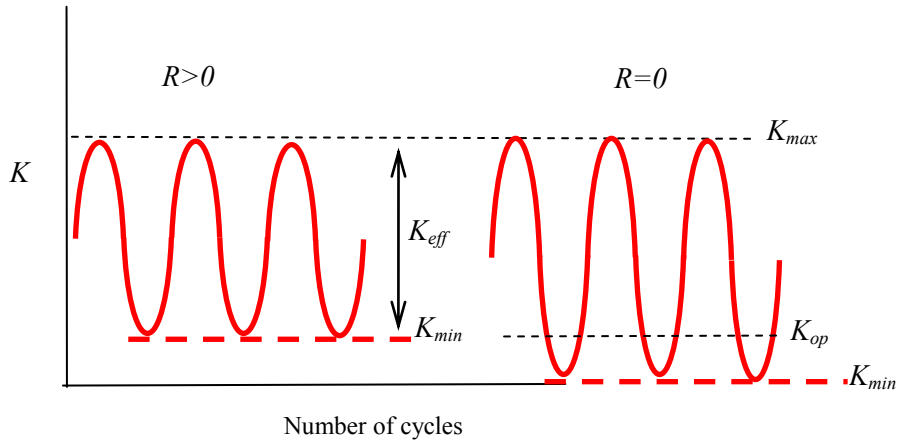

Figure 8.18 Stress intensity factor at crack opening at different stress ratio (R) values.

It is based on the fact that the faces of a fatigue crack subjected to zero-tension loading close during unloading, and compressive residual stresses act on the crack faces at zero load at R=0. An effective stress intensity factor range is defined by

$$(\Delta K)_{eff} = K_{\max} - K_{op} \tag{8.29a}$$

where K_{op} corresponds to the point at which the crack is fully open (**Figure 8.18**). Using the Paris equation we can find for Stage II,

$$\frac{da}{dN} = C(U\Delta K)^m \tag{8.29b}$$

where

$$U = \frac{K_{\max} - K_{op}}{K_{\max} - K_{\min}} \tag{8.29c}$$

It was experimentally found that

$$U = 0.5 + 0.4R \tag{8.29d}$$

where

$$R = \frac{K_{\min}}{K_{\max}} \text{ for } -0.1 \le R \le 0.7\,. \tag{8.29e}$$

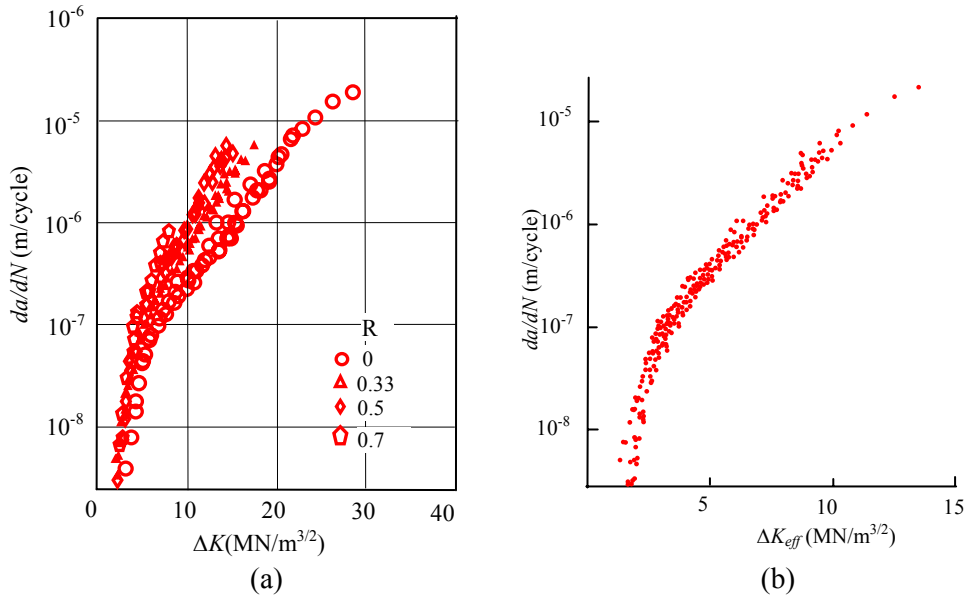

Figure 8.19 Crack growth rate and stress intensity factor range for different stress ratios, R= 0, 0.33, 0.5, and 0.7: (a) crack closure included [After Hudson, 1969][47]; and (b) crack closure excluded for ΔK_{eff}. [After Elber 1971] [48]

Figure 8.19(a) shows crack growth rate (*da/dN*) as a function of stress intensity factor range (ΔK) for different stress ratios, R= 0, 0.33, 0.5, and 0.7, displaying the stress ratio effect. The crack growth rate (*da/dN*) is re-plotted as a function of effective stress intensity factor range (ΔK_{eff}) in **Figure 8.19(b)** according to Equation (8.29b). It appears that a single curve fits the data from a wide range of stress ratios.

8.9 Variable amplitude loading

The prediction of the fatigue crack growth under a variable amplitude loading by simply summing up the individual fatigue lives from respective constant amplitude loads in the loading history may lead to conservative values due to the overload effect. However, the Paris equation may be applicable if we find an appropriate distribution function of ΔK for a *small* block of loads. Barsom[49] demonstrated that the root-mean-square value of the stress intensity factor is useful, which is given by

$$\Delta K_{rms} = \sqrt{\frac{\sum_{i=1}^{n_f} (\Delta K_i)^2}{n_f}} \tag{8.30a}$$

where n_f is the number of loading amplitudes for each block or random cycles with a stress intensity factor range of ΔK_i for various variable loading types as given in **Figure 8.20**. Accordingly, the Paris equation becomes

$$\frac{da}{dN}=C\left(\Delta K_{rms}\right)^m . \tag{8.30b}$$

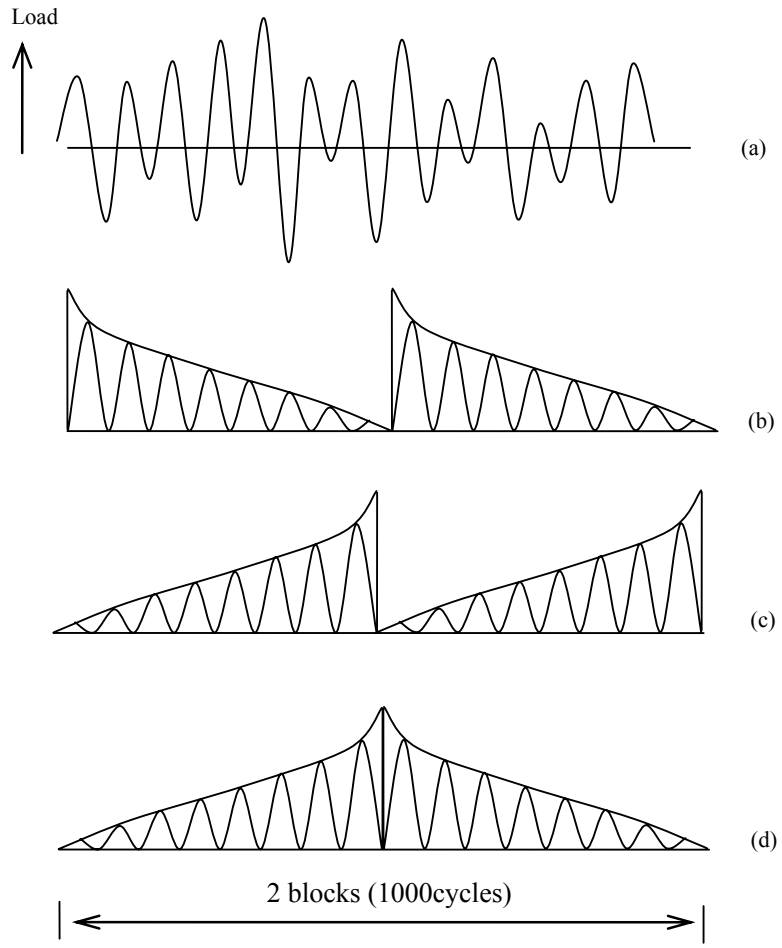

Figure 8.20 Variable amplitude loading: (a) random sequence, (b) descending sequence, (c) ascending sequence, and (d) combined ascending-descending sequence.

It has been found that the average fatigue crack growth rate (da/dN) under random sequence or ordered-sequence loading fluctuation spectra is approximately equal to the rate of fatigue crack growth obtained under constant amplitude cyclic loading.

8.10 Fatigue near threshold and measurement methods

The fatigue threshold stress intensity factor range (ΔK_{th}) is the one that corresponds to zero crack growth although it can be defined by an arbitrary crack growth rate for practicality. Most fatigue data do not show a clear ΔK_{th}. In designing structural components subjected to cyclic loading it is important to determine the fatigue threshold stress intensity factor (ΔK_{th}), below which a crack does not grow. However, important as it is, a 'true' ΔK_{th} is difficult to measure since this requires very long testing times. Usually, near-threshold fatigue crack growth rates of less than 10^{-10} m/cycle are determined and then used to estimate ΔK_{th}. Even so, obtaining the near-threshold crack, growth data is a tedious time-consuming procedure. Also, the threshold data vary depending on the experimental technique so that a thorough understanding of various techniques is important for all users of threshold data.

The method desired should be able to reduce ΔK as quickly as possible without load history effects to reach a very low crack growth rate (da/dN), but if ΔK is reduced abruptly it causes the retardation in fatigue crack growth resulting in a higher value than true near-ΔK_{th}. Load shedding can be conducted either manually or continuously by computerised automated control. The automated technique is preferred to avoid the intensive manual labour for processing raw data from measurements of crack length positions with corresponding loads. Also, a load-shedding schedule is required to efficiently minimise the load retardation effects. In this section, various methods employing load-shedding schedule will be introduced.

Continuous K-decreasing methods

A continuous K-decreasing method was proposed by Saxena et al[50] and recommended by ASTM E24 Committee with

$$\Delta K = \Delta K_i \exp\left[C\left(a - a_i\right)\right] \tag{8.31a}$$

Here (ΔK_i, a_i) and (ΔK, a) are initial and instantaneous values respectively of applied stress intensities and crack lengths. The constant C has a physical dimension of length given by

$$C = \frac{1}{\Delta K}\frac{d\Delta K}{da} \leq 0.08 mm^{-1} \tag{8.31b}$$

A limit on C assumes that there is a gradual decrease in ΔK so that the rate of the fractional change of the estimated plastic zone size (r_p) remains constant with increase in a and that there is no overload effect on crack growth if the decrease is sufficiently gradual. The acceptable values of C depend on test conditions. If K-increasing and K-decreasing fatigue data agree with each other, then the chosen value of C is permitted. This means that C can only be selected from separate experiments if it is not already established for the particular material to be tested. Accordingly, this method requires very long testing times.

Load shedding using a damping coefficient

A load shedding method proposed by Bailon et al[51] employs

$$\Delta P = \Delta P_i \exp\left(-QN\right) \tag{8.32a}$$

where ΔP and ΔP_i are the instantaneous and initial load, N is the number of elapsed cycles and Q is a damping coefficient given by

$$Q = \frac{1}{r_p}\frac{dr_p}{dN} \tag{8.32b}$$

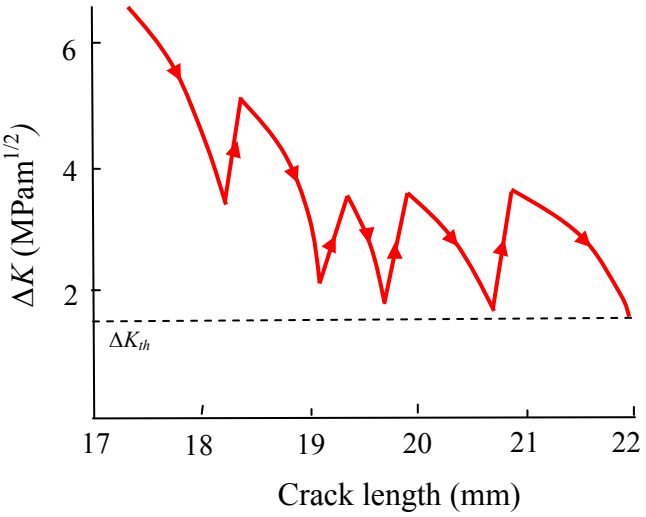

Figure 8.21 Load shedding using a damping coefficient. [After Bailon et al, 1981]

The basic principle of this method is to approach ΔK_{th} by steps of load shedding according to Equation (8.32a) until crack arrests at ΔK_a (subscript *a* denotes arrest) which is larger than ΔK_{th} due to overloading effects (**Figure 8.21**). The test is resumed with a new set of values for Q (half the previous magnitude) and ΔP_i (and hence ΔK_i, which is half the sum of the original ΔK_i and the associate ΔK_a). Values of ΔK_a, which are similar for the last two or three iterative steps indicate that ΔK_{th} has been reached. As opposed to the ASTM method for which *dK/da* is maintained constant, this method uses decreasing *dK/da* gradients in the load shedding program. It was claimed that this method provides 50% better efficiency than the ASTM method. However, it also requires some preliminary tests to determine the best damping coefficient Q.

Conditional loading by iteration

The principle of the method, proposed by Kim et al[52] is to search ΔK corresponding to a given *da/dN* by an iteration scheme conditionally. The condition is imposed on the crack growth rate. If the current crack growth rate $(da/dN)_c$ is higher or lower than the initially set $(da/dN)_i$, K_{max} is either decreased according to

$$K_{\max(n)}=K_{\max(n-1)}-\frac{K_{\max(i)}}{2^n} \tag{8.33a}$$

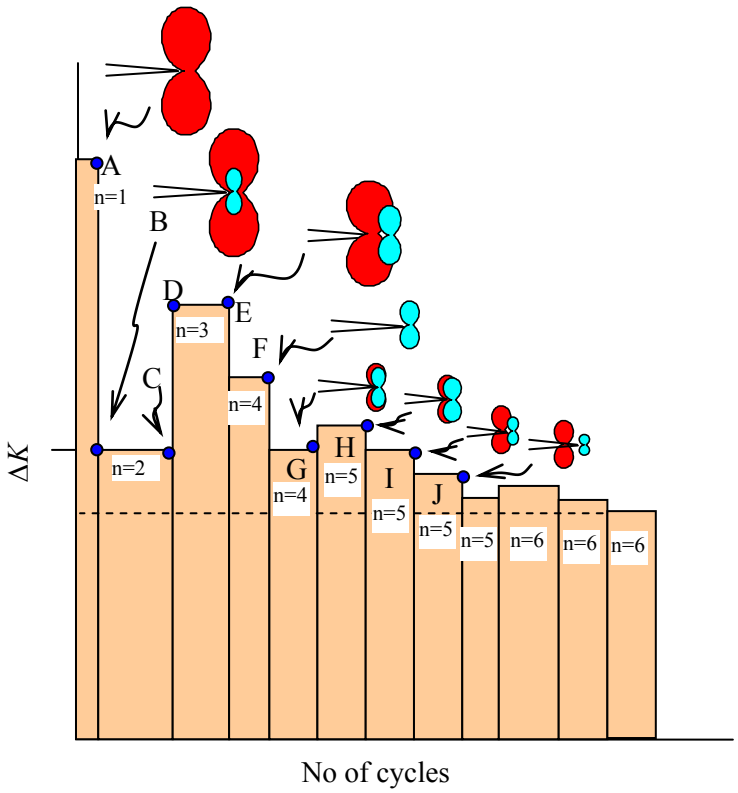

Figure 8.22 Illustration of conditional loading.

or increased according to

$$K_{\max(n)}=K_{\max(n-1)}+\frac{K_{\max(i)}}{2^n} \tag{8.33b}$$

where n is the number of iterations and $K_{max(i)}$ is an initially set relatively high stress intensity factor range. The procedure follows as illustrated in **Figure 8.22**. Point A is at the first allocated $K_{max\ (1)}$ and hence at the largest plastic zone size at a stress ratio (R) so that $(da/dN)_c$ is higher than $(da/dN)_i$. Accordingly, Equation (8.33a) applies to get to point B with n=2 at which overloading effect is high due to the large drop of $K_{max\ (1)}$ to $K_{max\ (2)}$ and as a result, the condition $(da/dN)_c<(da/dN)_i$ is found at point C and Equation (8.33b) with n=3 applies to get to point D for $K_{max\ (3)}$. If $(da/dN)_c>(da/dN)_i$ at point E and crack grows out of calculated plastic zone due to overload, Equation (8.33a) with n=4 applies to decrease the loading. Further, decrease in loading follows since $(da/dN)_c>(da/dN)_I$ with the same n=4 to reach point G. The same conditional loading continues for the subsequent points H, I, J and so on. The iteration is terminated when the following convergence criterion is satisfied,

$$\text{Tolerance}\leq\left|\frac{K_{\max(n-1)}-K_{\max(n)}}{K_{\max(n-1)}}\right|. \tag{8.33c}$$

At the end of the iterative procedure the current and previous plastic zone sizes become essentially the same, being defined by a low tolerance (say 2%) set in the computer program. Also, to avoid overloading effects, the crack growth may be allowed to advance twice as long as the plastic zone created by the previous ΔK only when $(da/dN)_c>(da/dN)_i$. The crack tip plastic zone size is calculated according to the Dugdale's plastic zone model i.e. $r_p = (\pi/8)(K_{max}/\sigma_{ys})^2$. The procedure is summarised in **Figure 8.23** and comparisons of the efficiency of ASTM and the present methods for near-threshold crack growth measurement at R=0.1 and 5Hz are given in **Table 8.2**.

The threshold fatigue data points at low da/dN values measured with the present method for a uPVC pipe material is shown in **Figure 8.24**.

da/dN (m/cycle)	ΔK_i (MPa $m^{1/2}$)	Tolerance[a] (%)	Duration of test	
			ASTM	Current method
4.3×10^{-9}	0.7	6.67	53.10	17.34
1.49×10^{-9}	0.7	2.17	160.80	22.45
10×10^{-9}	0.2	1.8	-[b]	225.66

[a] Tolerance limit set for the present test method only but ASTM method with C= 0.08 mm^{-1} in Equation (8.31a).

[b] Not available because of unnecessary long times.

Table 8.2 Comparison of the efficiency of ASTM and the present methods for near-threshold crack growth measurement at R=0.1 and 5Hz. [After Kim and Mai, 1988]

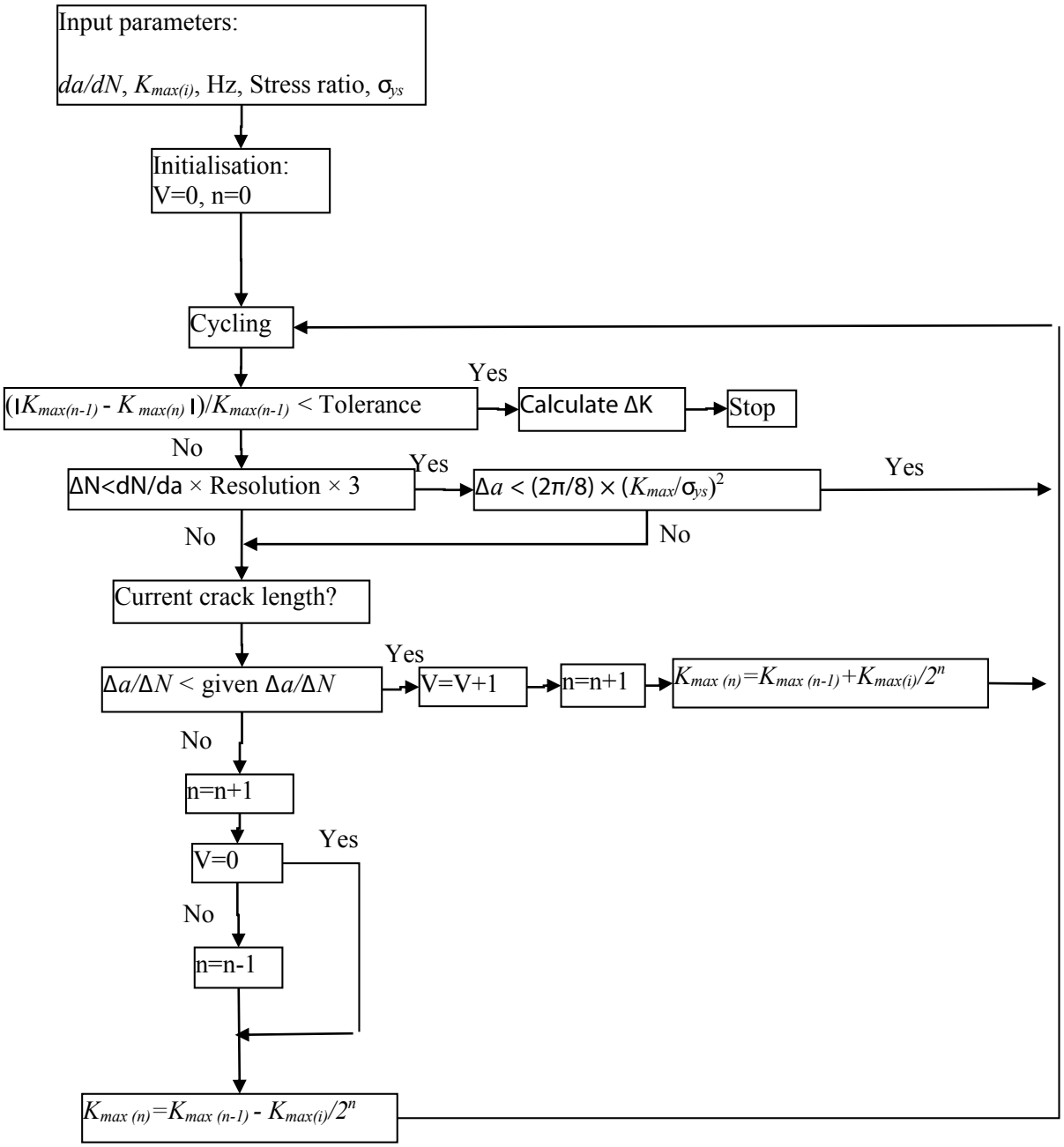

Figure 8.23 Flowchart of the conditional loading by iteration: Resolution is for a travelling microscope for crack length measurement; R is the stress ratio; and σ_{ys} is yield stress. [After Kim and Mai, 1988]

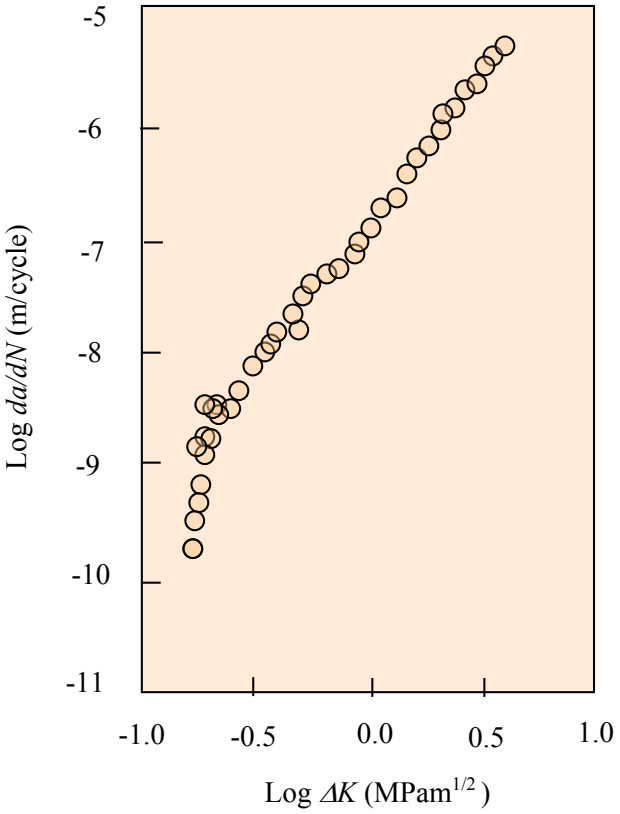

Figure 8.24 Fatigue crack growth of uPVC pipe material.[After Kim and Mai, 1988]

A variation of the method can be made if we keep K_{max} constant for measuring a ΔK corresponding to a da/dN. The same algorithm can be used by replacing K_{max} with ΔK in Equation (8.33a) and (8.33b). Since there is no overloading effect when K_{max} is constant, near – can be obtained more quickly than any other method. However, it is difficult to obtain near-ΔK_{th} for low stress ratios because it is not possible to obtain near- at a particular stress ratio nominated.

8.11 Interpretation of fatigue crack growth in and Diagrams

The incorporation of the threshold ΔK_{th} on a force (P)- displacement (u) diagram may be useful for understanding from a different perspective. As shown in **Figure 8.25 (a)** and **(b)** for stress ratios, R =0 and R > 0 respectively, three different Stages are indicated. Stage I is the area of near-threshold fatigue growth. The crack growth in Stage II is governed under the Paris equation, and Stage III includes near- and catastrophic failure, as also described in **Figure 8.13**. On loading from point 0 to B, fatigue crack starts to grow, which is well below the static fracture point C. As the fatigue crack further grows, stiffness decreases and reaches point D at which catastrophic fracture takes place. When the loading is not high enough, however, for crack growth, the threshold at point A and along the line AE can be identified for specimens with different crack lengths. Threshold-K_{max} can be converted into G (energy release rate) and a G_{th} locus of magnitude $\left(\frac{K^2_{\max\,(th)}}{E})\right)$ for plane stress or $\left(\frac{K^2_{\max\,(th)}}{E}(1-\nu^2)\right)$ plane strain is found, the shape of which of course depends the geometry of the test specimen.

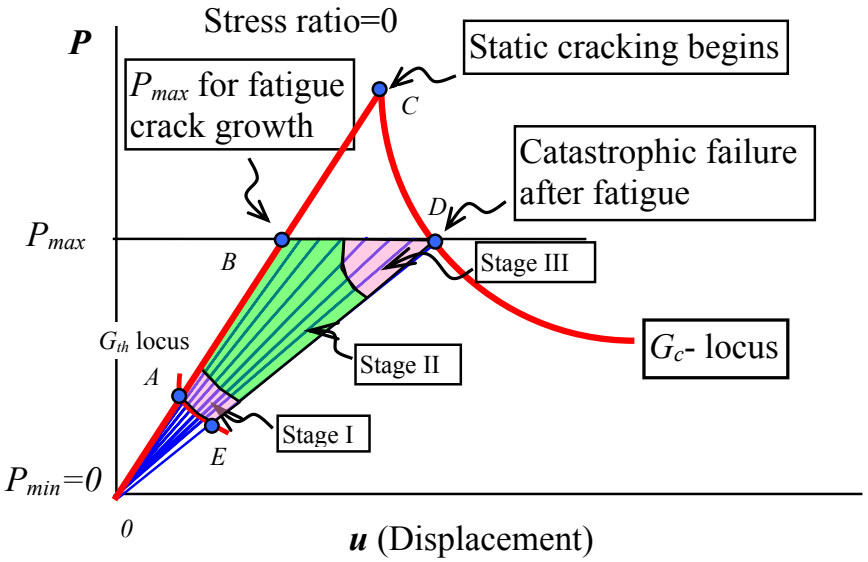

(a)

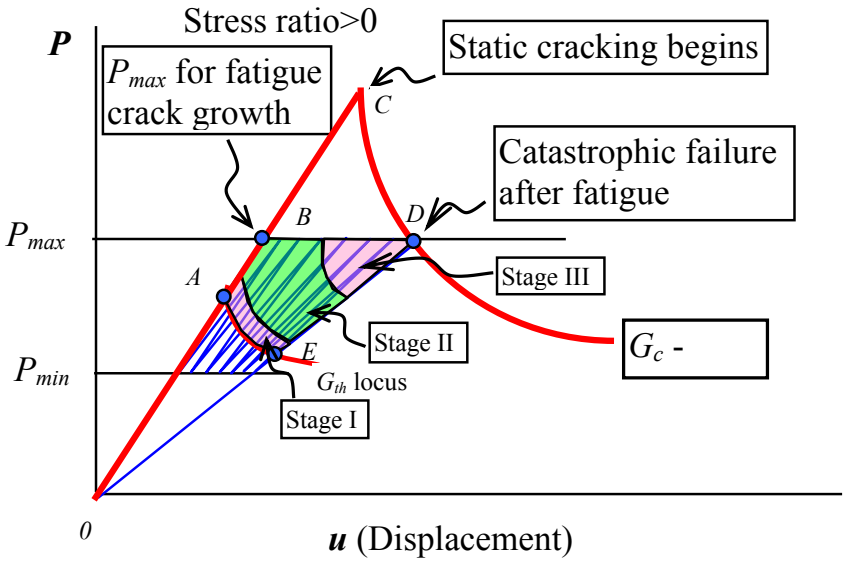

(b)

Figure 8.25 Interpretation of constant load range fatigue crack growth in *P-u* diagram when there is a fatigue threshold G_{th}.

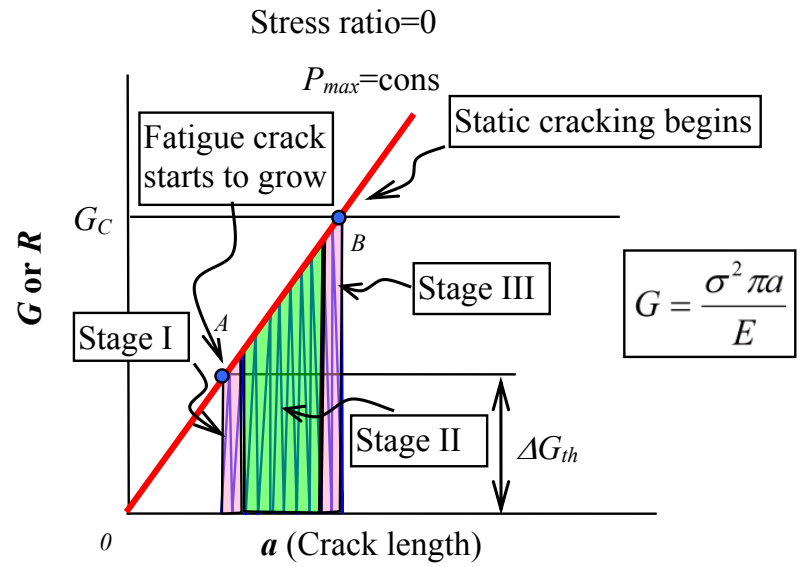

(a)

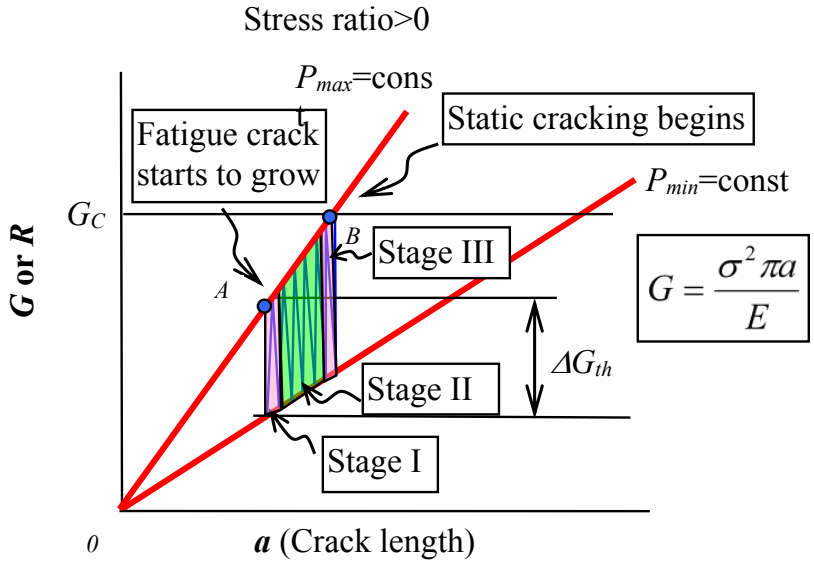

Figure 8.26 Interpretation of constant load range fatigue crack growth in *G-a* diagram when there is a fatigue threshold ΔG_{th}.

The same information (with the same symbols) can be shown on a *G*-*a* (or *R*-*a*) diagram (**Figure 8.26).** For both stress ratios, R = 0 and R > 0, radial lines are drawn for constant loads, P_{max} and $P_{min,}$, and varying crack length (*a*) according to $G = \frac{\sigma^2 \pi a}{E}$. The fatigue crack growth start at point A and grows until point B at which *G* becomes the critical value G_c (or *R*) and catastrophic failure takes place. As the crack length decreases for a given loading condition, Stage I area is found, at which near-threshold fatigue crack growth takes place. Again, the crack growth in Stage II is governed under the Paris equation, and Stage III includes near- and catastrophic failure, as also described in **Figure 8.13**.

8.12 Short crack behaviour in near-threshold fatigue

The short crack is referred to as the one that is comparable with microscopic features such as grain size and small defects. An example of short surface crack behaviour is given in **Figure 8.27.** Its crack growth rate does not vary monotonically but fluctuate, displaying peaks and valleys, which is sensitive to grain boundaries. The short cracks are also sensitive to the orientation of the grain. Thus, the crack growth would smoothly increase if all grains are favourably oriented, or zigzag otherwise, with partial or complete arrest in some cases. Such behaviour is illustrated in comparison with a long crack in **Figure 8.28**. Also, it is obvious that the crack growth rates of short cracks are higher than that of the long crack. The anomalous behaviour of the small cracks does not obey the same propagation laws which we apply to the long cracks. The stress intensity factor range (ΔK) is not as much useful for the fail-safe design if the crack is smaller than some critical length, typically 1 mm in metallic or polymeric materials.

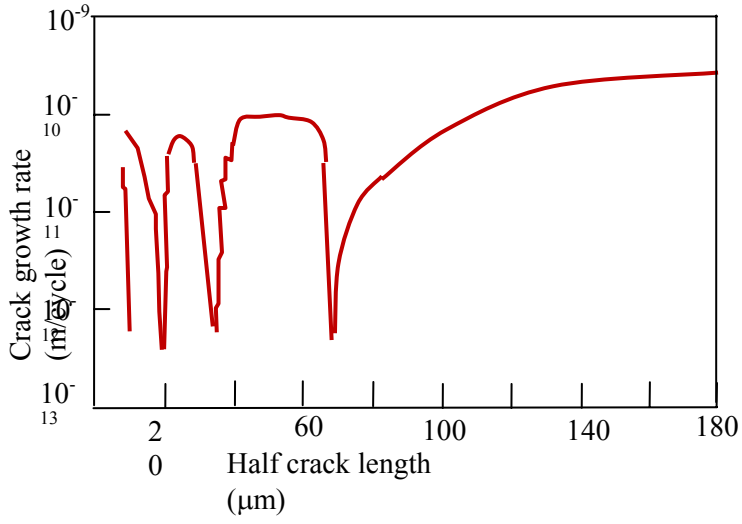

Figure 8.27 Growth behaviour of short cracks in Al 2024-T3 during cyclic loading at R=-1 and 20 kHz. [Blom et al, 1986][53]

Another aspect of short crack is associated with the crack closure. According to one-dimensional plastic zone size (r_p) equation

$$r_p = \frac{K_I^2}{2\pi\sigma_{ys}^2} = \frac{\sigma^2 a}{2\sigma_{ys}^2}, \qquad \text{(bis 6.1a)}$$

r_p is proportional to the crack length (a). In other words, as the crack length decreases, the compressive residual stress created by the plastic deformation decreases and hence the crack closure diminishes. Some supporting evidence is given in **Figure 8.29**. Near-threshold stress intensity for small and large cracks are shown in the figure for difference between effective ΔK_{th} and apparent ΔK_{th} due to diminished crack closure effect.

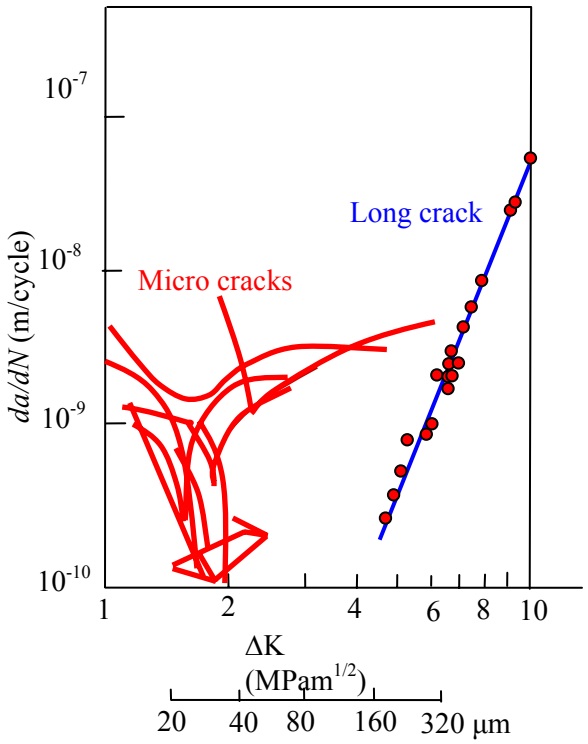

Figure 8.28 Crack growth behaviour of short and long cracks in aluminium alloy. [After Chan and Lankford, 1983][54]

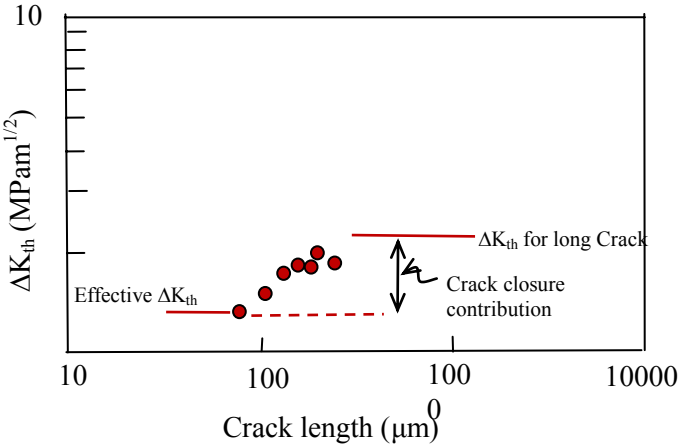

Figure 8.29 Data for threshold stress intensity for small and large cracks for difference between effective ΔK_{th} and apparent ΔK_{th} due to diminished crack closure effect. [Blom et al, 1986]

Scatter is an essential feature of short-crack data because individual small cracks behave differently. The analysis based on continuum mechanics for long cracks is hardly applicable to the anomalous behaviour of the short cracks. Then, an important question arises as to how we conduct the fail-safe design against small cracks. The important steps may be to

a) define the difference between short and long cracks,
b) find common variables between short and long cracks, and
c) apply the relevant theories for short and/or long cracks.

We know that the behaviour of small cracks is reflected in a S-N curve with scattered data points and the long crack is still validly treated within the framework of continuum mechanics. We also know that the common variables are applied stress and crack length (a), allowing us to display two different equations based on the two different approaches together on a σ-a plane. The stress intensity factor for threshold (ΔK_{th}) with a corresponding applied stress range ($\Delta\sigma_{th}$) is given by

$$\Delta K_{th} = \Delta\sigma_{th}\sqrt{\pi a} \tag{8.34a}$$

so that

$$\log \Delta\sigma_{th} = \log \frac{\Delta K_{th}}{\sqrt{\pi}} - \frac{1}{2}\log a\,. \tag{8.34b}$$

This equation is plotted on logarithmic scales in **Figure 8.30** with the fatigue limit ($\Delta\sigma_0$). The fatigue limit is independent of the crack length.

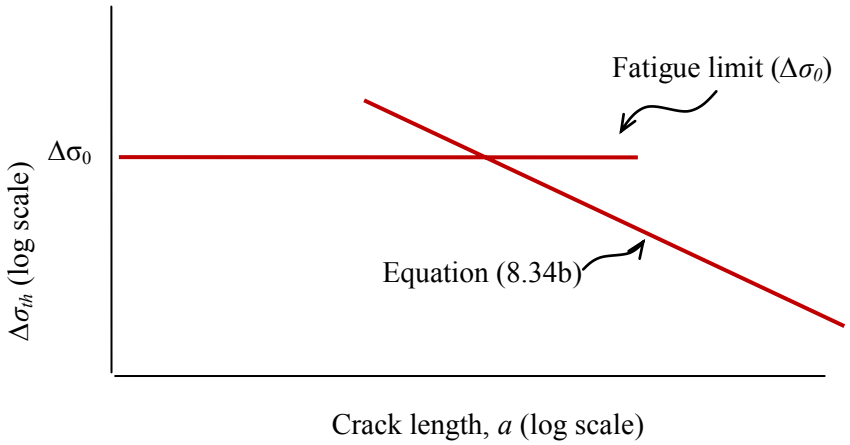

Figure 8.30 Kitagawa plot[55] of threshold stress range $\Delta\sigma_0$ as a function of crack length and fatigue limit ($\Delta\sigma_0$).

The limitations of the stress intensity factor approach are clear in the figure. As the crack length approaches zero, $\Delta\sigma_{th}$ approaches ∞ with a slope of 0.5 according to Equation (8.34b). However, we know that if the crack length is zero, for a perfectly polished specimen, the threshold stress for fatigue is not infinity, but is equal to the fatigue limit ($\Delta\sigma_0$). Therefore, the crack length at which two lines intersect with each other becomes the *demarcation point* between short and long cracks. The representation shown in **Figure 8.30** is often called a 'Kitagawa' plot after one of its originators. The plot also explains that the small cracks grow at applied ΔK values lower than ΔK_{th} measured for long cracks.

In practice, the experimental data for near-threshold takes the form shown in **Figure 8.31**. The measured threshold data points deviate from Equation (8.34) for the long crack and eventually merge with the fatigue limit. The curved region on the figure is lower than the fatigue limit or the long crack threshold stress. It may be useful to describe the characteristics of two different crack lengths in addition to the *demarcation point* (a_0) although those are not explicitly definitive due to the smooth transition:

a) a_1 is the length at which the fatigue behaviour deviates from the fatigue limit. As such, it is the longest crack length at which the fatigue limit is still a material property. Therefore, if inherent crack lengths of a material are longer than a_1, its fatigue limit may be lowered and hence is no longer the material property. Accordingly, it is possible that some materials would not have a fatigue limit if they contain relatively long cracks produced during manufacturing.
b) a_2 is the length at which its behaviour deviates from that of long-crack for the transitional behaviour.

Such a transitional behaviour can be described by adding a constant length (a_0) to the crack length (a), i.e.

$$\Delta K_{th} = \Delta\sigma_{th}\sqrt{\left[\pi\left(a + a_0\right)\right]}. \qquad (8.35)^{56}$$

As the crack length decreases, according to this equation, the constant length (a_0) constitutes an increasing fraction of (a_0 +a) until at very short lengths. An example is given in **Figure 8.32(a)** for a_0 =2 and ΔK_{th} = 20. The curve and fatigue limit are dependent on the choice of a_0 value. If we choose a shorter length a_0 =1, the curve displays a higher fatigue limit as shown in **Figure 8.32(b)**. Equation (8.35) may be useful for an initial estimation using only near threshold-ΔK_{th}. The value of a_0, however, does not a physical basis for understanding the transitional behaviour.

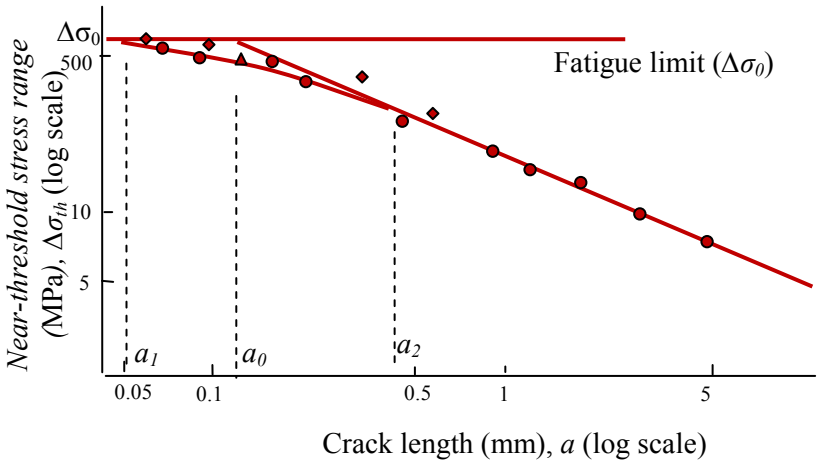

Figure 8.31 Typical experimental behaviour of short cracks, plotted on the Kitagawa diagram. [After Kitakawa and Takahashi, 1976]

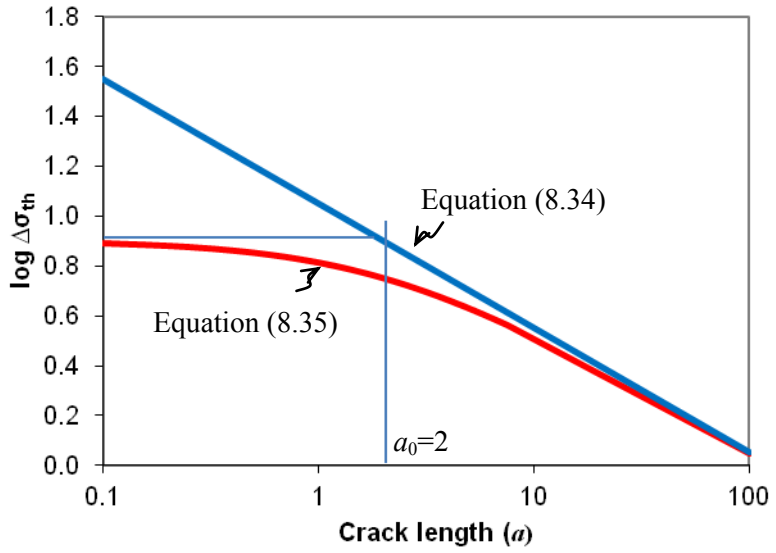

(a)

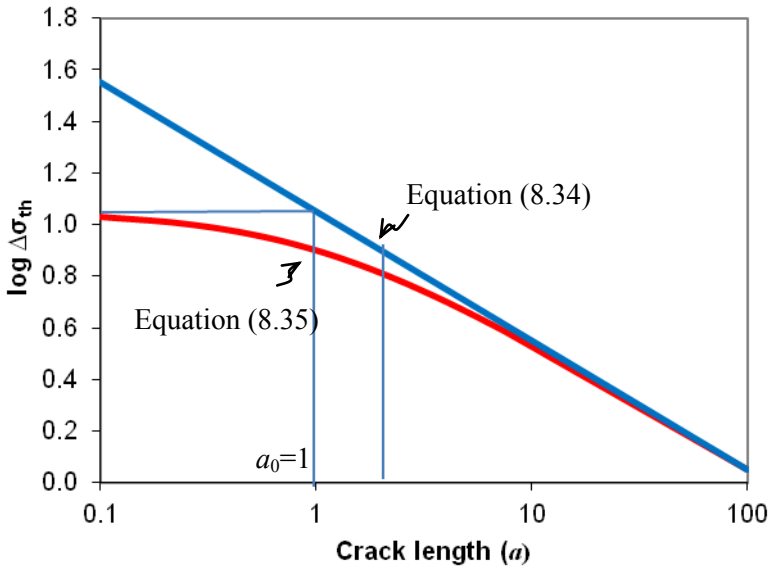

(b)

Figure 8.32 Comparison of Equations (8.34) and (8.35) for different crack lengths (a_0) = 1 and 2 with $\Delta\sigma_{th}$ =31.5 (or log ($\Delta\sigma_{th}$) =1.5).

9 Endnotes

1. H.S. Kim and P. Ma, "Correlation between stress-whitening and fracture toughness in rubber modified epoxies", Journal of Applied Polymer Science, Vol 61, pp. 659–662, 1996.
2. H.S. Kim, "Fracture Surface Morphology in Thermosets Modified with Hollow Microspheres", Journal of Applied Polymer Science, Vol 105, pp. 3287–3294, 2007.
3. M.M. Frocht, Photoelasticity, New York: John Wiley & Sons, Inc., 1941.
4. H.S. Kim and P. Ma, "Mode II fracture mechanisms of PBT modified brittle epoxies", Journal of App.lied Polymer Science, Vol 69, pp. 405–415, 1998
5. H.M. Westergaard, "Bearing pressures and cracks", Journal of App.lied Mechanics, Vol. 61, pp. A49–53, June 1939.
6. G.C. Sih, P.C. Paris and F. Erdogan, Crack-tip, stress-intensity factors for plane extension and plate bending problems, Transactions of the ASME, Journal of Applied Mechanics, pp. 306–312, June 1962.
7. D.S. Dugdale, "Yielding of Steel Sheets Containing Slits", Journal of Mechanics and Physics of Solids, Vol. 8, pp. 100–101, 1960.
8. A.G. Atkins and Y.-W. Mai, "Elastic and Plastic fracture", Ellis Horwood Limited, 1988.
9. J.C. Newman and I.S. Raju, "An empirical stress intensity factor equation for the surface crack", Engineering Fracture Mechanics, Vol. 15, pp. 185–192, 1981.
10. F. Erdogan and G.C. Sih, On the crack extension in plates under plane loading and transverse shear, Journal of Basic Engineering, pp. 519–727, December 1963.
11. F. Erdogan and G.C. Sih, "On the crack extension in plates under plane loading and transverse shear", Journal of Basic Engineering, pp. 519–727, December 1963.
12. G.R. Irwin, "Plastic zone near a crack and fracture toughness", Mechanical and Metallurgical Behaviour of Sheet Materials, Proceedings, Seventh Sagamore Ordnance Materials Conference, pp. IV63–78, 1960.
13. G.T. Hahn, P.N. Mincer and A.R. Rosenfield, "The Fe-3Si steel etching technique for local strain measurement", Experimental Mechanics, 11(6), June 1971, pp. 248–253.
14. G.T. Hahn, P.N. Mincer and A.R. Rosenfield, "The Fe-3Si steel etching technique for local strain measurement", Experimental Mechanics, 11(6), pp. 248–253, June 1971.
15. G.T. Hahn, A.K. Mukherjee and A.R. Rosenfield, "Plastic zone formation and stable crack growth in high-strength alloy sheets", Engineering Fracture Mechanics, Vol 2, pp. 273–286, 1971.
16. A.J. Kinloch and S.J. Shaw, "The fracture resistance of a toughened epoxy adhesive", Journal of Adhesion, Vol 12, p. 59, 1981.
17. A.J. Kinloch and S.J. Shaw, "The fracture resistance of a toughened epoxy adhesive", Journal of Adhesion, Vol 12, p. 59, 1981.
18. J.E. Strawley, "Wide range stress intensity factor expression for ASTM E 399 standard fracture toughness specimens", NASA Technical Memorandum, NASA TM X – 71881, March 1976.

19. G.R. Irwin, "Structural aspect of brittle fracture", App.lied Materials Research, Vol 3, pp. 65–81, 1964.
20. A.A. Griffith, The phenomena of rupture and flow in solids, Philosophical Transactions of the Royal Society of London. Series A., Vol 221, pp. 163–198, 1921.
21. R.S. Rivlin and A.G. Thomas, Journal of Polymer Science, Vol 10, p. 291, 1953.
22. C.R. Joe and B.H. Kim, International Journal of Fracture, Vol 44: p. 15, 1990.
23. B. Cotterell and J.K. Reddel, International Journal of Fracture, Vol 13, p. 267, 1977.
24. Y.-W. Mai, and B. Cotterell, International Journal of Fracture, Vol 24, p. 229, 1984.
25. C.M. Muscat-Fenech and A.G. Atkins, International Journal of Fracture, Vol 67, pp. 69–80, 1994.
26. J.S.S.Wong, D. Ferrer-Balas, R.K.Y. Li, Y.-W. Mai, M.L. Maspoch and H.J. Sue, Acta Materialia, Vol 51, p. 4929, 2003.
27. H.S. Kim, and J. Karger-Kocsis, "Tearing resistance of some co-polyester sheets", Acta Materialia, Vol 52, pp. 3123–3133, 2004.
28. H.S. Kim, and J. Karger-Kocsis, "Tearing resistance of some co-polyester sheets", Acta Materialia, Vol 52, pp. 3123–3133, 2004.
29. G.P. Marshal, J.G. Williams and C.E. Turner, "Fracture toughness and absorbed energy measurements in impact tests on brittle materials", Journal of Materials Science, Vol 8, pp. 949–956, 1973.
30. J. Goodman, "Mechanics app.lied to engineering", Vol. 1, Longmans, Green and Co. Ltd, 9th Edition, 1942.
31. W. Hwang and K.S. Han, "Fatigue of composites – fatigue modulus concept and life prediction", Journal of composite materials, Vol 20, pp. 154–165, 1986.
32. H.S. Kim and J. Zhang, "Fatigue damage and life prediction of glass/vinyl ester composites", Journal of Reinforced Plastics and Composites, Vol 20, pp. 838–848, 2001.
33. H.S. Kim and J. Zhang, "Fatigue damage and life prediction of glass/vinyl ester composites", Journal of Reinforced Plastics and Composites, Vol 20, pp. 838–848, 2001.
34. J. Goodman, "Mechanics app.lied to engineering", Vol. 1, Longmans, Green and Co. Ltd, 9th Edition, p. 634, 1942.
35. A.Z. Palmgren, Z. Ver. Dt. Ing Vol 68, p.339, 1924.
36. M.A. Miner, "Cumulative damage in fatigue", Journal of App.lied Mechanics, Vol. 12 (3), pp. A159–A164, 1945.
37. P. Paris and F. Erdogan, "A critical Analysis of Crack Propagation Laws", Transactions of the ASME, pp. 528–534, December 1963.
38. S. Glasstone, K.J. Laidler, and H. Eyring, "The theory of rate processes", McGraw-Hill, New York, 1941.
39. K. Krausz and A.S. Krausz, Proceedings of the 11th Canadian Fracture Conference edited by A.S. Krausz, Ottawa, Canada, (Martinus Nijhoff, Dordrecht, Boston, 1984), p. 131, June 1984.
40. H.S. Kim and Y.W. Mai, "Effect of temperature on fatigue crack growth in unplasticised polyvinyl chloride (uPVC)", Journal of Materials Science, Vol 28, pp. 5479–5485, 1993.

41. G.P Marshall, L.H. Coutts and J.G. Williams, "Temperature effects in the fracture of PMMA", Journal of Materials Science, Vol. 9, p. 1409, 1974.
42. J.G. Williams, "A model of fatigue crack growth in polymers", Journal of Materials Science, Vol. 12, p. 2525, 1977.
43. H.S. Kim and X.M. Wang, "Temperature and frequency effects on fatigue crack growth of uPVC", Journal of Materials Science, Vol 29, pp. 3209–3214, 1994.
44. Wolf Elber, "The significance of fatigue crack closure", Damage Tolerance in Aircraft Structures, ASTM STP486, pp. 230–242, 1971.
45. O.E.Wheeler, "Spectrum loading and crack", Journal of Basic Engineering, Transactions of the ASME, pp. 181–186, 1972.
46. Wolf Elber, "The significance of fatigue crack closure", Damage Tolerance in Aircraft Structures, ASTM STP486, pp. 230–242, 1971.
47. C.M. Hudson, "Effect of stress ratio on fatigue-crack growth in 7075-T6 and 2024-T4 aluminum specimens", NASA TN D-5390, National Aeronautics and Space Administration, 1969.
48. Wolf Elber, "The significance of fatigue crack closure", Damage Tolerance in Aircraft Structures, ASTM STP486, pp. 230–242, 1971.
49. J.M. Barsom, "Fatigue-crack growth under variable-amplitude loading in ASTM A514-B steel", in Progress in Flaw Growth and Fracture Toughness Testing, ASTM STP 536, American Society for Testing and Materials, pp. 147–167, 1973.

50. A. Saxena, S.J. Hudak, J.K. Donald, and D.W. Schmidt, "Computer-controlled decreasing stress intensity technique for low rate fatigue crack growth testing", Journal of Testing and Evaluation, Vol 6, p. 167, 1978.
51. J.P. Bailon, P. Chappuis, and J. Masourrave, "A rapid experimental method for measuring the threshold stress intensity factor" in 'Fatigue Thresholds' (Ed. J. Backlund, A.F. Blom and C.J. Beevers), EMAS, Warly, UK, Vol. 1, p. 113, 1981.
52. H.S. Kim, Y.W. Mai and B. Cotterell, "Fatigue crack propagation in unplasticized polyvinylchloride (uPVC), Part 2; Near-threshold fatigue crack growth", Polymer, Vol 29, pp. 277–286, 1988.
53. A.F. Blom, A. Hedlund, W. Zhao, A. Fathulla, B. Weiss, and R. Stickler, "Short fatigue crack growth behaviour in AL 2024 and Al 7475, in The Behaviour of Short Fatigue Cracks, EGF Pub. 1 (Edited by K.J. Miller and E.R. De los Rios) Mechanical Engineering Publication, London, pp. 37–66, 1986.
54. K.S. Chan and J. Lankford, "A crack-tip strain model for the growth of small fatigue cracks", Scripta Metallurgica, Vol. 17, pp. 529–532, 1983.
55. H. Kitagawa and S. Takashima, "Application of fracture mechanics to very small cracks or the cracks in the early stage", In: Proceedings of the Second International Conference on Mechanical Behavior of Materials. Metals Park, OH: ASM, p. 627–31, 1976.
56. M.H. El Haddad, K.N. Smith, and T.H. Topper, "Fatigue crack propagation of short cracks", Journal of Engineering Materials and Technology", Transactions of the ASME, Vol 101, pp. 42–46, 1979.